Imperial College London

Towards Attosecond Measurement of Dynamics in Multi-Electron Systems

Tsen-Yu (Judy) Hung

May 2014

Thesis submitted in partial fulfilment of the requirements for the degree of Doctor of Philosophy of Imperial College London and the Diploma of Imperial College

Laser Consortium, Quantum Optics and Laser Science
Department of Physics, Blackett Laboratory
Imperial College London

Declaration

I proffer this thesis as my own work which I have done to satisfy the Ph.D. requirements. Any work by others has been either cited, quoted or accredited.

Abstract

Recent developments in laser science have made it possible to experimentally study ultrafast electron dynamics in atoms and molecules directly by using ultrashort pulses on the order of tens of attoseconds. It is paramount, both for current understanding and planning of future experiments and applications, that we decipher how short pulses interact with the medium. We model attosecond dynamics of multi-electron systems following three themes: (1) propagation and distortion of pulses in absorbing noble gases, (2) simulation of atoms and molecules under the effects of pump and probe pulses, (3) coherence and polarization effects on transient absorption.

First, using the Kramers-Kronig relations and a fast and stable numerical algorithm based on Möbius transformations, we model the distortion of XUV pulses propagating in noble gases. Our simulations show rich features including pulse stretching, partial narrowing, partial apparent super-luminality, and tail development.

Second, we deploy the density matrix formalism using Lindblad terms and the three Hilbert spaces method, incorporating multi-channel and Auger ionization compactly and consistently, to model coherence observed in pump-probe attosecond transient absorption studies of Kr II. We explain how coherent noble cation states are produced. Density matrix elements for the excited Kr II $3d_{3/2}$ and $3d_{5/2}$ levels caused by a resonant z-polarized 80 eV 150 as probe pulse are simulated and the resulting population densities and induced dipole moments are analyzed, including nonlinear contributions. In order to model pulse propagation, we develop absorption theory for arbitrary polarization angle and point out how coherence effects distort

the Beer-Lambert law and discuss experimental implications.

Third, we investigate non-adiabatic effects in attosecond dynamics in molecules driven by a laser field. We use the Algebraic Diagrammatic Construction method and Arnoldi-Lanczos TDSE programs to simulate N_2 and oligocenes for 400 nm, 800 nm and 1.6 μm wavelengths with various laser intensities and polarizations. We determine the onset of non-adiabaticity in N_2, benzene and naphthalene.

Last, but not least, I describe my experimental contribution to the new Imperial College beamline.

To my children

Acknowledgements

First, I would like to thank my thesis supervisor, Prof. Jon Marangos, for giving me the opportunity to obtain my Ph.D., for providing my thesis topic and for instrumental guidance throughout.

Special thanks go out to Prof. Vitali Averbukh and Marco Ruberti for providing the ADC and ALTDSE codes and a pleasant collaboration.

I would like to thank Prof. Jo Haigh and Prof. Lesley Cohen for their help and support during my Ph.D.

Both for his support during my Princeton PPL years and introducing me to Imperial College, I would like to thank Prof. Steve Cowley of the Culham Centre for Fusion Energy.

I would like to thank Dr. Bridgette Cooper and Laila Bahmanpour for all their assistance with MOLCAS, Martin Morris for IT support, and Simon Burbidge for HPC support.

Thanks to Judith Baylis, Loli Sanchez, and Marcia Salviato for all their assistance.

Last but not least, thanks go out to Prof. Peter Hagelstein of MIT for introducing me to laser physics and starting me on this journey, and to the late Prof. Eugene Wigner for pointing me to the heart of the matter: "Where is the atom?"

Contents

List of Figures

Chapter 1

Introduction

Since the development of ultrashort pulsed lasers, the study of ultrafast phenomena has become a reality. With time resolution down to femtoseconds, or even attoseconds, the harnessing of such light pulses opens the door to the exploration of the dynamics of molecules and atoms. Time-resolved studies of such processes give new meaning to the study of atomic and molecular physics, as the ability to capture electron dynamics, frame-by-frame, as in movie making, can provide revelations and insights into the fundamentals of chemical reactions and atomic processes. Time-resolved spectroscopy is essential for advancing further understanding of nanotechnology and beyond.

1.1 Motivation

Recent developments in laser science have made it possible to experimentally study ultrafast electron dynamics in atoms and molecules directly by using ultrashort pulses on the order of tens of attoseconds[1]. The semi-classical Bohr model of the hydrogen atom sets the relevant timescale of 152 as for the orbital period of the electron in the ground state.

It is paramount, both for current understanding and planning of future experiments and applications, that we decipher how short pulses are re-shaped by propagation through a

sample. Experimentalists have been successful in producing ultrashort XUV pulses, but the practical question is: to what extent can these pulses retain their integrity when travelling through a gaseous medium. To this end, we design a technique to compute this process and perform numerical simulations. Our results show the limits on pulse width due to the necessary relationship between distortion and absorption which is a direct result of causality.

Experimental advances[2] have made it possible to obtain partial information on density matrices for multi-level systems using transient attosecond absorption. In order to get a firm handle on the relationship between the density matrix and the experimental absorption result, we perform a detailed analysis for the case of Kr II. As a theoretical basis for the analysis of coherent absorption data, we develop a Liouvillian model for the description of ionization from Kr I to Kr II and from Kr II to multi-cations. Our simulations allow for how pump pulses coherently populate the lower states of Kr II, and how density matrix elements evolve in time under resonant driving by the probe pulse. The simulation allows us to compare multi-level dynamics with our understanding of two-level systems and allows us to study nonlinearities and indicate the range of applicability of perturbation theory.

In pursuance of understanding probe pulse propagation in an absorbing medium, inclusive of coherence effects, we develop the necessary perturbative absorption theory. First, this theory provides for verifiable predictions regarding the polarization angle dependence. Second, it allows us to solve coherent absorption propagation which explicitly violates the Beer-Lambert law. We explain how these findings materially affect the translation from experimental absorption data to implied density matrix elements.

The Imperial College QOLS Theory group has been developing numerical simulations for molecules for studying their electron dynamics. One of the current topics of research is: for what molecules and for what pump wavelengths and laser intensities do non-adiabatic effects become substantial?

1.2 Organization of Thesis

We start with a background description of the theory and technology of strong field physics in Chapter 2, describing the theory and practice of high harmonic generation. The author's contribution to the new beamline can be found in Appendix A.

In Chapter 3, we use the Kramers-Kronig relations to model a Gaussian pulse propagating in an absorbing medium. We perform numerical calculations using a customized analytic method, which utilizes a special Möbius transformation in the complex plane. We discuss and present our results for a broad band Gaussian pulse centered at 15 eV - 30 eV propagated through a noble gas, such as Ar and He, at different density-distances.

In Chapter 4, we use the density matrix formalism using Lindblad terms and three Hilbert spaces to model coherence observed in pump-probe attosecond transient absorption studies of Kr II. We not only use Lindblad terms to describe Auger decay of Kr II to Kr III and higher, but we also develop the Lindblad formalism to describe multichannel ionization from Kr I to Kr II that is both compact and physically consistent. The Kr parameters, such as dipole moments, have been generated using the relativistic atomic package, GRASP2K, and a detailed comparison with others, including MIT's has been provided.

In Chapter 5, we obtain results for coherent ionization using few-cycle NIR 800 nm pump laser fields for Ne, Ar, Kr and Xe. We explain how coherent Kr II states are produced including the special symmetry of the density matrix due to the electric dipole interaction with the pump. Density matrix elements for the excited Kr II $3d_{3/2}$ and $3d_{5/2}$ levels resulting from a resonant z-polarized 80 eV 150 as probe pulse are simulated. The resulting population densities and induced dipole moments, for resonant absorption in this multi-level system, are analyzed and decomposed into nonlinear contributions up to order four.

In Chapter 6, we revisit the topic of pulse propagation. In order to model probe pulse propagation in a Kr II gas, we develop perturbative absorption theory for arbitrary linear polarization angle of the probe pulse vs. that of the pump pulse. It is shown that coherence

effects are strongly polarization angle dependent, which provides an experimental avenue to learn more about the underlying density matrix. The ubiquitous Beer-Lambert law is based on the assumption of direct proportionality between induced polarization and the incident electric field for each spectral frequency independently. However, in the presence of coherence, this assumption is not true and leads to a material difference in pulse propagation. We show how coherence effects distort the Beer-Lambert law and discuss experimental implications.

In Chapter 7, we investigate non-adiabatic effects in attosecond dynamics in molecules. We use the Algebraic Diagrammatic Construction (ADC) and Arnoldi-Lanczos TDSE programs by Averbukh *et al.* We perform extensive simulations for N_2 and oligocenes for 400 nm, 800 nm and 1.6 μm wavelengths with various laser intensities, as well as differently oriented linear pulse polarizations plus circular polarization. While non-adiabatic effects for small molecules are small for the range of photon energies and pulse intensities we studied, they are substantial for larger molecules.

We conclude the thesis with a summary.

Chapter 2

Background to Strong Field Physics

We discuss the interaction of light and matter, strong field physics for high harmonic generation (HHG), and the Three-Step Model.

2.1 The Interaction of Light and Matter

The electromagnetic interaction between light and matter described in this thesis shows up in three incarnations. First are the Maxwell equations which provide a classical macroscopic description of the propagation of electric and magnetic fields in a medium which we shall deploy in Chapter 6 in our analysis of pulse propagation in the presence of coherence. The Maxwell equations in SI units [3] are,

$$\begin{aligned} \nabla \cdot D &= \rho & \nabla \cdot B &= 0 \\ \nabla \times E &= -\partial_t B & \nabla \times H &= J + \partial_t D \\ D &= \epsilon_0 E + P & B &= \mu_0 (H + M) \end{aligned} \tag{2.1}$$

where E is the electric field, B is the magnetic field, ρ is the free charge density, J is the free current density, P is the polarization density (i.e. the electric dipole moment per volume), M

is the magnetization density (i.e. magnetic dipole moment per volume). The auxiliary fields D and H are defined by the last line, sometimes called the constitutive relations.

Second, we will use the Lorentz force equation in this chapter in the non-relativistic limit to model classical orbits of electrons in the three-step-model (TSM) of high harmonic generation (HHG).

The Lorentz force law is given by [4],

$$\frac{d}{dt}\frac{m\vec{v}}{\sqrt{1-v^2}} = q\left(\vec{E} + \vec{v}\times\vec{B}\right) \tag{2.2}$$

where m is the rest mass, v is the velocity, q is the electric charge of the particle.

Third, assuming the dipole approximation, we use a product of the incident electric field and the dipole operator as an interaction term in the quantum Hamiltonian for an atom or molecule, known as the length gauge. This semiclassical description of light matter interaction can be solved with the time-dependent Schrodinger equation, or more generally with the Liouville-von Neumann equation for density matrices which we do in Chapter 4.

In order to produce HHG radiation, the electric field of the pump pulse must be sufficiently strong. We now estimate an upper-bound for how strong this field has to be and the corresponding peak intensity. For simplicity we shall focus on the hydrogen atom for our estimation of what is required to tear away an electron from an atom. The force between two electric charges is:

$$\mathbf{F_E} = \frac{q_1 q_2}{4\pi\epsilon_0 r^2}\hat{\mathbf{r}} \tag{2.3}$$

where $\mathbf{F_E}$ is the electric force of the charges, q_1 and q_2, with distance r and $\hat{\mathbf{r}}$ is the unit vector pointing from q_1 to q_2, and ϵ_0 is the permittivity constant in free space. The Bohr radius is defined as:

$$r_{\text{Bohr}} = \frac{4\pi\epsilon_0\hbar^2}{me^2} \tag{2.4}$$

where $\hbar$ is the reduced Planck constant, m is the mass of the electron, and e is the electric charge. The Bohr radius is equal to approximately 0.53 Å. Thus, the electric field is $5.124\times$

10^{11} V/m. The intensity of a plane wave is related to the electric field as [5],

$$I = \frac{1}{2} v_p \epsilon_0 \epsilon_1 \mu_1 |E|^2 = \frac{1}{2} c \epsilon_0 n |E|^2 \tag{2.5}$$

where v_p is the phase velocity, n is the refractive index, and c is the vacuum velocity of light. Therefore, the intensity is 3.486×10^{20} Wm^{-2} or 3.486×10^{16} Wcm^{-2}. This intensity can be achieved by very powerful lasers which only have become achievable recently.

2.2 High Harmonic Generation (HHG)

2.2.1 Background and Theory

The phenomenon of high harmonic generation is a manifestation of intense interactions of light and matter. The study of interaction of light and matter has been completely transformed by the invention of the laser (Light Amplification by Stimulated Emission of Radiation). When applied with sufficiently high intensity, laser beams can cause nonlinear effects. Experimentally this was demonstrated by Franken *et al.* with a ruby laser in 1961 [6], soon after the invention of lasers. This second harmonic generation (SHG) in Franken's experiment was, however, quite weak, with an energy conversion of about 10^{-8}. Anecdotally, when you check the original publication [6], no evidence remains in the reproduced graph, purportedly due to a molysomophobic editor!

In the interest of simplicity, one would like to treat electrons semiclassically, which turns out to be a valid approach. The mitigating circumstances being that a high photon number allows for a classical treatment of the E field, the electrons spend most of their orbit time in a continuum and away from a bound state, and lastly the electrons stay non-relativistic. Consequently, the order of the high harmonics that can be reached can be shown to be determined by examining the energy that an electron can acquire under intense electric fields plus the ionization potential. A short pulsed laser, such as a femtosecond laser, with mJ of output energy can produce an electric field strong enough to facilitate tunnel ionization,

whereby the Coulomb potential of the atom is distorted. As the electrons are freed and being accelerated within the laser cycle, the electrons acquire energy from the driving laser. When the electric field turns negative in the laser cycle, the electrons return and recollide with the ions and release the kinetic energy acquired and the ionization potential as photon energy. One can calculate this energy by describing the motion of the electrons classically from Newton's law of motion in an electromagnetic field,

$$m\vec{\mathbf{a}} = -e(\vec{\mathbf{E}} + \vec{\mathbf{v}}_e \times \vec{\mathbf{B}}) \tag{2.6}$$

where m is the mass of the electron, $\vec{\mathbf{a}}$ is the acceleration experienced by the electron, e is the electric charge, $\vec{\mathbf{E}}$ is the electric field, $\vec{\mathbf{v}}_e$ is the velocity of the electron, and $\vec{\mathbf{B}}$ is the magnetic field. Note that the Lorentz force, for electron orbits leaving and returning to the ion, has the effect of shifting the electron sideways putting it at a distance fron the ion and consequently suppressing HHG. Because for a monochromatic linearly polarized elctromagnetic wave the amplitudes E and cB are identical the relative importance of the Lorentz force is v/c. For non-relativistic regimes, therefore, the Lorentz force can be ignored.

With the assumption that the electric field exerted is sinusoidal and for simplicity, in one-dimension, the equation of motion reduces to,

$$\begin{aligned} ma &= -eEsin\omega t \\ \frac{dv}{dt} &= -\frac{eE}{m}sin\omega t \\ v &= \frac{eE}{\omega m}cos\omega t \end{aligned} \tag{2.7}$$

where E is the amplitude of the electric field, ω is the angular frequency of the field, and v is the velocity. From this, we can solve for the ponderomotive energy U_p as the average cycle energy of the electron in the laser field,

$$U_p = \frac{1}{2}m\langle v^2\rangle = \frac{1}{2}\frac{e^2E^2}{m\omega^2}\langle cos^2(\omega t)\rangle = \frac{e^2E^2}{4m\omega^2} \tag{2.8}$$

The intensity, I, of electromagnetic waves such as a laser is related to the electric field

amplitude, E, and refractive index n by [5],

$$I = \frac{1}{2} c\epsilon_0 n |E|^2 \tag{2.9}$$

Substituting this equation into the expression for ponderomotive energy, one obtains the relation of ponderomotive energy as a function of the intensity and wavelength (λ) of the laser,

$$U_p = \frac{e^2}{8m\pi^2 c^3 \epsilon_0} \frac{1}{n} I\lambda^2 \tag{2.10}$$

For a Ti:Sapphire laser of 800 nm in wavelength, at an intensity of 10^{14} W cm^{-2}, the ponderomotive energy U_p is about 6 eV. By using a TOPAS laser at about 2μm wavelength, with the same intensity, this energy is multiplied by more than sixfold, close to 40 eV.

2.2.2 Derivation of the HHG Cutoff in the Three-Step Model

The Three-Step-Model (TSM) first proposed by Corkum *et al.*[7] makes a long list of assumptions and simplifications, using aspects of both classical and quantum mechanics while avoiding a full treatment and still managing to paint a very useful and quantitatively relevant physical picture of the HHG process. It assumes that the electron tunnels out into the continuum due to the electric field of the ambient laser field at zero initial velocity. The electron is then swept away from and back to the ion due to the electric field; this is treated in a purely classical manner. The process is non-relativistic and the magnetic field of the ambient field is ignored. Also, the electric field of the ion itself is ignored. The electron is recaptured by the ion and high harmonic photons are emitted. We also add the assumption of a linearly polarized laser field, as elliptic polarization will cause the returning electron to miss the ion. A fuller quantum-mechanical treatment [8] is needed to accurately explain the spectral line intensities, capturing issues such as the overlap of the electron and ion wavepackets and the importance of the flight time of the electron to wavepacket spreading.

During the sweep away and back the electron can classically pick up a maximum amount of kinetic energy, which we derive here, and which is the cause of the sharp cutoff of the HHG

spectrum. With the assumption that the electron is released into the continuum with zero velocity and at the origin, we can solve for the motion of the electron,

$$\begin{aligned} ma &= -eEcos(\omega t) \\ mv &= -\frac{eE}{\omega}(sin(\omega t) - sin(\omega t_i)) \\ mx &= \frac{eE}{\omega^2}(cos(\omega t) - cos(\omega t_i)) + \frac{eE}{\omega}(t - t_i)sin(\omega t_i) \end{aligned} \tag{2.11}$$

where ω is the angular frequency of the laser field, E is the amplitude of the laser electric field, t is time, t_i is the ionization time of the electron and m is the mass of the electron. Newton's equation was integrated in such a way as to ensure that both $x(t_i) = 0$ and $v(t_i) = 0$ in accordance with the TSM. Because the derivation of the cutoff is usually skipped in papers and textbooks on HHG, and because some slight inaccuracies have been propagating through literature since Corkum's original paper, we will explicitly derive it here.

The objective is to find orbits such that when the electron is recaptured $x(t_r) = 0$ the velocity $|v(t_r)|$ will be maximized. Moving to phase coordinates, $\alpha = \omega t_i$ and $\beta = \omega t_r$, the optimization problem becomes

$$\textbf{maximize} \qquad |sin(\beta) - sin(\alpha)| \tag{2.12}$$

$$\textbf{subject to} \qquad 0 = cos(\beta) - cos(\alpha) + (\beta - \alpha)sin(\alpha) \tag{2.13}$$

Differentiating gives us the following system,

$$0 = -d\alpha\, cos(\alpha) + d\beta\, cos(\beta) \tag{2.14}$$

$$0 = d\alpha(\beta - \alpha)cos(\alpha) - d\beta(sin(\beta) - sin(\alpha)) \tag{2.15}$$

which needs to be degenerate for non-trivial solutions to exist. In other words the matrix multiplying $d\alpha$ and $d\beta$ must have zero determinant. Using the fact that $cos(\alpha)$ cannot be zero, as this would correspond to the electron never leaving the ion, we obtain

$$0 = sin(\beta) - sin(\alpha) - (\beta - \alpha)cos(\beta) \tag{2.16}$$

$$0 = cos(\beta) - cos(\alpha) + (\beta - \alpha)sin(\alpha) \tag{2.17}$$

where the first line represents the solvability of the system above and the second line repeats the constraint that $x = 0$ upon return of the electron. Upon inspection we see the symmetry $cos(\beta) = -sin(\alpha)$ and $sin(\beta) = -cos(\alpha)$ which implies $\alpha + \beta = \frac{3\pi}{2} \bmod 2\pi$.

Substituting for β the two lines above collapse into one equation for α

$$cot(\alpha) = \frac{3\pi}{2} - 1 - 2\alpha \tag{2.18}$$

which we solve numerically as $\alpha \approx 0.3134075$ radians or $\alpha \approx 17.96°$. Note that Corkum originally had estimated $\alpha \approx 17°$ which has been often quoted, however, 18° would have been closer to the mark. Note that α and β add up to exactly 270°, and also that the electron flight time is $(\beta - \alpha)/2\pi \approx 0.6502$ of the full field cycle. Notice also that there are further solutions every half period (modulo π). The maximized $|sin(\beta) - sin(\alpha)|$ is ≈ 1.25959, which means

$$\frac{1}{2}mv_{\max}^2 = \frac{e^2E^2}{2m\omega^2}(sin(\beta) - sin(\alpha))^2 \approx 3.1731\,U_p \tag{2.19}$$

leading to the familiar result

$$E_{\text{cutoff}} = I_p + 3.1731\,U_p \tag{2.20}$$

where E_{cutoff} is the energy cutoff, I_p is the ionization potential and U_p is the ponderomotive energy.

2.2.2.1 Ionization

Even when the photon energy of the pump field is significantly smaller than the ionization energy of the target(e.g. 1.55 eV photon energy of an 800 nm Ti:Sapphire laser compared to the ionization potential of 10-20 eV), ionization can occur due to absorption of multiple photons, which is a strongly intensity dependent process. Starting from intensities of around 10^{12}W/cm^2, we see multi-photon ionization (MPI) and above-threshold ionization (ATI) [9] as illustrated in Figure (2.1). The ionization rate for MPI, is given by [10]

$$\Gamma_N = \sigma_N I^N \tag{2.21}$$

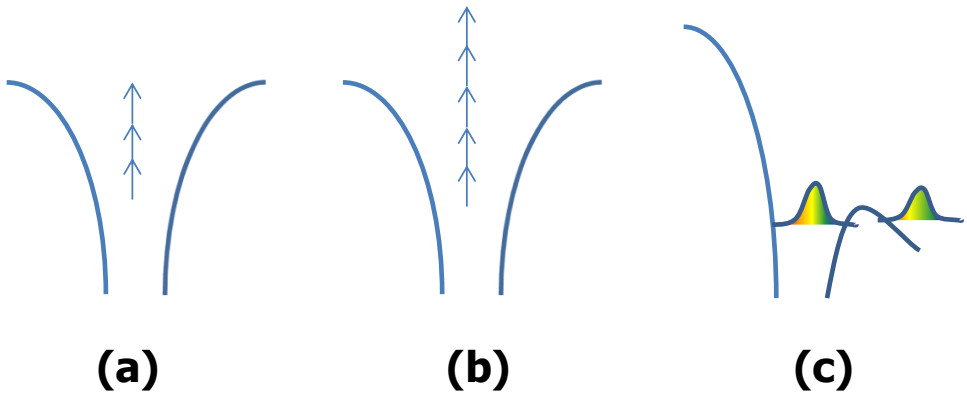

Figure 2.1: Ionization processes for strong field: (a) Multi-Photon Ionization (MPI); (b) Above Threshold Ionization (ATI), (c) Tunnel Ionization and Over-The-Barrier-Ionization (OTBI)

and that for ATI by [10]

$$\Gamma_{N+s} = \sigma_{N+s} I^{N+s} \tag{2.22}$$

where I is the laser intensity, σ is the cross section, N is the minimum number of photons for ionization and s is the extra number of photons absorbed.

Between 10^{13} W/cm^2 to 10^{14} W/cm^2, the electric field has a strong enough effect on the Coulomb potential surface to make tunnelling significant, see Figure (2.1). Using ADK theory [11], it can be shown that the ionization rate for the tunnelling process is exponentially suppressed for small electric field,

$$\Gamma \sim e^{-\frac{2(2I_p)^{3/2}}{3E}} \tag{2.23}$$

where I_p is the ionization potential.

The total potential, composed of a Coulombic and a laser field contribution, is

$$V(x) = -\frac{Ze^2}{4\pi\epsilon_0|x|} + exE_L cos(\omega t) \tag{2.24}$$

Inert Gas	I_P (eV)	I_{OTBI} (W m^{-2})
He	24.581	1.460e19
Ne	21.565	8.641e18
Ar	15.760	2.465e18
Kr	14.000	1.535e18
Xe	12.130	8.651e17

Table 2.1: Calculated I_{OTBI} (W m^{-2} for inert singly ionized gases with ionization potential I_P, taken from [12])

where Z is the charge state of the atom, ϵ_0 is the free space permittivity, e is the electric charge, E_L is the laser field, ω is the angular frequency of the laser. From this we can calculate how far the potential barrier gets pushed down during the laser cycle. Equating this minimum barrier height with the ionization energy we can solve for the barrier ionization electric field, and the corresponding OTBI intensity [10],

$$I_{\mathrm{OTBI}} = \frac{1}{2} c\epsilon_0 E_{\mathrm{OTBI}}^2 = I_p^4 \frac{\pi^2 c \epsilon_0^3}{2Z^2 e^6} \tag{2.25}$$

We have calculated I_{OTBI} for singly ionized noble gas atoms, see Table 2.1.

The tunnelling time of this process compared to the laser time period is known as the Keldysh factor. Tunnel ionization time is in essence determined by the mean free time of the electron traversing a barrier of width $\frac{I_p}{eE}$, with average electron velocity of $(\frac{I_p}{m})^{1/2}$. Up to frequencies on the order of,

$$\omega_t = \frac{eE}{\sqrt{2mI_p}} \tag{2.26}$$

the tunnel effect is controlled by the instantaneous value of the laser field.

The Keldysh factor is given by

$$\gamma \equiv \frac{T_t}{T} = \frac{\omega}{\omega_t} = \frac{\omega\sqrt{2mI_p}}{eE} = \sqrt{\frac{I_p}{2U_p}} \tag{2.27}$$

or in a more useful form,

$$\frac{1}{\gamma^2} = \frac{e^2 E^2}{2m\omega^2 I_p} = \frac{2\pi e^2}{mc\omega^2 I_p}\frac{W}{R^2} \tag{2.28}$$

where W stands for the power of the laser, and R its beam radius[13].

When $\gamma \ll 1$ the tunneling time is much shorter than the laser cycle and we are in the tunneling regime. When $\gamma \gg 1$ the tunneling time is much longer than the laser cycle and we are in the MPI regime.

Chapter 3

Propagation

Experimental laser physics has progressed to the point of being able to produce pulses under 100 attoseconds of duration [1]. Precisely because of the short durations of these pulses they must have very broad spectra, by the bandwidth theorem ($\Delta\nu\Delta t \geq 0.441$ for Gaussian pulses), and a good part of the spectra will be of high enough energy to ionize a typical medium. Therefore, we expect to see strong absorption above ionization thresholds and strong phase rotation above and below these thresholds. With an eye on the use of sub-femtosecond pulses both in fundamental research and practical applications, we are led to the question of how exactly do these pulses distort when travelling through gaseous media. The largest effect on the shape of the pulse can be modelled by utilizing the Kramers-Kronig relations.

In this section we derive the Kramers-Kronig relations and apply them to derive the real index of refraction from published experimental absorption data. We assume throughout that the magnetic susceptibility μ is 1. We also ignore conductivity contributions [16] for our purposes.

3.1 The Dielectric Permeability

We assume a linear and causal relationship between the electric displacement field D and the electric field E [16]

$$D(t) = E(t) + \int_0^\infty f(\tau)E(t-\tau)d\tau \tag{3.1}$$

where $f(t)$ is a response function which, because of causality, must be zero for $t < 0$. Also, for the response to make physical sense, $f(t)$ must be continuous which means that we have $f(0^+) = 0$. The convolution can be rewritten in angular frequency space as $D(\omega) = \epsilon(\omega)E(\omega)$ with

$$\epsilon(\omega) = 1 + \int_0^\infty f(\tau)e^{i\omega\tau}d\tau \tag{3.2}$$

Please note the Fourier transform convention here differs with some other areas of physics in the treatment of the sign of angular frequency as well as a proportional factor of 2π. Because $E(t)$, $D(t)$ and $f(t)$ are real functions we must have that $\epsilon(-\omega) = \epsilon^*(\omega)$ for real ω from which it follows that $\mathrm{Re}\,\epsilon(\omega)$ is an even function and $\mathrm{Im}\,\epsilon(\omega)$ is an odd function. When we expand Equation (3.2) for very high frequencies we find

$$\epsilon(\omega) = 1 - \frac{f'(0^+)}{\omega^2} + ... \tag{3.3}$$

where we have assumed that f has a Taylor expansion at 0^+ and have used $f(0^+) = 0$. Therefore, $\mathrm{Re}\,\epsilon(\omega) - 1$ drops off at least as fast as ω^{-2} and $\mathrm{Im}\,\epsilon(\omega)$ drops off at least as fast as ω^{-3} because it is odd. Note that the ω^{-2} behavior can also be understood as the response of asymptotically free electrons whose polarization contribution follows from doubly integrating their acceleration caused by a high frequency electric field.

3.2 Derivation for the Dielectric Permeability

There are a number of ways to derive the Kramers-Kronig equation but we will use contour integration. The crux of the matter is causality which means that any response function can only be non-zero for positive time. In other words the response function is invariant under multiplication with the Heaviside step function, 0 for negative time and 1 for positive time. The Fourier transform of the regularized step function gives

$$\int_0^\infty dt e^{-\varepsilon t} e^{i\omega t} = \frac{1}{\varepsilon - i\omega} = \frac{\varepsilon + i\omega}{\omega^2 + \varepsilon^2} = 2\pi \left(\frac{1}{2}\delta(\omega) + \frac{i}{2\pi} P \frac{1}{\omega} \right) \tag{3.4}$$

where ε is a positive infinitesimal, δ is the Dirac delta function and P stands for principal part integration. The righthand side of the equation above is the ω space representation of the projector onto positive times in t space. Note that the operator language used is shorthand for the underlying proper contour integration. The derivation goes through when the response function is analytic in the upper half plane and drops off faster than ω^{-1} at infinity. Causality dictates that

$$\epsilon(\omega) - 1 = \left(\frac{1}{2}\delta(\omega) + \frac{i}{2\pi} P \frac{1}{\omega} \right) * (\epsilon(\omega) - 1) \tag{3.5}$$

where $*$ stand for convolution. Writing out the convolution and collecting terms we get

$$\epsilon(\omega) = 1 + \frac{1}{\pi i} P \int_{-\infty}^{\infty} \frac{[\epsilon(\omega') - 1]}{\omega' - \omega} d\omega' \tag{3.6}$$

which is the Cauchy integral identity for functions analytic in the upper half plane.

Splitting ϵ into its real and imaginary parts, and using their respective even- and oddness to fold the integral we obtain the Kramers-Kronig relations [16]

$$\begin{aligned} \operatorname{Re}\epsilon(\omega) &= 1 + \frac{2}{\pi} P\int_0^\infty \frac{\omega' \operatorname{Im}\epsilon(\omega')}{\omega'^2 - \omega^2} d\omega' \\ \operatorname{Im}\epsilon(\omega) &= -\frac{2\omega}{\pi} P\int_0^\infty \frac{[\operatorname{Re}\epsilon(\omega') - 1]}{\omega'^2 - \omega^2} d\omega' \end{aligned} \tag{3.7}$$

where we recognize the Hilbert transforms between the real and imaginary parts.

3.3 Derivation for the Index of Refraction

Here is where the magic of analytic functions comes in. The derivations above have a very broad application to functions analytic in the upper half plane. What's more, we can use any analytic map of ϵ and the Kramers-Kronig relations still apply, as long as we make sure not to create any poles or branch cuts in said half plane, and heed some subtleties of convergence at infinity. For example, the relations apply to powers of ϵ leading to the generalized Kramers-Kronig relations [17].

Another way to look at causality is that response functions which are bounded and L_2 integrable are closed under scalar multiplication, addition, multiplication and convolution in t space. This last fact is easily checked. It immediately follows that the response functions have all these four properties in ω space also, where multiplication and convolution swap roles. So using maps that have a local Tayor expansion (i.e. analytic) produce new valid response functions.

We can take the square root of $\epsilon(\omega)$ using $\epsilon(\omega) = (n_r(\omega) + i\kappa(\omega))^2$ such that $\operatorname{Re}\epsilon = n_r^2 - \kappa^2$ and $\operatorname{Im}\epsilon = 2n_r\kappa$, where $n_r(\omega)$ is the real index of refraction and $\kappa(\omega)$ is the extinction coefficient. The Kramers-Kronig relations then also apply to $n = n_r + i\kappa$ itself, including the fact that n_r is even and κ is odd in ω space [16].

$$\begin{aligned} n_r(\omega) &= 1 + \frac{2}{\pi} P\int_0^\infty \frac{\omega' \kappa(\omega')}{\omega'^2 - \omega^2} d\omega' \\ \kappa(\omega) &= -\frac{2\omega}{\pi} P\int_0^\infty \frac{[n_r(\omega') - 1]}{\omega'^2 - \omega^2} d\omega' \end{aligned} \tag{3.8}$$

A simple monochromatic attenuating wave $\exp[i\frac{\omega}{c}((n_r + i\kappa)z - ct)]$ shows that the amplitude attenuation is $\exp[-\omega\kappa z/c]$ and we can, therefore, define the absorption coefficient (i.e. intensity attenuation coefficient) $\alpha = 2\kappa\omega/c$, which gives the useful relationship

$$n_r(\omega) = 1 + \frac{c}{\pi} P\int_0^\infty \frac{\alpha(\omega')}{\omega'^2 - \omega^2} d\omega' \tag{3.9}$$

For a gas with absorption cross section $\sigma(\omega)$ and density n_d we have

$$\alpha(\omega) = \sigma(\omega) n_d \tag{3.10}$$

and we use this result to compute the real index of refraction from cross section data.

3.4 Numerical Methods

Although there is an obvious pole in the principal part integral of the formulae above, this does not constitute much of a numerical problem in practice, as long as the numerator in each integral is a smooth function that is sufficiently differentiable. We have implemented three different methods for calculating these integrals and they all produce consistent and accurate results which can, for instance, be tested on exactly solvable examples such as damped oscillators, versus one another, or via round trip tests (e.g. determining imaginary part from the real part from the imaginary part).

The first method reconstructs $\kappa(\omega)$ from absorption cross sections onto an equidistant grid of ω values and a simple Simpson's integration rule proves adequate. The second method integrates piece-wise cubic fits analytically. For both these methods care must be taken

in extrapolating the tail. For instance the left tail between 0 and the lower ω cut-off can be extrapolated with an odd function, while the right tail can be fit a power law or an exponential, making sure it decays rapidly enough. In the interest of convergence we must also make sure that $\kappa(\omega)$ is everywhere positive for positive ω.

The third method is altogether more interesting. It exploits analytic behavior of the Kramers-Kronig relations, and is much faster. There is a natural way to take advantage of analyticity by the following Möbius map onto the unit circle

$$z = \frac{\omega_c + i\omega}{\omega_c - i\omega} \tag{3.11}$$

The positive ω axis gets mapped to the upper half of the unit circle and the negative axis gets mapped to the lower half. Note that our method works for any choice of the angular frequency ω_c but it should be chosen such that all the salient features of the function are well distributed over the circle. Choosing a typical midrange value will do.

We now have mapped our real and odd input function $\kappa(\omega)$ onto the circle $\kappa(z)$. The next step is to perform a Fast Fourier Transform on the circle, then remove all the negative frequencies and double the amplitude of the positive frequencies, then perform an inverse Fast Fourier Transform. The result is that we have turned a real function into a complete analytic function. The real part of this analytic function is now $n_r - 1$ as a function of z, which can be mapped back to the real ω axis by using the inverse Möbius map. The whole story works equivalently when determining the imaginary part from the real part.

We choose the following z-grid on the circle, with corresponding ω values on the real axis

$$\begin{aligned} z_k &= e^{2\pi i k/N}, \qquad\qquad k = 0, ..., N-1 \\ \omega_k &= \omega_c \tan(\pi k/N) \end{aligned} \tag{3.12}$$

where N is large and a power of 2. The ω grid has a tangent distribution, which is in a certain sense ideal for this problem, and κ values are imported from regular data grids and

$n_r - 1$ values are exported to regular data grids through interpolation. Note that the point $\omega = \pm\infty$ gets mapped to $z = -1$, and the analytic function must be zero there and have a power of at least $(z+1)^2$. Once N and ω_c are chosen we are only required to provide function values on the ω tangent grid. Note that the method is fast because it uses FFT to compute the entire spectrum at once, in contrast with direct integration methods which perform an integration for every point.

Mapping the upper half complex plane to the unit disk is a well-known technique in complex function theory [18]. The interpretation of the FFT as a finite order Laurent series on the circle, and the analytic continuation into the complex plane it implies, is natural. Hilbert transforms using conformal maps and fast discrete transforms are treated in [19]. We have not found examples of our tangent grid technique in the extensive computational Kramers-Kronig literature.

3.5 Ideal Edge

A typical behavior of κ is that it starts out very low and, moving up in energy, suddenly jumps up when an ionization energy is crossed and decays slowly afterwards. The K-edge and higher edges exhibit this pattern.

It is instructive, and numerically useful, to find exact analytic solutions for κ that decay as an integer power-law. You can do the Kramers-Kronig principal integral explicitly or use analyticity directly and study the branchcuts. Either way we can derive the form factor functions $\mathcal{F}_n$ valid for $y > 0$ using the Heaviside stepfunction χ and where $y = \omega/\omega_{\text{edge}}$.

$$\begin{aligned}
\mathcal{F}_1(y) &= -\frac{1}{\pi}\left(\frac{1}{y}\ln\left|\frac{1-y}{1+y}\right|\right) + \frac{i}{y}\chi(y-1) \\
\mathcal{F}_2(y) &= -\frac{1}{\pi}\left(\frac{1}{y^2}\ln\left|1-y^2\right|\right) + \frac{i}{y^2}\chi(y-1) \\
\mathcal{F}_3(y) &= -\frac{1}{\pi}\left(\frac{1}{y^3}\ln\left|\frac{1-y}{1+y}\right| + \frac{2}{y^2}\right) + \frac{i}{y^3}\chi(y-1) \\
\mathcal{F}_4(y) &= -\frac{1}{\pi}\left(\frac{1}{y^4}\ln\left|1-y^2\right| + \frac{1}{y^2}\right) + \frac{i}{y^4}\chi(y-1)
\end{aligned} \tag{3.13}$$

The index of refraction is related to the form factor in the following way

$$n_r(\omega) - 1 + i\kappa(\omega) = \kappa_{\text{edge}}\mathcal{F}_n(\omega/\omega_{\text{edge}}) \tag{3.14}$$

The pattern for different orders becomes readily clear and we see how multipole corrections are introduced in order to make the functions analytic at $y = 0$. For higher order form factors we derive the following recursion relationship, again either from the Kramers-Kronig integrals directly or from analytic considerations,

$$\mathcal{F}_{n+2}(y) = \frac{1}{y^2}\left(\mathcal{F}_n(y) - \frac{2}{\pi n}\right) \tag{3.15}$$

We show some examples in Figure (3.1). For increasing ω the behavior for n_r is that it starts out above 1, then rises to a logarithmic singularity, then drops off below 1 (anomalous dispersion) and then slowly rises back to 1 for very high energies. This is the rough shape for all situations we will be looking at for the energy ranges and pulses we are interested in. Note that the logarithmic singularity is not a problem in practice. First, in any actual physical setting the singularity would be smoothed out. Second, the logarithmic singularity is integrable against a continuous spectrum and will yield finite answers for real pulses. The place where more care is needed is when the frequency spectrum of the pulse has a strong and narrow peak right around the ionization energy at the edge, which is usually not the case.

Other than providing nice analytic insight into the relationship between κ and n_r the ideal edge is also useful numerically. The fact that κ rises suddenly causes numerical problems for interpolation schemes. We, therefore, first subtract an ideal edge from experimentally determined κ data so that the step is removed, then perform the Kramers-Kronig transformation numerically on the difference, and then add the ideal edge back in using the analytic formula. This leads to better stability of the n_r calculation. We have not chosen a particular order κ decay power n as this can be fitted to experimental data if one wishes. Calculations show that numerical results are not sensitive to the value of n, the important point being that the step in κ is handled rather than an accurate fit to the tail.

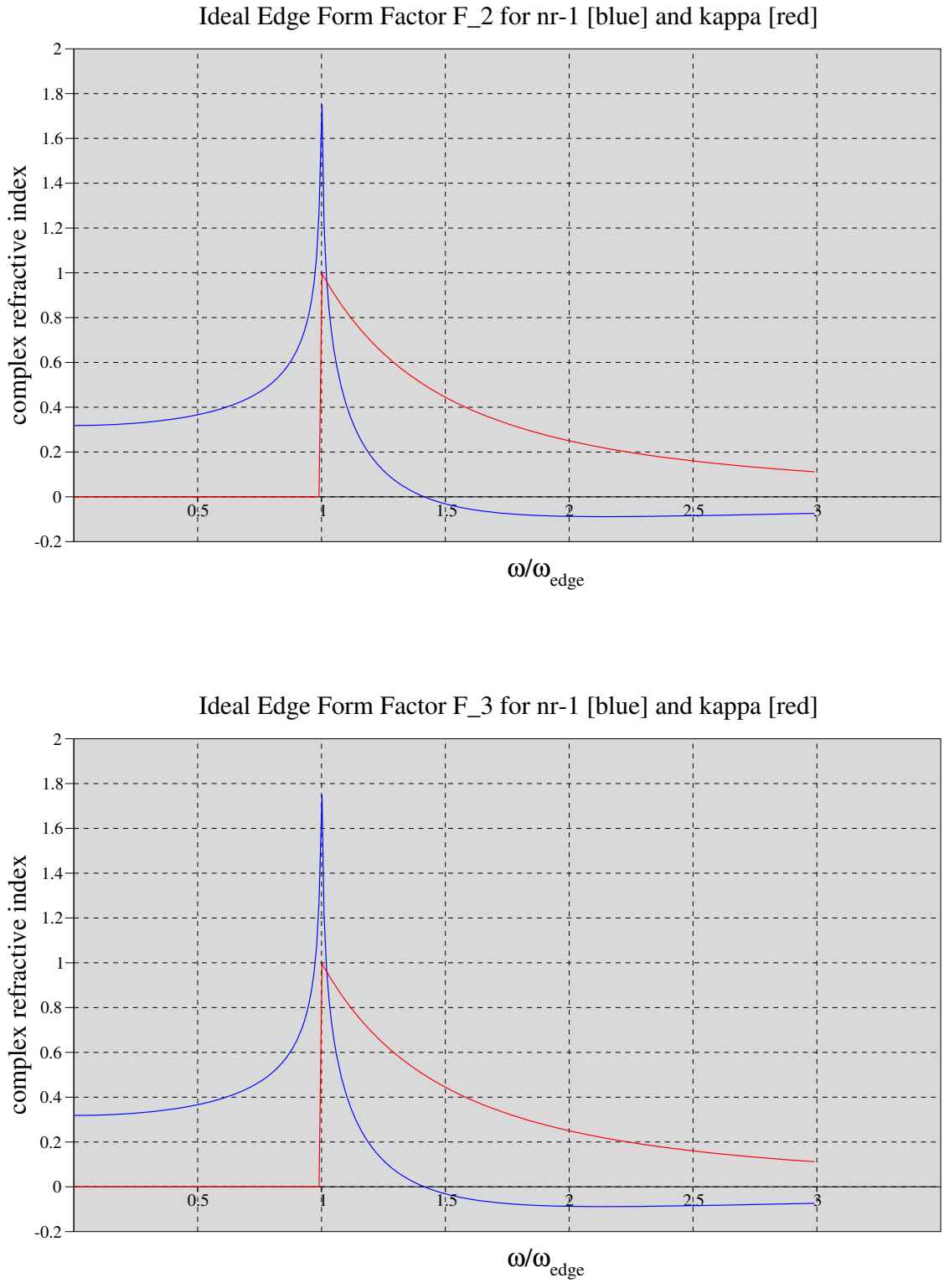

Figure 3.1: Ideal edge form factors $\mathcal{F}_2$ and $\mathcal{F}_3$. $n_r - 1$ is shown in blue and κ is shown in red. The horizontal axis is ω/ω_{edge} and the vertical axis is dimensionless. The logarithmic singularity has been tempered for graphing.

3.6 Free Electrons

Thus far we have ignored the presence of free electrons due to ionization, and we will happily continue to do so, but we do have to provide evidence why this would be alright. Solving $m\ddot{x} = -eE\cos(\omega t)$ we get $x = \frac{eE}{m_e\omega^2}\cos(\omega t)$. The polarization is $P = -exn_e$ where n_e is the free electron density. Because $P = \epsilon_0\chi E$ we obtain $\chi = -\frac{n_e e^2}{\epsilon_0 m_e \omega^2}$. The relative permittivity $\epsilon = 1 + \chi$, or dielectric permeability if you will, is [20]

$$\epsilon = 1 - \frac{\omega_p^2}{\omega^2} \tag{3.16}$$

with the plasma frequency ω_p defined as

$$\omega_p^2 = \frac{n_e e^2}{\epsilon_0 m_e} \tag{3.17}$$

In an experimental setup where the intensity halves every (say) 10 cm we necessarily have large κ and n_r will deviate far from 1. On the other hand, at room temperature, a pressure of 0.015 mbar and assuming one free electron per atom we find that $\hbar\omega_p = 0.007$ eV. Since the central energy of our pulses is around 20 eV, we see that the electron plasma contribution is very small indeed. Additionally, because Al-filters are used in handling and shaping, the pulses energies below 10 eV are severely suppressed and for this we can blame the "free" conduction electrons in the metal itself.

3.7 Pulse Envelope

While for a rapidly oscillating E-field with slowly varying amplitude the determination of the envelope may seem obvious, this becomes less clear for short distorted pulses. A practical definition would be to construct a complex signal using only the positive frequencies of the real E-field signal, and take its norm as the envelope. As an aside, note that this

construction is very much analogous to the analytic machinery that lies behind the Kramers-Kronig relations. Starting with a real E-field $E(t)$, we form its Fourier transform $E(\omega)$, with the property $E(-\omega) = E^*(\omega)$ because the physical electric field is real. We now construct the new analytic signal $\tilde{E}$ in frequency space.

$$\begin{aligned} \tilde{E}(\omega > 0) &= 2E(\omega) \\ \tilde{E}(0) &= E(0) \\ \tilde{E}(\omega < 0) &= 0 \end{aligned} \tag{3.18}$$

After Fourier transforming back to time space we get the complex signal $\tilde{E}(t)$. Note that the real part of this complex signal is the E-field we started out with, $\mathrm{Re}\,\tilde{E}(t) = E(t)$. The rest of the complex signal is the imaginary companion signal. We define the envelope as the norm of the complex signal, $A(t) = |\tilde{E}(t)|$. This construction works in the expected way for familiar pulse shapes. For example, when $E(t) = e^{-t^2/2a^2}\cos(\omega t - \phi)$ then $\tilde{E}(t) = e^{-t^2/2a^2}e^{i(\omega t - \phi)}$ and $A(t) = e^{-t^2/2a^2}$, where we have used a positive ω. It must be realized that in contrast to ideal pulses the envelope of a distorted pulse will likely undulate but will oscillate less than the physical E-field. Also, the positive frequency construction works nicely for Gaussian pulses which drop off quickly both in time and in frequency space. For pulses with heavier tails, however, the envelope constructed can be very wide.

3.8 Pulse Distortion

In this section we study the distortion of a pure Gaussian E-field pulse in a gaseous environment. First the pulse is split into its monochromatic components. Consider a monochromatic wave $e^{i\omega(nx-ct)/c}$ where the index of refraction is $n = n_r + i\kappa$. Observing the wave at location x at the adjusted time coordinate $t' = t - x/c$ gives

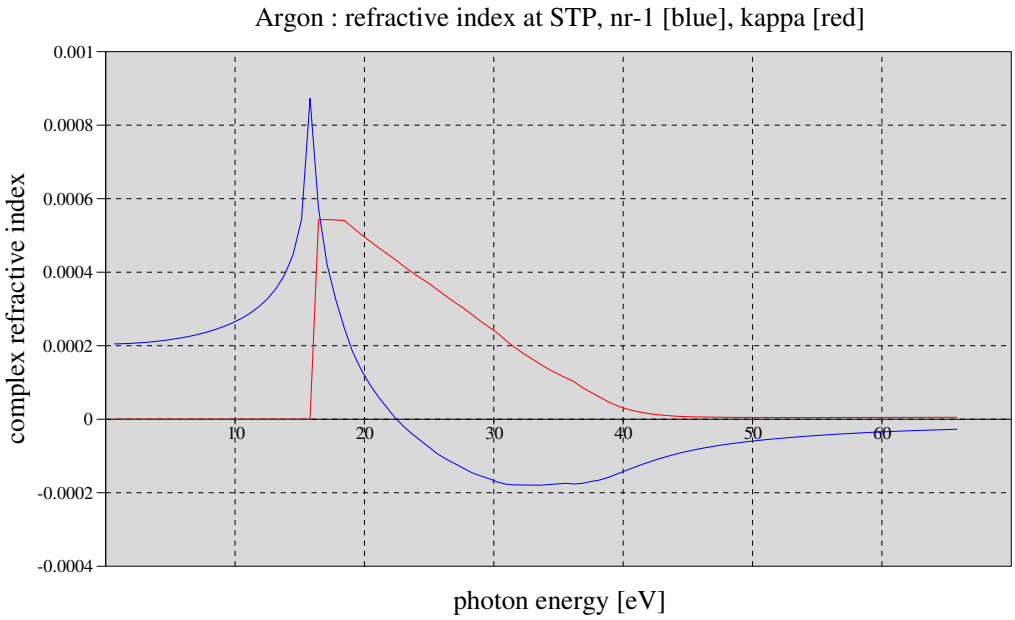

Figure 3.2: The real and imaginary part of the refractive index, $n_r - 1$ and κ respectively for Argon gas, plotted on the vertical axis versus photon energy in units of eV on the horizontal axis, based on Henke data [21], at STP (T=273.15K, P=101.325kPa).

$$e^{-i\omega t'} e^{i\frac{\omega}{c}(n_r-1)x} e^{-\frac{\omega}{c}\kappa x} \tag{3.19}$$

where the product $\omega\kappa$ is always non-negative to ensure absorption. Both κ and $n_r - 1$ are proportional to the gas density n_d so the relevant concept of interest is the density-distance $D_d = n_d x$ where x is the distance travelled through the gas. For an experimental situation of inhomogenous gas density, say in a jet, the density-distance is really an integral of the density encountered along the optical path. Each monochromatic wave experiences absorption from $\kappa(\omega)$ and phase rotation from $n_r(\omega) - 1$. The pulse is reconstituted at position x and the resulting pulse is computed as a function of time t'.

We show the pulse distortion for argon (ionization energy 15.76 eV) and helium (ionization

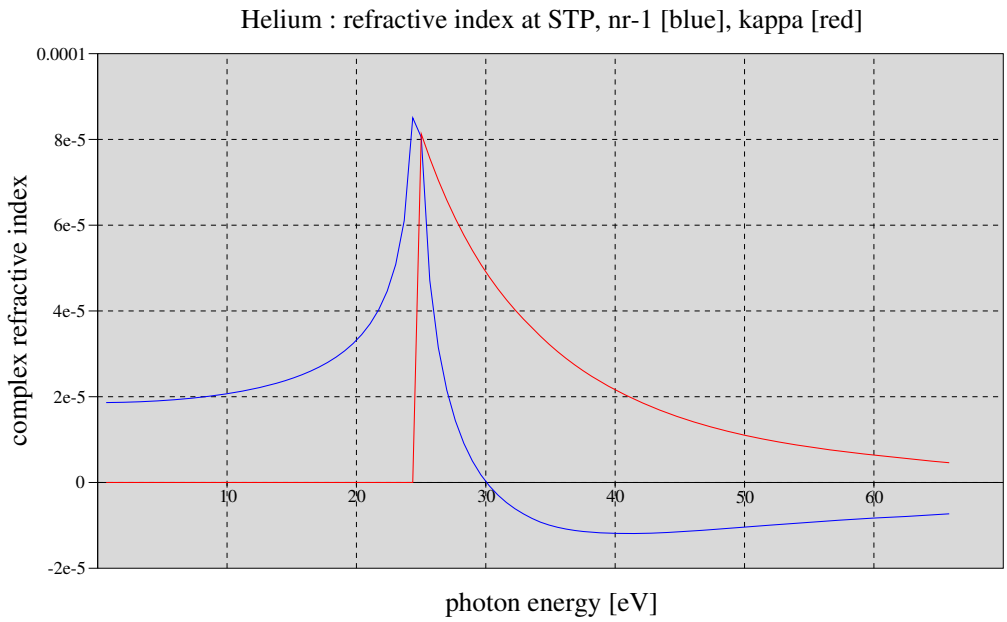

Figure 3.3: The real and imaginary part of the refractive index, $n_r - 1$ and κ respectively for Helium gas, plotted on the vertical axis versus photon energy in units of eV on the horizontal axis, based on Henke data [21], at STP (T=273.15K, P=101.325kPa).

energy 24.59 eV) for a number of Gaussian pulses for different central energies and bandwidths and for a number of density-distances, see Figures (3.4) through (3.10). We see that the distortion can be severe, introducing a delayed rise, undulations and fattening of the tail for positive t', as can be expected from causality, assuming a narrow (in time) pulse going in. Note that in the extreme absorption case for a pulse with central energy far above the ionization edge, that only frequencies from the transparent region below the ionization energy would survive and the resulting signal would be sinusoid like, i.e. it wouldn't be a pulse any more.

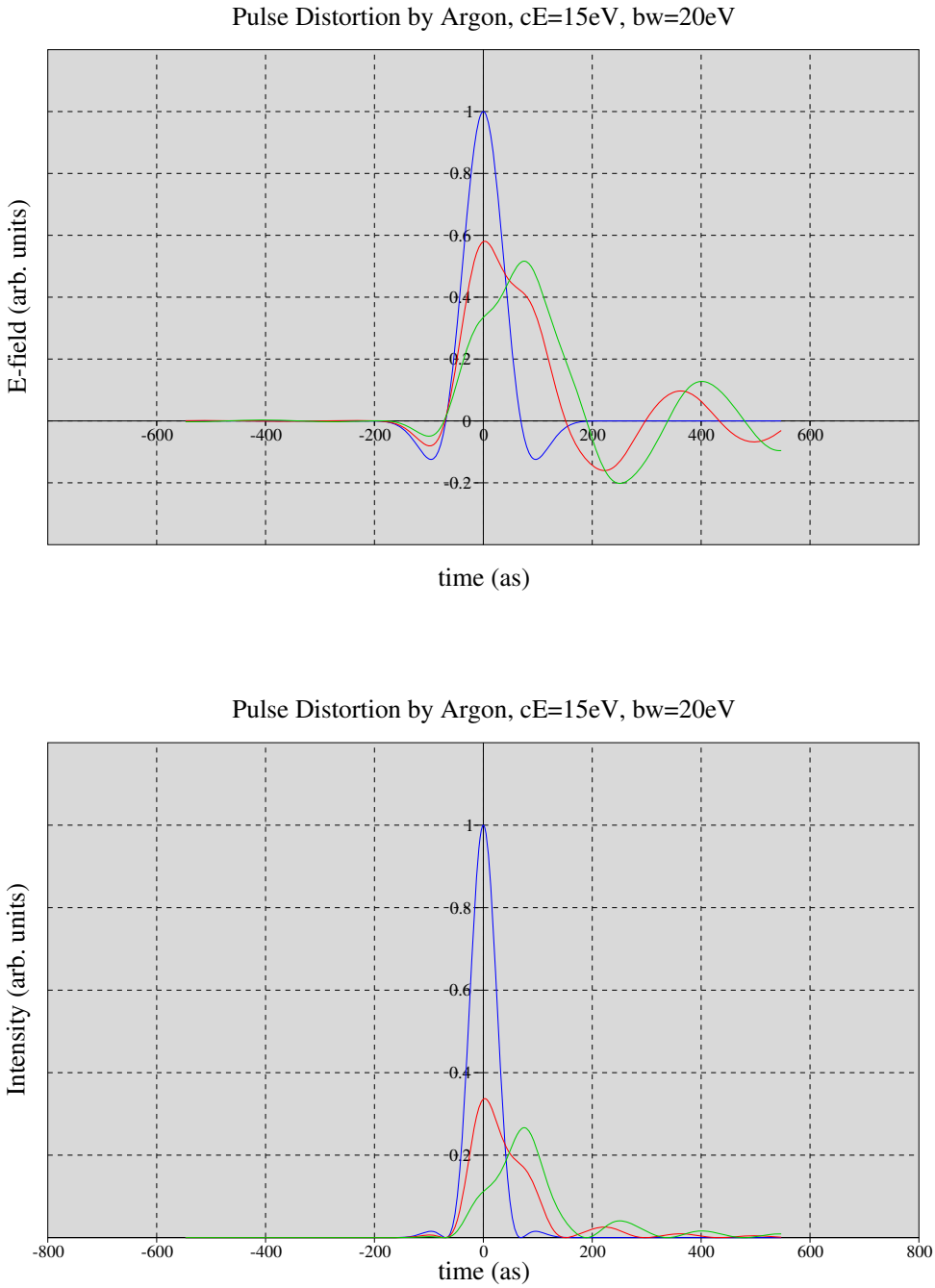

Figure 3.4: Gaussian Pulse of Central Energy 15 eV with Bandwidth of 20 eV, plotted in blue, through Argon Gas at different density-distances, dd: 7.5×10^{20} m^{-2} in red and 1.5×10^{21} m^{-2} in green plotted against time in *as* units. Top figure is the E-field and Bottom figure is the intensity in arbitrary unit.

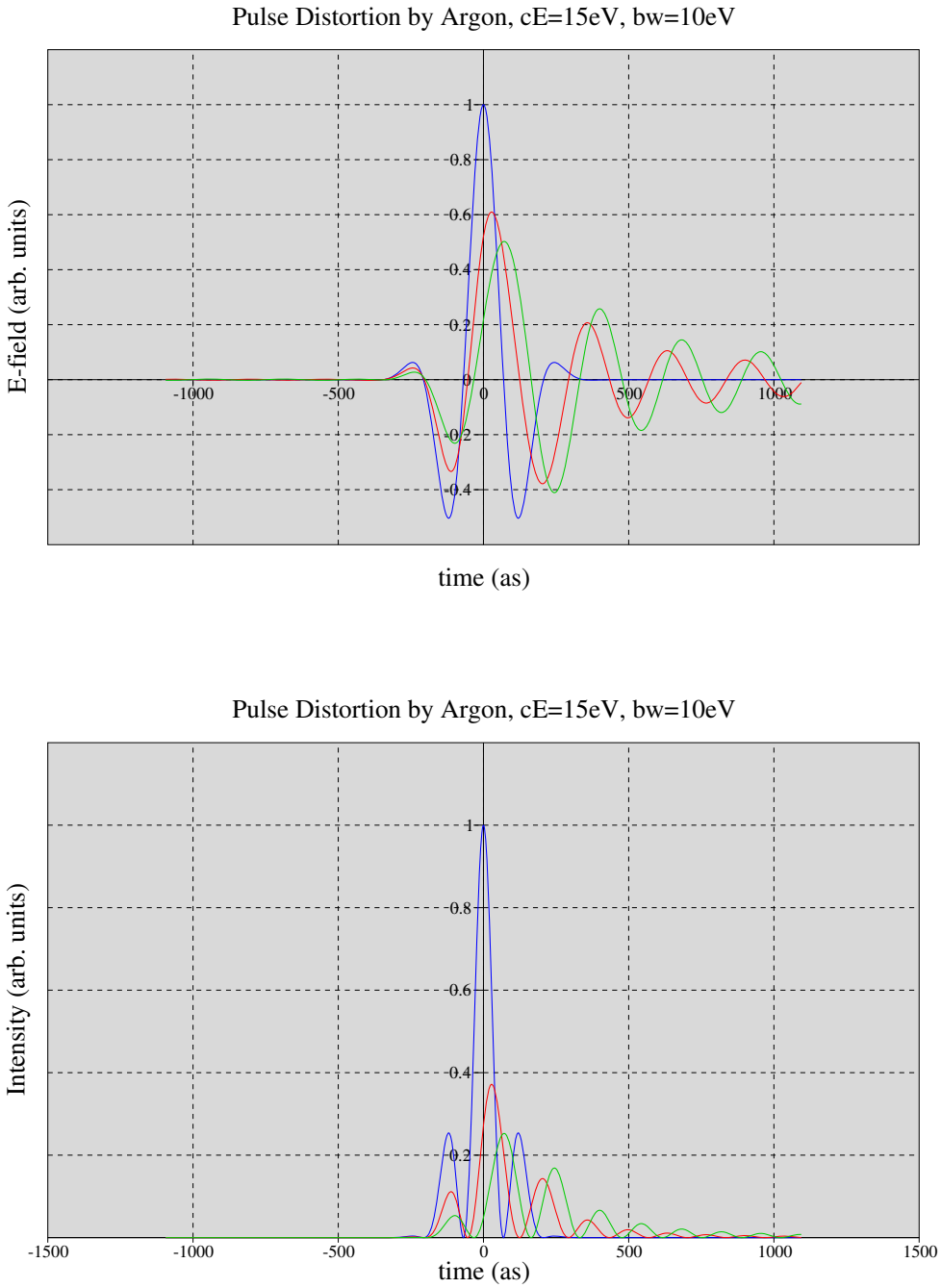

Figure 3.5: Gaussian Pulse of Central Energy 15 eV with Bandwidth of 10 eV, plotted in blue, through Argon Gas at different density-distances, dd: 7.5×10^{20} m^{-2} in red and 1.5×10^{21} m^{-2} in green plotted against time in *as* units. Top figure is the E-field and Bottom figure is the intensity in arbitrary unit.

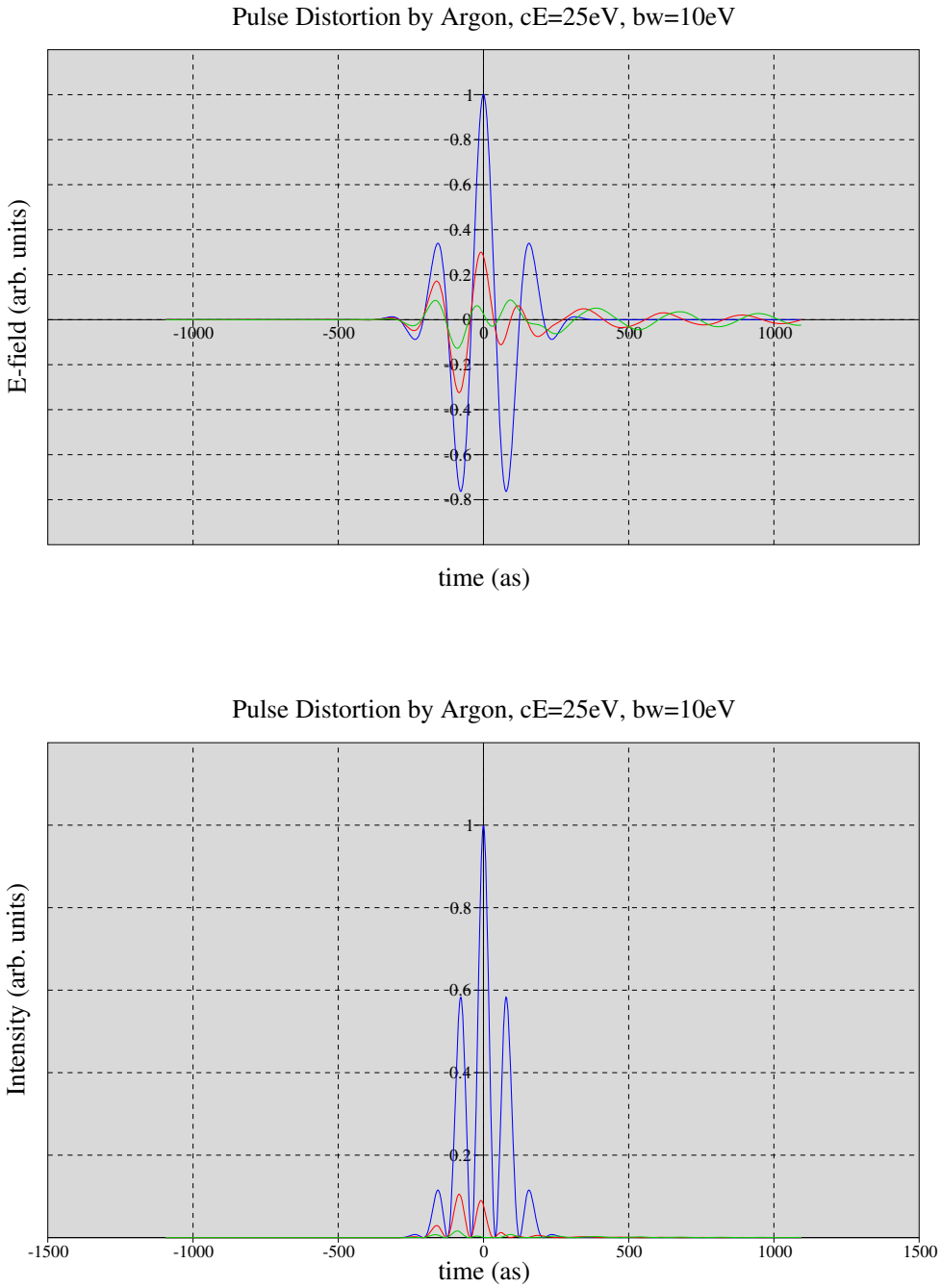

Figure 3.6: Gaussian Pulse of Central Energy 25 eV with Bandwidth of 10 eV, plotted in blue, through Argon Gas at different density-distances, dd: 7.5×10^{20} m^{-2} in red and 1.5×10^{21} m^{-2} in green plotted against time in *as* units. Top figure is the E-field and Bottom figure is the intensity in arbitrary unit.

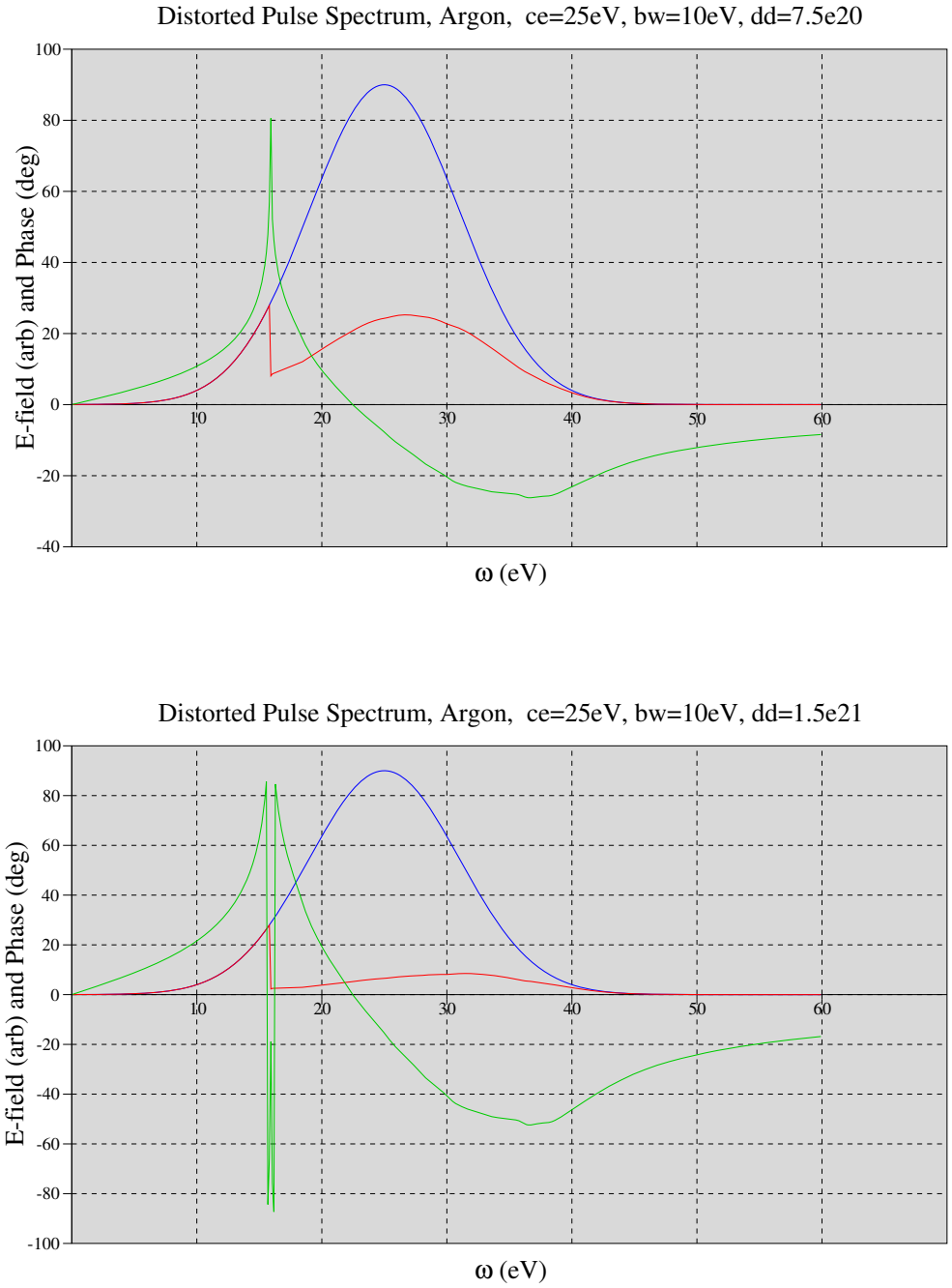

Figure 3.7: Argon: Spectral Plot of E(ω), input E(ω) in blue of Central Energy 25 eV with Bandwidth of 10 eV, output E(ω) in red in arbitrary units, and Phase in green in degrees vs. wavelength in eV at different density-distances. The Top plot is for density-distance of 7.5 $\times 10^{20}$ m^{-2} and the Bottom plot is for density-distance of 1.5 $\times 10^{21}$ m^{-2}.

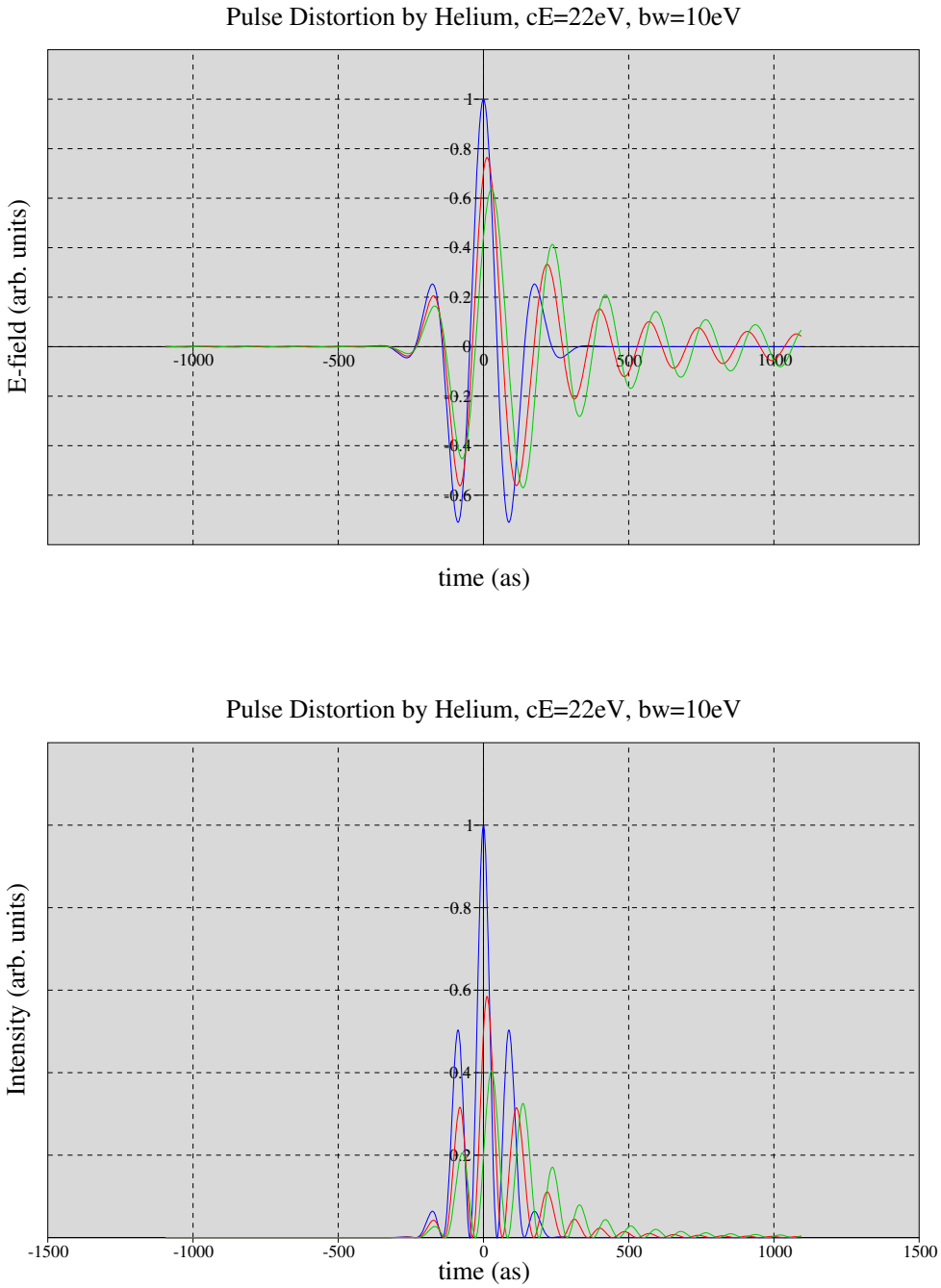

Figure 3.8: Gaussian Pulse of Central Energy 22 eV with Bandwidth of 10 eV, plotted in blue, through Helium Gas at different density-distances, dd: 3.0 $\times 10^{21}$ m^{-2} in red and 6.0 $\times 10^{21}$ m^{-2} in green plotted against time in *as* units. Top figure is the E-field and Bottom figure is the intensity in arbitrary unit.

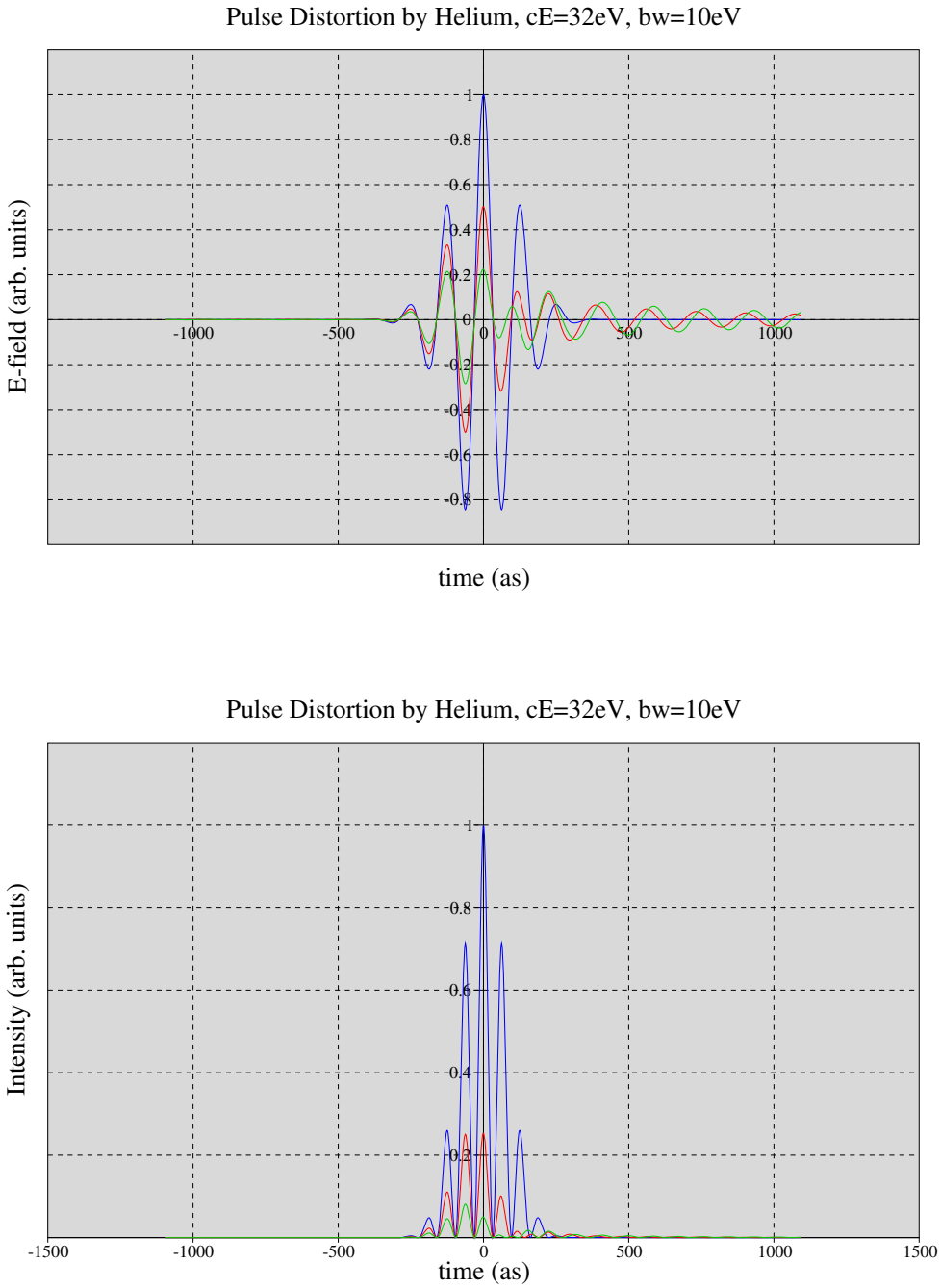

Figure 3.9: Gaussian Pulse of Central Energy 32 eV with Bandwidth of 10eV, plotted in blue, through Helium Gas at different density-distances, dd: 3.0 $\times 10^{21}$ m^{-2} in red and 6.0 $\times 10^{21}$ m^{-2} in green plotted against time in *as* units. Top figure is the E-field and Bottom figure is the intensity in arbitrary unit.

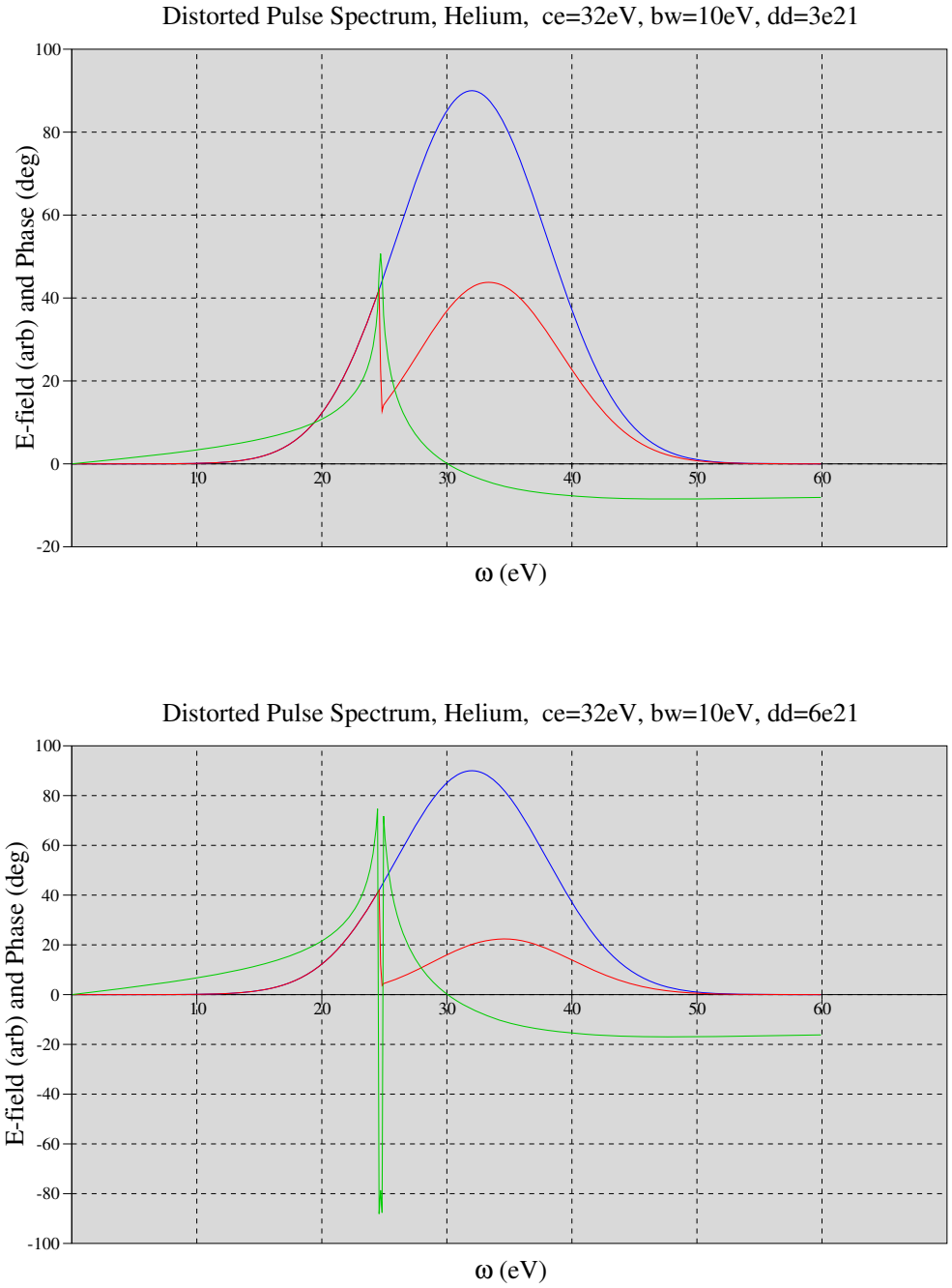

Figure 3.10: Helium: Spectral Plot of E(ω), input E(ω) in blue of Central Energy 32 eV with Bandwidth of 10eV, output E(ω) in red in arbitrary units, and Phase in green in degrees vs. wavelength in eV at different density-distances. The Top plot is for density-distance of 3.0 $\times 10^{21}$ m^{-2} and the Bottom plot is for density-distance of 6.0 $\times 10^{21}$ m^{-2}.

3.9 Interpretation of Results

Even though the strong absorption and phase rotation in our simulations have a complicated effect on the temporal pulse shape, there are some broad features. When studying our pulse distortion results for argon and helium for pulses of different central energy and bandwidth, the following interesting patterns emerge. For pulses that have their central energy below the ionization edge, and therefore most of the pulse's energy is in this spectral region, we generally see absorption, pulse broadening, pulse retardation and the development of a long undulating tail. From Figure (3.2) we can see normal dispersion before the ionization edge with a rapidly increasing real part of the refractive index which can help us understand the retardation effects. Consistent with this explanation, we see that the retardation effects are larger when the pulse bandwidth is smaller and therefore concentrating more of the pulse's energy in the normal dispersion region.

For pulses with a central energy above the ionization edge, and therefore having most of their energy above this edge, we see a very different pattern. We observe absorption and pulse narrowing resulting in apparent superluminality which we explain in Section 3.9.2. According to Figure (3.2) the region just above the ionization edge has strong anomalous dispersion. Note that we need to have strong absorption but not total absorption to see pulse narrowing and apparent superluminality. Pulse advancement is stronger for pulses with a narrower bandwidth which concentrate more of their energy in the anomalous dispersion region. If the pulse travels very far into the medium, all energy above the ionization energy will be depleted with only negligible absorption below the ionization edge which means all remaining energy is in the normal dispersion region and anomalous dispersion effect will be absent even though the original pulse had its central energy above the ionization edge. In Figure (3.11) we show how the time-width of the pulse changes as the pulse travels through argon gas. The time-width is calculated by weighting by the square of the electric field. Note that while the time-width grows significantly at first it tends to slow down when all frequencies at and above the ionization edge are absorbed and the remaining spectrum stabilizes. The rapid

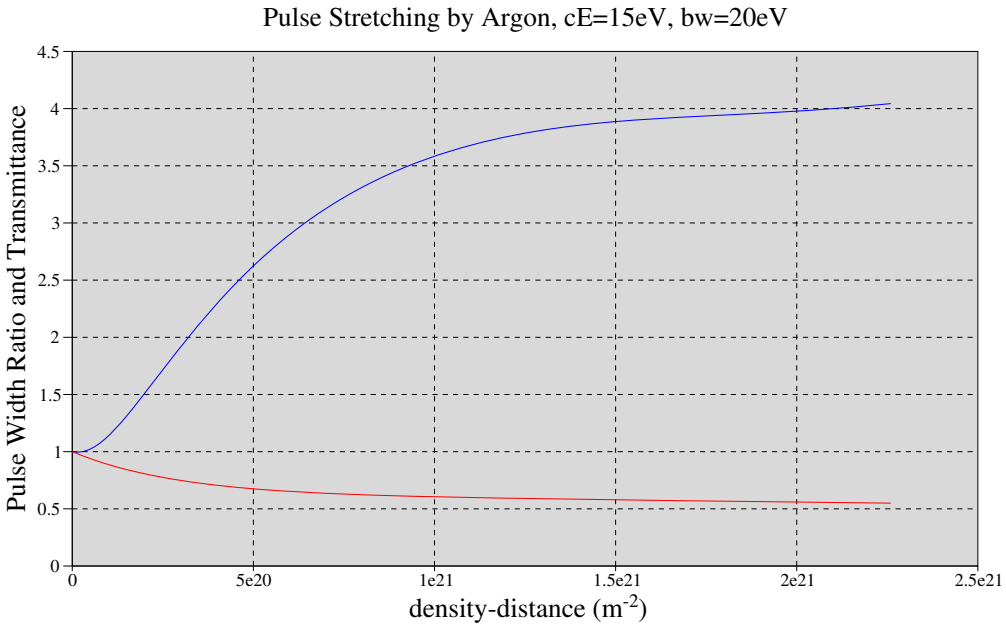

Figure 3.11: Pulse stretching for Argon with central energy 15 eV and bandwidth 20 eV. We show the ratio of the time standard deviation (weighted by E^2) of the distorted pulse versus the undistorted pulse in blue. We show the fraction of transmitted pulse energy in red.

widening is due to the effective narrowing of the spectrum. For larger density-distances the widening effect due to dispersion will take over.

3.9.1 Resonance Lines before the Edge

For argon, there are a few resonance lines before the edge. We will examine one of the strongest lines in detail, $3s^2 3p^6 {}^1\mathrm{S}_0$-$3s^2 3p^5 4s^2 \mathrm{P}_{1/2}$ of 104.822 nm with Einstein's A coefficient of 5.1×10^8 s^{-1} [12]. The spectral linewidth due to natural broadening is extremely narrow and is on the order of 10^9 Hz. The actual linewidth is dominated by Doppler broadening [22], and is on the order of $10^{10} - 10^{11}$ Hz at room temperature, which corresponds to $\Delta\omega/\omega_0$ of 10^{-6}, which is very narrow. Consequently, for the broad band pulses we are interested in, resonance lines only absorb a tiny fraction of the overall energy of the pulse. The effect of the resonance lines on the temporal shape of the pulse is many orders of magnitude below

that of the effect of the ionization edge.

3.9.2 Superluminality

Looking at Figure (3.9) there is an apparent shift of the pulse backward in time. Now the whole point of this chapter is causality, analyticity in the upper half-plane and the Kramers-Kronig relations that follow from this principle. The response function is strictly causal so how can there be wavepackets appearing to travel faster than the speed of light. We will loosely follow Diener [23] for an explanation.

Much of the confusion surrounding supposed faster-than-light propagation of wave-packets stems from faulty human intuition which evolved from the dynamics of solid objects. We tend to identify the front, middle and back of an ingoing pulse with those of the outgoing pulse. This, however, is very misleading and the underlying wave mechanics is much more subtle.

Look at the response function

$$\int \frac{d\omega}{2\pi} e^{-i\omega t'} e^{i\frac{\omega}{c}(n(\omega)-1)x} \tag{3.20}$$

where $n(\omega) = n_r(\omega) + i\kappa(\omega)$ is the complex index of refraction. Now imagine this response function acts on a narrow-band pulse centered on ω_1 and also assume that $n(\omega)$ is smooth around ω_1 and can be Taylor expanded there. Then we find

$$
\begin{aligned}
&\int \frac{d\omega}{2\pi} e^{-i\omega t'} e^{i\frac{\omega}{c}(n(\omega)-1)x} \\
=&\int \frac{d\omega}{2\pi} e^{-i(\omega_1+\omega)t'} e^{\frac{i}{c}(\omega_1+\omega)(n(\omega_1+\omega)-1)x} \\
=&e^{-i\omega_1 t'} e^{\frac{ix}{c}(\omega_1+i\partial_{t'})(n(\omega_1+i\partial_{t'})-1)} \int \frac{d\omega}{2\pi} e^{-i\omega t'} \\
=&e^{-i\omega_1 t'} e^{\frac{ix}{c}(\omega_1+i\partial_{t'})(n(\omega_1+i\partial_{t'})-1)} \delta(t') \\
=&e^{-i\omega_1 t'} e^{\frac{ix}{c}\omega_1(n(\omega_1)-1)} e^{\frac{ix}{c}(n_g(\omega_1)-1)i\partial_{t'}+\dots} \delta(t') \\
\approx&e^{-i\omega_1 t'} e^{\frac{ix}{c}\omega_1(n(\omega_1)-1)} \delta(t'-\frac{x}{c}(n_g-1))
\end{aligned}
\tag{3.21}
$$

where we have defined $n_g(\omega) = n(\omega) + \omega n'(\omega)$ such that the group velocity is $c_g = c/n_g$ which may very well be superluminal. Note this approximation is only valid when acting on narrow-band pulses. We see that for superluminal group velocities the pulse, roughly speaking, gets pushed backward in time although this is a misleading interpretation.

In the more general case response functions tend to look like damped oscillations. In short, the front of the wave packet travels no faster than the speed of light, the response function acting on the leading edge of the ingoing pulse can be constructive while the response function acting on the middle and trailing edge of the ingoing pulse can be destructive, creating an out-going pulse that, by judging the location of its maximum amplitude, seems to have travelled faster than light in vacuum. However, no information nor energy has travelled superluminally.

The physical situation we are interested in does not involve narrow- but broad-band pulses. Also, the index of refraction is not a very smooth or uneventful function of the angular frequency. Nevertheless, although the situation is much more complicated, partial apparent superluminality can still be observed.

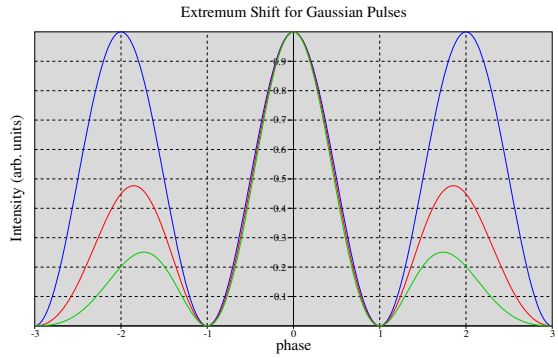

Figure 3.12: Gaussian envelope moves extrema inward.

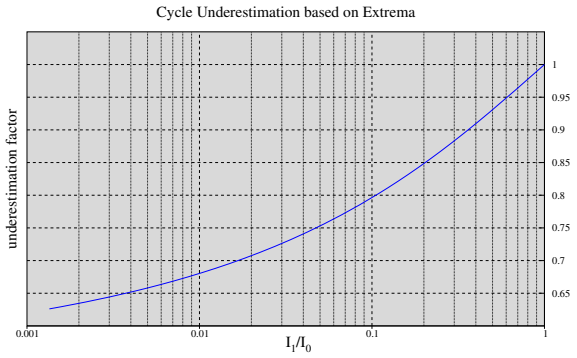

Figure 3.13: Cycle underestimation factor for first side-lobe extremum.

3.9.3 Estimating Time-scales from Extrema

When visually inspecting pulse intensity graphs as a function of time one often tries to estimate the central frequency of the pulses by looking at the maxima. This works well for narrow-band pulses but there is an issue for broad-band pulses. Consider the ideal case of an intensity profile that is the product of a $\cos^2$ and a Gaussian curve. Multiplying with the Gaussian does not move the zeroes of the cosine but zero intensities are often hard to accurately locate in intensity graphs due to noise and background signals. Peak locations are much less affected by noise and background. However, the Gaussian factor pushes the location of the peak maxima over considerable distances towards the center, leading to an underestimation of the oscillation time-scale and an overestimation of the corresponding frequency or energy. We have graphed a correction factor for side-peak to central peak intensity ratios.

As an example using Figure (3.4) we estimate the cycle from the time separation between the two intensity side maxima of the undistorted pulse to be 190 as. The amplitude ratio versus the main peak we estimate at 0.126 which implies an intensity ratio of 0.0159. Looking up this ratio in Figure (3.13) we find a correction factor of 0.69. Therefore, the correct cycle

should be 190/0.69 is 275 as. As a sanity check, the central energy of the pulse is 15 eV which corresponds to 276 as. We can see that our estimation is correct and that the correction factor is material.

3.10 Instrumental Broadening

In this section we study the effect of instrumental broadening of the spectral linewidth. The common method of modelling the limited resolution of the instrument is to use a Gaussian function. The resultant signal detected is consequently a convolution of the spectral linewidth and a Gaussian distribution. We can express this mathematically as:

$$\Upsilon(\omega) = f(\omega) \otimes g(\omega) \tag{3.22}$$

where $\Upsilon(\omega)$ represents the detected signal, $f(\omega)$ is the inherent spectral signal and $g(\omega)$ represents the Gaussian instrumental function. If the spectral lineshape is determined primarily by Doppler broadening, the resultant detected signal can be thought of as a convolution of a Gaussian function with a Gaussian function. The FWHM of the resultant signal, δ_R is related to the FWHM of the two Gaussian functions, δ_f and δ_g by

$$\delta_R{}^2 = \delta_f{}^2 + \delta_g{}^2 \tag{3.23}$$

In the case of the $1s3p$ dressed He absorption line as described by Chen *et al.*[24], the Doppler linewidth is less than 1 meV at 300 K while the measured linewidth as extrapolated in the paper is around 100 meV. The Gaussian linewidth is mainly determined by the instrumental resolution in this instance.

3.11 Conclusion

We have performed propagation simulations of attosecond, and therefore broad-band, pulses in Ar and He gas and studied the resulting pulse distortions. We first described the Kramers-Kronig relations which pertain to the dependence between the real and imaginary part of the

index of refraction. Then we developed an efficient computational method utilizing Möbius transformations and the Fast Fourier Transform. We also derived analytical solutions for ideal ionization edges, both to further our understanding of absorption and phase rotation a well as a tool to improve numerical convergence. Because of the broad-band nature of the pulses a significant part of their spectra falls above the ionization edges of Ar and He which leads to large distortions. The pulse distortions obtained include very rich features such as pulse stretching, partial narrowing, partial apparent super-luminality, and tail development. These distortions are relevant for the interpretation of experimental data and are also important for future practical applications. It would be interesting to investigate this rich behavior in future experiments.

Chapter 4

Theory of Multi-Electron Systems and Dynamics

In order to describe pump-probe transient absorption experiments we need to model ionization processes between neutral atoms, cations and multi-cations, and excitation processes in cations. To this end, we use the density matrix formalism which is capable of modelling open quantum systems of ensembles of atoms, and keeping track of all coherences and probability flows. We develop the necessary theory and apply the formalism to noble gases. Good reviews of density matrix operator theory can be found in Blum [27] and Mukamel [28].

4.1 Density Matrix Theory

While the pure wavefunction approach to quantum mechanics has been very successful, there are a number of reasons why this method may not always be sufficient as it assumes a single system isolated from its environment. The first reason is that there always is some interaction with the environment and that we cannot expect the wavefunction for the system to factor out, i.e. $\Psi_{\text{universe}} \neq \Psi_{\text{system}} \times \Psi_{\text{environment}}$. The second reason is that we often want to describe a statistical ensemble of systems, e.g. a gas of atoms or molecules, which cannot be expected to

all have been prepared in exactly the same pure state, and we lack the exact phase information among them. The third reason is that we sometimes want an economic description of complex systems without having to track in detail where the constituent particles are. This introduces the problem of how to handle particle exchange with the environment, e.g. ionization.

The density matrix operator formalism by von Neumann [25] addresses all these issues in one swoop. The density matrix can be interpreted as a probability weighted combination of pure states and is thus able to describe statistical ensembles as well as pure states, when needed. While interactions with the environment can be very complicated and intractable, the density matrix formalism allows for effectively averaging over environmental variables resulting in the simplest possible yet non-trivial consistent quantum dynamics. This approximation of effective interaction with the environment is achieved through Lindblad terms [26] which prove very useful in the description of physical systems. The standard example is spontaneous decay (of excited states in atoms) where the transitions are caused by thermal background photons, and the totality of interactions can be captured in a few effective decay rates. While from the pure wavefunction point of view these decay rates are rather ad hoc, they are a perfectly natural consequence of the density matrix formalism. Another example would be ionization.

4.1.1 Construction

For a pure state $|\Psi\rangle$ we construct the density operator ρ

$$\rho = |\Psi\rangle\langle\Psi| \tag{4.1}$$

and for a non-pure state we combine several pure wave functions, which do not have to be orthogonal but we will choose them to be normalized, and weight them with a probability mass p_n. We have that the p_n are real, non-negative, and their sum can be interpreted as a total particle number or unity, depending on the way we choose to normalize the density operator. We shall adhere to the convention that $\sum_n p_n = 1$, so the p_n can be interpreted as

probabilities.

$$\rho = \sum_n p_n |\Psi_n\rangle\langle\Psi_n| \tag{4.2}$$

Note that ρ is a Hermitian operator by construction

$$\rho^\dagger = \rho \tag{4.3}$$

For any wavefunction $|a\rangle$ we find

$$\langle a|\rho|a\rangle = \sum_n p_n \langle a|\Psi_n\rangle\langle\Psi_n|a\rangle = \sum_n p_n \left|\langle\Psi_n|a\rangle\right|^2 \geq 0 \tag{4.4}$$

Also,

$$\mathrm{tr}\,\rho = \sum_n p_n \,\mathrm{tr}\left(|\Psi_n\rangle\langle\Psi_n|\right) = \sum_n p_n \langle\Psi_n|\Psi_n\rangle = 1 \tag{4.5}$$

where we have used the trace operator[27]. This means that in any orthonormal and complete basis the diagonal matrix elements of ρ are non-negative, sum to one, and can be interpreted as the probability of finding the system in the state corresponding to that particular basis function.

In order to understand the difference between a coherent (pure state) density operator and a non-coherent one we will look at both extremes. Say we have an orthonormal basis and the pure state $|\Psi\rangle = \sum_a c_a|a\rangle$. Then $\rho_{ab} = \langle a|\rho|b\rangle = c_a^* c_b$. The off-diagonal elements express the coherence corresponding to the underlying pure state. What if the coefficients c_a are not actually well known? As an example take $c_a = \sqrt{p_a}e^{i\phi_a}$ and assume that the phases ϕ_a are completely randomized. Averaging over this ensemble gives $\rho_{ab} = \langle c_a^* c_b\rangle = \sqrt{p_a p_b}\langle e^{i(\phi_b - \phi_a)}\rangle = p_a\delta_{ab}$ so off-diagonal elements have averaged out to zero and the density operator has become completely diagonal. Note that a pure state cannot produce such a diagonal density matrix.

An N by N diagonal and non-degenerate density matrix requires an ensemble of at least N wavefunctions to construct.

For the expectation of an operator Q in a generally non-coherent state we can use the natural choice of summing over the ensemble of wavefunctions[27]

$$\begin{aligned} \langle Q \rangle &= \sum_n p_n \langle \Psi_n | Q | \Psi_n \rangle \\ &= \mathrm{tr}(\rho Q) \end{aligned} \tag{4.6}$$

A measure of purity can be obtained by computing $\mathrm{tr}\,\rho^2$ which is 1 for a pure state and, otherwise, smaller.

A futher useful fact is that the elements of the density matrix, in some orthonormal basis, are bounded by 1

$$|\rho_{ab}| = \left| \sum_n p_n \langle a|\psi_n\rangle\langle\psi_n|b\rangle \right| \leq \sum_n p_n = 1 \tag{4.7}$$

4.1.2 Time Evolution and the Liouville Equation

If the unitary propagator is known we can solve for the time dependency of ρ

$$\begin{aligned} \rho(t) &= \sum_n p_n |\Psi_n(t)\rangle\langle\Psi_n(t)| \\ &= \sum_n p_n U(t,t_0)|\Psi_n(t_0)\rangle\langle\Psi_n(t_0)|U^\dagger(t,t_0) \\ &= U(t,t_0)\rho(t_0)U^\dagger(t,t_0) \\ &= U(t,t_0)\rho(t_0)U(t_0,t) \end{aligned} \tag{4.8}$$

Now, because for all the component wavefunctions we have the Schrödinger equation $i\partial_t|\Psi_n\rangle = H|\Psi_n\rangle$ [29] and, therefore, also the adjoint $-i\partial_t\langle\Psi_n| = \langle\Psi_n|H$, we can derive

$$\begin{aligned} i\partial_t\rho &= \sum_n p_n\big((i\partial_t|\Psi_n\rangle)\langle\Psi_n| + |\Psi_n\rangle(i\partial_t\langle\Psi_n|)\big) \\ &= \sum_n p_n\big(H|\Psi_n\rangle\langle\Psi_n| - |\Psi_n\rangle\langle\Psi_n|H\big) \\ &= [H,\rho] \end{aligned} \tag{4.9}$$

which is the Liouville von Neumann equation [28] and which just as easily could have been derived from the properties of the unitary propagator. The time evolution of the density operator is driven by its commutator with the Hamiltonian.

As an aside, the equation of motion for the density matrix is reminiscent of that for operators in the Heisenberg picture, but there is an important difference. Consider a time-independent operator A: its expectation under a pure wave-function as a function of time is $\langle A\rangle_t = \langle\Psi_t|A|\Psi_t\rangle = \langle\Psi_0|A_H|\Psi_0\rangle$ where $A_H = e^{i\int_0^t H} A e^{-i\int_0^t H}$ is the operator in the Heisenberg picture. We then have $i\partial_t A_H = -[H, A_H]$. Notice the minus sign. It is important that the equation $i\partial_t\rho = [H,\rho]$, as per the construction above, is interpreted in the Schrödinger picture.

For the special case of a time-independent Hamiltonian and using the orthonormal eigenfunctions as a basis, so the Hamiltonian is diagonal, Equation (4.9) can be written as

$$i\partial_t\rho_{ab} = (E_a - E_b)\rho_{ab} \tag{4.10}$$

where $\rho_{ab} = \langle a|\rho|b\rangle$. This can be solved as

$$\rho_{ab}(t) = e^{-i(E_a-E_b)(t-t_0)}\rho_{ab}(t_0) \tag{4.11}$$

so the diagonal elements are constant in time while the off-diagonal elements oscillate according to the energy difference. In general, the Liouville von Neumann equation can be expanded on a basis and takes the form

$$i\partial_t \rho_{ab} = \sum_{cd} L_{ab,cd}\rho_{cd} \tag{4.12}$$

which is called the Liouville equation [28]. In short-hand

$$i\partial_t \rho = L\rho \tag{4.13}$$

where the Liouvillian L is now a super operator, having two pairs makes four indices. This notation is called the Liouville representation.

Using the Liouville von Neumann equation we can easily show, using properties of the trace operator, that the trace and the purity, and in fact the trace of any power of the density operator, are invariant in time. This should be obvious from the fact that ρ propagates in time by being sandwiched between two unitary propagators but it is nice to verify this invariance property from the dynamical equations. Do note that we are talking about a closed quantum system here.

$$\begin{aligned} i\partial_t \operatorname{tr}\rho &= \operatorname{tr}\left([H,\rho]\right) = 0 \\ i\partial_t \operatorname{tr}\rho^n &= n\operatorname{tr}\left(\rho^{n-1}[H,\rho]\right) = 0 \end{aligned} \tag{4.14}$$

If an operator Q is not explicitly time dependent then the evolution of its expectation is given by [27]

$$i\partial_t\langle Q\rangle = i\partial_t \operatorname{tr}\rho Q = \operatorname{tr}([H,\rho]Q) = \operatorname{tr}(\rho[Q,H]) \tag{4.15}$$

so we see that if Q commutes with the Hamiltonian its expectation will be time invariant, just as we are used to from pure states.

4.1.3 Density Operator Perturbation Theory

We want to solve the density matrix as a function of time when it is affected by a perturbation in the Hamiltonian

$$\begin{aligned} i\partial_t \rho &= [H, \rho] \\ i\partial_t \rho' &= [H + W, \rho'] \end{aligned} \tag{4.16}$$

with boundary condition $\rho'(t_0) = \rho(t_0)$ because we assume there is no perturbation on or before time t_0. If the unitary propagators are known we can write

$$\begin{aligned} \rho(t) &= U(t, t_0)\rho(t_0)U(t_0, t) \\ \rho'(t) &= U'(t, t_0)\rho'(t_0)U'(t_0, t) \end{aligned} \tag{4.17}$$

so using the expansion we have for U' we can write down a solution for ρ'.

There is another path to the same answer. Define an interaction picture view of the density operator by pulling it back to time t_0 by use of the unperturbed unitary propagator U.

$$\begin{aligned} W_I(t; t_0) &\equiv U(t_0, t)W(t)U(t, t_0) \\ \rho'_I(t; t_0) &\equiv U(t_0, t)\rho'(t)U(t, t_0) \end{aligned} \tag{4.18}$$

then, after some algebra, we find the Liouville von Neumann equation [28]

$$i\partial_t \rho'_I(t; t_0) = [W_I(t; t_0), \rho'_I(t; t_0)] \tag{4.19}$$

so the transformation to the interaction picture made the background Hamiltonian H disappear from the commutator. It is instructive to look at the trivial case when W is zero always, then ρ_I must be constant in t according to the dynamical equation

$$\rho_I(t;t_0) = U(t_0,t)\rho(t)U(t,t_0) = U(t_0,t)U(t,t_0)\rho(t_0)U(t_0,t)U(t,t_0) = \rho(t_0) \tag{4.20}$$

so the unperturbed density operator is indeed constant in the interaction picture.

We can solve the Liouville von Neumann equation for ρ'_I order by order in the perturbation W

$$\rho'_I(t;t_0) = \sum_{n=0}^{\infty} \rho'_{I,n}(t;t_0) \tag{4.21}$$

which gives us

$$\begin{aligned} &i\partial_t \rho'_{I,0}(t;t_0) = 0 \\ &i\partial_t \rho'_{I,n}(t;t_0) = [W_I(t;t_0), \rho'_{I,n-1}(t;t_0)] \qquad\qquad n \geq 1 \end{aligned} \tag{4.22}$$

Because of the assumption of no perturbation on or before t_0 we have that

$$\rho'_{I,0}(t;t_0) = \rho(t_0) \tag{4.23}$$

and

$$\rho'_{I,n}(t_0;t_0) = 0 \qquad\qquad n \geq 1 \tag{4.24}$$

Integrating the differential equation for $n \geq 1$ gives

$$\rho'_{I,n}(t;t_0) = (-i)\int_{t_0}^{t} dt_n [W_I(t_n;t_0), \rho'_{I,n-1}(t_n;t_0)] \tag{4.25}$$

We see that we can derive the high orders by induction, which causes a nesting of commutators and putting it all together we get [28]

$$\rho_I'(t;t_0) = \rho(t_0) + \sum_{n=1}^{\infty}(-i)^n \int_{t_0}^{t} dt_n \dots \int_{t_0}^{t_1} dt_1 [W_I(t_n;t_0), \dots [W_I(t_1;t_0), \rho(t_0)] \dots] \tag{4.26}$$

4.2 Open Quantum Systems

The purpose of this section is to derive a generalization of the closed-system von Neumann equation $\dot{\rho} = -i[H, \rho]$ to open systems and study its properties. We develop the Lindblad [26] formalism which not only allows for an efficient description of the effective interaction with the environment of a quantum system but can also handle particle exchange. For example, when describing Auger decay, we can forego the complete time-dependent Schrödinger equation modelling of a very large number of internal states of the atom combined with the position and momentum of the escaping electron, and reduce this intricate picture to effective decay rates.

There is a broad literature ranging from formal derivations, e.g. Lindblad [26] to microscopic derivations [30], to stochastic approaches [31]. We will choose a variant of the stochastic approach as it is efficient in getting to the core of the mathematical structure and because of its affinity with physical intuition.

4.2.1 Deriving the Lindblad Form

Consider an open quantum system, by which we mean a quantum system that interacts with a large environment. The combination of the system and the environment is a closed system and evolves unitarily. However we often know precious little about the environment and would prefer not to model it. Is there a way to somehow average out the effects of the environment and model our quantum system with some effective form? Due to the

interactions with the outside the evolution of the system will not be unitary. What we do retain is that the density matrix has trace one, is Hermitian and that it is non-negative (all its eigenvalues are non-negative), which is crucial in avoiding negative probabilities. Let us try to construct such a theory.

In analogy with the unitary evolution $U\rho U^\dagger$ that we know from closed systems we try something a bit more general

$$\rho(t+dt) = S(t+dt,t)\rho(t)S^\dagger(t+dt,t) \tag{4.27}$$

so ρ will stay Hermitian by construction. For the closed case we have $S = U = 1 - iHdt$. For the open case we would like to include the bumps the system receives from the environment which happen at a much shorter timescale than the timescales which are relevant for our system of study. Note that the assumption of fast environmental fluctuations, and the assumption that the environment very quickly forgets how it interacted with our system, is known as the Markov property. From this point on we will restrict ourselves to the Markov case.

We model environmental fluctuations as random stochastics, working on an N-dimensional Hilbert space,

$$S = 1 + Vdz + (-iH + W)dt \tag{4.28}$$

where S, V and W are N by N complex matrices, W is a correction term we will soon derive, and dz drives the fluctuations. The term dz is a stochastic infinitesimal, familiar from Brownian motion random walks, and is of order $\sqrt{dt}$ in such a way that it has expectations $<dz>= 0$ and $<dzdz>= dt$, similar to Ito calculus. Note that we use the bracket notation to indicate averaging over the fluctuations. We need to update our formula to indicate this averaging [31]

$$\rho + d\rho = \langle S\rho S^\dagger \rangle = \rho + dt\left(\rho(W^\dagger + iH) + (W - iH)\rho + V\rho V^\dagger\right) \tag{4.29}$$

where we dropped the time dependence in the notation. Now because $\operatorname{tr}\rho = 1$ and we want to preserve this trace, we must have $\operatorname{tr} d\rho = 0$. So for all valid densities ρ we must have that $0 = \operatorname{tr}\left(\rho(W^\dagger + iH) + (W - iH)\rho + V\rho V^\dagger\right) = \operatorname{tr}\rho\left(W^\dagger + W + V^\dagger V\right)$ from which it follows that we must have $0 = W^\dagger + W + V^\dagger V$. We choose

$$W = -\frac{1}{2}V^\dagger V \tag{4.30}$$

Note that W can only be determined up to an anti-Hermitian term, but this can always be absorbed in $-iH$. Putting it all together.

$$\dot{\rho} = -i[H, \rho] + V\rho V^\dagger - \frac{1}{2}V^\dagger V\rho - \frac{1}{2}\rho V^\dagger V \tag{4.31}$$

Of course, we could have more than just one type of fluctuation. We could have as many as we like

$$\rho + d\rho = \sum_n \gamma_n \langle S_n \rho S_n^\dagger \rangle \tag{4.32}$$

where $\gamma_n \geq 0$ and $\sum_n \gamma_n = 1$. This gives, using the same H for all but different V_n,

$$\dot{\rho} = -i[H, \rho] + \sum_n \gamma_n \left(V_n \rho V_n^\dagger - \frac{1}{2}V_n^\dagger V_n \rho - \frac{1}{2}\rho V_n^\dagger V_n\right) \tag{4.33}$$

The first part of this equation is the same as the von Neumann equation, familiar from the unitary evolution of closed systems. The new part on the right is called the Lindblad form

[26] and it can cause damping and decoherence. The γ_n can easily be absorbed in the V_n by rescaling. It is important to point out that there is no unique separation between the system Hamiltonian H and the Lindblad form, something we already encountered during the derivation. To make this fact explicit, consider the following invariance which leaves $\dot{\rho}$ unchanged [26]

$$\begin{aligned} V_n &\to V_n + c_n 1 \\ H &\to H - \frac{i}{2}\sum_n \gamma_n(c_n^* V_n - c_n V_n^\dagger) + s\,1 \end{aligned} \tag{4.34}$$

where the c_n are complex numbers and s is real. Although we can add as many types of fluctuations as we want we are in fact dealing with a linear map from an N by N complex matrix to a N by N complex matrix. This means that at most N^4 free coefficients are involved, and in fact many fewer due to the Hermiticity and trace constraints. This means that for any soup of fluctuations the Lindblad form can always be decomposed into a finite set of generators V_n, see Kraus [32].

4.2.2 Positivity and the Lindblad Form

We know that the Hermiticity and trace of ρ are now preserved but what is the guarantee that the density matrix stays non-negative during its evolution? Adding just any term on the right of the von Neumann equation will often lead to negative probabilities. It is important to understand how the Lindblad form avoids this.

The density matrix ρ at time t is Hermitian and has orthonormal eigen vectors $|n\rangle$ with eigenvalues r_n. Note we are talking about the eigenvectors of the density matrix, not the Hamiltonian. We have the usual properties $\rho|n\rangle = r_n|n\rangle$, $\langle m|n\rangle = \delta_{mn}$, $1 = \sum_n |n\rangle\langle n|$ and $\rho = \sum_n r_n|n\rangle\langle n|$. Moving forward dt in time the eigenvectors and eigenvalues change $(\rho + d\rho)(|n\rangle + d|n\rangle) = (r_n + dr_n)(|n\rangle + d|n\rangle)$. Expanding to first order and applying a bra from the left we get the familiar result from first order perturbation theory $dr_n = \langle n|d\rho|n\rangle$

or

$$\dot{r}_n = \langle n|\dot{\rho}|n\rangle \tag{4.35}$$

Because $\langle n|[H,\rho]|n\rangle = 0$ we see that only the Lindblad form can have an effect on the eigenvalues of ρ, as we expected already because unitary transformations could not affect those eigenvalues. For notational simplicity we shall use the Lindblad form $V\rho V^\dagger - \frac{1}{2}V^\dagger V\rho - \frac{1}{2}\rho V^\dagger V$. Extending our argument below to a summation over different V's is trivial [26].

$$\begin{aligned}
\dot{r}_n &= \langle n|\dot{\rho}|n\rangle \\
&= \langle n|V\rho V^\dagger|n\rangle - r_n\langle n|V^\dagger V|n\rangle \\
&= \sum_k \langle n|V|k\rangle r_k \langle k|V^\dagger|n\rangle - r_n \sum_k \langle n|V^\dagger|k\rangle\langle k|V|n\rangle \\
&= \sum_k r_k|V_{nk}|^2 - r_n\sum_k |V_{kn}|^2
\end{aligned} \tag{4.36}$$

Start with a valid density matrix, $r_k \geq 0$ for all k. Now if it happens to be the case that $r_n = 0$ for some n then it follows that $\dot{r}_n \geq 0$ from our derivation above. So zero eigenvalues never go negative, but stay zero or increase: this is how a pure state gets mixed. If $r_n > 0$ for some n then if follows that

$$\frac{\dot{r}_n}{r_n} \geq -\sum_k |V_{kn}|^2 \tag{4.37}$$

so when V is bounded then there is a maximum decay rate for the movement of eigenvalues to zero, they can never get there in finite time.

4.2.3 The Liouvillian

We start with the von Neumann Lindblad equation

$$\dot{\rho} = -i[H, \rho] + \sum_V \left(V\rho V^\dagger - \frac{1}{2} V^\dagger V \rho - \frac{1}{2} \rho V^\dagger V \right) \tag{4.38}$$

where we sum over different V and any factors γ have been absorbed in the V's themselves. Now ρ is an N by N matrix, and we are mapping linearly to $\dot{\rho}$ which is of the same size. The map itself is, therefore, of size N^2 by N^2. This map is called the Liouvillian $\mathcal{L}$. Note that the density operator ρ is a linear operator, i.e. a matrix that maps vectors into vectors, while the Liouvillian $\mathcal{L}$ maps linear operators into linear operators (called a superoperator), i.e. a supermatrix that maps matrices into matrices.

So the von Neumann Lindblad equation can be written as

$$\dot{\rho} = \mathcal{L}\rho \tag{4.39}$$

Note that we follow the Breuer[30] convention here, and not Mukamel[28]. We define $\mathcal{L} = -iL$ where L was used in Equation (4.13). We write out the map exactly, working in some orthonormal basis,

$$\mathcal{L}_{ab,nm} = -i\delta_{bm} H_{an} + i\delta_{an} H_{mb} + \sum_V \left(V_{an} V^*_{bm} - \frac{1}{2}\delta_{bm} (V^\dagger V)_{an} - \frac{1}{2}\delta_{an} (V^\dagger V)_{mb} \right) \tag{4.40}$$

In practice the pair index (a, b) is mapped into a single index $Na + b$. This index form of the Liouvillian is used in numerical simulation. Note that there are two ways to view the Liouvillian, which we will switch between frequently. One is as a superoperator that maps N by N matrices into N by N matrices. Another is as a N^2 by N^2 matrix that maps N^2 by 1 vectors into N^2 by 1 vectors.

If there were no Lindblad term then $\mathcal{L}$ would be anti-Hermitian, as expected for unitary evolution. But the Lindblad term, as a rule, breaks that symmetry and, in general $\mathcal{L}$ isn't anti-Hermitian but a much more general N^2 by N^2 matrix, as needed for damping and dephasing. Yet it has a lot of structure. The Liouvillian has the following interesting symmetry

$$\mathcal{L}_{ab,nm} = \mathcal{L}^*_{ba,mn} \tag{4.41}$$

which can be checked from the index formula for $\mathcal{L}$ or directly from the fact that ρ and $\dot{\rho}$ are Hermitian.

Also, because $0 = \mathrm{tr}\,\dot{\rho} = \sum_a \dot{\rho}_{aa} = \sum_{anm} \mathcal{L}_{aa,nm}\rho_{nm}$ which is true for all densities ρ, we must have

$$\sum_a \mathcal{L}_{aa,nm} = 0 \tag{4.42}$$

for all pairs nm. In other words δ_{ab} is a left-eigenvector of $\mathcal{L}$ with eigenvalue zero. Because of this trace constraint it follows that there must also always exist a right eigenvector with zero eigenvalue; this is called the steady state solution if H and V are constant in time.

4.2.4 Spectrum of the Liouvillian

Let's have a look at the right-eigenvectors, usually just called eigenvectors, of the Liouvillian $\mathcal{L}f = \lambda f$. Then, using the symmetries of the Liouvillian we find

$$\sum_{nm} \mathcal{L}_{ab,nm} f_{nm} = \lambda f_{ab} \Rightarrow \sum_{nm} \mathcal{L}^*_{ab,nm} f^*_{nm} = \lambda^* f^*_{ab} \Rightarrow \sum_{nm} \mathcal{L}_{ba,mn} f^\dagger_{mn} = \lambda^* f^\dagger_{ba} \tag{4.43}$$

so when the N by N matrix f is a right-eigenmatrix of the superoperator $\mathcal{L}$ with eigenvalue λ then its adjoint $f^\dagger$ is also a right-eigenmatrix of the superoperator $\mathcal{L}$, this time with eigenvalue

λ^*. This means that if the eigenvalue has a non-zero imaginary part (read oscillatory) then the eigenvalues and their corresponding eigenmatrices must come in pairs. If the eigenvalue is real (read non-oscillatory) it means that f and $f^\dagger$ are proportional, so we can always rescale with a phase factor to make f Hermitian.

Let's check what we've learned so far with the simplest case; a zero Lindblad term. Then evolution is purely unitary. If the spectrum of the Hamiltonian is $\{E_n\}$ and we work in the Hamiltonian eigenbasis, then we know that the density matrix elements oscillate according to the difference spectrum $\{-i(E_n - E_m)\}$ and this must be the spectrum of the Liouvillian itself. The eigenmatrices are very simple in this case, just a 1 at element (n, m) and zero everywhere else. We can easily check that complex eigenvalues do come in pairs and that the eigen matrices are the adjoints of each other. Also, there are N, real eigenvalues which are all zero, and which correspond to diagonal matrices, which can indeed be chosen to be Hermitian.

The left-eigenvectors of the Liouvillian are defined by $g^\dagger \mathcal{L} = \lambda g^\dagger$ and, again using the symmetries of the Liouvillian it is easy to show that if g is a left-eigenvector with eigenvalue λ then $g^\dagger$ is also an eigenvector, this time with eigenvalue λ^*. So again we get the pairing of complex eigenvalues and for real eigenvalues we have Hermitian eigenmatrices. Because we know from density matrix trace preservation that $\sum_a \mathcal{L}_{aa,nm} = 0$ it follows that the identity matrix is a left-eigenmatrix of the Liouvillian superoperator with eigenvalue zero.

It is a happy fact that the spectrum derived for right-eigenvectors and that for left-eigenvectors is always one and the same. This is most easily seen by reformulating the eigen requirement in terms of the characteristic equation

$$\det(\mathcal{L} - \lambda 1) = 0 \tag{4.44}$$

which treats left and right on the same footing. For an eigenvalue lambda there must be both a linear dependence between the columns and, separately, between the rows to make the determinant zero. The left and right eigenvectors are orthogonal to each other because [33]

$$\lambda_n g_n^\dagger f_m = g_n^\dagger \mathcal{L} f_m = \lambda_m g_n^\dagger f_m \tag{4.45}$$

so if $\lambda_n \neq \lambda_m$ then $g_n^\dagger f_m = 0$. We can always achieve by scaling, or by rearrangement in degenerate cases, to have orthonormality

$$g_n^\dagger f_m = \delta_{nm} \tag{4.46}$$

In one of those confusing notational changes when going from N^2-dimensional Liouville superspace to N by N matrix space we have

$$g_n^\dagger f_m = \sum_{ab} g_{n,ab}^* f_{m,ab} = \sum_{ab} g_{n,ba}^\dagger f_{m,ab} = \mathrm{tr}\, g_n^\dagger f_m \tag{4.47}$$

where the notation on the left is the complex dot product in N^2 dimensional space and the notation on the right involves matrices. We can use the relation

$$\mathrm{tr}\, g_n^\dagger f_m = \delta_{nm} \tag{4.48}$$

to decompose the density

$$\begin{aligned} c_n &= \mathrm{tr}\, g_n^\dagger \rho \\ \rho &= \sum_n c_n f_n \end{aligned} \tag{4.49}$$

If we decompose the initial density like this and assume that the Hamiltonian and the Lindblad form are constant in time then we have a complete decomposition of the time development

$$\rho(t) = \sum_n \mathrm{tr}\left(g_n^\dagger \rho(0)\right) f_n e^{\lambda_n t} \tag{4.50}$$

so we have achieved the decomposition of the density matrix into Liouvillian eigen-densities. Because we know that every element of the density matrix is bounded $|\rho_{ab}| \leq 1$ it follows that every eigenvalue of the Liouvillian has non-positive real part, so damping can and does happen, but exponential growth cannot.

For completeness we also show that the Liouvillian super operator can now be expanded like so

$$\mathcal{L} = \sum_n \lambda_n f_n g_n^\dagger \tag{4.51}$$

There always is at least one eigenvalue that is exactly zero whose left-eigenmatrix is the identity, which is associated with trace conservation, and whose right-eigenmatrix is the steady-state density. Let's index this left-eigenmatrix with 0, then we have [33]

$$\delta_{0n} = \mathrm{tr}\, g_0^\dagger f_n = \mathrm{tr}\, f_n \tag{4.52}$$

so f_0 isn't traceless because it is the steady state, but all other f_n must be traceless.

4.2.5 Transitions

We can imagine that the environment, e.g. a bath of electromagnetic radiation at a certain temperature, causes transitions in our system of study

$$V_{(nm)} = c_{nm} |n\rangle\langle m| \tag{4.53}$$

which should be understood as an environment influence that causes a transition from system Hamiltonian eigenstate $|m\rangle$ to state $|n\rangle$ with some complex amplitude c_{nm}. The coefficients of V on the Hamiltonian eigenbasis are, rather tautologically, $V_{(nm)ab} = c_{nm}\delta_{an}\delta_{bm}$. Taking the sum over N^2 interactions of this type we get the LvN equation [30][34]

$$\dot{\rho}_{ab} = \left(-i(E_a - E_b) - \frac{1}{2}(\tilde{\gamma}_a + \tilde{\gamma}_b)\right)\rho_{ab} + \delta_{ab}\sum_m \gamma_{am}\rho_{mm} \tag{4.54}$$

where $\gamma_{nm} = |c_{nm}|^2 \geq 0$ and $\tilde{\gamma}_a = \sum_n \gamma_{na}$. We see that for $a \neq b$ the ρ_{ab} are decoupled and decay exponentially at the rate $\frac{1}{2}(\tilde{\gamma}_a + \tilde{\gamma}_b)$. On the diagonal we find

$$\dot{\rho}_{aa} = \sum_m \gamma_{am}\rho_{mm} - \tilde{\gamma}_a\rho_{aa} \tag{4.55}$$

Reinterpreting the diagonal elements of the density matrix as probabilities $q_a = \rho_{aa}$ because they are real, non-negative and sum to one, we write this last equation as

$$\dot{q}_a = \sum_m \gamma_{am}q_m - \gamma_{ma}q_a \tag{4.56}$$

which is known as the Pauli master equation, or simply the rate equation. The term $\gamma_{am}q_m$ describes the influx into state a coming from state m and the term $\gamma_{ma}q_a$ shows the out-flux from state a into state m.

4.3 Three Spaces

We model cations with three Hilbert spaces and use krypton as an example. The first space is one-dimensional and describes neutral atoms which act as a source of cations due to ionization. The second space is the cations themselves, for instance for Kr II we focus on the $4p_{3/2}$,

$4p_{1/2}$, $3d_{5/2}$ and $3d_{3/2}$ levels which make for a 16-dimensional space, counting degeneracies. Full dimensionality is required here to allow for the correct modelling of pump and probe pulses of different polarizations. The third space is one-dimensional and describes multi-cations and acts as a sink for processes such as Auger decay. See Figure (5.1) showing a diagram for krypton. The communication between the three spaces is provided by the Lindblad term in the Liouvillian. This three space setup allows us to formulate consistent evolution equations for the reduced density matrix, preserving Hermiticity, positive-definiteness and overall probability. This construction provides the most compact self-consistent description of cation evolution, generation and decay processes, which are crucial for proper pumping and transient absorption simulations.

While the description of decay processes through decay parameters, which is a Lindblad term in disguise, is a very old practice indeed, its sister process which generates rather than decays cations, is not. The advantage of having such a compact description of cation generation is that no first-principle modelling is required, the symmetries of ionization are very tractable and the parameters allowed within this formulation are very clear. Multi-channel ionization modelling from first principles [35] is unsatisfactory so far in that it predicts cation generation in the $4p_{3/2}$ $m = 3/2$ vs. $m = 1/2$ channel that is 7 times too low compared to experiment. We can fit to experimental data as this production ratio is a parameter of the generation process in our construction. We use our generation process to derive coherences for Ne, Ar, Kr and Xe.

4.3.1 Flow between Hilbert Spaces

The density matrix formalism is very powerful and can in fact be used to describe the communication and probability flow between different Hilbert spaces, for example between a neutral atom and a cation. We derive how this can be accomplished. We repeat the very important Equation (4.40) for the Liouvillian [26].

$$\mathcal{L}_{ab,nm} = -i\delta_{bm}H_{an} + i\delta_{an}H_{mb} + \sum_V \left(V_{an}V^*_{bm} - \frac{1}{2}\delta_{bm}(V^\dagger V)_{an} - \frac{1}{2}\delta_{an}(V^\dagger V)_{mb} \right) \tag{4.57}$$

Now split up the space into two, using Latin indices for the first and Greek indices for the second space

Coherence between different Hilbert spaces is meaningless and the elements of ρ connecting the spaces must stay zero at all times. In other words the density matrix is block-diagonal. This give us the constraints $\mathcal{L}_{a\beta,**} = \mathcal{L}_{\alpha b,**} = 0$ for all a, b, α and β. The $*$ stand for any index, Latin or Greek. The Hamiltonians operate on their respective Hilbert spaces and, therefore, have no cross terms and do respect these constraints. The Lindblad form is more interesting. The constraints allow for two types of solutions for V. The first is the trivial solution where V is block-diagonal, which means that the two Hilbert spaces have nothing to do with each other whatsoever. The second type is what we are after

$$V = \begin{pmatrix} 0 & N \\ M & 0 \end{pmatrix} \tag{4.58}$$

This type of Lindblad form provides communication between the two spaces and allows probability to flow. We spell out the dynamics of $\dot{\rho} = \mathcal{L}\rho$ for this form [26]

$$\begin{aligned}
\mathcal{L}_{ab,nm} &= -i\delta_{bm}H_{an} + i\delta_{an}H_{mb} - \frac{1}{2}\sum_M \left(\delta_{bm}(M^\dagger M)_{an} + \delta_{an}(M^\dagger M)_{mb} \right) \\
\mathcal{L}_{\alpha\beta,\nu\mu} &= -i\delta_{\beta\mu}H_{\alpha\nu} + i\delta_{\alpha\nu}H_{\mu\beta} - \frac{1}{2}\sum_N \left(\delta_{\beta\mu}(N^\dagger N)_{\alpha\nu} + \delta_{\alpha\nu}(N^\dagger N)_{\mu\beta} \right) \\
\mathcal{L}_{ab,\nu\mu} &= \sum_N N_{a\nu}N^*_{b\mu} \\
\mathcal{L}_{\alpha\beta,nm} &= \sum_M M_{\alpha n}M^*_{\beta m}
\end{aligned} \tag{4.59}$$

Of course, other Lindblad forms restricted to the respective spaces can easily be added on top.

Notice that for the evolution of the density matrix traces in the Latin and Greek index spaces we have

$$\mathrm{tr}_a\,\dot{\rho} = -\,\mathrm{tr}_a \sum_M M^\dagger M\rho + \mathrm{tr}_\alpha \sum_N N^\dagger N\rho = -\,\mathrm{tr}_\alpha\,\dot{\rho} \tag{4.60}$$

so N makes probability flow from Greek to Latin and M makes probability flow from Latin to Greek space, while the total trace, which is one, is conserved.

We can simplify by making the Greek space one-dimensional which turns M and N into vectors. The density matrix dynamics can then be written as

$$\begin{aligned}
\dot{\rho}_{\alpha\alpha} &= -\sum_N |N|^2 \rho_{\alpha\alpha} + \sum_M \sum_{nm} M_n M_m^* \rho_{nm} \\
\dot{\rho}_{ab} &= \sum_{nm} \left(-i\delta_{bm} H_{an} + i\delta_{an} H_{mb}\right) \rho_{nm} \\
&\quad + \sum_N N_a N_b^* \rho_{\alpha\alpha} - \frac{1}{2} \sum_M \left(M_a^* \sum_n M_n \rho_{nb} + M_b \sum_m M_m^* \rho_{am} \right)
\end{aligned} \tag{4.61}$$

4.3.2 The Source

There is a long tradition in atomic and nuclear physics to describe decay processes with simple decay rates, while the underlying physical processes are rather complicated and involve a very large number of states. This effective decay description, with a compact and simple mathematical structure, has been very successful in the description of resonances, line widths, cross-sections, scattering etc. We apply the same philosophy to ionization processes, recognizing the intricate physical processes that lie beneath, but trying to find the simplest non-trivial description via the Lindblad term in the Liouville -von Neumann equation for the reduced density matrix.

Say a one-dimensional Greek space acts as a source (i.e. the neutral atoms) and we neglect the back-flow (i.e. electron re-capture), $M = 0$, while there are a number of ionization processes

going on, which we index with k. Ionization produces cations, whose levels we index with Latin indices. Equation (4.61) simplifies to the pure source equation

$$\begin{aligned}\dot{\rho}_{\alpha\alpha} &= -\sum_k |N^{(k)}|^2 \rho_{\alpha\alpha} \\ \dot{\rho}_{ab} &= \sum_{nm} \left(-i\delta_{bm} H_{an} + i\delta_{an} H_{mb}\right) \rho_{nm} + \sum_k N_a^{(k)} N_b^{(k)*} \rho_{\alpha\alpha}\end{aligned} \tag{4.62}$$

Looking at the diagonal elements ρ_{aa} we see that the neutral atoms pump probability into the cations at the detriment of its own probability $\rho_{\alpha\alpha}$. Of course the N vector is time dependent which is how we, for instance, can model the influence of a pump pulse.

The question remains how the vectors $N^{(k)}$ can be chosen to provide an effective description of ionization, and how much choice we have in the matter in the first place. First we note that the set of $N^{(k)}$ has gauge symmetry, meaning that many of these sets can produce the same density matrix and, therefore, the same physical expectation values for Hermitian operators. We will use this gauge symmetry to simplify the $N^{(k)}$ set.

In Section 5.1.1 we derive the symmetries the density matrix must have, assuming neutral atoms start out completely incoherent and are then pumped by a z-polarized electric dipole interaction. The symmetry constraints are that m is conserved and that there is a m to $-m$ symmetry due to spatial symmetries which can be derived via the Wigner-Eckart theorem. Note that both ρ and $\dot{\rho}$ observe these symmetries.

For the case of Krypton II, with levels $4p_{3/2}$ and $4p_{1/2}$ with fourfold and twofold degeneracy respectively and picking a helpful (partial) gauge, while respecting the density matrix symmetries, we parametrize (using $N_{j,m}^{(k=m)}$ notation) with the parameters π_i. Note that these parameters can be viewed as square-roots of ionization rates as more succinctly described in the source equation (4.62).

$$
\begin{aligned}
N^{(3/2)}_{3/2,\,3/2} &= N^{(-3/2)}_{3/2,-3/2} = \pi_1 \\
N^{(1/2)}_{3/2,\,1/2} &= N^{(-1/2)}_{3/2,-1/2} = \pi_2 \\
N^{(1/2)}_{1/2,\,1/2} &= -N^{(-1/2)}_{1/2,-1/2} = \pi_3
\end{aligned}
\tag{4.63}
$$

The minus sign is essential. The index k now plays the role of m_j channel. Note that the parameters π_i are in general complex but there is gauge symmetry left to pin them down further. The phase of π_1 is irrelevant but the phase difference between π_2 and π_3 shows up in the density matrix as the phase of the coherence term between $4p_{j=3/2,m=1/2}$ and $4p_{j=1/2,m=1/2}$. Of course, this phase can be removed by a unitary transformation on the density matrix. In that case all parameters can be chosen to be real. We use this parametrization to compute coherences after the pump pulse in Section 5.1.2.

In practice, we set the overall scale of the ionization vectors $N^{(k)}$ by the ADK approximation, referencing only the energy levels. Our description allows for different cation production rates in the respective m channels, and we introduce these differences as multipliers on the overall ADK rates. These relative production rates are, therefore, an input to our effective model. For our simulations we use experimental data by Goulielmakis *et al.* [2] to set the relative production rate in the $m = 3/2$ channel. It is important to note that published first-principle calculations for the ionization of krypton produce population ratios in the $4p_{j=3/2,m=3/2}$ vs. $4p_{j=3/2,m=1/2}$ channels that are much too low (by a factor 7 or so) compared to experiment [2][36]. First-principle multi-channel ionization modelling still has some ways to go.

4.3.3 The Sink

The opposite construction is that of a pure sink, which is a catch-all Hilbert space which we choose to be one-dimensional. For example, when cations ionize to dications and beyond,

and for the problem at hand we do not wish to model the details of the dications, then we can use such a sink space to absorb the probability flow and keep the density matrix formulation consistent. Here, again, we neglect back flow (so no electron recapture) to keep things simple. This means that $N = 0$ in this case. For instance, Auger processes can move cations, in the Latin index space we intend to study in some detail, to di- and multi-cation space, whose details we explicitly omit. We assume the Auger processes for the different energy levels of the cation are independent processes so we need a separate M vector for each level. Let's call these M^c. This vector has elements M^c_a which are all zero except for one $M^c_a = \delta_{ac}\sqrt{\gamma_c}e^{i\phi_c}$ where γ_c is real and non-negative and ϕ_c is an arbitrary phase. Filling this into Equation (4.61) leads to, using the Hamiltonian eigen-basis,

$$\begin{aligned} \dot{\rho}_{\alpha\alpha} &= \sum_c \gamma_c \rho_{cc} \\ \dot{\rho}_{ab} &= (-iE_a + iE_b - \tfrac{1}{2}\gamma_a - \tfrac{1}{2}\gamma_b)\rho_{ab} \end{aligned} \tag{4.64}$$

so we get particularly simple exponential decay where the γ_c are the decay rates, or, if you wish, the FWHM of the Lorentzian lineshape.

It is interesting to see how exponential decay follows very naturally for the density matrix formalism over a collection of Hilbert spaces when this is not at all as straightforward in the usual quantum mechanical formulation over the combined Hilbert space, including emitted particles and such. To quote Merzbacher [37]: "... the fact remains that the exponential decay law, for which we have so much empirical support ..., is not a rigorous consequence of quantum mechanics but the result of somewhat delicate approximations." Using second order time-dependent perturbation theory Wigner and Weisskopf [37][38][39] derived an approximation for the decay of a discrete state. This works when an initial discrete state couples into a dense or continuous target space of states, e.g. by the emission of a particle, resulting in exponential decay, associated with a Lorentzian line-shape where γ_c is the FWHM of the intensity. The coupling of the continuum of target states back to the discrete state is marred by destructive interference with the result that probability does not flow back. The irony is

that while the physical target space is necessarily huge to make exponential decay happen we can model it with just a one-dimensional sink in the density matrix formalism.

4.3.4 Field Free Evolution and the Free Liouvillian Eigenbasis

The eigen-structure of the field free Liouvillian is rather simple except for one subtlety regarding decay into the sink. We can ignore the source and we use indices a through n for the cation space, while reserving the index s to indicate the sink. The dynamic equations are

$$\begin{aligned}
\dot{\rho}_{ab} &= i(-E_a + E_b)\rho_{ab} - \frac{1}{2}(\gamma_a + \gamma_b)\rho_{ab} \\
\dot{\rho}_{aa} &= -\gamma_a \rho_{aa} \\
\dot{\rho}_{ss} &= \sum_a \gamma_a \rho_{aa}
\end{aligned} \tag{4.65}$$

Note that the unphysical, cross Hilbert space, density matrix elements ρ_{as} and ρ_{sa} are always zero.

$$\begin{aligned}
\lambda_{as} &= i(-E_a + E_s) & \rho_{as}(t) &= 0 \\
\lambda_{sa} &= i(-E_s + E_a) & \rho_{sa}(t) &= 0
\end{aligned} \tag{4.66}$$

When a is not equal to b we see that the dynamics are diagonal and evolve with eigenvalue

$$\begin{aligned}
\lambda_{ab} &= i(-E_a + E_b) - \frac{1}{2}(\gamma_a + \gamma_b) \\
\rho_{ab}(t) &= \rho_{ab}(0)\ e^{\lambda_{ab} t}
\end{aligned} \tag{4.67}$$

However, the set of ρ_{aa} and ρ_{ss} are coupled. Their time dependence is easily solved

$$\begin{aligned}\rho_{aa}(t) &= \rho_{aa}(0)e^{-\gamma_a t} \\ \rho_{ss}(t) &= \rho_{ss}(0) + \sum_a \rho_{aa}(0)\ (1 - e^{-\gamma_a t})\end{aligned} \tag{4.68}$$

which shows exponential decay of the probabilities in cation space. Note that total probability is conserved as all the flow is collected by the sink.

In order to model field free evolution properly, for instance for use in perturbation theory, we need the left and right eigenvectors of the Liouvillian. The right eigenvectors serve as a basis for the density matrix while the left eigenvectors serve as projectors onto these basis vectors [33]. For ρ_{ab}, $a \neq b$, ρ_{as} and ρ_{sa} these eigenvectors are trivial and the left and right are the same. In the diagonal space of ρ_{aa} and ρ_{ss} we have the dynamics

$$\begin{pmatrix} \vdots \\ \dot{\rho}_{aa} \\ \vdots \\ \dot{\rho}_{ss} \end{pmatrix} = \begin{pmatrix} \ddots & & & \\ & -\gamma_a & & \\ & & \ddots & \\ \cdots & \gamma_a & \cdots & 0 \end{pmatrix} \begin{pmatrix} \vdots \\ \rho_{aa} \\ \vdots \\ \rho_{ss} \end{pmatrix} \tag{4.69}$$

where all empty entries are zero and dotted entries in the matrix are filled with negative or positive γ values, as indicated. The right eigenvectors $f^{(aa)}$ of the matrix are

$$\begin{aligned} \lambda_{aa} = -\gamma_a, \quad f_b^{(aa)} = \delta_{ab}, \quad f_s^{(aa)} = -1 \\ \lambda_{ss} = \ 0, \qquad f_b^{(ss)} = 0, \qquad f_s^{(ss)} = \ 1 \end{aligned} \tag{4.70}$$

The left eigen vectors $g^{(aa)}$ are

$$\begin{aligned} \lambda_{aa} = -\gamma_a, \quad g_b^{(aa)} = \delta_{ab}, \quad g_s^{(aa)} = \ 0 \\ \lambda_{ss} = \ 0, \qquad g_b^{(ss)} = 1, \quad g_s^{(ss)} = \ 1 \end{aligned} \tag{4.71}$$

Note that the left and right eigenvectors are orthonormal with respect to each other.

With an eye on introducing dipole interaction later we can ask what the difference is between the matrix elements of the dipole operator in the expanded free Hamiltonian eigen basis versus those in the free Liouvillian eigen basis. General matrices would indeed have changed matrix elements because the basis has changed due to the Lindblad term. We know that the electric dipole matrix in the expanded free Hamiltonian basis has lots of zero entries due to symmetries and forbidden transitions. The free Liouvillian basis is only different in the subspace of ρ_{aa} and ρ_{ss}. Due to parity considerations the dipole operator is exactly zero in this subspace. This leads us to the important conclusion that the matrix elements of the dipole operator in the free Liouvillian eigen basis are exactly the same as those in the expanded free Hamiltonian eigen basis, simplifying our analysis of perturbative expansions.

To recap, combining the cation indices a and multi-cation sink index s we can capture all Liouvillian eigenvalues by the formula [30]

$$\boxed{\lambda_{\alpha\beta} = i(-E_\alpha + E_\beta) - \frac{1}{2}(\gamma_\alpha + \gamma_\beta)} \tag{4.72}$$

remembering that λ_{as} and λ_{sa} are unphysical, $\gamma_s = 0$ and that the eigenvectors associated with λ_{aa} and λ_{ss} are non-trivial, needed for the description of the proper probability flow between cations and multi-cations. Note also that under complex conjugation $\lambda^*_{\alpha\beta} = \lambda_{\beta\alpha}$.

4.3.5 Dipole Interaction

When the atom is in the presence of a linearly polarized external electric field we have, using the length gauge, a contribution to the Hamiltonian in the form of $-F(t)D$, where F is the time dependent electric field and D is the dipole operator, usually chosen to be polarized in the $\hat{z}$ direction.

The contribution of this interaction term to the evolution of the density matrix is

$$\dot{\rho} = \ldots - iF(t)\,[\rho, D] \tag{4.73}$$

this should be interpreted as in addition to the dynamics already present from the free Hamiltonian and Lindblad terms. Going to the expanded free Hamiltonian eigenbasis and working out the contribution to the Liouvillian we get

$$\mathcal{L}_{ab,nm} = \ldots - iF(t)\,(-\delta_{bm}D_{an} + \delta_{an}D_{mb}) \tag{4.74}$$

4.4 Relativistic Atomic Calculations

In order to numerically simulate attosecond transient absorption we need energy levels, electric dipole moments, Auger decay rates and spontaneous emission rates. Although some limited energy level data is experimentally available, the dipole moments are generally obtained theoretically. Because of the high Z atoms and higher energies involved, a proper calculation requires sophisticated atomic modelling including relativistic effects. We compare our results using the GRASP2K package [40], which is described in Appendix D, with the results obtained by the MPQ Group (Max-Planck-Institute für Quantenoptik in Garching) using the GRASP92 package [41]. Also, in order to procure numbers from a completely independent code base, we present results from MIT [42] which supersedes the old Lawrence Livermore YODA codes.

4.4.1 Kr II Experimental and Theoretical Data

The MPQ Group performed attosecond transient absorption experiments on Kr II, see Goulielmakis *et al.*[2], and analyzed their results in terms of a four level system, comprising of (Ar)$3d^{10}4s^24p^5\ {}^2P^\circ_{3/2}$,(Ar)$3d^{10}4s^24p^5\ {}^2P^\circ_{1/2}$, (Ar)$3d^94s^24p^6\ {}^2D_{5/2}$, and (Ar)$3d^94s^24p^6\ {}^2D_{3/2}$.

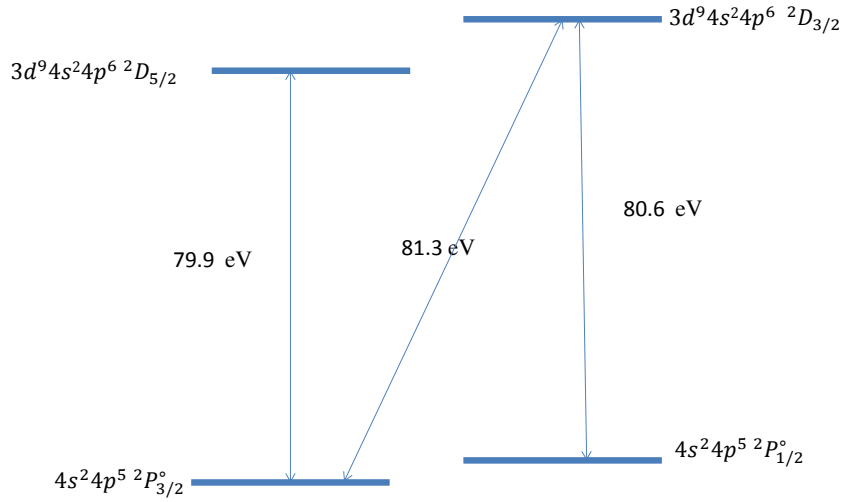

Figure 4.1: Kr II energy levels with $4p^{-1}_{3/2}$,$4p^{-1}_{1/2}$, $3d^{-1}_{5/2}$, $4p^{-1}_{5/2}$ configurations

See Figure 4.1. It is these four levels, or rather 16 levels counting degeneracy, that we will use for our simulation. Looking at cations, according to the selection rules, dipole allowed transitions are possible between odd parity and even parity and that $\Delta J = 0, \pm 1$, $J = 0 \not\leftrightarrow 0$. Consequently, transitions are dipole allowed between $^2D_{3/2}$ and $^2P^\circ_{3/2}$, $^2P^\circ_{1/2}$, between $^2D_{5/2}$ and $^2P^\circ_{3/2}$, and not allowed between $^2D_{5/2}$ and $^2P^\circ_{1/2}$, as $\Delta J = 2$.

4.4.2 Energy Levels

According to the NIST database [12], the split between $^2\mathrm{P}^\circ_{1/2}$ and $^2\mathrm{P}^\circ_{3/2}$ of Kr II is 5370.10 cm^{-1} (0.6658 eV). From MPQ's results, we know that the transition energies of $4\mathrm{p}^{-1}_{3/2}$-$3\mathrm{d}^{-1}_{5/2}$, $4\mathrm{p}^{-1}_{1/2}$-$3\mathrm{d}^{-1}_{3/2}$, $4\mathrm{p}^{-1}_{3/2}$-$3\mathrm{d}^{-1}_{3/2}$ are 79.9 eV, 80.6 eV, and 81.3 eV respectively. Although no error analysis of these values is provided in the paper, such as a limit on systematic errors, the FWHM of the absorption lines is on the order of 0.6 eV mainly driven by the resolution of their EUV spectrometer. Setting the ground state, which is $^2\mathrm{P}^\circ_{3/2}$ at zero, the MPQ

Transition		ΔE (eV)			
Upper Level	Lower Level	This Work	MIT	MPQ^T	MPQ^E
$3d^{-1}_{5/2}\,^2D_{5/2}$	$4p^{-1}_{3/2}\,^2P_{3/2}$	79.128	79.097	79.8	79.9
$3d^{-1}_{3/2}\,^2D_{3/2}$	$4p^{-1}_{3/2}\,^2P_{3/2}$	80.388	80.432	81.1	81.3
$3d^{-1}_{3/2}\,^2D_{3/2}$	$4p^{-1}_{1/2}\,^2P_{1/2}$	79.768	79.792	80.4	80.6

Table 4.1: Comparing Kr II theoretical transition energies from our work, GRASP2K, MIT code, and MPQ, both theoretical(T) GRASP92, and experimental(E) indicated by the superscripts

experimental results imply relative energy levels of $^2P^\circ_{1/2}$ at 0.7 eV, $^2D_{5/2}$ at 79.9 eV, and $^2D_{3/2}$ at 81.3 eV, noting that 0.7 eV is consistent with the NIST data. We compare transition energies for the various software packages against the MPQ experimental values in Table 4.1.

We see that the transition energies computed by ourselves using GRASP2K and those by MIT are consistent within 0.04 eV. The MPQ theoretical results using GRASP92, however, lie 0.7 eV higher and are closer to their experimental results. Computations using the GRASP package require a multitude of input parameters which we discuss in Appendix D.

The published MPQ results[2] do not provide a complete set of input parameters for GRASP so we cannot pin down the reason for the difference in computed values.

4.4.2.1 Dipole Moments

When computing oscillator strengths, the agreement between the new GRASP code we use and the old GRASP code MPQ used is very close. Furthermore, the consistency with the MIT numbers is good. This gives us some confidence in the numerical values of the dipole moments. Please see Table 4.2 for this comparison. However, for a proper simulation oscillator strengths are not enough because of phase information of the dipole moment itself is missing. In the ideal case of pure LS coupling, these phases, which in that case amount to a consistent set of plus and minus signs, can be derived from geometrical arguments using Racah W coefficients

	Oscillator Strengths(a.u.)		
Transition	*This Work*	*MIT*	*MPQ*^{T}
$\lvert\langle 4p^{-1}_{3/2}\lVert D\rVert 3d^{-1}_{5/2}\rangle\rvert^2$	0.1190	0.1114	0.119
$\lvert\langle 4p^{-1}_{3/2}\lVert D\rVert 3d^{-1}_{3/2}\rangle\rvert^2$	0.0126	0.0119	0.0126
$\lvert\langle 4p^{-1}_{1/2}\lVert D\rVert 3d^{-1}_{3/2}\rangle\rvert^2$	0.0692	0.0655	0.0695

Table 4.2: Comparing Kr II theoretical oscillator from our work, GRASP2K, MIT code, and MPQ using GRASP92

or Wigner $6-j$ symbols, see Appendix F.

The dipole moments are proportional to the line factor $\langle L'S'J'||r^1||LSJ\rangle$

$$\begin{aligned}
\langle 1\ \ 1/2\ \ 3/2\,||r^1||\,2\ \ 1/2\ \ 5/2\,\rangle &= \sqrt{6/5} \\
\langle 1\ \ 1/2\ \ 3/2\,||r^1||\,2\ \ 1/2\ \ 3/2\,\rangle &= -\sqrt{2/15} \\
\langle 1\ \ 1/2\ \ 1/2\,||r^1||\,2\ \ 1/2\ \ 3/2\,\rangle &= \sqrt{2/3}
\end{aligned} \tag{4.75}$$

These line factors can be found in Appendix F. This implies that the oscillator strengths should appear in the ratios $9:1:5$. We show the scaled oscillator strengths in Table 4.3. The scaled values are fairly constant for all software packages and indicate that LS-coupling is a good approximation. This fact allows us to use the phase information from the LS-coupling line factors to derive dipole moments from oscillator strengths.

4.4.2.2 Spontaneous Emission

We can use the dipole moments given above to compute spontaneous emission rates, see Table 4.4. The fastest emission rate given in the table corresponds to a time scale of 10^4 femtoseconds, which means this decay process is very much slower than Auger decay and that this decay time is very much slower than the dynamics of our attosecond probe pulse. Therefore, when simulating attosecond transient absorption, we will ignore spontaneous emission.

	LS Scaled Oscillator Strengths(a.u.)		
Transition	*This Work*	*MIT*	*MPQ*^{T}
$\|\langle 4p^{-1}_{3/2}\|D\|3d^{-1}_{5/2}\rangle\|^2/9$	0.0132	0.0124	0.0132
$\|\langle 4p^{-1}_{3/2}\|D\|3d^{-1}_{3/2}\rangle\|^2/1$	0.0126	0.0119	0.0126
$\|\langle 4p^{-1}_{1/2}\|D\|3d^{-1}_{3/2}\rangle\|^2/5$	0.0138	0.0131	0.0139

Table 4.3: Comparing Kr II scaled theoretical oscillator from our work, GRASP2K, MIT code, and MPQ using GRASP92 in order to verify that LS-coupling is a good approximation

	Spontaneous Emission(s^{-1})	
Transition	*This Work*	*MIT*
$\|\langle 4p^{-1}_{3/2}\|D\|3d^{-1}_{5/2}\rangle\|^2$	6.3e10	5.9e10
$\|\langle 4p^{-1}_{3/2}\|D\|3d^{-1}_{3/2}\rangle\|^2$	7.0e09	6.6e09
$\|\langle 4p^{-1}_{1/2}\|D\|3d^{-1}_{3/2}\rangle\|^2$	3.7e10	3.5e10

Table 4.4: Comparison of spontaneous emission rates for Kr II

	Auger decay rate in meV	
Kr II Level	*Theo.*	*Expt.*
$3d_{5/2}^{-1}$	90.0	88(4)
$3d_{3/2}^{-1}$	88.6	88(4)

Table 4.5: Comparison of Auger decay rates for Kr II. Theoretical values are taken from [43], and the experimental values are from [44].

4.4.2.3 Auger Decay

In Table 4.5 we provide Auger decay rates for Kr II $3d_{5/2}^{-1}$ and $3d_{3/2}^{-1}$ levels. Auger decay is a fast ionization process and needs to be taken into account in our attosecond transient absorption calculations. The decay rate of 88 meV corresponds to 0.00323 a.u. or 7.5 fs. The probe pulses we will investigate range from 200 as to 500 as with delays after pump ionization from 0 to 10 fs. The decay of the excited states can be appreciable for these delays. We will use the value of 88 meV throughout.

4.5 Conclusion

In this chapter we developed the mathematical machinery needed for our simulations in the next chapter. We described the density matrix operator formalism and derived the Liouville von Neumann equation including Lindblad terms. With the help of Lindblad terms we developed the three space source-cation-sink methodology to describe ionization processes between neutral atoms, cations and multi-cations.

We also calculated energy levels and oscillator strengths for krypton using GRASP2K and compared our results with other authors, including independent software packages. We now have all elements in place to start simulations of the dynamics of multi-electron atoms.

Chapter 5

Dynamics in Multi-Electron Atoms

In this chapter we use the "three spaces" method developed in Section 4.3, as illustrated in Figure (5.1). We simulate the ionization of Kr I (the source) into Kr II by the pump pulse, populating the $4p^{-1}$ levels. Furthermore, we simulate the excitation of Kr II to the $3d^{-1}$ levels by a probe pulse. The effects of Auger decay are modelled by transitions from Kr II to Kr III (the sink). In order to perform these simulations we solve the Liouvillian ordinary differential equations by means of a fourth order Runge-Kutta method, please see Appendix C.

5.1 Ionization

When modelling transient absorption one often simply injects initial level populations without worrying about the generation process. However, one must be very careful in choosing the initial conditions if we want to obtain physically meaningful answers, as those conditions must respect certain symmetries they inherited from the pump pulse. Our three-space formalism guarantees consistency and naive injection is replaced by a cation generation process.

In this chapter we derive symmetry relations that are adhered to by the density matrix when atoms are subjected to a linearly polarized pump pulse and we assume electric dipole

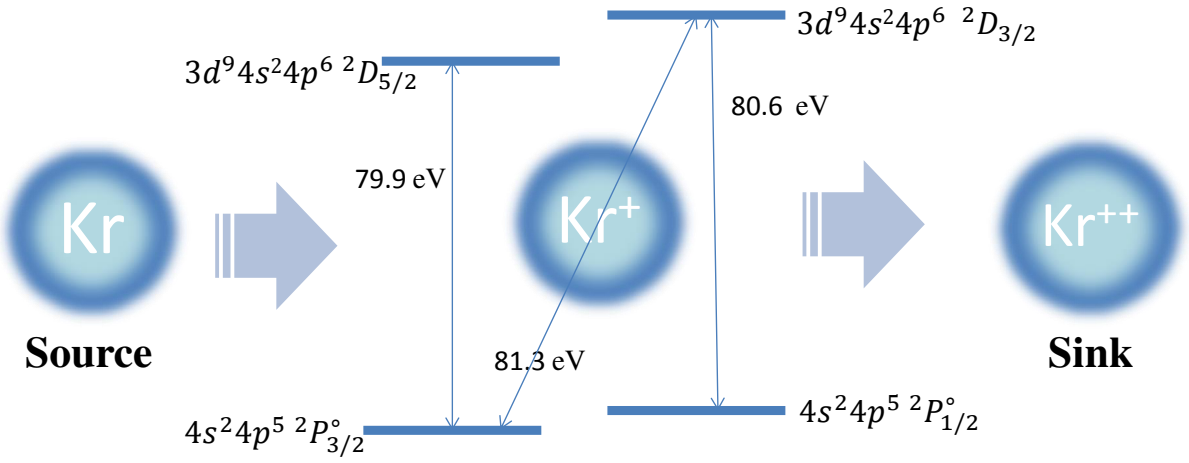

Figure 5.1: Diagram of the source-cation-sink model with the relevant Kr II energy levels.

interaction in the dipole approximation only. These relations are derived from geometrical properties of the Wigner-Eckart factors and parity considerations and are valid to all orders of perturbation theory. We translate these symmetries of the density matrix to symmetries of the cation generation process, allowing for consistent cation production.

We present new results using our formalism to derive coherences between the $p_{3/2}$ and $p_{1/2}$ levels of Ne, Ar, Kr and Xe for a wide range of pump pulse strengths and time durations. Results are given in Tables 5.2 through 5.5 and we provide physical explanations for their properties.

5.1.1 Symmetries of Ionization

Ionization can not produce just any physically valid density matrix. In other words: there are symmetry constraints between the coherence terms, which we shall now investigate. Assume a pump pulse that is linearly polarized in the z-direction and assume that the ionization process is dominated by electric dipole interaction (E_1), ignoring all else. Note that this discussion is very general and does not require detailed knowledge of the ionization process

nor any intermediate levels involved but does derive symmetries portrayed by the reduced density matrix in cation space during and after the pump pulse.

Assuming all states have well defined parity we know that transitions induced by electric dipole interaction must flip parity. From the perspective of high order perturbation theory we see that an odd number of dipole interactions must flip parity while an even number must preserve parity.

Because the electric field of the pump pulse is only in the z-direction it can not affect a torque on the atomic system around this axis, which means

$$\Delta m = 0 \tag{5.1}$$

In other words, states from different energy levels, but with the same m, evolve as separate spaces, where m is the eigenvalue of the j_z operator. The cross terms in the total Hamiltonian, including pump pulse interaction, between spaces of different m are exactly zero. However, this does not mean that the different m spaces are completely independent because there is an inherent symmetry in the dipole matrix elements themselves. The reason for this can be found in the Wigner-Eckart theorem. We have a connection between the m and $-m$ spaces, see Appendix E,

$$\langle j_f\, -m|T_0^1|j_i\, -m\rangle = (-)^{j_i - j_f + 1}\langle j_f\, m|T_0^1|j_i\, m\rangle \tag{5.2}$$

where we have indicated initial and final subscripts. Note that for the matrix element to be non-zero we must have that $j_i - j_f$ is an integer and actually must be -1, 0 or 1. The interesting part is the sign factor $(-)^{j_i - j_f + 1}$. When we use high order perturbation theory these sign factors are multiplied and we see that all the j values of the intermediate levels drop out.

$$\begin{cases} (-)^{j_i - j_f} & \text{even number of interactions,} \quad \text{same parity} \\ (-)^{j_i - j_f + 1} & \text{odd number of interactions,} \quad \text{opposite parity} \end{cases} \tag{5.3}$$

So the sign factor for an interaction to any order can be captured by

$$p_i p_f (-)^{j_i - j_f} = \frac{p_f e^{-i\pi j_f}}{p_i e^{-i\pi j_i}} \tag{5.4}$$

where the p values are the parities and are either 1 or -1. The fraction written in the equation above shows that there is a unitary transformation between m and $-m$ space. This unitary transformation is diagonal and has elements $pe^{-i\pi j}$. Note that the construction above works for any states $|j_i m_i\rangle$ and $|j_f m_f\rangle$ as long as they are eigenstates of the field free Hamiltonian and have well-defined parity. The states we use in this thesis are $4p_{3/2}$ and $4p_{1/2}$ for noble gas cations. Now assume that the neutral atoms, before the pump pulse, are incoherent. This is a reasonable assumption because, given enough time, interactions with the environment would destroy all coherence, such as spontaneous emission, collisions or what have you. After applying a z-polarized pump pulse and assuming only electric dipole interactions the resulting density matrix must have the symmetries described. This density matrix can be rather large if it is to describe all the physics going on, but we myopically focus on a few relevant levels only and reduce this large density matrix by tracing out extraneous freedoms. The resulting reduced density matrix still has the symmetries described above. If the pump pulse is followed by a probe pulse that is also z-polarized then all these symmetries will be preserved, which would not be true, of course, for a probe pulse polarized in a different direction. Note that we will always be talking about the reduced density matrix, realizing that the world is bigger than the states we are focussing on, but the term 'reduced' is often dropped.

As a concrete example, we look at Kr II. The ground state is $4p_{3/2}$ and the level directly above is $4p_{1/2}$. These levels are split due to LS-coupling (to a good approximation). The degeneracy of the $4p_{3/2}$ is fourfold, with $j = 3/2$, $m \in \{-3/2, -1/2, 1/2, 3/2\}$, while the $4p_{1/2}$

state has twofold degeneracy $j = 1/2$, $m \in \{-1/2, 1/2\}$. The parities of $4p_{3/2}$ and $4p_{1/2}$ are both odd, so only an even number of electric dipole interactions can contribute to the reduced density matrix describing these states.

Because the pump pulse is strong field but has photon energy below the ionization threshold we see that any higher states would be exponentially suppressed and we will treat them as non-populated after the pump pulse. This leaves us with $4+2=6$ levels, counting degeneracies. The (reduced) density matrix is thus a 6 by 6 matrix. Note that there is no unity trace constraint on this matrix because we allow cations entering and leaving. However, this matrix must be Hermitian, $\rho_{j_i m_i; j_f m_f} = \rho^*_{j_f m_f; j_i m_i}$, which makes for 15 complex plus 6 real degrees of freedom, or 36 real degrees of freedom in general.

However, these degrees of freedom are very much reduced because we assume linearly polarized pumping by electric dipole interaction. First, the terms in the density matrix that have differing m must be zero. This reduces the degrees of freedom to 2 complex plus 6 real, which is equivalent to 10 real. Second, the m to $-m$ symmetry further reduces this by half to 5 real degrees of freedom. These 5 degrees of freedom can be interpreted as follows. Three of them are diagonal (i.e. populations), namely those for $\rho_{3/2,1/2;\,3/2,1/2}$, $\rho_{3/2,3/2;\,3/2,3/2}$ and $\rho_{1/2,1/2;\,1/2;1/2}$. The other two are the size and the phase of the (off-diagonal) coherence $\rho_{3/2,1/2;\,1/2,1/2}$.

Because m is conserved we can lighten the notation by defining

$$\rho^{(m)}_{j_f, j_i} = \rho_{j_f m; j_i m} \tag{5.5}$$

We write out the m to $-m$ symmetry explicitly and apply the sign factor $(-)^{j_i - j_f}$ for an even number of dipole interactions

$$\begin{cases} \rho^{(-3/2)}_{3/2,3/2} = \rho^{(3/2)}_{3/2,3/2} \\ \rho^{(-1/2)}_{3/2,3/2} = \rho^{(1/2)}_{3/2,3/2} \\ \rho^{(-1/2)}_{1/2,1/2} = \rho^{(1/2)}_{1/2,1/2} \\ \rho^{(-1/2)}_{3/2,1/2} = -\rho^{(1/2)}_{3/2,1/2} \end{cases}$$

To sum up: we have 5 real parameters that define the reduced density matrix. They are the 4 non-negative real numbers $\rho^{(3/2)}_{3/2,3/2}$, $\rho^{(1/2)}_{3/2,3/2}$, $\rho^{(1/2)}_{1/2,1/2}$ and $|\rho^{(1/2)}_{3/2,1/2}|$ plus the phase $\arg\left(\rho^{(1/2)}_{3/2,1/2}\right)$.

The symmetries we derived above must be respected by our source formulation of ionization describe in Section 4.3.2. In that section we use vectors N to parametrize the Lindblad term that models the injection of cations into cation space from the source which is neutral space. The m versus $-m$ symmetry discussed here puts a constraint on the phase relations between some elements of N.

5.1.2 Coherent Ionization

Element	First Ionization [eV]	$^2P_{1/2} - {}^2P_{3/2}$ [eV]
Ne	21.565	0.0967
Ar	15.760	0.1774
Kr	14.000	0.6658
Xe	12.130	1.3064

Table 5.1: First ionization energies of noble elements and the relative level of the first excitation of the cation, based on NIST data[12].

The noble elements Ne, Ar, Kr and Xe all have a ground state of the singly ionized ion of the type $^2P_{3/2}$, with a first excited state of type $^2P_{1/2}$ lying slightly above, due to LS-coupling. We list the first ionization energies and the LS-coupling energy level splits in Table 5.1. With increasing atomic number the neutral noble atom becomes easier to ionize and the LS-coupling for the lowest states of the cation becomes stronger.

Using ADK [11] as an approximation for ionization rates we calculate multichannel ionization. Two issues are important to point out. First, ADK is only a rough estimate of ionization rates but is reasonable for an NIR pump and the ionization energies relevant to our investigations. Second, our cation generation process allows for tuning the production rates in the different m channels, so we can connect with experimentally observed data.

One interesting feature is the presence of coherence between the ${}^2P_{3/2}$ and ${}^2P_{1/2}$ levels during and after the ionization process. We define the amount of coherence as follows [2]

$$g(t) = \frac{\left|\rho^{(1/2)}_{3/2,1/2}\right|}{\sqrt{\rho^{(1/2)}_{3/2,3/2}\ \rho^{(1/2)}_{1/2,1/2}}} \tag{5.6}$$

where the superscripts indicate we are looking at the $m_j = 1/2$ levels only and the subscripts indicate the j values of the two energy levels involved. We present the results of our pump simulation in Figure (5.2), where we have used a 4-cycle 800 nm pump pulse with electric field amplitude of 0.08 a.u. Furthermore, we present for pulses up to 10 cycles and amplitudes from 0.04 a.u. to 0.10 a.u in Tables 5.2 through 5.5.

The patterns exhibited in these results can be quite readily understood. The regime we are in is ionization through tunneling, which means the ion population gets a kick every half-cycle of the pump pulse when the field is near an extremum. However, due to the energy difference between ${}^2P_{3/2}$ and ${}^2P_{1/2}$ the density matrix element between these levels will acquire a phase factor before receiving a contribution from the next kick. It follows that coherence is achieved, or should we say maintained, much more easily when LS-coupling is weak as for the lighter noble species, because phase rotations will be less and destructive interference is mollified. This argument applies when there are a fair number of half cycle kicks to contend with. When the field amplitude becomes very large the conversion of neutral atoms to cations becomes very substantial. In the limit of strong pump fields the supply of neutral atoms becomes rapidly depleted so the ionization process is effectively reduced to very few half-cycles, promoting coherence. We can see this effect prominently in the tables for the heavier noble species, as they have a lower ionization threshold. This also explains why in Figure (5.2), for the given pump parameters, Xe manages to maintain higher coherence than

Kr while having stronger LS-coupling.

As an aside, the Keldysh parameter does not become large over the range of electric field strengths we investigate and ADK can be a reasonable approximation. As a reference, $\gamma = 1$ (at 800 nm) is achieved by an electric field of Ne 0.072 au, Ar 0.062 au, Kr 0.058 au, Xe 0.054 au. Note that γ is inversely proportional to the electric field. As a direction for future research, choosing a better ionization approximation, such as Yudin-Ivanov [45], can produce more accurate ionization rates but is not expected to have much of an effect on the coherences. This is because ionization is dominated by contributions near the extrema of the incident electric field and because the achieved coherence fractions are dominated by the phase rotation effect between extrema due to the LS-coupling energy split, as explained above.

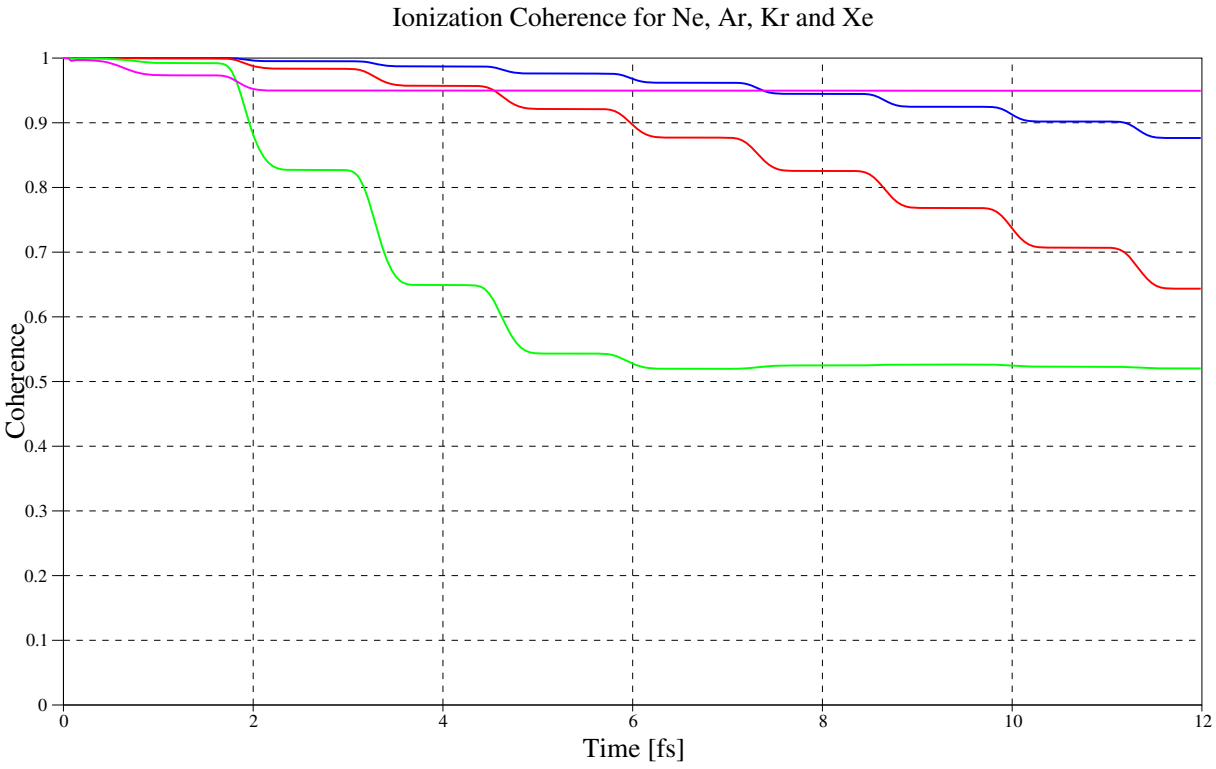

Figure 5.2: Coherence of ionization between $^2P_{3/2}$ and $^2P_{1/2}$ for Ne(blue), Ar(red), Kr(green) and Xe(magenta), using a 4-cycle 800 nm pump pulse with an amplitude of 0.08 a.u.

Ne	0.04	0.05	0.06	0.07	0.08	0.09	0.10
1	100	100	100	100	100	100	100
2	100	100	100	100	100	100	100
3	99	99	99	99	99	99	99
4	98	98	98	98	98	98	98
5	97	97	97	97	97	97	97
6	96	96	96	96	96	96	96
7	94	94	94	94	94	94	94
8	92	92	92	92	92	92	92
9	90	90	90	90	90	90	90
10	88	88	88	88	88	88	88

Table 5.2: Coherence in percentage between $P_{1/2}$ and $P_{3/2}$ for Neon for an 800 nm pump pulse. The rows are the number of cycles of the pump pulse, the columns are the amplitude of the pump pulse in a.u.

Ar	0.04	0.05	0.06	0.07	0.08	0.09	0.10
1	100	100	100	100	100	100	100
2	98	98	98	98	98	98	97
3	96	96	96	96	96	96	97
4	92	92	92	92	93	93	96
5	89	89	89	89	90	91	95
6	88	87	87	87	87	89	94
7	82	82	82	82	82	86	94
8	76	76	76	76	77	82	93
9	69	69	69	69	71	79	93
10	62	62	62	62	64	79	93

Table 5.3: Coherence in percentage between $P_{1/2}$ and $P_{3/2}$ for Argon for an 800 nm pump pulse. The rows are the number of cycles of the pump pulse, the columns are the amplitude of the pump pulse in a.u.

Kr	0.04	0.05	0.06	0.07	0.08	0.09	0.10
1	100	99	99	99	99	99	99
2	81	81	80	81	83	90	98
3	54	54	54	55	65	87	98
4	25	27	28	33	56	86	98
5	12	12	13	22	53	86	98
6	0	2	5	18	52	86	98
7	17	17	17	23	52	86	98
8	23	23	23	27	53	86	98
9	20	20	20	25	52	86	98
10	11	11	12	20	52	86	98

Table 5.4: Coherence in percentage between $P_{1/2}$ and $P_{3/2}$for Krypton for an 800 nm pump pulse. The rows are the number of cycles of the pump pulse, the columns are the amplitude of the pump pulse in a.u.

Xe	0.04	0.05	0.06	0.07	0.08	0.09	0.10
1	99	97	97	97	97	98	99
2	24	24	32	69	95	98	99
3	25	25	32	68	95	98	99
4	21	21	30	68	95	98	99
5	9	11	26	68	95	98	99
6	7	9	25	68	95	98	99
7	17	17	26	68	95	98	99
8	2	5	24	68	95	98	99
9	12	12	24	68	95	98	99
10	7	8	24	68	95	98	99

Table 5.5: Coherence in percentage between $P_{1/2}$ and $P_{3/2}$ for Xenon for an 800 nm pump pulse. The rows are the number of cycles of the pump pulse, the columns are the amplitude of the pump pulse in a.u.

5.2 Probe Simulation Results

In this chapter we perform numerical simulations of the time development of the density matrix in the Liouvillian formalism for the Kr II $4p_{3/2}$, $4p_{1/2}$, $3d_{5/2}$ and $3d_{3/2}$ levels coupled by electric dipole interaction to a probe pulse. Back-reaction on the electromagnetic field and probe propagation dynamics will be treated in subsequent chapters. Results here should be interpreted in the single cation or low density limit. In the regime of interest it is shown that a good fraction of the results can be qualitatively understood by comparing to two-level toy models. It is numerically verified that higher order effects are small for electric fields below 0.2 au and that we are justified to develop the lower order absorption formulae of Sections 6.2 and 6.3.

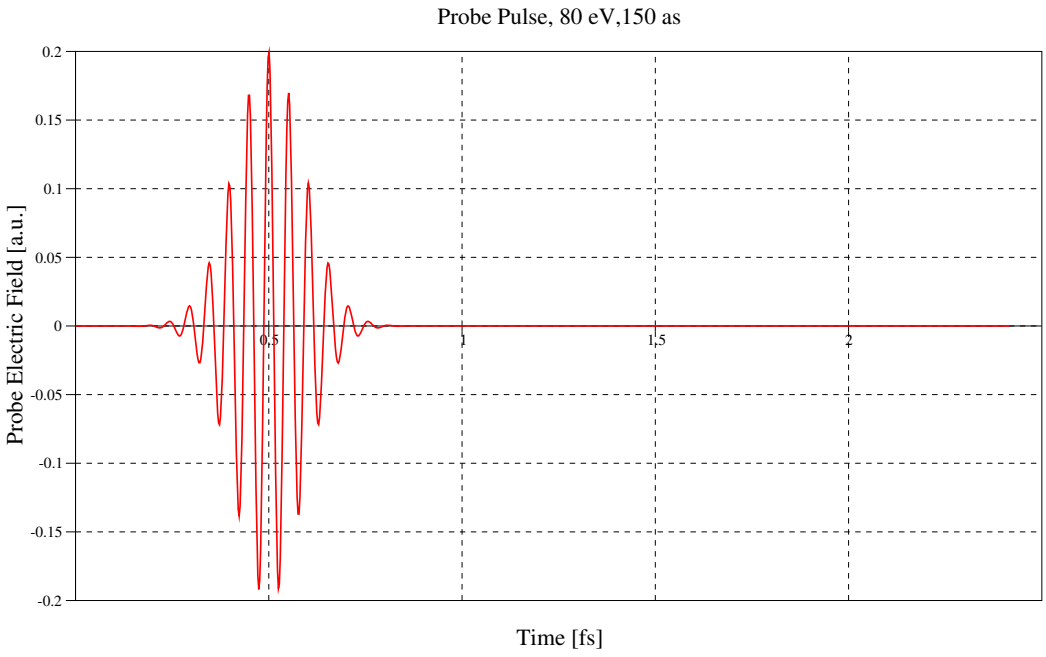

Figure 5.3: A probe pulse centered at 80 eV and a width of 150 as, with a peak amplitude of 0.2 au.

5.2.1 The Probe Pulse

For most of the numerical experiments in this chapter we will use a Gaussian pulse, centered at 80 eV, 150 as width, central phase 0, linearly polarized in the z-direction and a peak electric field of 0.2 au. Please see Figure (5.3). We have positioned the center of the pulse at 0.5 fs on the time axis for convenience and it is to be understood that the pump pulse, also assumed linearly polarized in the z-direction, has populated the Kr II $4p$ levels before time $t = 0$ fs. The peak intensity of this pulse is 1.4×10^{15} W/cm^2 which is in the Free Electron Laser (FEL) regime. Although FEL pulses of sub-femtosecond duration are still to be realized (hopefully in the near future), we would like to push the envelope and choose the intensity of the probe pulse firmly above those that are usual for HHG in order to test for the onset of nonlinear effects. Our results will show that even for pulses this strong the nonlinear effects in our model for krypton are small.

5.2.2 Resonant vs. Non-Resonant Driving Probe Pulse

The simulation results for the evolution of the diagonal elements of the density matrix for the Kr II excited states are shown in Figures (5.4) and (5.5), for a 150 as probe pulse of 80 eV and 60 eV center energy respectively, illustrating the difference between resonant and non-resonant driving by the probe.

Both graphs show some interesting features which we will now explain. We can understand what is going on by looking at a simple two-level toy model where we set the energy gap and the coupling to the external force to unity for convenience, starting with the entire population in the ground state

$$H = \begin{pmatrix} 0 & f(t) \\ f(t) & 1 \end{pmatrix}, \qquad \rho(0) = \begin{pmatrix} 1 & 0 \\ 0 & 0 \end{pmatrix} \tag{5.7}$$

where $f(t)$ is the time dependent external force. Using $i\dot{\rho} = [H, \rho]$ and perturbatively expanding in f we find

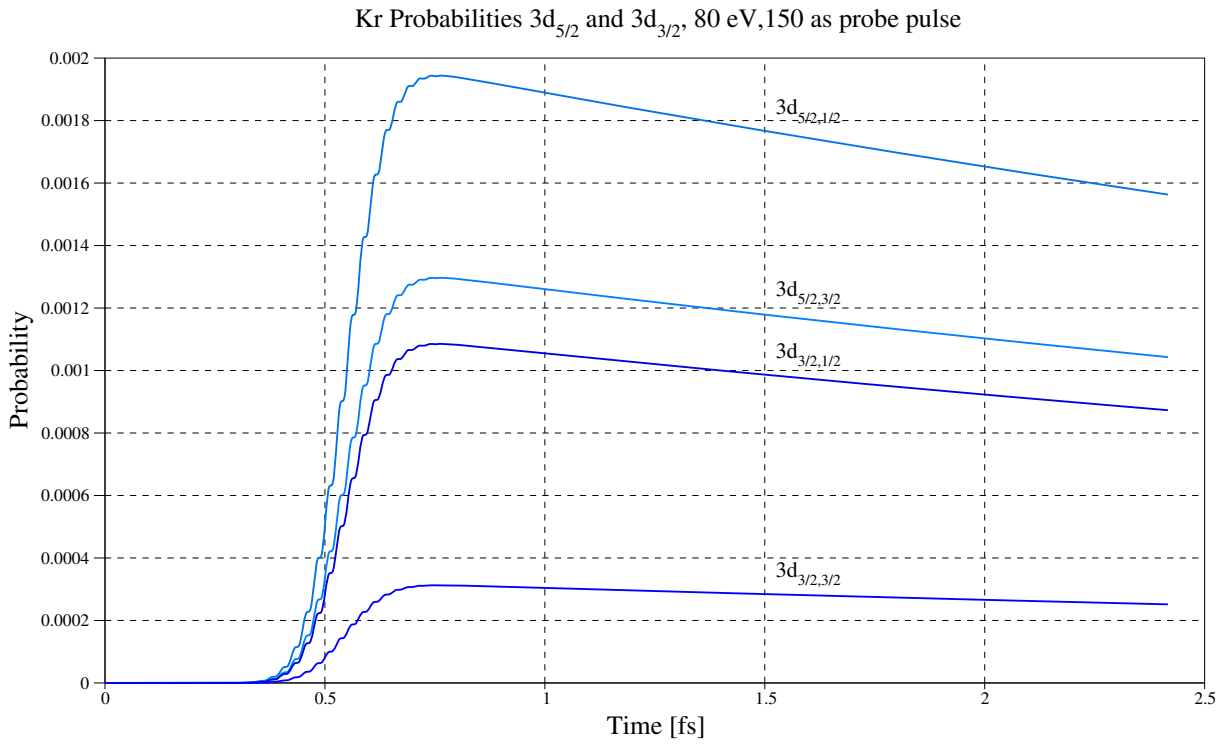

Figure 5.4: Population probabilities of the excited Krypton cation $3d_{5/2}$ and $3d_{3/2}$ states, resonantly driven by a 80 eV, 150 as, 0.2 au peak amplitude probe pulse polarized in the z-direction. Note how populations for the excited states are built up in a step-like fashion due to resonance with the driving probe. Note that $m = 5/2$ for $3d_{5/2}$ is absent due to the forbidden dipole transition. Negative m values have the same population due to symmetry. The curves are dropping due to Auger decay turning cations into multi-cations.

$$\begin{aligned}\dot{\rho}_{01} &= i\rho_{01} + if(\rho_{00} - \rho_{11}) = i\rho_{01} + if + \mathcal{O}(f^3)\\ \dot{\rho}_{11} &= 2f\,\mathrm{Im}\,\rho_{01}\end{aligned} \tag{5.8}$$

with solutions

$$\rho_{01} = ie^{it}\int_0^t dt' f(t')e^{-it'} + \mathcal{O}(f^3) \tag{5.9}$$

$$\rho_{11} = \left(\int_0^t dt' f(t')\cos(t')\right)^2 + \left(\int_0^t dt' f(t')\sin(t')\right)^2 + \mathcal{O}(f^4) \tag{5.10}$$

We see that in order for ρ_{11} to grow appreciably the driving force f must have a significant spectral amplitude around frequency one. As an example of exact resonance consider the pure sine wave starting at time zero $f(t > 0) = A\sin(t)$. In that case we have

$$\rho_{11} = \frac{A^2}{4}\left(t^2 - t\sin(2t) + \tfrac{1}{2} - \tfrac{1}{2}\cos(2t)\right) + \mathcal{O}(A^4) \tag{5.11}$$

so the population of the excited state ρ_{11} grows quadratically in time modulated by a variation at double frequency. In the rotating wave approximation these double frequency terms would have been ignored. Also, we have implicitly made the assumption that ρ_{11} is small compared to one so the quadratic growth can be viewed as the very early stages of a Rabi oscillation if you wish.

The growth rate of ρ_{11} to second order in perturbation theory is

$$\dot{\rho}_{11} = A^2 t\sin^2(t) \geq 0 \tag{5.12}$$

So the growth rate oscillates between 0 and A^2t but is never negative. This results in step-like growth of the excited population, growing in larger and larger steps (for a constant amplitude driving force) but never retracing.

For a more realistic pulse with growing and waning amplitude we have to adjust the analysis, but two prominent features of resonant excitation remain. First, during the body of the pulse the growth of the excited population is near quadratic which leads to the conclusion that, for a symmetric pulse, the excited population grows three times more during the second half of the pulse as compared with the first half. Second, the excited population grows in step-like fashion, without retracing.

For the non-resonant case the integrals $\int_0^t dt' f(t')\cos(t')$ and $\int_0^t dt' f(t')\sin(t')$ do not amount to much. If the probe pulse can be neglected on and before time zero and if time t is large enough that the probe can also be neglected thereafter we are basically looking at a Fourier transform. For a 150 as Gaussian pulse the width is 12 eV which means that for resonances around 80 eV a 60 eV pulse would be exponentially suppressed. Note that if the integration

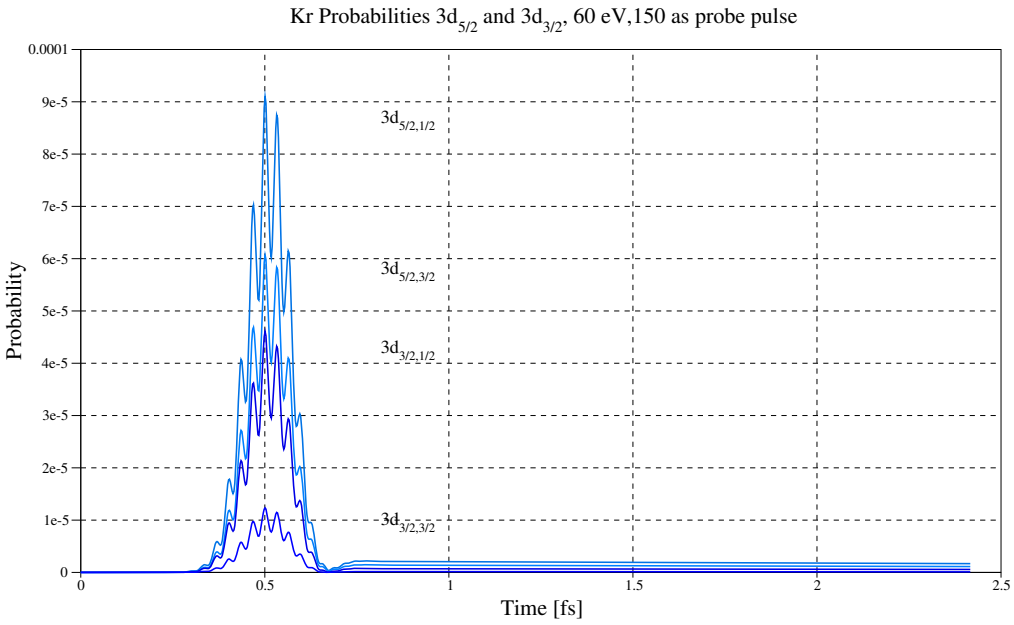

Figure 5.5: Population probabilities of the excited Krypton cation $3d_{5/2}$ and $3d_{3/2}$ states, non-resonantly driven by a 60 eV, 150 as, 0.2 au peak amplitude probe pulse polarized in the z-direction. Note that the excited population build-up is much smaller than for the 80 eV pulse and also that the effects are mostly self-cancelling by the end of the pulse. Note that $m = 5/2$ for $3d_{5/2}$ is absent due to the forbidden dipole transition. Negative m values have the same population due to symmetry.

interval does not cover the vast majority of the pulse the integrals can be quite a bit larger which leads to the self-canceling give-and-take scenario where the first half of the pulse gives (builds up the excited population) and the second half takes (almost) all back. So, for symmetric pulses we have that the ratio between excited population build-up for the second half versus the first half of the pulse is near 3 for the resonant case and near -1 far away from resonance.

These properties of the two level system to lowest order in perturbation theory are borne out by the full many-level simulation of the Kr II ion to all orders. We can clearly see the resonant (80 eV) driving in Figure (5.4), with both the near quadratic growth and the growth

steps. As a comparison we also show non-resonant driving (60 eV) in Figure (5.5) where the excited populations can not coherently grow and where we also see the self-cancellation effect of the first half of the pulse versus the second half.

Note that for much weaker probe pulses, such as those for HHG, the results are nearly identical (after appropriate scaling) because we are still in the linear regime.

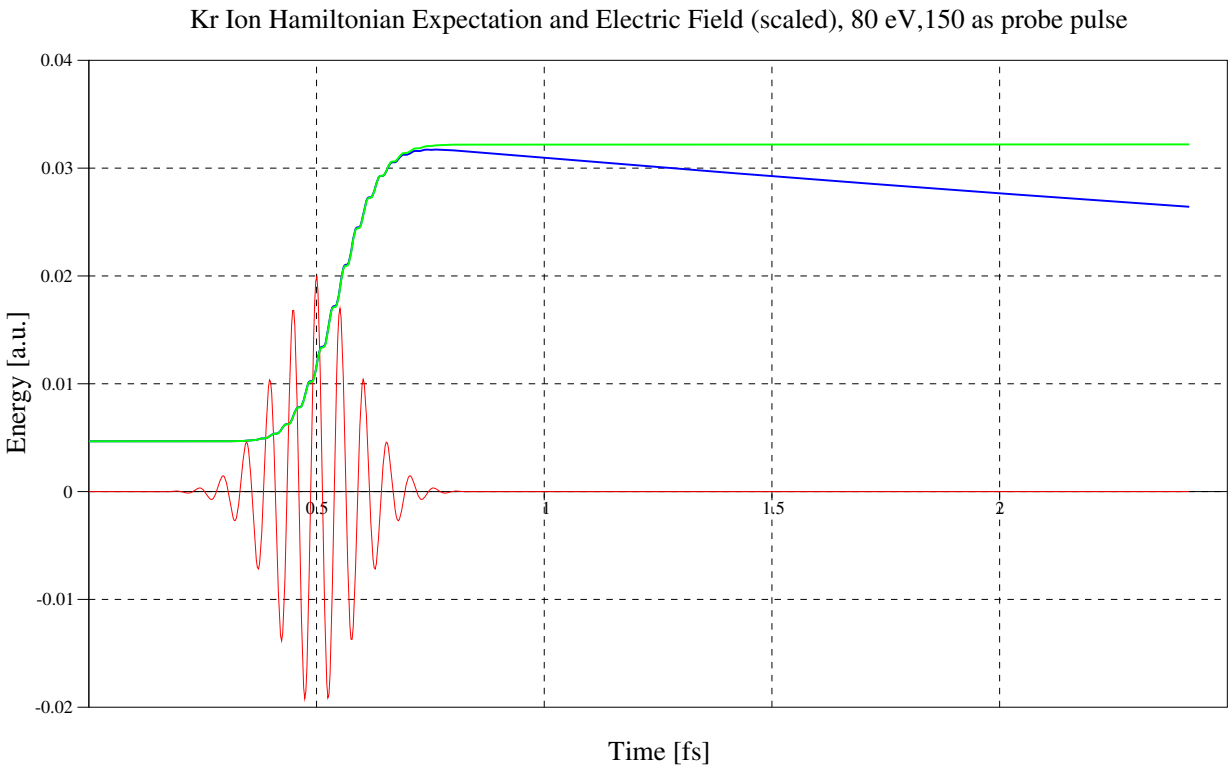

Figure 5.6: Hamiltonian expectation for a Krypton cation, resonantly driven by a 80 eV, 150 as, 0.2 au peak amplitude probe pulse polarized in the z-direction. The red curve shows the electric field of the probe pulse (arbitrary units). The blue curve shows the Hamiltonian expectation of the cation. The green curve, which overlaps the blue curve for a large part is constructed from the starting expected energy, the time derivative of the electric field and the polarization. This construction follows the expected Hamiltonian very closely except for the fact that it does not account for Auger decay. The initial non-zero value of the expectation is due to the initial population in the Kr II $4p_{1/2}$ level, which lies 0.7 eV higher than the Kr II $4p_{3/2}$ which we have used as the reference for zero energy.

5.2.3 Induced Polarization and Absorption

In Figure (5.6) we graph the Hamiltonian expectation of cations as a function of time as influenced by the probe pulse. We have used the $4p_{3/2}$ level as a reference for defining the zero energy level. Because the density matrix was prepared by the pump pulse (before time 0) to be in a mixture of $4p_{3/2}$ and $4p_{1/2}$ states we start out with a positive expectation because $4p_{1/2}$ lies a little higher. A 150 as, 80 eV, 0.2 au probe pulse resonantly drives the cations and we see the typical near quadratic growth and step-like growth we have seen before for the diagonal elements of the density matrix themselves. Auger decay is evident, which reduces the cation density.

In Figure (5.7) we show the polarization induced by the probe pulse. Because the polarization is determined by off-diagonal elements of the density matrix the size should grow approximately linearly with time in first order perturbation theory.

Indeed the amplitude of the induced polarization at the center of the pulse is about half of that right after the pulse. Note the phase delay between the electric field and the polarization. We tested the much weaker HHG pulses as well resulting in the same phase delays.

In Figure (5.8) we show the same induced polarization calculation but then simulated for a longer time. After the probe pulse is gone the induced polarization shows some complicated behavior. The free time evolution of the induced polarization only depends on off-diagonal elements which phase rotate in correspondence with the energy levels they are connected to. We can explain Figure (5.8) with three effects. First, there is a fast oscillation due to the average electric dipole transition from $4p$ to $3d$; this is around 80 eV, or a 0.053 fs oscillation. Second, because of energy differences between the dipole transitions, which range from 0.6 eV to 1.3 eV, we see beat effects on oscillation time scales from 3 to 7 fs. Third, there is exponential decay due to Auger transitions, on a decay time scale of 7.5 fs. We also ran the induced polarization simulation for a much weaker probe pulse, more realistic for the HHG regime, of $E = 0.01$ au which corresponds to 3.5×10^{12} W/cm^2, see Figure (5.9). We see that the result, up to a factor, is very much the same as before so we can say that HHG is safely in the linear regime. We will investigate the onset of nonlinearities in the next few sections.

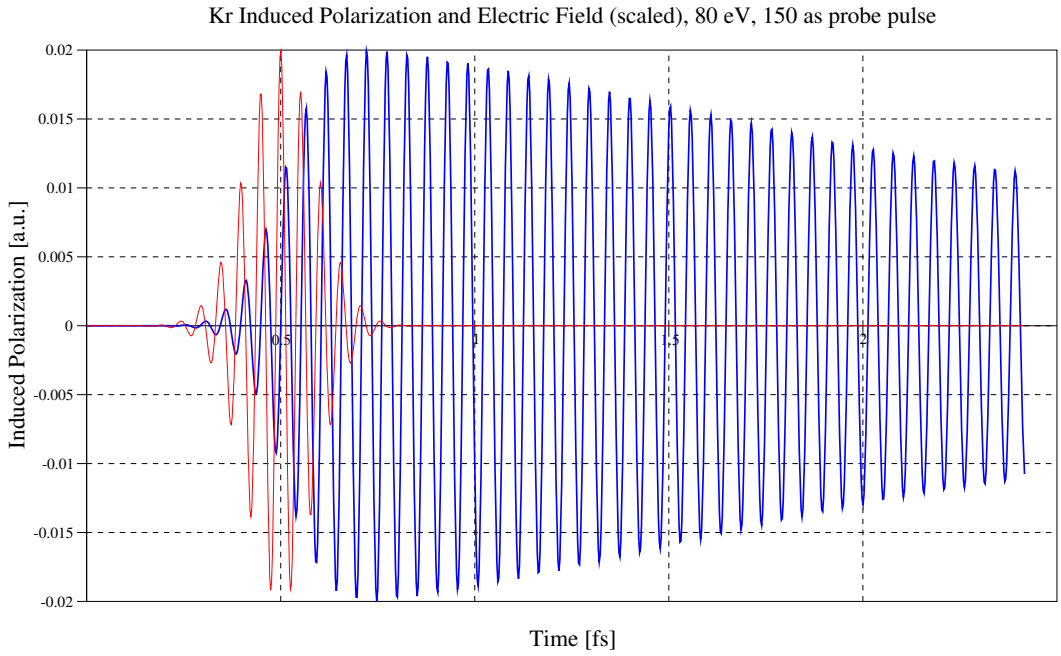

Figure 5.7: Induced polarization for a Krypton cation, resonantly driven by a 80 eV, 150 as, **0.2 au** peak amplitude probe pulse polarized in the z-direction. The red curve shows the electric field of the probe pulse (arbitrary units). The blue curve shows the polarization of the cation. The width of the graph is 2.5 fs.

The relationship between induced polarization and energy absorption is a rather simple one which we now explain. When we have a time dependent Hamiltonian $H = H_0 - f(t)D$, where the free Hamiltonian H_0 is time independent, the dipole operator D is time independent and $f(t)$ is a time dependent external field then the time evolution of the expectation of the Hamiltonian (energy) is given by

$$\frac{d}{dt}\langle H\rangle = \frac{d}{dt}\operatorname{tr}\rho H = \operatorname{tr}(\dot{\rho}H + \rho\dot{H}) = \operatorname{tr}(-i[H,\rho]H - \rho\dot{f}D) = -\operatorname{tr}(\rho\dot{f}D) = -\dot{f}\langle D\rangle \quad (5.13)$$

Note that we neglected Lindblad terms for $\dot{\rho}$ here. When we look carefully in Figure (5.7) we see that the electric field is 90 degrees out of phase with the expectation of the dipole operator (induced polarization) in such a way that when the time derivative of the electric field is positive then the induced polarization is negative. In this way the resonant driving force allows for the maximum rate of energy transfer into the cations. Note that, Auger decay

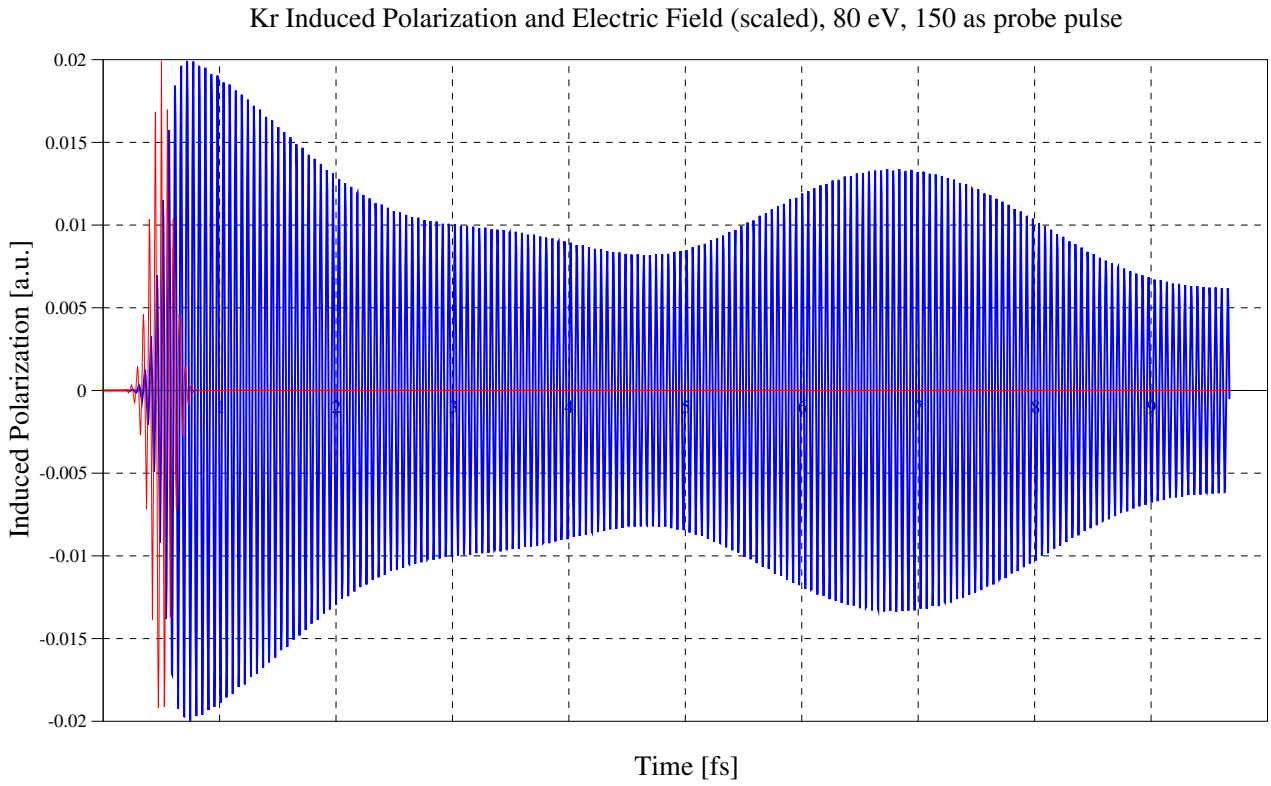

Figure 5.8: Induced polarization for a Krypton cation, resonantly driven by a 80 eV, 150 as, **0.2 au** peak amplitude probe pulse polarized in the z-direction. The red curve shows the electric field of the probe pulse (arbitrary units). The blue curve shows the polarization of the cation. The width of the graph is 10 fs.

aside, Figure (5.6) can be reconstructed from Figure (5.7) by $\langle H \rangle = -\int \dot{f} \langle D \rangle$. This means that the amount of energy absorbed by the system is the time integral of the negative time derivative of the probe electric field times the expected induced polarization. To repeat, note that we did not use any Lindblad terms in the derivation above so this simple construction of energy transfer is oblivious to Auger decay.

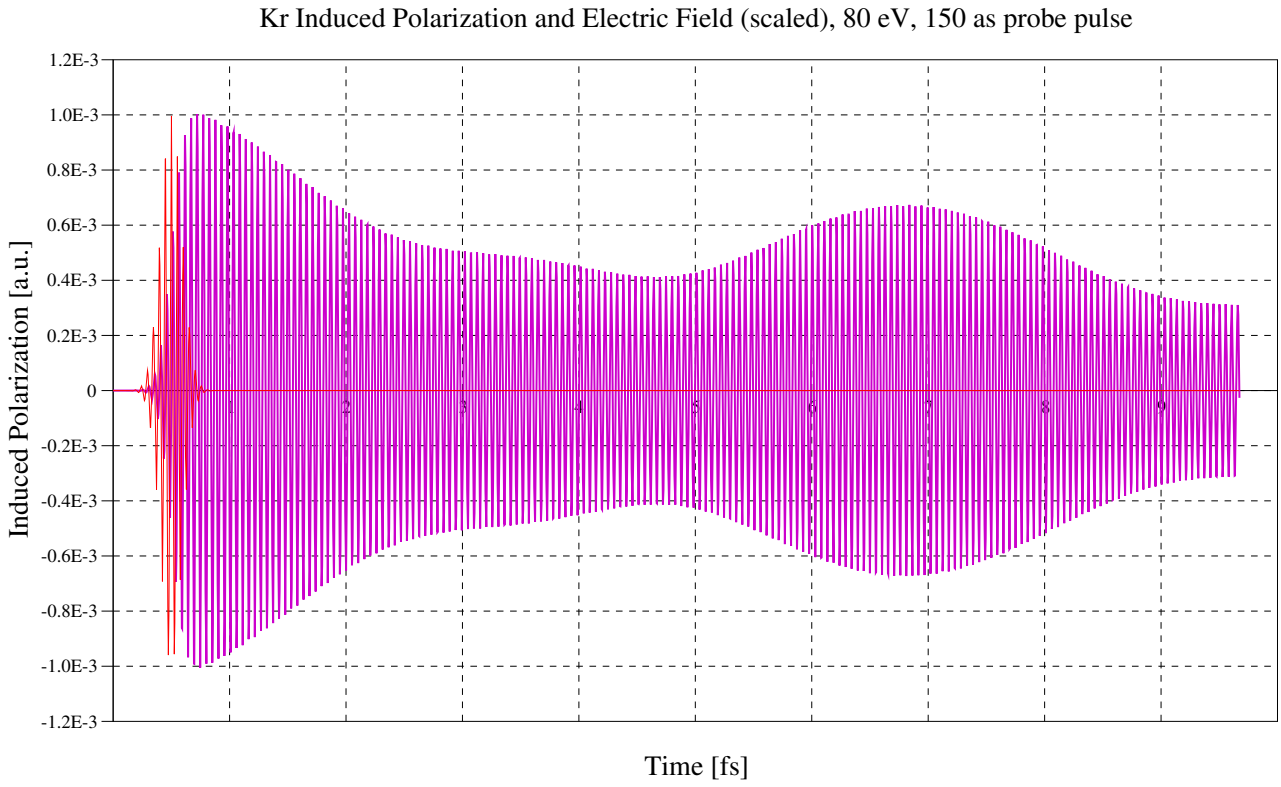

Figure 5.9: Induced polarization for a Krypton cation, resonantly driven by a 80 eV, 150 as, **0.01 au** peak amplitude probe pulse polarized in the z-direction. The red curve shows the electric field of the probe pulse (arbitrary units). The purple curve shows the polarization of the cation. The width of the graph is 10 fs.

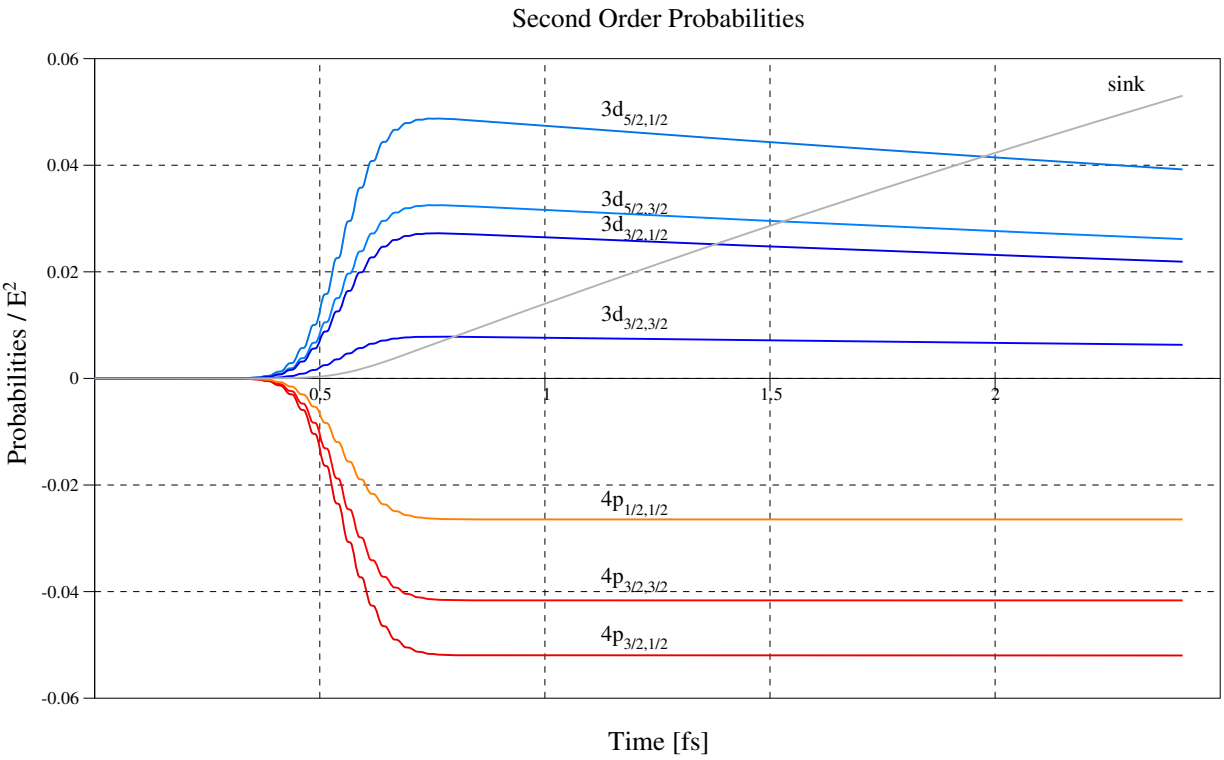

Figure 5.10: Second order perturbative contribution to population probabilities for a Krypton cation, resonantly driven by a 80 eV, 150 as, 0.2 au peak amplitude probe pulse polarized in the z-direction. Note that ground state probabilities for $4p$ are depleted in order to build excited state probabilities for $3d$. Notice the decay of $3d$ states due to Auger transitions into multi-cations, which are represented by the sink. Probabilities are scaled with the square of the peak electric field amplitude of the probe pulse.

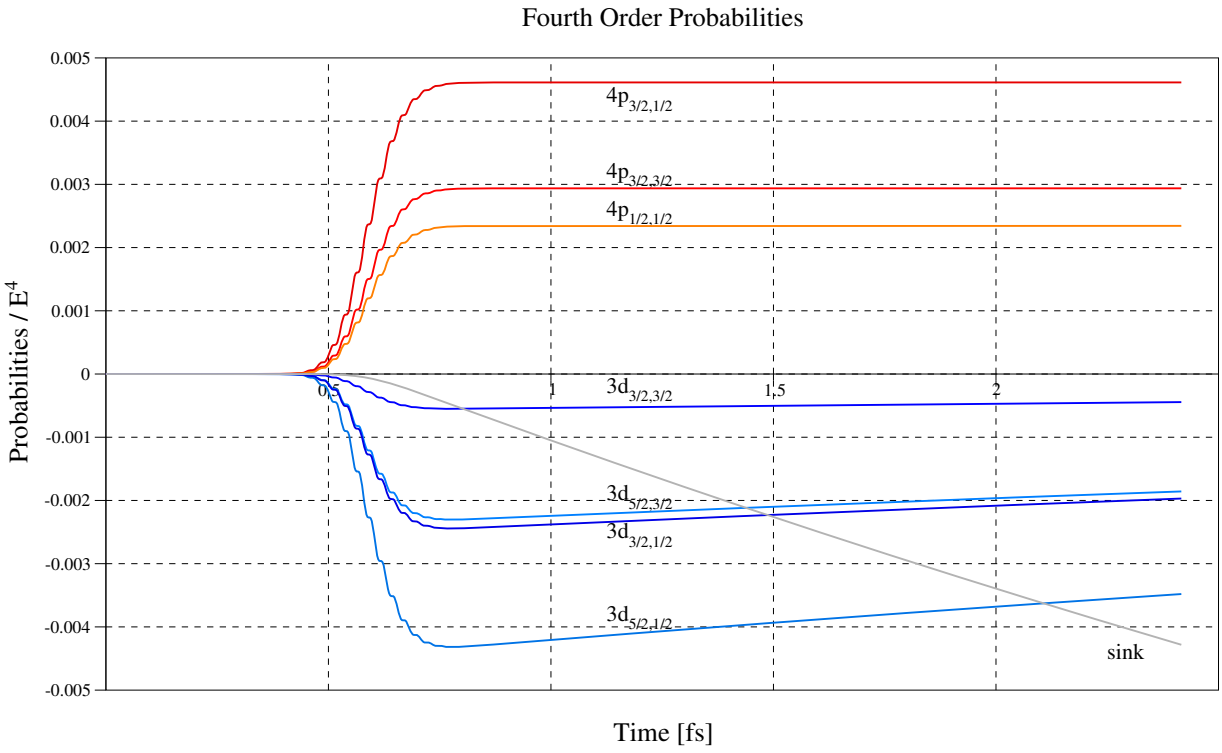

Figure 5.11: Fourth order perturbative contribution to population probabilities for a Krypton cation, resonantly driven by a 80 eV, 150 as, 0.2 au peak amplitude probe pulse polarized in the z-direction. Note that the fourth order effect works in the opposite direction from the second order effect. Probabilities are scaled with the fourth power of the peak electric field amplitude of the probe pulse.

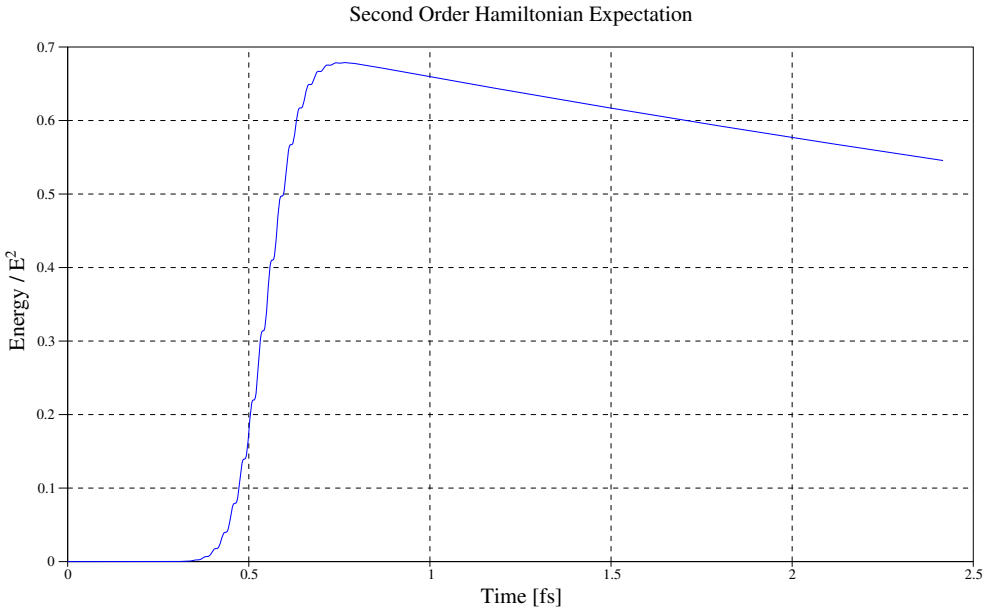

Figure 5.12: Second order perturbative contribution to the Hamiltonian expectation for a Krypton cation, resonantly driven by a 80 eV, 150 as, 0.2 au peak amplitude probe pulse polarized in the z-direction. Note how energy is resonantly absorbed in step-like fashion and also the effects of Auger decay. Energies are scaled with the square of the peak electric field amplitude of the probe pulse.

5.2.4 Nonlinear Effects and the Numerical Perturbative Expansion

Even though our simulation for Kr II handles 16+2 levels (including full degeneracy) and could in principle handle many more, we must always bear in mind the levels and continua not captured by this. For the simulation to make sense we must have that the electric dipole interaction is dominant and that other levels and continua are energetically far enough away. A very strong probe electric field would of course violate this by causing ionization but if the field is not too strong then ionization should be exponentially suppressed.

When we assume we are in a safe regime for the probe strength we can analyze how the density matrix depends polynomially on the probe electric field strength, in other words a

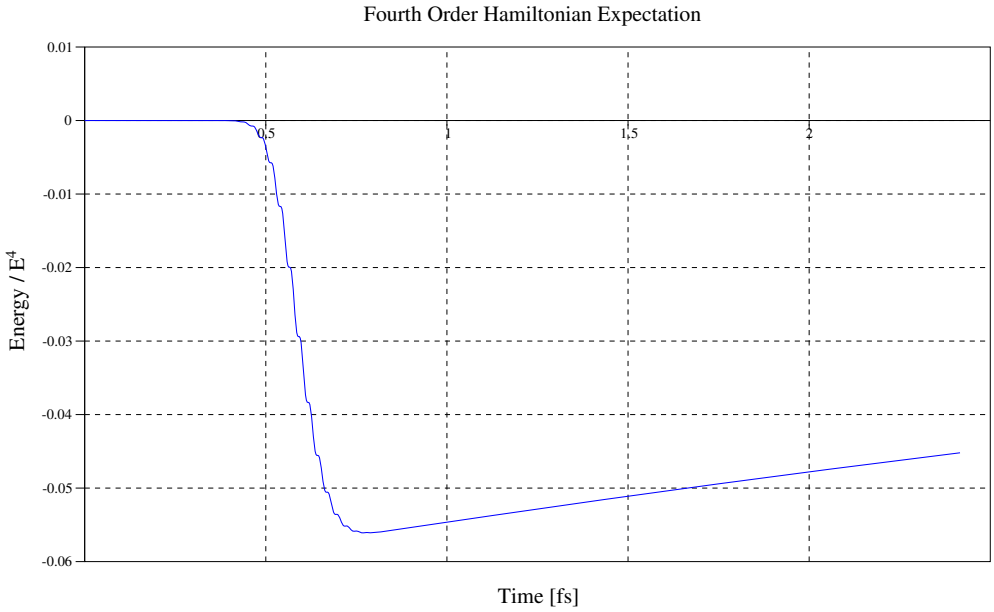

Figure 5.13: Fourth order perturbative contribution to the Hamiltonian expectation for a Krypton cation, resonantly driven by a 80 eV, 150 as, 0.2 au peak amplitude probe pulse polarized in the z-direction. Note how the fourth order effect is opposite in sign from the second order effect and is rather small in size for reasonable probe electric field strength. Energies are scaled with the fourth power of the peak electric field amplitude of the probe pulse.

perturbative expansion. In principle it is possible to compute this expansion analytically with perturbative density matrix theory but the formulae become cumbersome and unwieldy very quickly for higher orders. It is much easier to simulate one probe pulse multiplied by a set of scale factors. The set of results can be used to back-out the perturbative contributions. We have found that perturbative contributions up to order 8 can be recovered with good numerical accuracy. This does depend on the size of the contribution and the numerical quality of the simulation. Note that contributions to the diagonal of the density matrix are even in the probe electric field, as are the contributions to the expected Hamiltonian. The induced polarization is odd in the electric field.

In Figures (5.10) and (5.11) we show the second and fourth order terms for the populations a.k.a. probabilities a.k.a. density matrix diagonal elements for Kr II $4p$ and $3d$. Note how

probability is transferred from the $4p$ states to the $3d$ states. Note how the fourth order effect acts in the opposite direction from the second order effect. For a rather strong electric field of 0.2 au we see that the fourth order term provides a small correction of around -0.4%. Notice also that while the second order contribution at the time of the center of the probe pulse is about 1/4 of the value right after the pulse this ratio is actually close to 1/16 for the fourth order contribution. These ratios, 2^{-2} and 2^{-4} are consistent with quadratic and fourth power resonant growth during the body of the probe pulse.

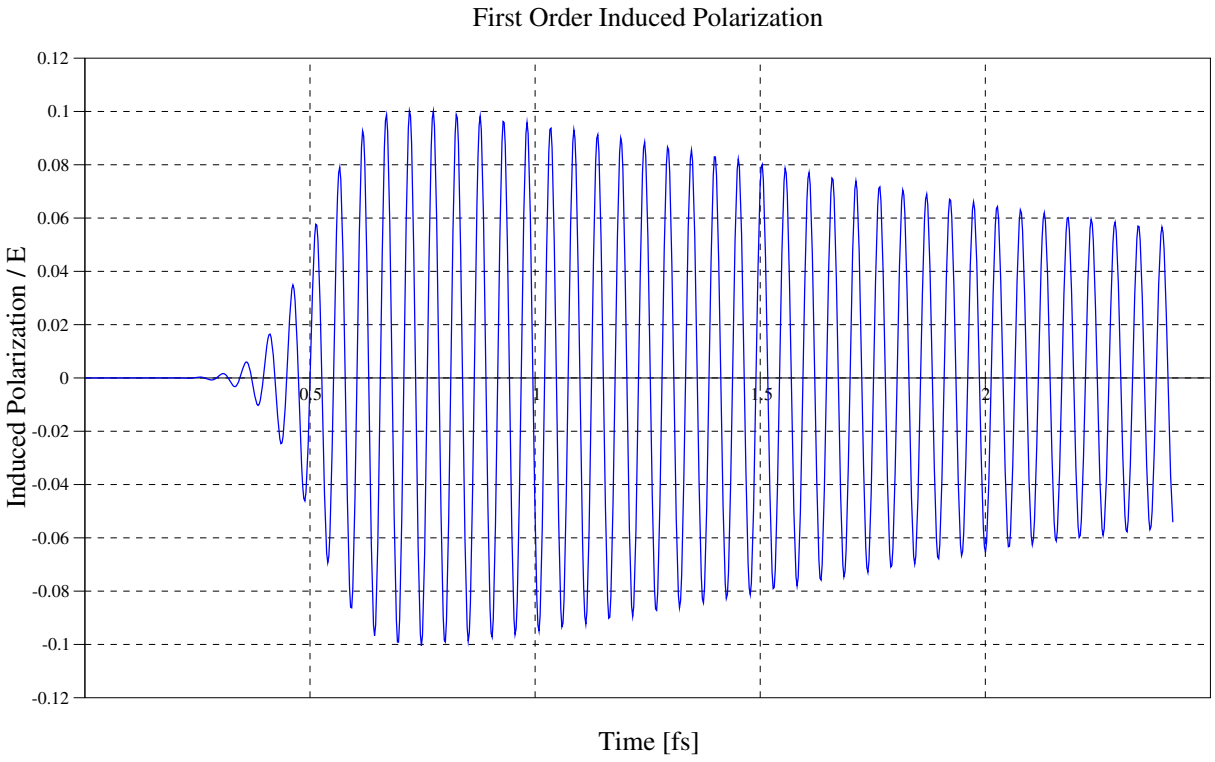

Figure 5.14: First order perturbative contribution to the induced polarization for a Krypton cation, resonantly driven by a 80 eV, 150 as, 0.2 au peak amplitude probe pulse polarized in the z-direction. Polarization is scaled with the peak electric field amplitude of the probe pulse.

The second and fourth order contributions to the expected Hamiltonian are shown in Figures (5.12) and (5.13) with, as expected, the same patterns as we saw for the probabilities. The first and third order contributions to the induced polarization are shown in Figures (5.14)

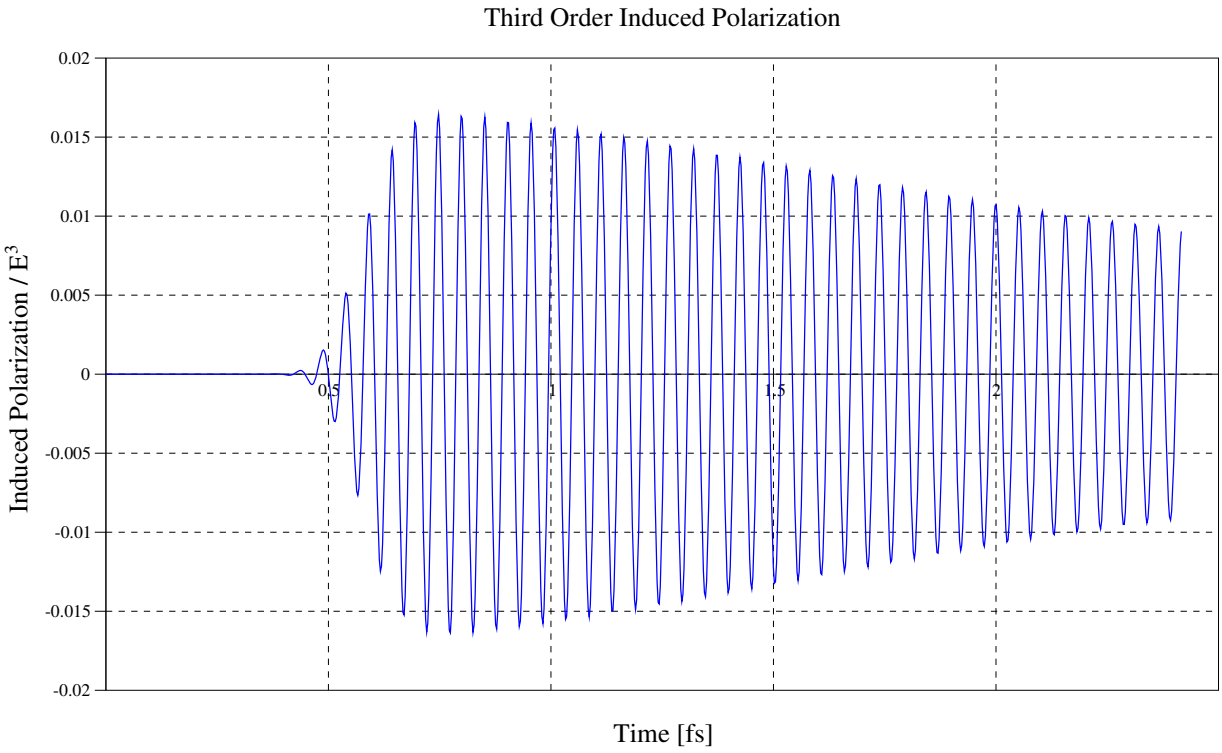

Figure 5.15: Third order perturbative contribution to the induced polarization for a Krypton cation, resonantly driven by a 80 eV, 150 as, 0.2 au peak amplitude probe pulse polarized in the z-direction. Note how the third order contribution has opposite sign from the first order contribution. Polarization is scaled with the third power of the peak electric field amplitude of the probe pulse.

and (5.15). We see that the third order effect acts in the opposite direction from the first order effect and is of relative size of about -0.7% for a probe peak electric field of 0.2 au. Looking again at the ratios for midway versus the end of the probe pulse we find about 1/2 for the first order and 1/8 for the third order. These values, 2^{-1} and 2^{-3}, are consistent with linear and cubic resonant growth during the body of the probe pulse.

It turns out that these higher order features of our multi-level system can be understood qualitatively and to some extent quantitatively in the context of the toy two-level model from Equation (5.8). When solving the toy-model non-perturbatively but with the simplifying rotating wave approximation and using an exactly resonant constant amplitude external force

$f(t) = A\sin(t)$ we find the familiar Rabi oscillation

$$\begin{aligned} \rho_{11} &= \sin^2(At/2) \\ \rho_{01} &= \tfrac{1}{2}e^{it}\sin(At) \\ \langle D\rangle &= \cos(t)\sin(At) \end{aligned} \tag{5.14}$$

with perturbative expansion in the external field strength A

$$\begin{aligned} \rho_{11} &= \tfrac{1}{4}A^2t^2 - \tfrac{1}{48}A^4t^4 + \dots \\ \langle D\rangle &= \cos(t)\cdot\left(At - \tfrac{1}{6}A^3t^3 + \dots\right) \end{aligned} \tag{5.15}$$

Comparing with the full Kr II simulation we observe the same oddness of the induced polarization $\langle D\rangle$, the evenness of excited population ρ_{11}, terms of order A^n grow resonantly as t^n and even the sign of the higher order terms versus the lower order ones is correct.

5.3 Conclusion

In this chapter we have simulated the effects of NIR pump and XUV probe pulses. We have used our source-cation-sink method to model the coherent multichannel ionization of noble gases and analyzed the dependence on the strength and length of the pump pulse. Our method, based on Lindblad terms, is very much simpler than full TDSE simulations of the ionization process and could be of practical use by itself or in the context of larger simulations. As a future direction of research it would be interesting to see how this method compares with more elaborate multi-channel ionization approaches. The implied density for $4p_{3/2}$ and $4p_{1/2}$ levels in the $m = \pm 1/2$ channels in the krypton experiment by Goulielmakis *et al.*[2] fit well both with our results and those from full TDSE treatments [35][36]. However, the implied diagonal density matrix elements by Goulielmakis *et al.* for $4p_{3/2}$ in the $m = \pm 3/2$ channels are very far (factor 7) off the mark compared to TDSE [35][36]. So more work needs

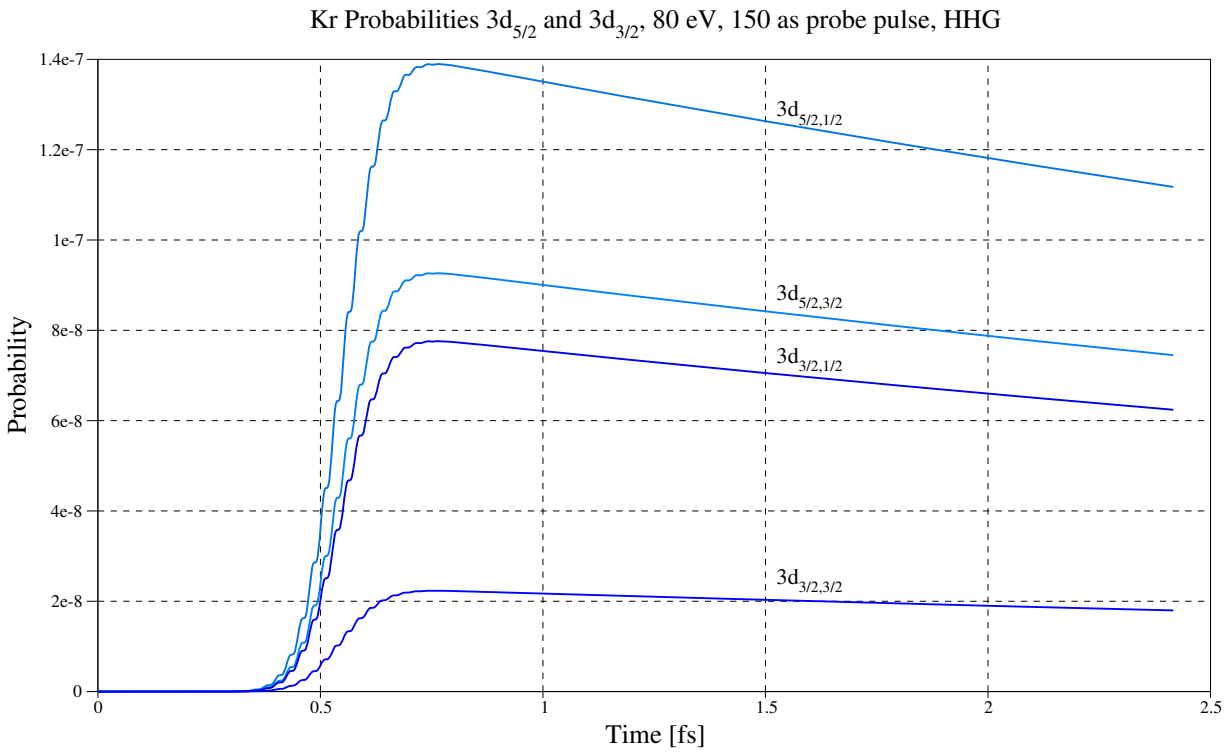

Figure 5.16: Population probabilities of the excited Krypton cation $3d_{5/2}$ and $3d_{3/2}$ states, resonantly driven by a 80 eV, 150 as, 0.001688 au peak amplitude probe pulse polarized in the z-direction, corresponding to 10^{11} W/cm^2, an intensity typical of HHG.

to be done here. Note that our method has no opinion on these relative populations but can accommodate the data by adjusting the π_i parameters from equation (4.63).

We simulated how probe pulses can resonantly populate the excited states of Kr II and studied in detail how populations, coherences and induced dipole moments evolved in time, including the effects of Auger decay. The onset of nonlinear effects can be estimated from the perturbative contributions we derived in the previous section. The probe peak electric field strength for which the second order and fourth order contributions to the excited populations are of equal strength is $E = 3.5$ au (corresponding to 4×10^{17} W/cm^2), while the electric field strength for which the first and third order contributions to the induced dipole are of

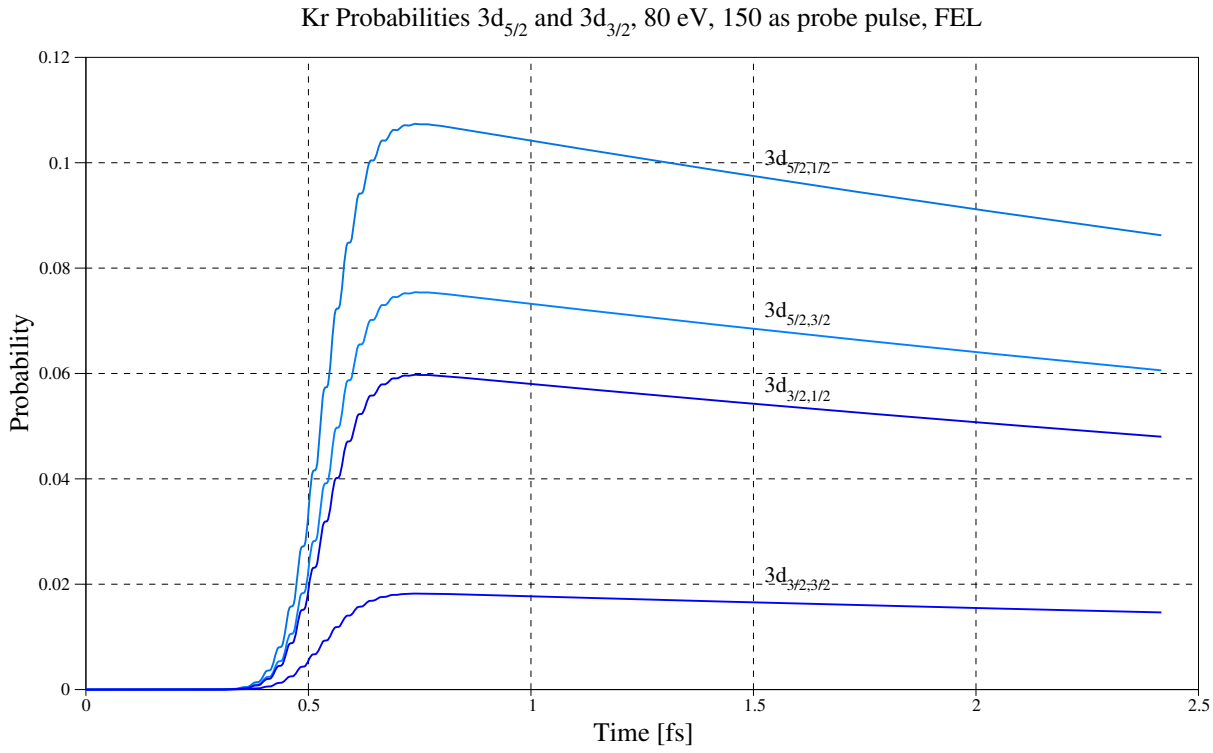

Figure 5.17: Population probabilities of the excited Krypton cation $3d_{5/2}$ and $3d_{3/2}$ states, resonantly driven by a 80 eV, 150 as, 1.688 au peak amplitude probe pulse polarized in the z-direction, corresponding to 10^{17} W/cm^2, an intensity typical of the free electron laser (FEL).

equal strength is $E = 2.4$ au (corresponding to 2×10^{17} W/cm^2). So nonlinear effects are not relevant for the typical HHG regime of 10^{12} W/cm^2, while they do become relevant for free electron laser (FEL) intensities which are on the order of 10^{17} W/cm^2, see Figure (5.17). We must be careful to note that some physical processes, such as non-Auger ionization into Kr III and beyond, go unmodeled here and that, therefore, the value 10^{17} W/cm^2 should be viewed rather as an upper limit for nonlinear onset. One reason why the modelling approach used here can work well quantitatively for a large range of intensities is that we focus on a small part of the spectrum (79 to 82 eV) and that we drive transitions in this spectral range resonantly. The working assumption is that unmodeled processes have no resonances in this

tight spectral range and would only manifest themselves as modest backgrounds. Of course when the probe field is too strong severe depletion and saturation effects come into play. To understand this in detail would require a full treatment of the multi-electron dynamics involving very extensive TDSE simulations with large numbers of levels. The development of free electron lasers has made it possible to start probing the regime of 10^{17} W/cm^2 so experimental answers to these questions are becoming possible. The most straightforward measure of nonlinearity would be to experimentally determine beyond which field strength the probe absorbance develops an interesting dependence on the probe intensity.

Chapter 6

Propagation Revisited

6.1 The Propagation Equation

In this chapter we derive the propagation equation for a laser pulse from the Maxwell equations, the induced polarization from low order density matrix perturbation theory and the Beer-Lambert absorption law for linear susceptibility. The derivation for the induced polarization is given in some detail and forms the basis for our results in Section 6.3 on the breaking of the Beer-Lambert law due to coherence.

6.1.1 Derivation of the Propagation Equation

To avoid any confusion we will use Système Internationale units throughout rather than Gaussian units. A good reference on electromagnetism using SI units is Grant & Phillips [3]. For Gaussian units please see Jackson [20].

We reduce the full Maxwell equations given in Equation (2.1) by making the usual approximation in optics that the free charge density, the free current and the magnetization can be neglected, see [34][46]. We get the simplified set

$$\begin{aligned} \nabla \cdot D &= 0 & \nabla \cdot B &= 0 \\ \nabla \times E &= -\partial_t B & \nabla \times B &= \mu_0 \partial_t D \\ D &= \epsilon_0 E + P \end{aligned} \tag{6.1}$$

from which we derive the wave equation

$$\nabla \times \nabla \times E = -\frac{1}{c^2}\partial_t^2 E - \mu_0 \partial_t^2 P \tag{6.2}$$

using $\epsilon_0 \mu_0 = 1/c^2$. Note the mathematical identity $\nabla \times \nabla \times E = \nabla(\nabla \cdot E) - \nabla^2 E$. Now assume that we are dealing with plane waves travelling in the x direction only and that E and P have no y and z dependence, and that E is polarized in the z direction, then

$$\left(\partial_x^2 - \frac{1}{c^2}\partial_t^2\right) E_z(x,t) = \mu_0 \partial_t^2 P_z(x,t) \tag{6.3}$$

We will drop the z index from this point. Factorizing the d'Alembertian gives

$$\left(\partial_x + \frac{1}{c}\partial_t\right)\left(\partial_x - \frac{1}{c}\partial_t\right)\mathcal{E}(x,t) = \mu_0 \partial_t^2 P(x,t) \tag{6.4}$$

where x and t are measured in the laboratory frame. We want to focus on the wave moving in the positive x-direction and adopt a new, local, coordinate system accordingly. In the new coordinate system $\{t' = t - x/c,\ x' = x\}$ we have, dropping the prime for x,

$$\partial_x\left(\partial_x - \frac{2}{c}\partial_{t'}\right)\mathcal{E}(x,t') = \mu_0 \partial_{t'}^2 P(x,t') \tag{6.5}$$

Going to Fourier space

$$\begin{aligned} \mathcal{E}(x,t') &= \int_{-\infty}^{\infty} \frac{d\omega}{2\pi} \hat{\mathcal{E}}(x,\omega) e^{-i\omega t'} \\ P(x,t') &= \int_{-\infty}^{\infty} \frac{d\omega}{2\pi} \hat{P}(x,\omega) e^{-i\omega t'} \end{aligned} \tag{6.6}$$

using the usual optics Fourier sign convention, we obtain

$$\left(\partial_x^2 + \frac{2i\omega}{c}\partial_x\right)\hat{\mathcal{E}}(x,\omega) = -\mu_0\omega^2\hat{P}(x,\omega) \tag{6.7}$$

We now assume that the electric field amplitude varies very slowly over the length scale $2\pi c/\omega$, which is the wavelength at angular frequency ω. This is known as the slowly varying envelope approximation (SVEA). This allows us to neglect the second order spatial derivative versus the first order one, resulting in [34][35][46][47]

$$\boxed{\partial_x\hat{\mathcal{E}}(x,\omega) = \frac{i}{2}\omega\mu_0 c\,\hat{P}(x,\omega)} \tag{6.8}$$

As we will later see, for the case that the polarization is directly proportional to electric field, that in order to be able to drop the second order derivative for the SVEA approximation there is an implicit assumption that the susceptibility χ is small $|\chi| \ll 1$, so that the relative permittivity $\epsilon = 1 + \chi$ gives a complex index of refraction $n = \sqrt{\epsilon} \approx 1 + \chi/2$.

6.1.2 Induced Polarization in Density Matrix Perturbation Theory

The derivation of induced polarization in low order perturbation theory can readily be guessed from ordinary (i.e. pure wavefunction) quantum theory, but is best to do a proper density matrix derivation as coherences are fundamental to the effects we are trying to describe. We could take two directions, either work in the expanded Liouvillian basis or work with the unexpanded density matrix itself. These approaches are completely equivalent but the latter is less notationally cumbersome so we'll take that path. The time evolution of the density matrix in matrix notation is

$$\dot{\rho} = -i[H_0 - \mathcal{E}D, \rho] - \tfrac{1}{2}\{\Gamma, \rho\} \tag{6.9}$$

where ρ is the density matrix, H_0 is the free Hamiltonian, $\mathcal{E}$ is the electric field, D is the dipole operator, Γ is the matrix of decay rates, the square brackets denote a commutator and

the curly brackets denote an anti-commutator. We will be working in a basis where both H_0 and Γ are diagonal and real. Also H_0, Γ and D are time independent, but $\mathcal{E}$ is time dependent. Note that ρ here denotes the singly charged cations we are studying and that the trace over cations is not conserved due to Auger decay into multi-cations, as described by Γ. We can expand the density matrix in orders of the electric field like so

$$\rho(t) = \rho^{(0)}(t) + \rho^{(1)}(t) + \dots \tag{6.10}$$

which leads to

$$\begin{aligned} \dot{\rho}^{(0)} &= -i[H_0, \rho^{(0)}] - \tfrac{1}{2}\{\Gamma, \rho^{(0)}\} \\ \dot{\rho}^{(1)} &= -i[H_0, \rho^{(1)}] - \tfrac{1}{2}\{\Gamma, \rho^{(1)}\} + i\mathcal{E}[D, \rho^{(0)}] \end{aligned} \tag{6.11}$$

To lighten notation we introduce the complex Hamiltonian

$$G = H_0 - \tfrac{1}{2}i\Gamma \tag{6.12}$$

and, therefore,

$$\begin{aligned} \dot{\rho}^{(0)} &= -iG\rho^{(0)} + i\rho^{(0)}G^\dagger \\ \dot{\rho}^{(1)} &= -iG\rho^{(1)} + i\rho^{(1)}G^\dagger + i\mathcal{E}[D, \rho^{(0)}] \end{aligned} \tag{6.13}$$

The field-free case is easily solved

$$\rho^{(0)}(t) = e^{-iGt}\rho_\odot e^{iG^\dagger t} \tag{6.14}$$

where we define $\rho_\odot = \rho^{(0)}(0)$ to be the density matrix at time zero.
The first-order correction can be solved as follows. Using Equation (6.13) we can write

$$(e^{iGt}\rho^{(1)}e^{-iG^\dagger t})^\bullet = i\mathcal{E}e^{iGt}[D, e^{-iGt}\rho_\odot e^{iG^\dagger t}]e^{-iG^\dagger t}$$
$$= i\mathcal{E}(e^{iGt}De^{-iGt}\rho_\odot - \rho_\odot e^{iG^\dagger t}De^{-iG^\dagger t}) \tag{6.15}$$

We now assume that $\mathcal{E}(t<0) = 0$ and $\rho^{(1)}(t<0) = 0$, then it follows that

$$\rho^{(1)}(t) = ie^{-iGt}\left(\int_0^t dt'\mathcal{E}e^{iGt'}De^{-iGt'}\right)\rho_\odot e^{iG^\dagger t} + h.c. \tag{6.16}$$

where $h.c.$ is the Hermitian conjugate.

The induced polarization is given by $P = \operatorname{tr}\rho D$. The first-order contribution due to the electric field is

$$P^{(1)} = \operatorname{tr}\rho^{(1)}D \tag{6.17}$$

so we can write

$$P^{(1)}(t) = i\operatorname{tr}\left(e^{-iGt}\left(\int_0^t dt'\mathcal{E}e^{iGt'}De^{-iGt'}\right)\rho_\odot e^{iG^\dagger t}D\right) + c.c. \tag{6.18}$$

where $c.c.$ is the complex conjugate. Note that using first order perturbation theory makes the dipole matrix elements show up twice in the induced polarization. The first is due to the fact that the strength of coupling to the laser field is proportional to the electric dipole elements so the density matrix of the excited states is as well. Secondly, the polarization represented by these excited states uses the dipole matrix elements again.

The electric field has the Fourier decomposition $\mathcal{E}(t) = \int_{-\infty}^{\infty}\frac{d\alpha}{2\pi}\hat{\mathcal{E}}(\alpha)e^{-i\alpha t}$ and $\hat{\mathcal{E}}(\alpha) = \int_{-\infty}^{\infty}dt\mathcal{E}(t)e^{i\alpha t}$, using the usual optics sign convention. For a treatment of density matrix perturbation theory and induced polarization calculations in Fourier space please see for instance Boyd [5][35][48].

Using that G is diagonal we find

$$\begin{aligned}\left(\int_0^t dt' \mathcal{E} e^{iGt'} D e^{-iGt'}\right)_{ab} &= \int_0^t dt' \mathcal{E} e^{iG_a t'} D_{ab} e^{-iG_b t'} \\ &= D_{ab} \int_{-\infty}^{\infty} \frac{d\alpha}{2\pi} \hat{\mathcal{E}}(\alpha) \int_0^t dt' e^{i(-\alpha+G_a-G_b)t'} \\ &= D_{ab} \int_{-\infty}^{\infty} \frac{d\alpha}{2\pi} \hat{\mathcal{E}}(\alpha) \frac{e^{i(-\alpha+G_a-G_b)t}-1}{i(-\alpha+G_a-G_b)} \end{aligned} \tag{6.19}$$

where $D_{ab} = \langle a|D|b\rangle$ and $D_{ba} = D_{ab}^*$ because D is Hermitian. Filling in this result in Equation (6.18) and summing over indices we obtain

$$P^{(1)}(t) = i \sum_{abc} D_{ab} \rho_{\odot bc} D_{ca} \int_{-\infty}^{\infty} \frac{d\alpha}{2\pi} \hat{\mathcal{E}}(\alpha) \frac{e^{i(-\alpha+G_c^*-G_b)t} - e^{i(-G_a+G_c^*)t}}{i(-\alpha+G_a-G_b)} + c.c. \tag{6.20}$$

Because $P^{(1)}(t \leq 0) = 0$ we have

$$\begin{aligned}\hat{P}^{(1)}(\omega) &= \int_0^{\infty} dt P^{(1)}(t) e^{i\omega t} \\ &= i \sum_{abc} D_{ab} \rho_{\odot bc} D_{ca} \int_{-\infty}^{\infty} \frac{d\alpha}{2\pi} \hat{\mathcal{E}}(\alpha) \frac{\frac{-1}{i(\omega-\alpha+G_c^*-G_b)} + \frac{1}{i(\omega-G_a+G_c^*)}}{i(-\alpha+G_a-G_b)} + c.c.(-\omega) \\ &= -i \sum_{abc} \frac{D_{ab} \rho_{\odot bc} D_{ca}}{(\omega-G_a+G_c^*)} \int_{-\infty}^{\infty} \frac{d\alpha}{2\pi} \frac{\hat{\mathcal{E}}(\alpha)}{(\omega-\alpha+G_c^*-G_b)} + c.c.(-\omega) \end{aligned} \tag{6.21}$$

where the $c.c.(-\omega)$ notation means the complex conjugate with ω replaced by $-\omega$. The integrals we just did above can sometimes be tricky because of concerns over the convergence of oscillatory integrals to infinity. However, one can determine by inspection that the decay parameters Γ work in concert with the non-zero elements of the dipole operator matrix in such a way that all integrals converge absolutely.

We will now show why and how the integral over α can be performed. First, because $G_a = E_a - \frac{1}{2}i\gamma_a$, we find that $\omega - \alpha + G_c^* - G_b = (\omega - \alpha + E_c - E_b) + \frac{1}{2}i(\gamma_c + \gamma_b)$, where the eigenvalues of the free Hamiltonian are given by E and the decay rates by γ. So the α integral has a pole in the upper half plane. Second, the electric field is zero before time $t = 0$ and can be represented by some linear combination of normalizable functions of the type

$\phi(r,s,t\geq 0)=e^{-irt-st}$ and $\phi(r,s,t<0)=0$, where r is real and s is real and positive. The Fourier transform is given by $\hat{\phi}(r,s,\alpha)=i/(\alpha-r+is)$, so $\hat{\phi}$ has a pole in the lower half of the complex plane. It follows that $\hat{\mathcal{E}}(\alpha)$ can be described by some pole density restricted to the lower half plane. The last ingredient we need is the integral $\int_{-\infty}^{\infty}\frac{dx}{(x-z_u)(x-z_l)}=\frac{2i\pi}{z_u-z_l}$ by the residue method, where z_u is in the upper half plane and z_l is in the lower half plane. Look at the integral where the first pole is in the upper half plane and the second pole is in the lower half plane

$$\int_{-\infty}^{\infty}\frac{d\alpha}{2\pi}\,\frac{1}{(\omega-\alpha+G_c^*-G_b)}\cdot\frac{i}{(\alpha-r+is)}=\frac{1}{(\omega+G_c^*-G_b)-r+is} \tag{6.22}$$

Because $\hat{\mathcal{E}}(\alpha)$ is a linear combination of functions of the type $i/(\alpha-r+is)$ we then have

$$\int_{-\infty}^{\infty}\frac{d\alpha}{2\pi}\,\frac{\hat{\mathcal{E}}(\alpha)}{(\omega-\alpha+G_c^*-G_b)}=-i\hat{\mathcal{E}}(\omega+G_c^*-G_b) \tag{6.23}$$

Equation (6.21) now becomes

$$\hat{P}^{(1)}(\omega)=-\sum_{abc}D_{ab}\rho_{\odot bc}D_{ca}\frac{\hat{\mathcal{E}}(\omega+G_c^*-G_b)}{(\omega+G_c^*-G_a)}\;+c.c.(-\omega) \tag{6.24}$$

Using $G_a=E_a-\frac{1}{2}i\gamma_a$ we have

$$\hat{P}^{(1)}(\omega)=-\sum_{abc}D_{ab}\rho_{\odot bc}D_{ca}\frac{\hat{\mathcal{E}}(\omega+E_c-E_b+\frac{1}{2}i(\gamma_c+\gamma_b))}{(\omega+E_c-E_a+\frac{1}{2}i(\gamma_c+\gamma_a))}\;+c.c.(-\omega) \tag{6.25}$$

Assume now that the cation density matrix ρ is prepared in such a way as to only have significant populations and coherences for low lying levels and, furthermore, that those low lying levels have no dipole interactions between them. In that case we can separate the low lying levels and the higher excited levels in our notation like so

$$\hat{P}^{(1)}(\omega)=\sum_{fbc}D_{fb}\rho_{\odot bc}D_{cf}\frac{\hat{\mathcal{E}}(\omega+E_c-E_b+\frac{1}{2}i(\gamma_c+\gamma_b))}{(E_f-E_c-\frac{1}{2}i(\gamma_f+\gamma_c))-\omega}\;+c.c.(-\omega) \tag{6.26}$$

where f is an index for an excited state (e.g. $3d_{5/2}$ and $3d_{3/2}$ for Kr II) and b and c denote low lying states (e.g. $4p_{3/2}$ and $4p_{1/2}$ for Kr II). A further simplification is that the decay rates for the low lying states are very small (but positive) compared with the (sub-)femtosecond time-scale we are interested in, while the decay rates for the excited states are deemed relevant (e.g. Auger decay). With these assumptions

$$\hat{P}^{(1)}(\omega) = \sum_{fbc} D_{fb}\rho_{\odot bc}D_{cf}\frac{\hat{\mathcal{E}}(\omega + E_c - E_b)}{(E_f - E_c - \frac{1}{2}i\gamma_f) - \omega} \quad + c.c.(-\omega) \tag{6.27}$$

For a sense of scale, for Kr II the energy difference $E_f - E_c$ varies from 79.8 eV to 81.1 eV and γ_f is 88 meV. Another simplification is achieved by realizing that for positive ω the counter-rotating term contained in $c.c.(-\omega)$ is very far from resonance and we shall neglect it. We will also drop the $\odot$ notation from this point and the ρ appearing in the formulae is the one prepared at time zero

$$\boxed{\hat{P}^{(1)}(\omega>0) = \sum_{fbc} D_{fb}\rho_{bc}D_{cf}\frac{\hat{\mathcal{E}}(\omega + E_c - E_b)}{(E_f - E_c - \frac{1}{2}i\gamma_f) - \omega}} \tag{6.28}$$

As mentioned above we might as well have derived the perturbative contributions to the induced polarization using the expanded basis instead. In that case

$$\dot{\rho} = \mathcal{L}\rho \tag{6.29}$$

where, using N levels, ρ is the density matrix expanded into a vector of length N^2, and the Liouvillian $\mathcal{L}$ is a time dependent matrix of size N^2 by N^2. Equation (6.29) can be solved formally as follows

$$\rho(t) = \overleftarrow{T}\, e^{\int_0^t \mathcal{L}(t')dt'}\rho(0) \tag{6.30}$$

where $\overleftarrow{T}$ is a time ordering operator making sure that Liouvillians of a later time are applied from the left. The Liouvillian for the problem we are studying has a particular structure

$$\mathcal{L}(t) = \mathcal{L}_0 + i\mathcal{E}(t)\mathcal{D} \tag{6.31}$$

where $\mathcal{L}_0$ is the static, time independent, field free Liouvillian comprised of the ionic Hamiltonian and Auger decay, $\mathcal{E}(t)$ is the time dependent external electric field and $\mathcal{D}$ is the Liouvillian version of the dipole operator defined via the commutator action of the dipole operator $[D, \rho]$. If we consider the external electric field as a perturbation we can expand our formal solution with the help of the following

$$\overleftarrow{T}\, e^{\int_0^t (\mathcal{L}_0 + i\mathcal{E}(t')\mathcal{D})dt'} = e^{t\mathcal{L}_0} + i\int_0^t dt_1\, e^{(t-t_1)\mathcal{L}_0}\mathcal{E}(t_1)\mathcal{D}e^{t_1\mathcal{L}_0} + \dots \tag{6.32}$$

where $\overleftarrow{T}$ is the time ordering operator which makes sure later times are positioned on the left. The subsequent derivation of the induced polarization follows the same steps as those for the unexpanded-basis above, all be it with more algebra.

6.1.3 The Susceptibility Ansatz and the Derivation of the Beer-Lambert Law

A crucial step is now to assume that $\hat{P}^{(1)}$ is proportional to the electric field $\hat{\mathcal{E}}$. This is a good approximation in many physical situations, but a rather poor one when we want to model coherent transient absorption more accurately as discussed in Section 6.3.
For this section we make the simplifying Ansatz

$$\hat{P}^{(1)}(x, \omega) = \chi^{(1)}(x, \omega)\hat{\mathcal{E}}(x, \omega) \tag{6.33}$$

where $\chi^{(1)}(x, \omega)$ is the linear susceptibility. In general $\hat{P}^{(1)}$ and $\hat{\mathcal{E}}$ are out of phase, i.e. χ is complex, which allows us to model waves being absorbed. To simplify matters even more we assume that we are operating in a homogeneous medium so that $\chi^{(1)}$ is not dependent on position

$$\chi^{(1)}(x,\omega) = \chi^{(1)}(\omega) \tag{6.34}$$

Integrating Equation (6.8) we get

$$\hat{\mathcal{E}}(x,\omega) = \hat{\mathcal{E}}(0,\omega)e^{i\omega x\chi^{(1)}(\omega)/(2c)} \tag{6.35}$$

and, finally, the Beer-Lambert law [49]

$$\boxed{|\hat{\mathcal{E}}(x,\omega)|^2 = |\hat{\mathcal{E}}(0,\omega)|^2 e^{-\omega x\,\mathrm{Im}\chi^{(1)}(\omega)/c}} \tag{6.36}$$

exhibiting exponential decay with distance x for the intensity of the wave.

6.2 Induced Polarization and Angular Dependence

In this chapter we provide new results on the probe vs. pump polarization angular dependence of induced polarization. We provide an extensive analysis on what density matrix information is measurable in transient absorption experiments, angular dependence and contributions from coherence.

It is important to emphasize that some results in the literature [2] have assumed a flat spectrum for the electric field which leads directly to proportionality between induced polarization and the electric field and thus to the Beer-Lambert law. Even when such an assumption is initially reasonable it can not hold when the probe pulse travels through an absorbing medium. We think that approximation is rather poor and we choose to solve the full dynamics instead. In Equation (6.46) we present the induced polarization with angular dependence and proper coherence dynamics. This result forms the basis for non-Beer-Lambert absorption in Section 6.3.

6.2.1 Dipole Operator Matrix Elements

For convenience we repeat the formula we derived for the induced polarization Equation (6.28)

$$\hat{P}^{(1)}(\omega>0) = \sum_{fbc} D_{fb}\rho_{bc}D_{cf}\frac{\hat{\mathcal{E}}(\omega + E_c - E_b)}{(E_f - E_c - \frac{1}{2}i\gamma_f) - \omega} \tag{6.37}$$

where the indices b and c signify low lying states, i.e. $4p_{3/2}$ and $4p_{1/2}$ for Krypton II, and f indicates an excited state, i.e. $3d_{5/2}$ or $3d_{3/2}$. The first step is to determine the dipole matrix elements D_{fb}.

The Hamiltonian contribution for light-matter interaction in the length gauge in the dipole approximation is

$$V_{\text{int}} = -\vec{D}\cdot\vec{\mathcal{E}} = -x\mathcal{E}_x - y\mathcal{E}_y - z\mathcal{E}_z \tag{6.38}$$

It is customary to choose the z-direction for the quantization of angular momentum. It is helpful, therefore, to choose the propagation of the laser pulse to be in the positive x-direction. Because electromagnetic fields are transversal we will then have that $\mathcal{E}_x = 0$. If (x, y, z) is a right handed system then so is $(z, -y, x)$. So if the laser pulse is linearly polarized at angle ϕ we have $\mathcal{E}_z = \mathcal{E}\cos(\phi)$ and $\mathcal{E}_y = -\mathcal{E}\sin(\phi)$, where $\mathcal{E}$ is the time dependent amplitude of the electric field. The interaction Hamiltonian is, therefore,

$$V_{\text{int}} = \mathcal{E}(t)\ (y\sin(\phi) - z\cos(\phi)) \tag{6.39}$$

The position vector $\vec{r}$ is of rank 1 and can be decomposed in spherical tensors in the following way [50]

$$\begin{cases} T^1_{-1} = \frac{x-iy}{\sqrt{2}} \\ T^1_0 \ = z \\ T^1_1 \ = \frac{-x-iy}{\sqrt{2}} \end{cases} \qquad \begin{cases} x = \frac{T^1_{-1}-T^1_1}{\sqrt{2}} \\ y = i\frac{T^1_{-1}+T^1_1}{\sqrt{2}} \\ z = T^1_0 \end{cases} \tag{6.40}$$

These spherical tensors are useful when computing dipole moments using the Wigner Eckart theorem. The interaction Hamiltonian can now be written as $V_{int} = -\mathcal{E}(t)D$, where

$$D = -\frac{i}{\sqrt{2}}\sin(\phi)\,T^1_{-1} + \cos(\phi)\,T^1_0 - \frac{i}{\sqrt{2}}\sin(\phi)\,T^1_1 \tag{6.41}$$

where ϕ is the polarization angle, $\mathcal{E}$ the amplitude of the electric field and D is the dipole operator.

For operators of rank one we have the following case of the Wigner-Eckart theorem, see Appendix E,

$$\langle j_1 m_1|T^1_q|j_2 m_2\rangle = (-)^{j_1-m_1}\begin{pmatrix} j_1 & 1 & j_2 \\ -m_1 & q & m_2 \end{pmatrix}\langle j_1||T^1||j_2\rangle \tag{6.42}$$

which gives the geometrical relationship between the matrix elements and the reduced matrix elements.

Let us have a look at Kr II. Consider the low lying states $4p_{3/2}$ and $4p_{1/2}$, and the excited states $3d_{5/2}$ and $3d_{3/2}$. Note that we prepare the cation density matrix coherently over the low-lying states $4p_{3/2}$ and $4p_{1/2}$. Due to parity constraints and Δj selection rules there are only three allowed electric dipole transitions (see Figure (4.1)), namely

$$\begin{aligned} 3d_{5/2} &\longleftrightarrow 4p_{3/2} \qquad E_{3d_{5/2}} - E_{4p_{3/2}} = 79.8 \text{ eV} \\ 3d_{3/2} &\longleftrightarrow 4p_{3/2} \qquad E_{3d_{3/2}} - E_{4p_{3/2}} = 81.1 \text{ eV} \\ 3d_{3/2} &\longleftrightarrow 4p_{1/2} \qquad E_{3d_{3/2}} - E_{4p_{1/2}} = 80.4 \text{ eV} \end{aligned} \tag{6.43}$$

where the energies are experimentally determined [2]. Although there are three resonances of interest there are five possible contributions to $D_{fb}\rho_{bc}D_{cf}$.

$$\langle 3d_{5/2}|D|4p_{3/2}\rangle\langle 4p_{3/2}|\rho|4p_{3/2}\rangle\langle 4p_{3/2}|D|3d_{5/2}\rangle$$
$$\langle 3d_{3/2}|D|4p_{3/2}\rangle\langle 4p_{3/2}|\rho|4p_{3/2}\rangle\langle 4p_{3/2}|D|3d_{3/2}\rangle$$
$$\langle 3d_{3/2}|D|4p_{1/2}\rangle\langle 4p_{1/2}|\rho|4p_{1/2}\rangle\langle 4p_{1/2}|D|3d_{3/2}\rangle$$
$$\langle 3d_{3/2}|D|4p_{3/2}\rangle\langle 4p_{3/2}|\rho|4p_{1/2}\rangle\langle 4p_{1/2}|D|3d_{3/2}\rangle$$
$$\langle 3d_{3/2}|D|4p_{1/2}\rangle\langle 4p_{1/2}|\rho|4p_{3/2}\rangle\langle 4p_{3/2}|D|3d_{3/2}\rangle \tag{6.44}$$

where the last two exist because of the coherence between the $4p_{3/2}$ and $4p_{1/2}$ states.
The excited state $3d_{5/2}$ only couples to one low state, namely $4p_{3/2}$. This means that Beer's law will apply to the 79.8 eV absorption line. The excited state $3d_{3/2}$ couples to two lower states, namely $4p_{3/2}$ and $4p_{1/2}$. Because of the coherence between the low-lying states and because $3d_{3/2}$ couples to them both, we will have coherence effects in the 80.4 eV and 81.1 eV absorption lines.

6.2.2 Polarization Angle Analysis

We now go through all five transitions which contribute to lowest order absorption. The polarization angle ϕ is the angle between the polarization of the probe versus the pump, which is z-polarized. For shorthand in the tables we write $s = \sin\phi$ and $c = \cos\phi$. The tables below consist of reduced matrix element factors and Wigner-Eckart factors. The rows are indexed by the m values for the final j, while the columns are indexed by the m values for the initial j.

$$\left|\langle 3d_{3/2}||T^1||4p_{1/2}\rangle\right|^2 \cdot \frac{1}{6} \cdot$$

	$-1/2$	$1/2$
$-1/2$	1	0
$1/2$	0	1

$$\langle 3d_{3/2}||T^1||4p_{1/2}\rangle \cdot \frac{\sqrt{10}}{60} \cdot \begin{array}{|c|cc|}\hline & -3/2 & -1/2 \\ \hline -1/2 & \frac{\sqrt{3}}{2}ics & -1+\frac{3}{2}s^2 \\ 1/2 & -\frac{\sqrt{3}}{2}s^2 & -\frac{3}{2}ics \\ \hline \end{array} \begin{array}{|cc|}\hline 1/2 & 3/2 \\ \hline \frac{3}{2}ics & \frac{\sqrt{3}}{2}s^2 \\ 1-\frac{3}{2}s^2 & -\frac{\sqrt{3}}{2}ics \\ \hline \end{array} \cdot \langle 4p_{3/2}||T^1||3d_{3/2}\rangle$$

$$\langle 3d_{3/2}||T^1||4p_{3/2}\rangle \cdot \frac{\sqrt{10}}{60} \cdot \begin{array}{|c|cc|}\hline & -1/2 & 1/2 \\ \hline -3/2 & \frac{\sqrt{3}}{2}ics & \frac{\sqrt{3}}{2}s^2 \\ -1/2 & 1-\frac{3}{2}s^2 & -\frac{3}{2}ics \\ 1/2 & \frac{3}{2}ics & -1+\frac{3}{2}s^2 \\ 3/2 & -\frac{\sqrt{3}}{2}s^2 & -\frac{\sqrt{3}}{2}ics \\ \hline \end{array} \cdot \langle 4p_{1/2}||T^1||3d_{3/2}\rangle$$

$$\left|\langle 3d_{3/2}||T^1||4p_{3/2}\rangle\right|^2 \cdot \frac{1}{60} \cdot \begin{array}{|c|cccc|}\hline & -3/2 & -1/2 & 1/2 & 3/2 \\ \hline -3/2 & 9-6s^2 & 4\sqrt{3}ics & -2\sqrt{3}s^2 & 0 \\ -1/2 & -4\sqrt{3}ics & 1+6s^2 & 0 & -2\sqrt{3}s^2 \\ 1/2 & -2\sqrt{3}s^2 & 0 & 1+6s^2 & -4\sqrt{3}ics \\ 3/2 & 0 & -2\sqrt{3}s^2 & 4\sqrt{3}ics & 9-6s^2 \\ \hline \end{array}$$

$$\left|\langle 3d_{5/2}||T^1||4p_{3/2}\rangle\right|^2 \cdot \frac{1}{60} \cdot \begin{array}{|c|cccc|}\hline & -3/2 & -1/2 & 1/2 & 3/2 \\ \hline -3/2 & 4+\frac{3}{2}s^2 & -\sqrt{3}ics & \frac{\sqrt{3}}{2}s^2 & 0 \\ -1/2 & \sqrt{3}ics & 6-\frac{3}{2}s^2 & 0 & \frac{\sqrt{3}}{2}s^2 \\ 1/2 & \frac{\sqrt{3}}{2}s^2 & 0 & 6-\frac{3}{2}s^2 & \sqrt{3}ics \\ 3/2 & 0 & \frac{\sqrt{3}}{2}s^2 & -\sqrt{3}ics & 4+\frac{3}{2}s^2 \\ \hline \end{array}$$

Table 6.1: Reduced matrix element factors and Wigner-Eckart factors. The rows are indexed by the m values for the final j, while the columns are indexed by the m values for the initial j.

Note that if we do not know anything about how the density matrix is prepared then absorption data can not be used to completely reconstruct this density matrix and can provide only partial information. Also, because of the angular dependence being channeled through

the three components $\{1, \sin\phi\cos\phi, \sin^2\phi\}$, measurements over three different angles in an ideal experiment would reveal all that can be known.

However, the situation can be vastly simplified and improved when we do presume structure. Assuming a pump pulse polarized in the z-direction and electric dipole interaction only we can simplify by using the ionization symmetries from Equation (5.6). The five transitions contributing to lowest order absorption then give us, in the $\rho^{(m_f=m_i)}_{j_f;\,j_i}$ notation,

$$\begin{aligned}
&\left|\langle 3d_{3/2}||T^1||4p_{1/2}\rangle\right|^2 \cdot \frac{1}{3} \cdot \rho^{(1/2)}_{1/2;\,1/2} \\
\langle 4p_{3/2}||T^1||3d_{3/2}\rangle\langle 3d_{3/2}||T^1||4p_{1/2}\rangle &\cdot \frac{\sqrt{10}}{30} \cdot (1-\tfrac{3}{2}\sin^2\phi)\,\rho^{(1/2)*}_{3/2;\,1/2} \\
\langle 4p_{1/2}||T^1||3d_{3/2}\rangle\langle 3d_{3/2}||T^1||4p_{3/2}\rangle &\cdot \frac{\sqrt{10}}{30} \cdot (1-\tfrac{3}{2}\sin^2\phi) \cdot -\rho^{(1/2)}_{3/2;\,1/2} \\
&\left|\langle 3d_{3/2}||T^1||4p_{3/2}\rangle\right|^2 \cdot \frac{1}{30} \cdot \left((9-6\sin^2\phi)\,\rho^{(3/2)}_{3/2;\,3/2} + (1+6\sin^2\phi)\,\rho^{(1/2)}_{3/2;\,3/2}\right) \\
&\left|\langle 3d_{5/2}||T^1||4p_{3/2}\rangle\right|^2 \cdot \frac{1}{30} \cdot \left((4+\tfrac{3}{2}\sin^2\phi)\,\rho^{(3/2)}_{3/2;\,3/2} + (6-\tfrac{3}{2}\sin^2\phi)\,\rho^{(1/2)}_{3/2;\,3/2}\right)
\end{aligned} \tag{6.45}$$

Incorporating this information we derive the induced polarization formula

$$\begin{aligned}
\hat{P}^{(1)}(\omega>0) = &\frac{1}{3} \cdot \rho^{(1/2)}_{1/2;\,1/2} \cdot \frac{\hat{\mathcal{E}}(\omega)\left|\langle 3d_{3/2}||T^1||4p_{1/2}\rangle\right|^2}{E_{3d_{3/2}} - E_{4p_{1/2}} - \frac{i}{2}\gamma_{3d_{3/2}} - \omega} \\
&+ \frac{1}{30} \cdot \left((9-6\sin^2\phi)\,\rho^{(3/2)}_{3/2;\,3/2} + (1+6\sin^2\phi)\,\rho^{(1/2)}_{3/2;\,3/2}\right) \cdot \frac{\hat{\mathcal{E}}(\omega)\left|\langle 3d_{3/2}||T^1||4p_{3/2}\rangle\right|^2}{E_{3d_{3/2}} - E_{4p_{3/2}} - \frac{i}{2}\gamma_{3d_{3/2}} - \omega} \\
&+ \frac{1}{30} \cdot \left((4+\tfrac{3}{2}\sin^2\phi)\,\rho^{(3/2)}_{3/2;\,3/2} + (6-\tfrac{3}{2}\sin^2\phi)\,\rho^{(1/2)}_{3/2;\,3/2}\right) \cdot \frac{\hat{\mathcal{E}}(\omega)\left|\langle 3d_{5/2}||T^1||4p_{3/2}\rangle\right|^2}{E_{3d_{5/2}} - E_{4p_{3/2}} - \frac{i}{2}\gamma_{3d_{5/2}} - \omega} \\
&+ \frac{\sqrt{10}}{30} \cdot (1-\tfrac{3}{2}\sin^2\phi)\,\rho^{(1/2)*}_{3/2;\,1/2} \cdot \frac{\hat{\mathcal{E}}(\omega+E_{4p_{3/2}}-E_{4p_{1/2}})\langle 3d_{3/2}||T^1||4p_{1/2}\rangle\langle 4p_{3/2}||T^1||3d_{3/2}\rangle}{E_{3d_{3/2}} - E_{4p_{3/2}} - \frac{i}{2}\gamma_{3d_{3/2}} - \omega} \\
&- \frac{\sqrt{10}}{30} \cdot (1-\tfrac{3}{2}\sin^2\phi)\,\rho^{(1/2)}_{3/2;\,1/2} \cdot \frac{\hat{\mathcal{E}}(\omega+E_{4p_{1/2}}-E_{4p_{3/2}})\langle 3d_{3/2}||T^1||4p_{3/2}\rangle\langle 4p_{1/2}||T^1||3d_{3/2}\rangle}{E_{3d_{3/2}} - E_{4p_{1/2}} - \frac{i}{2}\gamma_{3d_{3/2}} - \omega}
\end{aligned} \tag{6.46}$$

A lot can be gleaned from this formula. There are terms proportional in $\hat{\mathcal{E}}(\omega)$ that observe the Beer-Lambert law, and there are coherence terms that aren't and, therefore, break this

law. The $E_{3d_{5/2}}$–$E_{4p_{3/2}}$ absorption line does not interfere with the other lines and does observe the Beer-Lambert law. The $E_{3d_{3/2}} - E_{4p_{3/2}}$ and $E_{3d_{3/2}} - E_{4p_{1/2}}$ absorption lines do influence each other. The density matrix elements ρ in the formula above are those for the lower levels $4p_{3/2}$ and $4p_{1/2}$ and are to lowest order in perturbation theory and thus evolve with the free Hamiltonian. The diagonal terms are real and constant in time but the density matrix element $\rho^{(1/2)}_{3/2;1/2}$ is off-diagonal and a time-dependent complex number that phase rotates with time due to the energy difference $E_{4p_{3/2}} - E_{4p_{1/2}}$

$$\rho^{(1/2)}_{3/2;1/2}(t) = \rho^{(1/2)}_{3/2;1/2}(t_0)\ e^{-i(E_{4p_{3/2}} - E_{4p_{1/2}})(t-t_0)} \tag{6.47}$$

and, therefore, the induced polarization has a term that is periodic in the delay time between the probe and the pump pulse. This shows up as a periodic variation in the transient absorption of the lines $E_{3d_{3/2}} - E_{4p_{3/2}}$ and $E_{3d_{3/2}} - E_{4p_{1/2}}$ as a function of probe-pump time delay. We have made the angular dependence explicit which means that there are multiple independent ways to determine some of the density matrix elements which allows for a consistency check and an experimental validation of our modelling assumptions.
It is interesting to note that this formula becomes featureless when $\sin^2\phi = \frac{2}{3}$, i.e. a polarization angle of $\phi \approx 54.7°$.

$$\begin{aligned}
\hat{P}^{(1)}(\omega > 0,\ \phi = \arcsin\sqrt{\tfrac{2}{3}}) = {} & \frac{1}{3} \cdot \rho^{(1/2)}_{1/2;\,1/2} \cdot \frac{\hat{\mathcal{E}}(\omega)\left|\langle 3d_{3/2}||T^1||4p_{1/2}\rangle\right|^2}{E_{3d_{3/2}} - E_{4p_{1/2}} - \frac{i}{2}\gamma_{3d_{3/2}} - \omega} \\
& + \frac{1}{6} \cdot \left(\rho^{(3/2)}_{3/2;\,3/2} + \rho^{(1/2)}_{3/2;\,3/2}\right) \cdot \frac{\hat{\mathcal{E}}(\omega)\left|\langle 3d_{3/2}||T^1||4p_{3/2}\rangle\right|^2}{E_{3d_{3/2}} - E_{4p_{3/2}} - \frac{i}{2}\gamma_{3d_{3/2}} - \omega} \\
& + \frac{1}{6} \cdot \left(\rho^{(3/2)}_{3/2;\,3/2} + \rho^{(1/2)}_{3/2;\,3/2}\right) \cdot \frac{\hat{\mathcal{E}}(\omega)\left|\langle 3d_{5/2}||T^1||4p_{3/2}\rangle\right|^2}{E_{3d_{5/2}} - E_{4p_{3/2}} - \frac{i}{2}\gamma_{3d_{5/2}} - \omega}
\end{aligned} \tag{6.48}$$

In this case the coherences drop out and other transitions reduce to simple traces. It would be interesting to experimentally verify that indeed no coherence effect is present for this angle and there is no absorption dependence on the delay between the pump and the probe pulse. Because of the lack of coherence the three absorption lines act independently so we can get partial information about the density matrix by using the ordinary Beer-Lambert law. Indeed

$\hat{P}^{(1)}(\omega)$ is perfectly proportional to $\hat{\mathcal{E}}(\omega)$ for this angle. Note that there are two independent ways to measure the quantity $\rho^{(3/2)}_{3/2;\,3/2} + \rho^{(1/2)}_{3/2;\,3/2}$, which could serve as a consistency check.

6.3 How Coherence breaks Beer's Law

The Beer-Lambert law, i.e. the exponential decay of light intensity with distance, travelling through a homogeneous absorbing medium, is well known to be violated for dense media (due to scattering and screening) [51] and in nonlinear optics [52][53]. However, our focus here is on linear optics in dilute gases where this law can be broken[35] in the case of coherently prepared cations. This is due to the fact that the off-diagonal induced dipole response (in frequency space) can not be ignored in the coherent case.

In this chapter we present new results on the effects of coherence on absorption and the breaking of the Beer-Lambert law. We solve the transient absorption of a probe pulse travelling through a gas of Kr II cations, based on the induced polarization Equation (6.46) and the propagation Equation (6.8). Under the assumption of well resolved lines, i.e. that decay rate parameters are much smaller than the separations between resonances, we devise a method that derives the influence of absorption lines on one-another resulting in absorption profiles that are a linear mix of different spatially decaying exponentials, rather than one pure exponential as would be the case for Beer-Lambert spatial decay.

We investigate the practical consequences of our results on how coherent attosecond experimental absorption data should be interpreted.

6.3.1 Coherent Absorption

Note how Equation (6.28) simplifies in the case that ρ is incoherent

$$\hat{P}^{(1)}_{\text{incoh}}(\omega > 0) = \sum_{fb} \rho_{bb} |D_{fb}|^2 \frac{\hat{\mathcal{E}}(\omega)}{(E_f - E_b - \frac{1}{2} i\gamma_f) - \omega} \tag{6.49}$$

and in this case we see that the induced polarization is directly proportional to the electric field in ω space, while this is not true for the coherent case, which is a crucial difference.

The induced polarization Equation (6.28) displays resonances at

$$\omega_{fc} = E_f - E_c \tag{6.50}$$

these show up as absorption lines. They are well separated because the minimum distance for the Kr II levels we study is 0.6 eV, which is much larger than the Auger decay rate of 88 meV.

Under the assumption of well separated resonances we rewrite Equation (6.28) as follows, assuming positive ω,

$$\hat{P}^{(1)}(\omega_{fc} + \delta\omega) = \sum_{fbc} D_{fb}\rho_{bc}D_{cf}\frac{\hat{\mathcal{E}}(\omega_{fb} + \delta\omega)}{-\delta\omega - \frac{1}{2}i\gamma_f} \tag{6.51}$$

or better yet

$$\hat{P}^{(1)}_{fc}(\delta\omega) = -\frac{D_{cf}}{\delta\omega + \frac{1}{2}i\gamma_f}\sum_b D_{fb}\,\rho_{bc}\,\hat{\mathcal{E}}_{fb}(\delta\omega) \tag{6.52}$$

where $\hat{P}^{(1)}_{fc}(\delta\omega) = \hat{P}^{(1)}(\omega_{fc} + \delta\omega)$ and $\hat{\mathcal{E}}_{fb}(\delta\omega) = \hat{\mathcal{E}}(\omega_{fb} + \delta\omega)$. The interpretation is that all absorption lines ω_{fc} talk to each-other via the off-diagonal coherences of the density matrix. Rewriting the propagation Equation (6.8)

$$\partial_x\hat{\mathcal{E}}(x, \omega_{fc} + \delta\omega) = \tfrac{i}{2}\mu_0 c(\omega_{fc} + \delta\omega)\hat{P}^{(1)}(x, \omega_{fc} + \delta\omega) \tag{6.53}$$

or

$$\begin{aligned}\partial_x\hat{\mathcal{E}}_{fc}(\delta\omega) &= \tfrac{i}{2}\mu_0 c(\omega_{fc} + \delta\omega)\hat{P}^{(1)}_{fc}(x, \delta\omega) \\ &= -\tfrac{i}{2}\mu_0 c D_{cf}\left(\frac{\omega_{fc} + \delta\omega}{\frac{i}{2}\gamma_f + \delta\omega}\right)\sum_b D_{fb}\,\rho_{bc}\,\hat{\mathcal{E}}_{fb}(\delta\omega)\end{aligned} \tag{6.54}$$

So for each excited level f that has electric dipole interactions with low lying states, indicated by the indices b and c, we see that for the resonances between that excited state and those

low lying states the spatial evolution of the corresponding spectral components of the electric field are coupled by the coherences of the original density matrix.
The coupled spatial evolution is solvable as follows. Consider the matrix M, defined as

$$M_{cb}(\delta\omega) = \tfrac{i}{2}\mu_0 c D_{cf} \left(\frac{\omega_{fc} + \delta\omega}{\frac{i}{2}\gamma_f + \delta\omega} \right) D_{fb}\, \rho_{bc} \tag{6.55}$$

This matrix has eigenvalues $\lambda^{(n)}$ (which are complex), right-eigenvectors $\xi^{(n)}$ and left-eigenvectors $\eta^{(n)}$ so $M\xi^{(n)} = \lambda^{(n)}\xi^{(n)}$ and $\eta^{(n)}M = \lambda^{(n)}\eta^{(n)}$, where we choose that the left and right-eigenvectors are ortho-normalized with respect to each other. Because we keep $\delta\omega$ fixed, pick f constant and let the index c run over the low-lying states, we can interpret $\hat{\mathcal{E}}_{fc}(\delta\omega)$ as a vector. This vector can be decomposed as follows

$$\begin{aligned} \hat{\mathcal{E}}_f(\delta\omega) &= \sum_n a_n\, \xi^{(n)} \\ a_n &= \eta^{(n)} \cdot \hat{\mathcal{E}}_f(\delta\omega) \end{aligned} \tag{6.56}$$

where the a_n are the decomposition coefficients, and the index n runs over all eigenvectors of which there as many as there are low-lying states that couple to the excited state f.
We can decouple the spatial propagation equation by writing it in terms of these coefficients

$$\partial_x a_n = -\lambda^{(n)} a_n \tag{6.57}$$

with solution

$$a_n(x) = a_n(x{=}0)\; e^{-\lambda^{(n)} x} \tag{6.58}$$

The electric field in ω space can be reconstructed from these coefficients.

$$\boxed{\hat{\mathcal{E}}_{fc}(\delta\omega, x) = \sum_{nb} \eta_b^{(n)} \xi_c^{(n)}\, \hat{\mathcal{E}}_{fb}(\delta\omega, x{=}0)\; e^{-\lambda^{(n)} x}} \tag{6.59}$$

The conclusion is that in contrast to the incoherent case, where Beer's law applies and where the electric field decays spatially by exactly one exponential, for the coherent case we see that the electric field decays as a linear mix of exponentials.

When the diagonal elements of the density matrix dominate and the coherences are small the result will be decay of the electric field that is very close to Beer's law. However, when significant coherence is present very interesting phenomena can be observed such as how the phase of the coherence can cause either increased or decreased absorption and also the possibility of electric field revivals at one resonance due to the interaction with another resonance.

Using numerical estimates for the density matrix from Goulielmakis [2] we shall now compute these coherence effects. The ground state $4p_{3/2}$ has a degeneracy of 4 with $m \in \{-3/2, -1/2, 1/2, 3/2\}$ and $4p_{1/2}$ has a degeneracy of 2 with $m \in \{-1/2, 1/2\}$. See our discussion on ionization symmetry in Section 5.1.1. Let us now focus on the centers of the absorption lines, so pick $\delta\omega = 0$. Then

$$M_{cb} = \mu_0 c \frac{\omega_{fc}}{\gamma_f} D_{cf} D_{fb} \rho_{bc} \tag{6.60}$$

We now use the matrix elements worked out in Equation (6.46) to determine M.

The higher state $3d_{5/2}$ only couples to lower state $4p_{3/2}$ so the M matrix has a simple one by one sub-matrix representing this absorption line. Using the shorthand s for $\sin\phi$, where ϕ is the angle between the polarizations of the probe and pump pulses, we find

$$M^{(5/2)} = \frac{\mu_0 c n^+}{\gamma}(E_{3d_{5/2}} - E_{4p_{3/2}}) \cdot \frac{1}{30} \cdot \left((4+\tfrac{3}{2}s^2)\,\rho^{(3/2)}_{3/2;\,3/2} + (6-\tfrac{3}{2}s^2)\,\rho^{(1/2)}_{3/2;\,3/2}\right) \cdot \left|\langle 3d_{5/2}||T^1||4p_{3/2}\rangle\right|^2 \tag{6.61}$$

The higher state $3d_{3/2}$ couples to both lower states $4p_{3/2}$ and $4p_{1/2}$ and thus the M matrix has a two by two sub-matrix, describing these two absorption lines. In our notation for M the subscripts indicate the lower states and the superscript indicates the high state

$$
\begin{aligned}
M^{(3/2)}_{\frac{1}{2},\frac{1}{2}} &= \frac{\mu_0 c n^+}{\gamma}(E_{3d_{3/2}} - E_{4p_{1/2}}) \cdot \frac{1}{3} \cdot \rho^{(1/2)}_{1/2;\,1/2} \cdot \left|\langle 3d_{3/2}||T^1||4p_{1/2}\rangle\right|^2 \\
M^{(3/2)}_{\frac{3}{2},\frac{3}{2}} &= \frac{\mu_0 c n^+}{\gamma}(E_{3d_{3/2}} - E_{4p_{3/2}}) \cdot \frac{1}{30} \cdot \left((9-6s^2)\,\rho^{(3/2)}_{3/2;\,3/2} + (1+6s^2)\,\rho^{(1/2)}_{3/2;\,3/2}\right) \cdot \left|\langle 3d_{3/2}||T^1||4p_{3/2}\rangle\right|^2 \\
M^{(3/2)}_{\frac{3}{2},\frac{1}{2}} &= \frac{\mu_0 c n^+}{\gamma}(E_{3d_{3/2}} - E_{4p_{3/2}}) \cdot \frac{\sqrt{10}}{30} \cdot (1-\tfrac{3}{2}s^2)\,\rho^{(1/2)*}_{3/2;\,1/2} \cdot \langle 3d_{3/2}||T^1||4p_{1/2}\rangle\langle 4p_{3/2}||T^1||3d_{3/2}\rangle \\
M^{(3/2)}_{\frac{1}{2},\frac{3}{2}} &= \frac{\mu_0 c n^+}{\gamma}(E_{3d_{3/2}} - E_{4p_{1/2}}) \cdot -\frac{\sqrt{10}}{30} \cdot (1-\tfrac{3}{2}s^2)\,\rho^{(1/2)}_{3/2;\,1/2} \cdot \langle 3d_{3/2}||T^1||4p_{3/2}\rangle\langle 4p_{1/2}||T^1||3d_{3/2}\rangle
\end{aligned}
\tag{6.62}
$$

Note that for $M^{(5/2)}$ we have summed over the contributions from $m=3/2$, $m=1/2$, $m=-1/2$ and $m=-3/2$, while for $M^{(3/2)}$ we have summed over the contributions from $m=1/2$ and $m=-1/2$.

6.3.2 Computation of Coherent Absorption

The reduced matrix elements we use are based on GRASP calculations [2]

$$
\begin{aligned}
\langle 3d_{5/2}||D||4p_{3/2}\rangle &= \;\; 0.345 \text{ a.u.} \\
\langle 3d_{3/2}||D||4p_{3/2}\rangle &= -0.112 \text{ a.u.} \\
\langle 3d_{3/2}||D||4p_{1/2}\rangle &= \;\; 0.264 \text{ a.u.}
\end{aligned}
\tag{6.63}
$$

We get the matrix transition dipole matrix elements by applying the Wigner-Eckart factors, see Appendix E. For ρ we use the values derived by Goulielmakis *et al.* from experiment [2]

$$
\begin{aligned}
\rho^{(3/2)}_{3/2,3/2} &= 0.115\, n^+ \\
\rho^{(1/2)}_{3/2,3/2} &= 0.210\, n^+ \\
\rho^{(1/2)}_{1/2,1/2} &= 0.175\, n^+ \\
|\rho^{(1/2)}_{3/2,1/2}| &= 0.120\, n^+
\end{aligned}
\tag{6.64}
$$

where n^+ is the number density of the cations, which is also the trace of the density matrix. Using these values we get

$$M = \mu_0 c n^+ \begin{pmatrix} 6.19\,(1-0.083s^2) & 0 & 0 \\ 0 & 3.72 & 0.342\,(1-\frac{3}{2}s^2)\,e^{i\alpha} \\ 0 & -0.345\,(1-\frac{3}{2}s^2)\,e^{-i\alpha} & 0.481\,(1+0.468s^2) \end{pmatrix} \tag{6.65}$$

where the three dimensions of the matrix M are given by the three absorption lines $4p_{3/2} \to 3d_{5/2}$, $4p_{1/2} \to 3d_{3/2}$ and $4p_{3/2} \to 3d_{3/2}$. The first absorption line is independent and will follow the Beer-Lambert law. The latter two, however, interact due to coherence and have much more interesting absorption behavior.

In order to start calculations we need to have the initial values of the spectral components $\hat{\mathcal{E}}(\omega)$ at the center of each absorption line. The lines are all around 80 eV and lie within an interval of 1.3 eV. We will assume that the probe pulse is centered roughly around 80 eV and that its spectral width is substantially larger that 1.3 eV, i.e. that the pulse is very short. Goulielmakis *et al.* [2] use $\sim$ 80 eV central energy, $\sim$ 15 eV bandwidth for a sub 150 as pulse. This allows us to choose the three initial $\hat{\mathcal{E}}(\omega)$ the same in size. Of course, these cannot stay equal when the probe pulse propagates through the absorbing cation gas. We will also choose them to be in phase initially, for convenience. Choosing differing phases is not an issue (propagation in empty space would already cause that) but the only effect this has on the absorption results below is that coherence phase will be offset by a constant angle. Figure (6.1) is computed from our analytical solution for the absorption line and illustrates how the Beer-Lambert law is broken. On the x-axis we give the depth, in arbitrary units, which is proportional to the density of the cation gas and the distance travelled within that gas. On the y-axis we give the absorbance, which is defined as

$$A(x,\omega) = -\ln(I(x,\omega)/I(0,\omega)) \tag{6.66}$$

where x is the distance travelled and where the intensity $I(x,\omega)$ is proportional to $|\hat{\mathcal{E}}(x,\omega)|^2$. The three black lines show the incoherent case (thus Beer-Lambert compliant) for the ab-

sorption lines $4p_{3/2} \rightarrow 3d_{5/2}$, $4p_{1/2} \rightarrow 3d_{3/2}$ and $4p_{3/2} \rightarrow 3d_{3/2}$, where the first one is the steepest and the last one is the flattest. In the presence of coherence we see that the first line is not affected but the latter two are materially dependent on the size and phase of the coherence term. We show the coherence phases 0° (blue) through 180° (red) in steps of 45°. It is quite apparent that coherent absorption is dependent on the size of the coherence term, the phase of the coherence term and on the depth in interesting ways. The depth, as used in Figure (6.1) is not a very practical measure so we will now move to a more prudent basis for absorbance comparison. The coherence term is an off-diagonal density matrix element that phase rotates in time due to the energy difference between the $4p_{1/2}$ and $4p_{3/2}$ levels. Therefore, the intensity measured is periodic in the probe pulse delay time. As a point of comparison which can be readily determined from experimental data, we average the intensity over one or several cycles and use the absorbance of this average as our reference, see Figures (6.2) and (6.3). Note, due to the structure of the M matrix, that within our model this averaged intensity is exactly the same as the intensity derived for the 90° (or 270° if you wish) coherence phase.

In Figure (6.2) we analyze our absorption model for the case of the Kr II $4p_{1/2} \rightarrow 3d_{3/2}$ line. On the x-axis we show the absorbance for the probe pulse delay averaged intensity, while on the y-axis we show the ratio between the absorbance for a particular coherence phase and the absorbance of the averaged intensity. We show the coherence phases 0° (blue) through 180° (red) in steps of 45°. Note that the quantities on both axes are dimensionless and readily computed from experimental absorption data. Note that the 90° coherence phase (purple) absorbance is indeed identical to the absorbance of the averaged intensity.

We see that for shallow absorbance the absorbances vary as much as 10% due to the coherence angle. For deep absorbance we see the interesting effect of extinction, i.e. the electric field for this transition ω went to zero, and subsequent revival. This is because the lines interact and there is an exchange of energy across the spectrum. The electric field at frequency $4p_{1/2} \rightarrow 3d_{3/2}$ feeds on the frequency at $4p_{3/2} \rightarrow 3d_{3/2}$ to revive itself. All this, however, happens at a deep absorbance of around 4.6 which means at an average intensity of around 1%, which is a regime that is hard to access with any experimental accuracy. In practice

absorbances are kept below 1.

Figure (6.3) is the most relevant as this line is the most useful for calculating the implied coherence term. The explanation for the axes and the graphs is equivalent to the previous figure. Note how strongly the absorbance depends on the coherence phase and note how strongly this effect decays with increasing absorbance of the averaged intensity. The large contrast in absorbances for different coherence phases is, of course, very helpful in calculating the coherence term from fits to experimental data. But there is a large caveat. In [2] the naive approximation is used to force the induced polarization to be proportional to the electric field (in ω space, that is). This leads directly the Beer-Lambert law and allows for the computation of a cross-section formula.

However, their formula is only accurate in the limit of zero absorbance. Figure (6.2) shows how important the distinction is. When using the naive formula, but conducting the experiment at an absorbance of averaged intensity at around 0.15 (typical of the Goulielmakis *et al.* experiment [2]) you would underestimate the actual coherence term size by around 20%, as can be seen in Figure (6.3), where we use the fact that the absorbance dependence on the coherence size is near linear. The problem of Beer-Lambert law breaking was later realized by [35] where a full numerical simulation across the spectrum was undertaken to get an idea of its effect on implied density matrix elements. They found that the coherence term had been underestimated and upgraded their estimation of $|\rho^{(1/2)}_{3/2;1/2}|$ from 0.12 to 0.14, which is consistent with the correction predicted with our analytical model for coherent absorption and Beer-Lambert law breaking. Note what happens when we move to deeper absorbance. Say we would like to measure the $4p_{3/2} \rightarrow 3d_{3/2}$ line when 50% of its delay averaged intensity is absorbed, i.e. an absorbance of 0.693. Figure (6.3) then shows that the naive model underestimates the coherence term by a factor of 2.5, so the correction can become very large, even for experimentally reasonable absorbances.

Finally, although we have only used a probe versus pump polarization of 0° in the absorbance graphs so far, it must be realized that our coherent absorption model is richer still because we can also explore the dependence on this polarization angle. In Figure (6.4) we plot relative absorbances for the Kr II $4p_{3/2} \rightarrow 3d_{3/2}$ line. In order to make meaningful comparisons we

have calibrated the absorbance of the delay averaged intensity to be exactly at 0.2. Note how the polarization angle 0° is best experimentally because it has the highest contrast. Note how the pump-probe delay dependence disappears in Equation (6.46) at 54.7°. This 'magic angle' also has special significance in other fields, such as nuclear magnetic resonance spectroscopy. The $4p_{3/2} \rightarrow 3d_{5/2}$ and $4p_{1/2} \rightarrow 3d_{3/2}$ lines also have polarization dependence but these are weaker in proportion.

6.3.3 Implied Density Matrix Elements

We have seen that the naive Beer-Lambert law can be far off the mark in the presence of coherence, and that a more careful analysis is called for. Naive modelling only proved accurate enough for very shallow absorption of at most a few percent. In a practical range of absorbances, usually from 0.1 to 1.0 or so, we need to take coherence effects fully into account. Using the naive formula can lead to under- or overestimation of implied density matrix elements, depending on the absorption line. In the case of deep absorbance the interaction between lines can lead to extinctions and revivals. We have developed an analytical model to describe the evolution of the electric field spectral components as a complex linear mix of exponentials.

In practice one should use the polarization angle at 54.7°, verify the absence of probe delay time dependence, verify the applicability of the Beer-Lambert law in this case and compute the diagonal density matrix elements. Varying the polarization angle and collecting absorption data based on delay averaged intensity from all three lines leads to an over-complete set of information about the diagonal density matrix elements which is good for numerical accuracy but also an experimental test of the assumptions behind the model. Once the diagonal elements are known, then use the Kr II $4p_{3/2} \rightarrow 3d_{3/2}$ line to compute the implied coherence term, utilizing our coherent absorption model and the method of relative absorbance rates. A small number of iterations should suffice.

6.4 Conclusion

In this chapter we derive how an XUV probe pulse propagates through a medium of ionized krypton gas taking coherence effects into account. First we derived the induced dipole response to lowest order in perturbation theory and discussed its application to propagation when using the naive Beer-Lambert law. We then explicitly computed the induced dipole in terms of the Kr II transitions shown in Figure (5.1) and we give the explicit dependence on the angle between the polarization of the probe pulse and that of the pump pulse. Using this induced dipole formula we investigated the effect of coherence on XUV propagation through the ionized gas and found that the naive Beer-Lambert law is broken, a fact that is important for the interpretation of experimental absorption results.

The results of this chapter can guide future experiments in the following way. Assuming an experiment of the type performed by Goulielmakis *et al.*[2] one could first test for the predicted absorption dependence on the probe-pump polarization angle, especially checking that coherence effects disappear at 54.7°. Furthermore, using data from a set of angles should reduce errors in the implied density matrix elements.

The coherence effects on propagation can be tested by having both pump and probe pulse polarized in the z-direction, varying the delay time between probe and pump from 0 to 30 fs (to cover enough coherence cycles), and varying the density of Kr II atoms or path length to explore a range of absorbances. It is easiest to investigate the Kr II $4p_{3/2} \rightarrow 3d_{3/2}$ transition because it requires lower absorbances (compared to Kr II $4p_{1/2} \rightarrow 3d_{3/2}$) to see coherent absorption effects. Absorbances in the range of 0.0 - 1.2 should be studied. Note that Figure (6.3) predicts how the relative amplitude of the absorbance (and thus the contrast throughout the coherence cycle) falls off the higher the cation density-distance. This is also why applying the naive Beer-Lambert law to absorption data tends to underestimate the actual coherences in the density matrix because the naive absorption formulae are only valid in the zero absorbance limit.

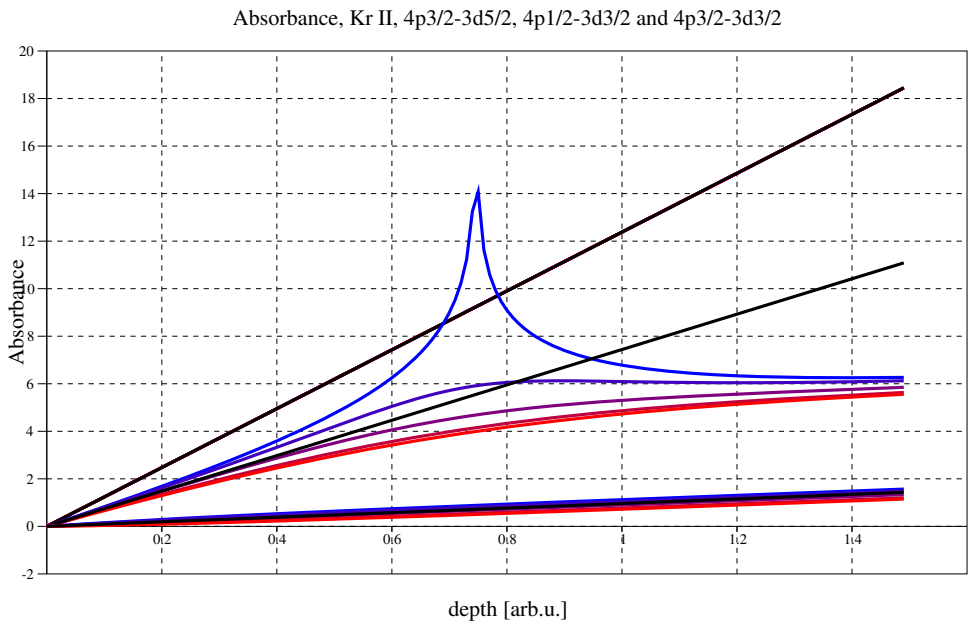

Figure 6.1: Absorbance of three absorption lines of Kr II. The three black lines represent the incoherent case, and thus following the Beer-Lambert law, in the order from steepest to flattest they are the lines $4p_{3/2} \rightarrow 3d_{5/2}$, $4p_{1/2} \rightarrow 3d_{3/2}$ and $4p_{3/2} \rightarrow 3d_{3/2}$. When coherence is present the latter two lines are dependent on the phase of the coherence term. We show the phases 0° (blue) through 180° (red) in steps of 45°. The probe polarization used here is 0°.

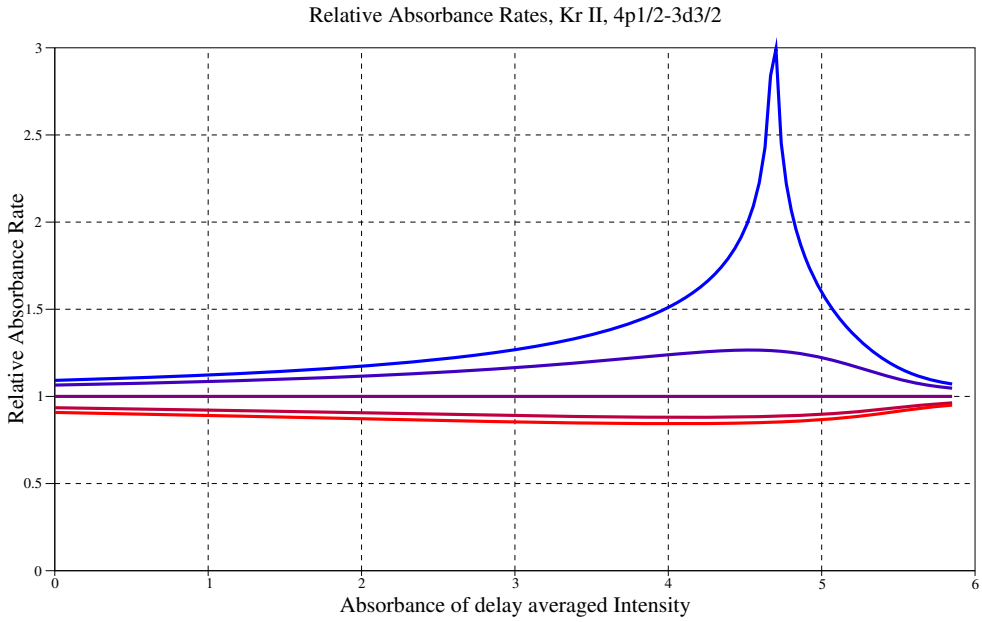

Figure 6.2: Relative absorbance of the Kr II $4p_{1/2} \rightarrow 3d_{3/2}$ line. Due to coherence the intensity is periodic in the probe delay time. This intensity is phase averaged and the absorbance derived from this is given as a practical reference on the x-axis. On the y-axis we plot the ratio of absorbance for a given coherence phase versus the absorbance of the delay averaged intensity. We show the coherence phases 0° (blue) through 180° (red) in steps of 45°. Note the dependence of the relative absorbance on the coherence phase and the phenomenon of extinction and revival in deep coherent absorption. The probe polarization used here is 0°.

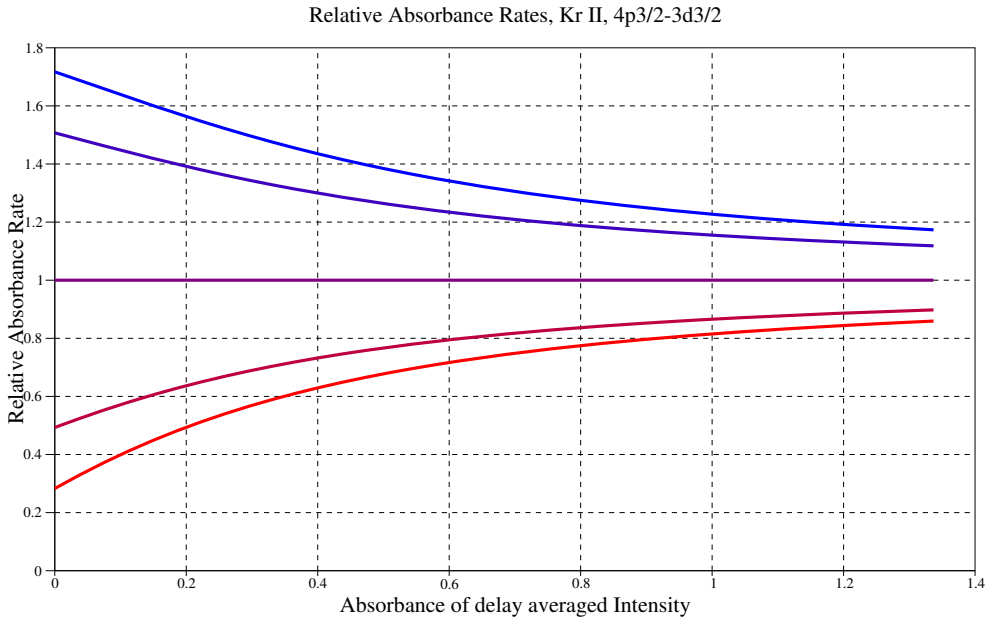

Figure 6.3: Relative absorbance of the Kr II $4p_{3/2} \rightarrow 3d_{3/2}$ line. Due to coherence the intensity is periodic in the probe delay time. This intensity is phase averaged and the absorbance derived from this is given as a practical reference on the x-axis. On the y-axis we plot the ratio of absorbance for a given coherence phase versus the absorbance of the delay averaged intensity. We show the coherence phases 0° (blue) through 180° (red) in steps of 45°. Note the strong dependence of relative absorbance on both the coherence phase and the absorbance level. The probe polarization used here is 0°.

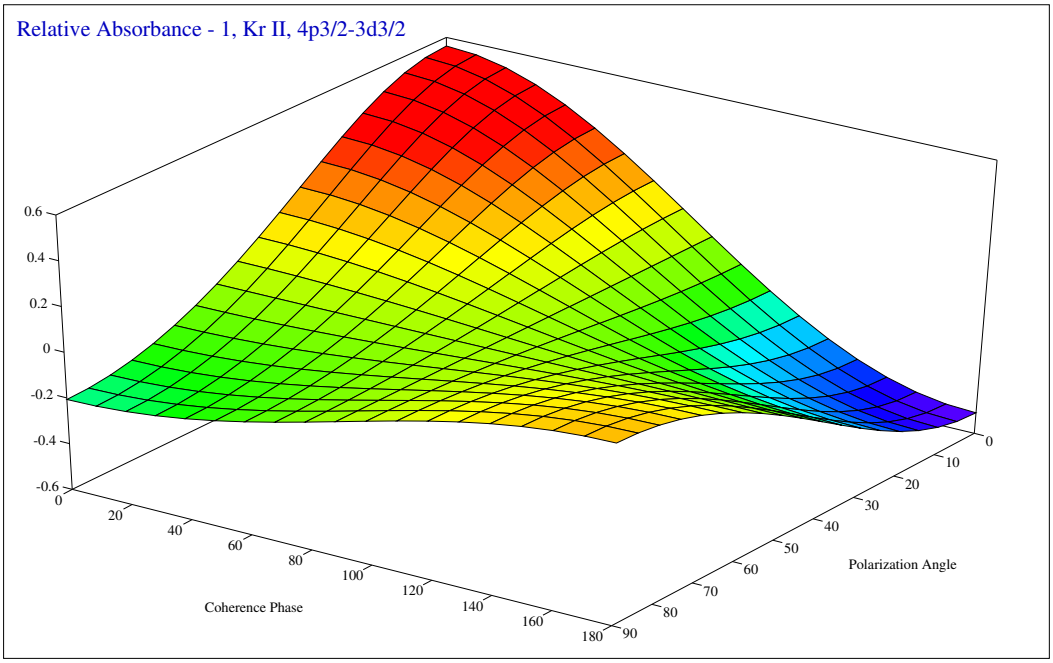

Figure 6.4: Relative absorbance, minus one, of the Kr II $4p_{3/2} \rightarrow 3d_{3/2}$ line for varying probe versus pump polarization angle and varying coherence phase. The absorbances are relative to the absorbance of the delay averaged intensity, which has been calibrated at 0.2. Note how the absorbance contrast across different coherence phases is best for polarization angle 0°, how the contrast disappears at angle 54.7°, and how it comes back again for larger angles. Note the effect at 90° polarization is weaker and opposite in sign compared to 0°.

Chapter 7

Attosecond Dynamics of Molecules

We extend our investigation of atomic attosecond physics to the computationally much more challenging dynamics of molecules. We perform copious simulations modelling photoexcitation and photoionization effects in N_2, benzene and naphthalene. We first describe recent experimental results regarding NIR pulse induced time-dependent molecular dipoles probed with attosecond timescale XUV pulses and we assess the regime of the applicability of the adiabaticity approximation. Second, we provide the Born-Fock derivation of the adiabatic approximation and examine adiabaticity in low-order perturbation theory, both far from and close to resonance, and we study when the induced dipole moment can be expected to be close to linear to the pump electric field. Third, we discuss the theory and numerical techniques behind our simulation of attosecond molecular dynamics, consisting of a description of Algebraic Diagrammatic Construction (ADC) and Lanczos-Arnoldi Time Propagation of the time-dependent Schrödinger equation. We use software packages developed by Averbukh *et al.*[54]

Finally, we present simulation results for N_2, benzene and naphthalene for pump wavelengths of 400 nm, 800 nm, and 1.6 μm, multiple polarization choices and at intensities ranging from 5×10^{12} - 5×10^{14} W/cm^2. We discuss our results and further work.

7.1 Recent Experimental Work

Recent results reported by MBI (Max Born Institute for Nonlinear Optics and Short Pulse Spectroscopy) in Berlin under the supervision of Vrakking [55] demonstrated experimentally electronic dynamics on attosecond scale for N_2, CO_2, and C_2H_4. In these experiments molecules were dressed by an 800 nm NIR pump pulse which caused a time-dependent induced dipole which, in turn, was probed by a 300 as XUV pulse of 35 eV central energy. Please note that in these experiments the probe pulse, while being much shorter than the pump pulse, happens during the pump pulse so they are overlapping in time. The experiments showed that the distortion of the electron cloud consistent with the induced time-dependent dipole leads to an ionization yield which is dependent on the phase of the electric field at the central time of the probe pulse. By changing the timing of the probe pulse, fluctuations in the ionization yield are seen with a periodicity half of that of the pump pulse as expected, corresponding to the extrema of the pump electric field. We can understand why, under the assumption of non-resonant pumping, that adiabaticity is a good approximation in these experiments because the NIR pump is relatively weak at 10^{12} W/cm^2 and the pump photon energy of 1.55 eV is well below ionization energy around 10 eV, so we can expect nonlinearities to be small and the induced dipole to be a nearly linear and nearly in phase with the dressing pump laser field. However, if a given molecule were to have a resonance near 1.55 eV, then the phase relationship between the induced dipole and the pump field would shift, but the periodicity in the ionization yield would not be materially affected.

The question then arises, for exploring attosecond dynamics of molecules with the typical NIR laser field intensities which are available, around 10^{14} W/cm^2, does adiabaticity still apply?

While during the pump pulse the induced dipole response can still be dominated by a contribution linear in the pump electric field, decidedly non-adiabatic effects will be seen for these higher intensities (and shorter pump wavelengths) to the excitation probabilities and the ionization yields. The clearest non-adiabatic effects can be seen post the pump pulse as evidenced in the ringing of the molecules due to the excited states and the depletion of the

ground state.

7.2 The Born-Fock Adiabatic Approximation

We derive the Born-Fock adiabatic law [56] [57] [58] and study when it does and does not apply. Consider a time dependent Hamiltonian $H(t)$ which we assume to have, for convenience, a discrete and non-degenerate spectrum at all times. The Hamiltonian has a time-dependent orthonormal eigen-basis $|n(t)\rangle$ which means $H(t)|n(t)\rangle = E_n(t)|n(t)\rangle$, where E_n are time-dependent energy eigen-values, and $\langle m(t)|n(t)\rangle = \delta_{mn}$. We will drop the explicit time dependence notation from this point. Because $\langle n|n\rangle = 1$ we derive by applying a time derivative that $\langle \dot{n}|n\rangle + \langle n|\dot{n}\rangle = 0$, in other words $\langle n|\dot{n}\rangle$ is purely imaginary. However, normalized eigenfunctions are only determined up to a phase so for $|n\rangle \to e^{i\alpha}|n\rangle$ we have $\langle n|\dot{n}\rangle \to \langle n|\dot{n}\rangle + i\dot{\alpha}$. This means we have the freedom to choose the angle $\alpha(t)$ such that

$$\langle n|\dot{n}\rangle = 0 \tag{7.1}$$

We can decompose any wave-function in the following suggestive way

$$|\Psi\rangle = \sum_n c_n e^{i\theta_n}|n\rangle \tag{7.2}$$

where the coefficients c_n are time-dependent and the angles are defined as $\theta_n = -\int_0^t E_n(t')dt'$. Writing out the Schrödinger equation $i\dot{\Psi} = H\Psi$ we get

$$|\dot{\Psi}\rangle = \sum_n \left((\dot{c}_n - iE_n c_n)e^{i\theta_n}|n\rangle + c_n e^{i\theta_n}|\dot{n}\rangle\right) = -iH|\Psi\rangle = \sum_n -ic_n E_n e^{i\theta_n}|n\rangle \tag{7.3}$$

so

$$\sum_n \dot{c}_n e^{i\theta_n}|n\rangle = -\sum_n c_n e^{i\theta_n}|\dot{n}\rangle \tag{7.4}$$

and applying $\langle k|$ from the left gives

$$\dot{c}_k = -\sum_n c_n e^{i(\theta_n - \theta_k)} \langle k|\dot{n}\rangle \tag{7.5}$$

From $H|n\rangle = E_n|n\rangle$ we have $\dot{H}|n\rangle + H|\dot{n}\rangle = \dot{E}_n|n\rangle + E_n|\dot{n}\rangle$. Again, applying $\langle k|$ from the left provides $\langle k|\dot{H}|n\rangle + E_k\langle k|\dot{n}\rangle = \dot{E}_n\delta_{kn} + E_n\langle k|\dot{n}\rangle$, which means that for $k \neq n$ we have $\langle k|\dot{n}\rangle = \langle k|\dot{H}|n\rangle/(E_n - E_k)$. Remembering that we choose $\langle n|\dot{n}\rangle = 0$ we can now write

$$\dot{c}_k = \sum_{n\neq k} c_n e^{i(\theta_n - \theta_k)} \frac{\langle k|\dot{H}|n\rangle}{(E_k - E_n)} \tag{7.6}$$

Note that we have made no approximation up to this point at all and the equation above is exactly equivalent to the Schrödinger equation. The conclusion is that even if the change in Hamiltonian is large, as long as it takes enough time to affect this change ($\dot{H}$ is small compared to the energy gap) then $\dot{c}_k$ is small and the population will stay (largely) in its eigenstate. Even when there is degeneracy the argument still works as long as $\langle n_1|H|n_2\rangle = 0$ for degenerate states n_1 and n_2.

7.3 Adiabaticity in Perturbation Theory

In order to understand the distinction between adiabaticity and diabaticity better we now turn to perturbation theory. We work with a time independent free Hamiltonian H_0 and a time dependent perturbing Hamiltonian $\delta H(t)$. In the Schrödinger picture

$$i|\dot{\Psi}(t)\rangle = (H_0 + \delta H(t))|\Psi(t)\rangle \tag{7.7}$$

We solve to second order in perturbation theory

$$|\Psi\rangle = e^{-iH_0 t}\left(1 - i\int_0^t dt_1 \delta H_I(t_1) - \int_0^t dt_2 \delta H_I(t_2)\int_0^{t_2} dt_1 \delta H_I(t_1) + \mathcal{O}(\delta H^3)\right)|0\rangle \tag{7.8}$$

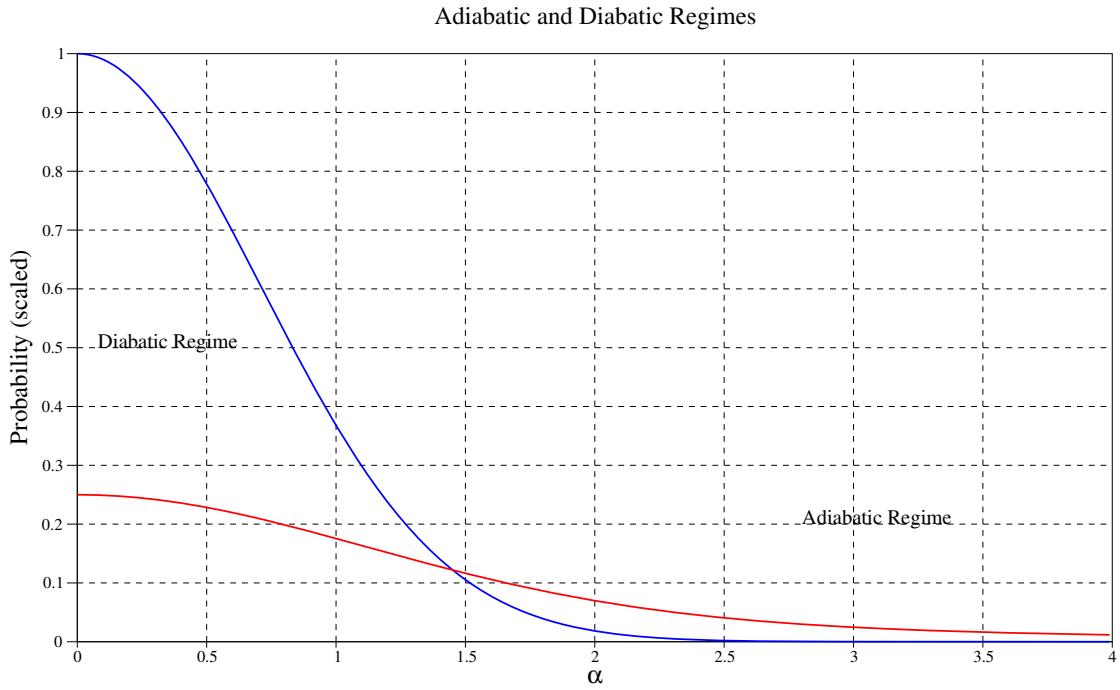

Figure 7.1: Illustration of diabatic versus adiabatic regimes by means of buildup of the excited population by a Gaussian driving pulse in a simple two-level system, computed to second order in perturbation theory. On the y-axis we show the probability of the excited state, with its maximum value rescaled to one. On the x-axis we show α which is a measure of distance from resonance. The blue curve is the excited population after the pulse, while the red curve is the excited population midway the pulse. In the diabatic regime we see resonant driving of the excited population, while in the adiabatic regime we see non-resonant population build-up with subsequent cancellation in the latter half of the pulse.

where $\delta H_I(t) = e^{iH_0 t}\delta H(t)e^{-iH_0 t}$ is the perturbing Hamiltonian in the interaction picture. Assuming electric dipole interaction we have that $\delta H_{00} = 0$ so the probability of staying in the ground state is

$$
\begin{aligned}
P_{00} = |\langle 0|\Psi\rangle|^2 &= 1 - \langle 0| \left(\int_0^t dt' \delta H(t') \right)^2 |0\rangle + \mathcal{O}(\delta H^4) \\
&= 1 - \sum_{n=1}^{\infty} \left| \int_0^t dt' e^{i(E_n - E_0)t'} \delta H_{n0}(t') \right|^2 + \mathcal{O}(\delta H^4) \\
&= 1 - \sum_{n=1}^{\infty} |D_{n0}|^2 \left| \int_0^t dt' e^{i(E_n - E_0)t'} f(t') \right|^2 + \mathcal{O}(f^4)
\end{aligned} \tag{7.9}
$$

where in the last line we have specialized to the electric dipole interaction $\delta H(t) = -f(t)D$, with $f(t \leq 0) = 0$. Notice that the third order term is zero which is a consequence of parity change of the dipole interaction.

We can use this result to understand how resonant and non-resonant pulse fields $f(t)$ drive the excitation out of the ground state and we can compare the excited population halfway through the pulse and after the pulse. Assuming a Gaussian pulse, and shifting the origin of time far to the left for a moment, the integrals involved are of the type

$$
\begin{aligned}
\int_{-\infty}^{\infty} dt\, e^{-\frac{1}{2}t^2 + i\alpha t} &= \sqrt{2\pi} e^{-\frac{1}{2}\alpha^2} \\
\int_{-\infty}^{0} dt\, e^{-\frac{1}{2}t^2 + i\alpha t} &= e^{-\frac{1}{2}\alpha^2} \int_{-\infty}^{0} dt\, e^{-\frac{1}{2}(t - i\alpha)^2} = e^{-\frac{1}{2}\alpha^2} \int_{-\infty}^{-i\alpha} dt\, e^{-\frac{1}{2}t^2} \\
&= e^{-\frac{1}{2}\alpha^2} \int_{-\infty}^{0} dt\, e^{-\frac{1}{2}t^2} - i e^{-\frac{1}{2}\alpha^2} \int_0^{\alpha} dt\, e^{\frac{1}{2}t^2} \\
&= \tfrac{1}{2}\sqrt{2\pi} e^{-\frac{1}{2}\alpha^2} - i\sqrt{2} D_+(\alpha/\sqrt{2})
\end{aligned} \tag{7.10}
$$

Where D_+ is the Dawson function defined as $D_+(x) = e^{-x^2} \int_0^x dt\, e^{t^2}$ [59]. What we end up comparing are the absolute square of these amplitudes so, after normalizing by a factor 2π we are comparing $e^{-\alpha^2}$ versus $\frac{1}{4}e^{-\alpha^2} + \frac{1}{\pi} D_+^2(\alpha/\sqrt{2})$, see Figure (7.1). We can clearly see the difference between the diabatic regime where the force is resonantly driving the system and the probabilities are built up to one quarter of its final value at the midpoint of the pulse, and the adiabatic regime where the probabilities are built up but then almost completely reversed resulting in a final state almost identical to the original state. Note the asymptotic behavior for large α: $\frac{1}{4}e^{-\alpha^2} + \frac{1}{\pi} D_+^2(\alpha/\sqrt{2}) \to \frac{1}{2\pi\alpha^2}$ which is huge compared with the exponentially

suppressed final value. Note that we have seen examples of the diabatic and adiabatic regimes for the Kr II system in Figures (5.4) and (5.5) respectively.
The induced dipole is, using $D_{00} = 0$,

$$\langle\Psi|D|\Psi\rangle = -2\sum_{n=1}^{\infty}|D_{0n}|^2\int_0^t dt' f(t')\sin((E_n - E_0)(t'-t)) + \mathcal{O}(f^3) \tag{7.11}$$

where the second order term drops out due to parity. When the spectral content of $f(t)$ is far below the energy gap $E_1 - E_0$, i.e. a very slowly changing Hamiltonian, we have the expansion.

$$\langle\Psi|D|\Psi\rangle = 2\sum_{n=1}^{\infty}|D_{0n}|^2\left(\frac{f(t)}{(E_n-E_0)} - \frac{\ddot{f}(t)}{(E_n-E_0)^3} + \frac{\dddot{f}(t)}{(E_n-E_0)^5} + \cdots\right) + \mathcal{O}(f^3) \tag{7.12}$$

We obtain in this adiabatic limit the familiar result that the induced dipole is directly proportional to the driving field $f(t)$. Note that this expansion is not valid at and above resonance and does in fact diverge in that case.

The considerations in this and the previous section apply generally (if the time derivative of the electric field is small enough) and provide some insight as to the meaning of adiabaticity. The study of actual molecules is necessarily much more involved, requiring a very high number of basis wavefunctions to model a faithful representation of the response to an incident pump pulse, with the associated excitations and ionization. We will now describe the computational methods to model molecules used to find out for which level of pump intensity non-adiabaticity sets in as a function of wavelength and polarization. For the adiabatic regime we do find that the induced dipole behaves as described above.

7.4 Algebraic Diagrammatic Construction

We describe the algebraic diagrammatic construction in the intermediate state representation (ISR-ADC) [60], which was originally derived in the polarization propagator formalism [61].

The methods used here are non-relativistic and assume the vertical approximation where nuclear coordinates are static.

In this section we closely follow the exposition of ADC theory by the Averbukh group at Imperial College [65][66]. Note that we use the ADC software suite by Averbukh *et al.* [54][65][66] for the simulations in this chapter. We can create $1p1h$, $2p2h$, etc., called the correlated excited states (CES) states, like so

$$\begin{aligned} |\Psi_I^0\rangle &= \hat{C}_I^\dagger |\Psi_0\rangle \\ \hat{C}_I^\dagger &= \{\hat{a}_a^\dagger \hat{a}_i; \hat{a}_a^\dagger \hat{a}_b^\dagger \hat{a}_j \hat{a}_k \ (a<b, j<k); \dots\} \end{aligned} \tag{7.13}$$

where $|\Psi_0\rangle$ is the exact ground state of the system, and where the $\hat{a}^\dagger$ are the particle creation and $\hat{a}$ are the particle annihilation (i.e. hole creation) operators in second quantization. The subscript convention is $(a, b, c, \dots)$ for unoccupied (virtual) orbitals, $(i, j, k, \dots)$ for occupied orbitals and $(p, q, r, \dots)$ for either kind.

Note that the $|\Psi_I^0\rangle$ states are not orthonormal so it is helpful to apply the Gram-Schmidt procedure to create a more convenient set of states. First project out the components along the ground state direction from each $1p1h$ state. Then orthonormalize these adjusted $1p1h$ states among themselves. Subsequently project out the components along the ground state and the adjusted $1p1h$ states directions from the $2p2h$ states. Then we orthonormalize these adjusted $2p2h$ states among themselves. We could do this for higher and higher levels ad infinitum. The states resulting from this procedure are called "excitation class orthogonalized" (ECO-CES) and the $\hat{C}$ operators are adjusted to $\widetilde{C}$

$$|\widetilde{\Psi}_I\rangle = \widetilde{C}_I^\dagger |\Psi_0\rangle \tag{7.14}$$

These ECO-CES states are also referred to as the intermediate states. The ADC secular matrix is defined as the matrix elements of the shifted Hamiltonian $\hat{H} - E_0$ on the ECO-CES basis

$$\mathcal{H}_{IJ} = \langle \widetilde{\Psi}_I | \hat{H} - E_0 | \widetilde{\Psi}_J \rangle = \langle \Psi_0 | \widetilde{C}_I [\hat{H}, \widetilde{C}_J^\dagger] | \Psi_0 \rangle \tag{7.15}$$

Now Møller-Plesset perturbation theory is used to improve upon the Hartree-Fock ground state to better include the effects of electron-electron correlation

$$|\Psi_0'\rangle = |\Psi_0^{\mathrm{HF}}\rangle + |\Psi_0^{[1]'}\rangle + |\Psi_0^{[2]'}\rangle + |\Psi_0^{[3]'}\rangle + \dots \tag{7.16}$$

where the first order correction $|\Psi_0^{[1]'}\rangle$ contains only double excitations ($2p2h$) w.r.t. the Hartree-Fock ground state and where the second order correction contains excitations from single through quadruple [60].
We solve the eigen-problem

$$\mathcal{H}V = V\Omega, \qquad V^\dagger V = 1 \tag{7.17}$$

where Ω is a diagonal matrix whose elements are the vertical eigenvalues $E_n - E_0$ and V is a unitary matrix whose columns are the orthonormal eigenvectors, and 1 is the identity matrix. The eigenstates of this problem can now be expressed in terms of the intermediate states like so

$$|\Psi_n\rangle = \sum_I V_{I,n} |\widetilde{\Psi}_I\rangle \tag{7.18}$$

The matrix elements D_{mn} of the dipole matrix on the eigen-basis are

$$\begin{aligned} D_{mn} &= \langle\Psi_m|\hat{D}|\Psi_n\rangle = \sum_{IJ} V_{I,m}^* \mathcal{D}_{IJ} V_{J,n} \\ \mathcal{D}_{IJ} &= \langle\widetilde{\Psi}_I|\hat{D}|\widetilde{\Psi}_J\rangle = \langle\Psi_0|\widetilde{C}_I \hat{D} \widetilde{C}_J^\dagger|\Psi_0\rangle \end{aligned} \tag{7.19}$$

where the $\mathcal{D}_{IJ}$ are the dipole operator matrix elements on the intermediate basis. In order to compute these matrix elements we use that dipole operator is a second quantization one-body operator and can be expressed as

$$\hat{D} = \sum_{rs} d_{rs} \hat{a}_r^\dagger \hat{a}_s \tag{7.20}$$

ADC(1) consists of single excitations only. The ADC(n) scheme has a particular hierarchy of approximations. For ADC(2) we quote reference [66]: " ... in ADC(2) the perturbation expansion of the secular matrix elements and of the dipole matrix elements extends through second, first, and zeroth order in the one-hole-one-particle (1h1p) block, the 1h1p-two-hole-two-particle (2h2p) coupling block, and the diagonal 2h2p block, respectively."

7.5 Lanczos-Arnoldi Time Propagation

The time dependent Schrödinger equation (TDSE) for the N-electron wavefunction $\Psi(\{\mathbf{r}\}, t)$ is

$$\dot{\Psi}(\{\mathbf{r}\}, t) = -i \left(H_0(\{\mathbf{r}\}) + \mathcal{E}(t) \cdot \sum \mathbf{r} \right) \Psi(\{\mathbf{r}\}, t) \tag{7.21}$$

where the Newton dot notation in this case represents the partial derivative with respect to time, $\{\mathbf{r}\}$ means the set of position vectors of the N electrons, H_0 is the field free time-independent Hamiltonian and $\mathcal{E}(t)$ is the time-dependent external electric field vector, utilizing the length gauge.
Now assume there is a time-independent complete basis $\Phi_q(\{\mathbf{r}\})$, not necessarily orthonormal, then we can expand

$$\Psi(\{\mathbf{r}\}, t) = \sum_q c_q(t) \Phi_q(\{\mathbf{r}\}) \tag{7.22}$$

where $c_q(t)$ is a vector of coefficients. Filling this in in the Schrödinger equation gives

$$S\dot{c}(t) = -i \left(H_0 - \mathcal{E}(t) \cdot D \right) c(t) \tag{7.23}$$

where $H_{0,nm} = \langle \Phi_n | H_0 | \Phi_m \rangle$ and $D_{i,nm} = \langle \Phi_n | D_i | \Phi_m \rangle$ are the free Hamiltonian and the dipole operator represented on the Φ basis and $S_{nm} = \langle \Phi_n | \Phi_m \rangle$ is the overlap matrix. Note that some authors, e.g. Guan *et al.* [64], use the $H_0 + \mathcal{E}(t) \cdot D$ convention, while we use $H_0 - \mathcal{E}(t) \cdot D$.

It is more convenient to work in an orthonormal basis, so after transforming $c' = S^{-\frac{1}{2}}c$, $H_0' = S^{-\frac{1}{2}}H_0S^{-\frac{1}{2}}$, $D' = S^{-\frac{1}{2}}DS^{-\frac{1}{2}}$ and dropping the primes we have

$$\dot{c}(t) = -i\left(H_0 - \mathcal{E}(t)\cdot D\right)c(t) \tag{7.24}$$

Because the electric dipole interaction has selection rule $\Delta L = 0, \pm 1$ and because the operator L^2 commutes with the field-free Hamiltonian it is convenient to split the Hilbert space of basis functions up into angular momentum blocks L. The field-free Hamiltonian will then be block-diagonal and the dipole operator will be block-tri-diagonal. Within each angular momentum block we can find the free Hamiltonian eigenbasis by solving the field-free eigenvalue problem $H_0v^L = Ev^L$ and thus making the field-free Hamiltonian diagonal.

For large systems the cost of directly computing the unitary time propagator $e^{-iH(t)\Delta t}$, where $H(t) = H_0 - \mathcal{E}(t)\cdot D$, is prohibitive. We can approximate this propagator with Krylov subspace methods at much smaller computational cost. Start with the wavefunction at time t represented by $c(t)$, then apply the Hamiltonian repeatedly. This span of vectors is called a Krylov space

$$\mathcal{K}_m = \text{span}\{c, Hc, H^2c, \ldots, H^{m-1}c\} \tag{7.25}$$

of dimension m. There is a clever iterative method, called the Lanczos-Arnoldi algorithm [62], that constructs an orthonormal basis for this Krylov space. Starting with $v_0 = 0, v_1 = c$ apply iteratively

$$\begin{aligned} \alpha_n &= v_n^\dagger H v_n \\ \beta_{n+1}v_{n+1} &= (H - \alpha_n)v_n - \beta_n v_{n-1} \end{aligned} \tag{7.26}$$

where β_{n+1} is chosen as to normalize v_{n+1}. This method produces an orthonormal set of vectors $\{v\}$. The tri-diagonal matrix formed from putting α on the diagonal and β on both sub-diagonals is a unitary transformation of the Hamiltonian restricted to this Krylov

space and thus has the same spectrum. This tri-diagonal matrix can be easily diagonalized with standard methods and the time propagator $e^{-iH_{\mathcal{K}}(t)\Delta t}$ is readily computed. Writing the transformation between the original space of dimension N (which can be very large) and the Krylov space of dimension m (which is much smaller) as the matrix Q (which is N by m), we have

$$c'(t+\Delta t) = Qe^{-iH_{\mathcal{K}}\Delta t}Q^{\dagger}c(t) \tag{7.27}$$

Notice that we explicitly preserve the norm $|c(t+\Delta t)| = |c(t)|$ which is an important advantage of this method because we will be interested in computing post pulse survival, excitation and ionization probabilities. In practice the Lanczos algorithm is performed in block fashion, i.e. using more than one vector v at a time. For this and further details on numerical convergence see Saad [63]. The Lanczos algorithm has been implemented in the software package ALTDSE [64], which forms part of the software suite by Averbukh *et al.* [54][65][66], which we use for the simulations in this chapter. Note that the Lanczos algorithm converges most quickly at the extremes of the energy spectrum so in practice we only look at the lower end of the spectrum and employ an energy cut-off.

Note that during one time step Δt the external electric field $\mathcal{E}$ is treated as constant. A common choice is to use $\mathcal{E}(t)$ i.e. the electric field at the start of the interval. However, we can do much better by choosing $\mathcal{E}(t+\Delta t/2)$ which better represents the values the electric field assumes over the interval. This doesn't matter much for post pulse analysis but it is important during the pulse when comparing the induced polarization with the external electric field to verify linear response in the adiabatic regime.

7.6 Simulation

We perform calculations on N_2, benzene and naphthalene, using both the ADC and Lanczos-Arnoldi time propagation software packages developed by Ruberti and Averbukh [54][65][66]. We first construct the basis sets using EMSL (The Environmental Molecular Sciences Labora-

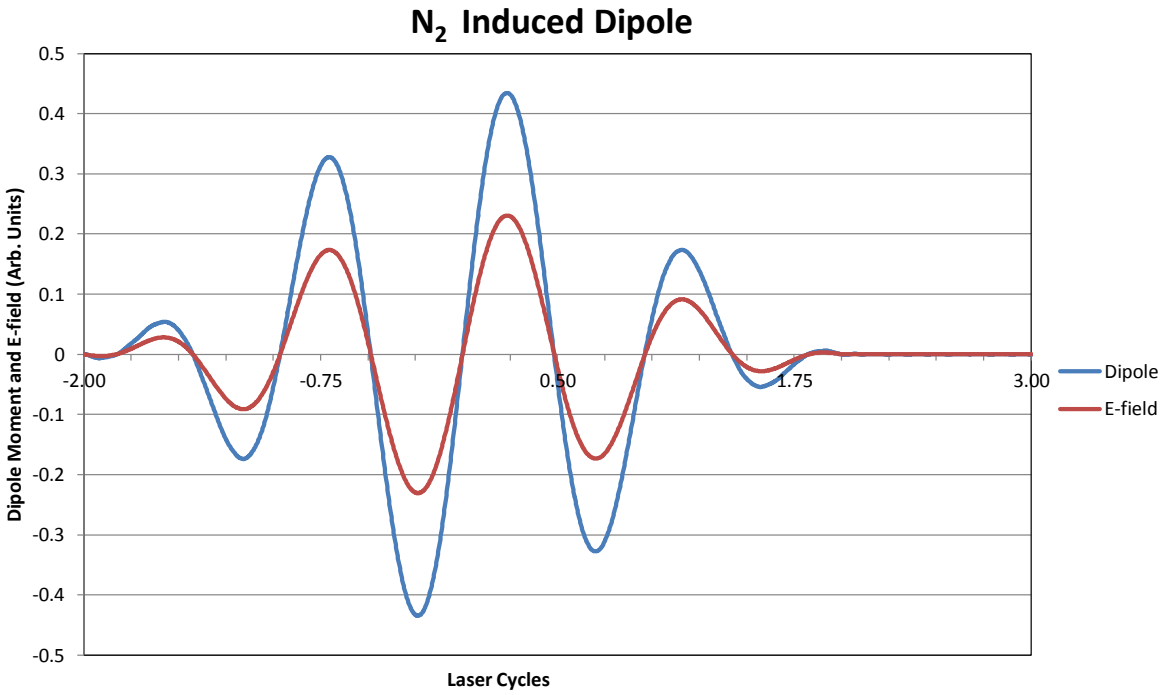

Figure 7.2: N_2 excited by a z-polarized, 800 nm 4-cycle $\sin^2$ pump pulse with intensity of 2×10^{13} W/cm^2. Both E-field and dipole moment are in arbitrary units as a function of laser cycles. We see near linear response during the pump pulse and negligible ringing and ionization yield post pulse, meaning N_2 is in the near adiabatic regime for these pulse parameters.

tory) Basis Exchange [67][68] and augment these with Kaufmann-Baumeister-Jungen (KBJ) continuum-like diffuse Gaussian functions [69]. The construction of the Hamiltonians is done by the MOLCAS (7.6) quantum chemistry package [70].

The basis set utilized for N_2 is aug-cc-pV5Z with additional 7s7p6d6f KBJ [71] diffuse Gaussian functions added in order to represent better the discretized electronic continuum. In the case of benzene (C_6H_6) and naphthalene ($C_{10}H_8$), the basis sets utilized are cc-pVTZ+2s4p3d for C and cc-pVTZ+1s1p1d for H.

We have run the simulations for few-cycle pump pulses of 800 nm, 400 nm, and 1.6 μm wavelengths with various intensities for linear polarizations, x, y and z, and for circular polarization. An example of the time-dependent induced dipole moment calculated is shown in Fig. (7.2). In this figure, N_2 is excited by a z-polarized, 800 nm 4-cycle $\sin^2$ pump pulse

with intensity of 2×10^{13} W/cm^2. The adiabatic approximation seems to be adequate for these pulse parameters, as we observe near linear response during the pump pulse and negligible effects post pulse. When we apply a 4-cycle 800 nm sin^2 z-polarized pump pulse with intensity of 1×10^{14} W/cm^2 to benzene, see Fig. (7.3), we see non-adiabatic effects, exhibited by the post pulse ringing of the induced dipole moment of about 0.5 a.u. as compared to the peak induced dipole moment of about 3.0 a.u. during the pulse. Note that both in Fig. (7.2) and Fig. (7.3) we have inverted the induced polarization output by the ALTDSE code because Guan *et al.* [64] use the $H_0 + \mathcal{E}(t) \cdot D$ convention, while we use $H_0 - \mathcal{E}(t) \cdot D$.

In this simulation, the computation time is predominantly determined by the size of the Hamiltonian matrix. Size of the Hamiltonian for N_2 of aug-cc-pV5Z + (7s7p6d6f) basis set, in an ADC(1) calculation is 749. For an ADC(2) calculation, the size of the matrix grows to 728,383, nearly a thousand-fold increase. The code allows for 3 parallel processes for linearly polarized molecules and 4 for circularly polarized molecules.

7.7 Results

We have used the post pulse survival probability of the ground state population as a stable gauge of (non-)Adiabaticity. Non-adiabaticity means that a system, initially in the ground state, after an interaction has come and gone, is not completely in the ground state anymore. Ground state depletion is, therefore, an appropriate measure and we use a hurdle of 10% depletion as in indicator for the boundary between the two regimes. We have run ADC(1) for N_2, benzene and naphthalene. In Fig. (7.4), we show the results for N_2, with its molecular axis in the z-direction, dressed by a pump laser pulse of 400 nm, 800 nm and 1.6 μm at intensities ranging from $5\times$ 10 ^{12} W/cm^2 - $5\times$ 10^{14} W/cm^2. We see that the adiabatic approximation is poor for intensities stronger than 10^{14} W/cm^2.

For oligocenes, such as benzene and naphthalene, we see significant non-adiabatic effects. The plane of the oligocenes is in the xy-plane. Starting off with benzene, excited by a 4-cycle sin^2 z-polarized laser pulse of 400 nm, 800 nm and 1.6 μm, we see nonadiabatic effects kick in earlier than for the case of N_2, at around 10^{13} W/cm^2. The effects are somewhat

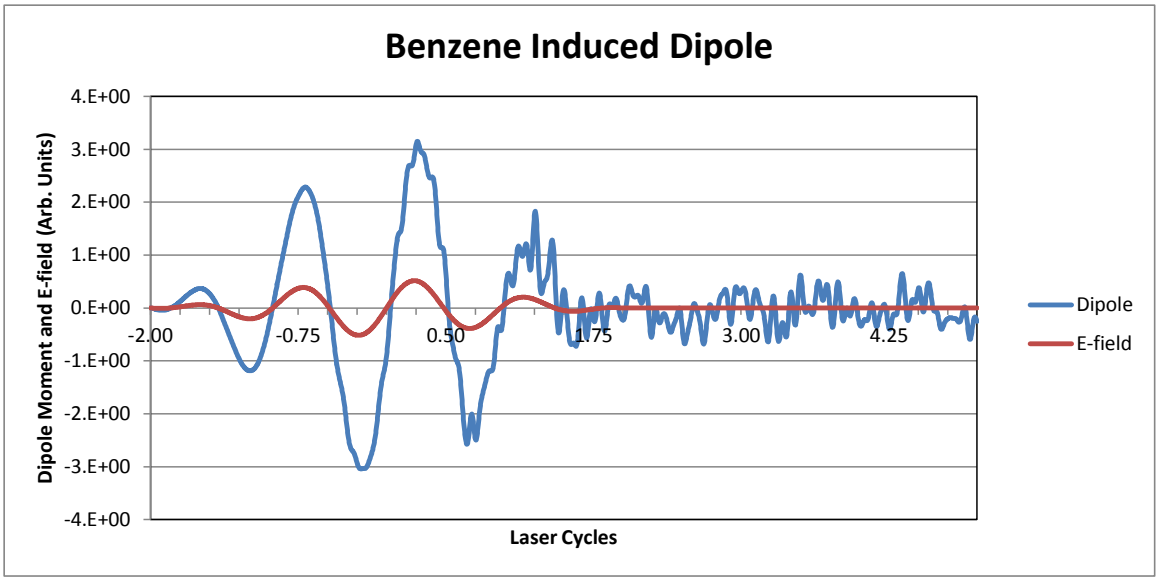

Figure 7.3: Benzene excited by a 4-cycle $\sin^2$ 800 nm z-polarized pulse with intensity of 1×10^{14} W/cm^2. Post pulse dipole moment in a.u. is plotted against the laser cycles. Note that the maximum dipole moment during the pulse is 3.0 a.u. and that therefore the post pulse ringing exhibited above is significant and evidence of non-adiabaticity.

smaller for x- and y- polarizations. The fact that the x- and y- polarization depletions are different yet similar and that the z- polarization depletion stands apart can be understood from benzene's xy-planar geometry. The results show that depletion effects are generally, though not always, stronger for the benzene z-polarization case. One classical hint why this may be true is that if we model the π-electron double-cloud as well separated from the carbon atoms and if we move this cloud, without deformation, in the xy-plane then the electrostatic energy increases. If we move the π-electron cloud, without deformation, in the z-direction

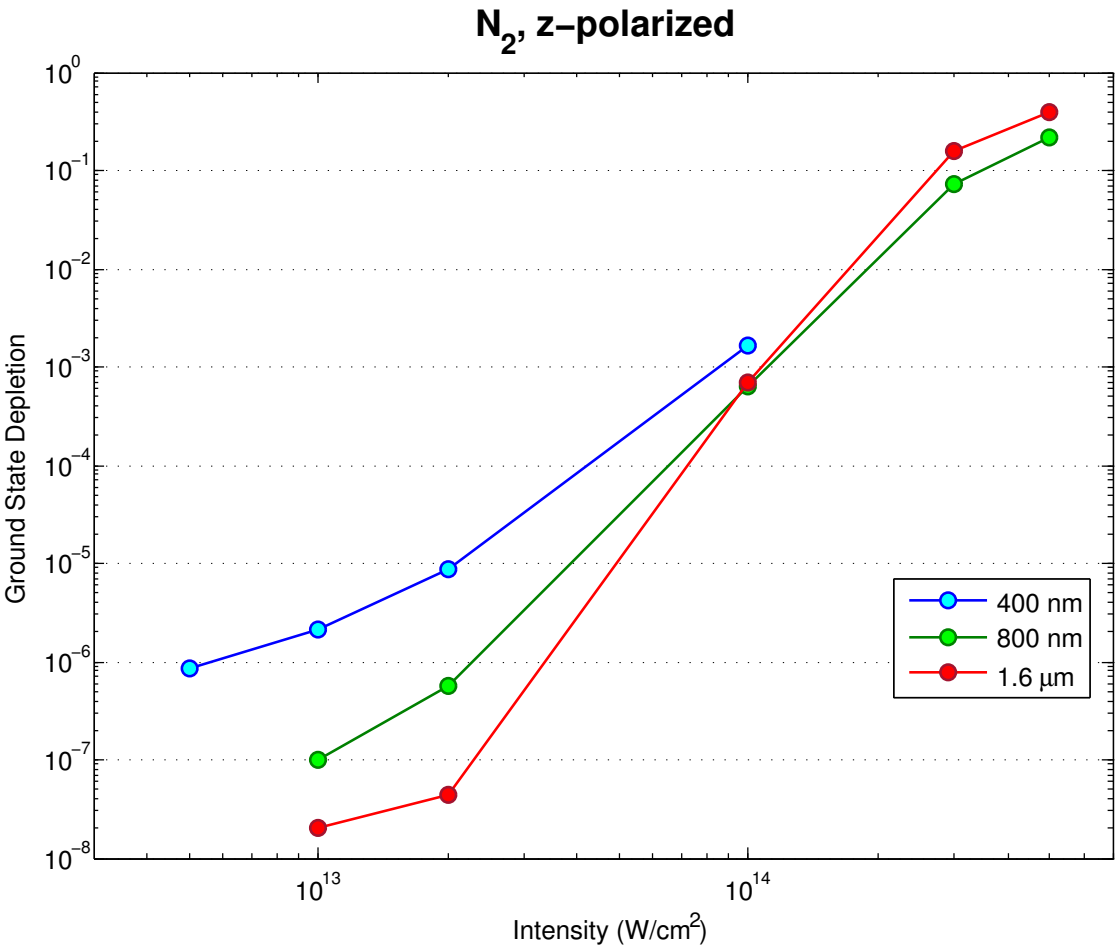

Figure 7.4: N_2 excited by a 4-cycle $\sin^2$ z-polarized laser pulse of 400 nm, 800 nm and 1.6 μm in wavelengths. Plot shows post pulse ground state depletion vs. the intensity. In the adiabatic approximation post pulse ground state depletion would be zero. The data above shows for intensities above $10^{14}\mathrm{W/cm}^{-2}$, more so for shorter wavelengths, that the adiabatic approximation is poor.

the electrostatic energy decreases. This gives us a clue why the polarizability of benzene can be stronger in the z-direction. However, a full quantum mechanical modelling of the benzene molecule is required to verify this. For the circularly polarized field, an interesting and strong effect is exhibited in the case of a 400 nm pulse.

In the case of naphthalene ($C_{10}H_8$), the results of the simulations are shown in Fig. (7.9) to (7.12). Again, the plane of the molecule is in the xy-plane. The results also show that the nonadiabatic effects kick in earlier, at 10^{13} W/cm^2 for linear polarizations, and at even lower intensity, around 5×10^{11} W/cm^2 for a 400 nm circularly polarized pump pulse.

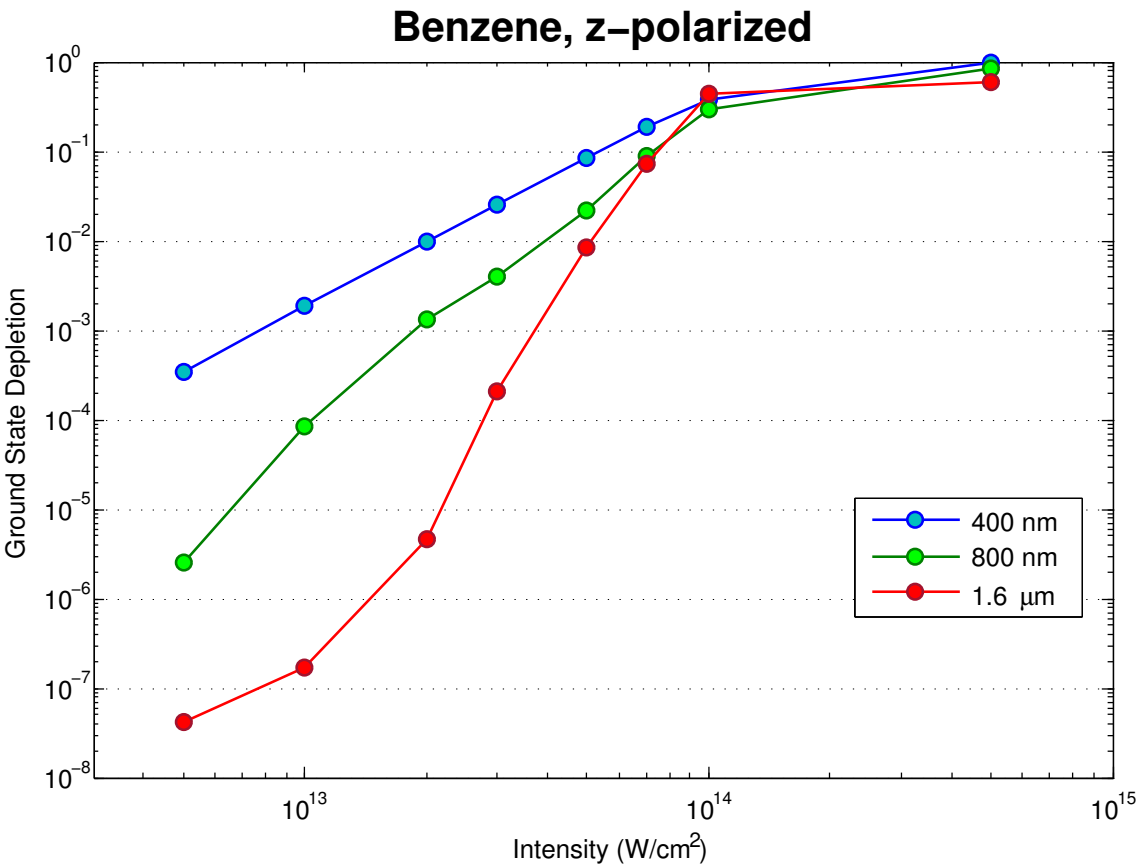

Figure 7.5: Benzene excited by a 4-cycle $\sin^2$ z-polarized laser pulse of 400 nm, 800 nm and 1.6 μm in wavelengths. Plot shows post pulse ground state depletion in logarithmic scale vs. the intensity. Nonadiabatic effects kick in earlier than for N_2, see fig. 7.4 and frequency dependence is stronger.

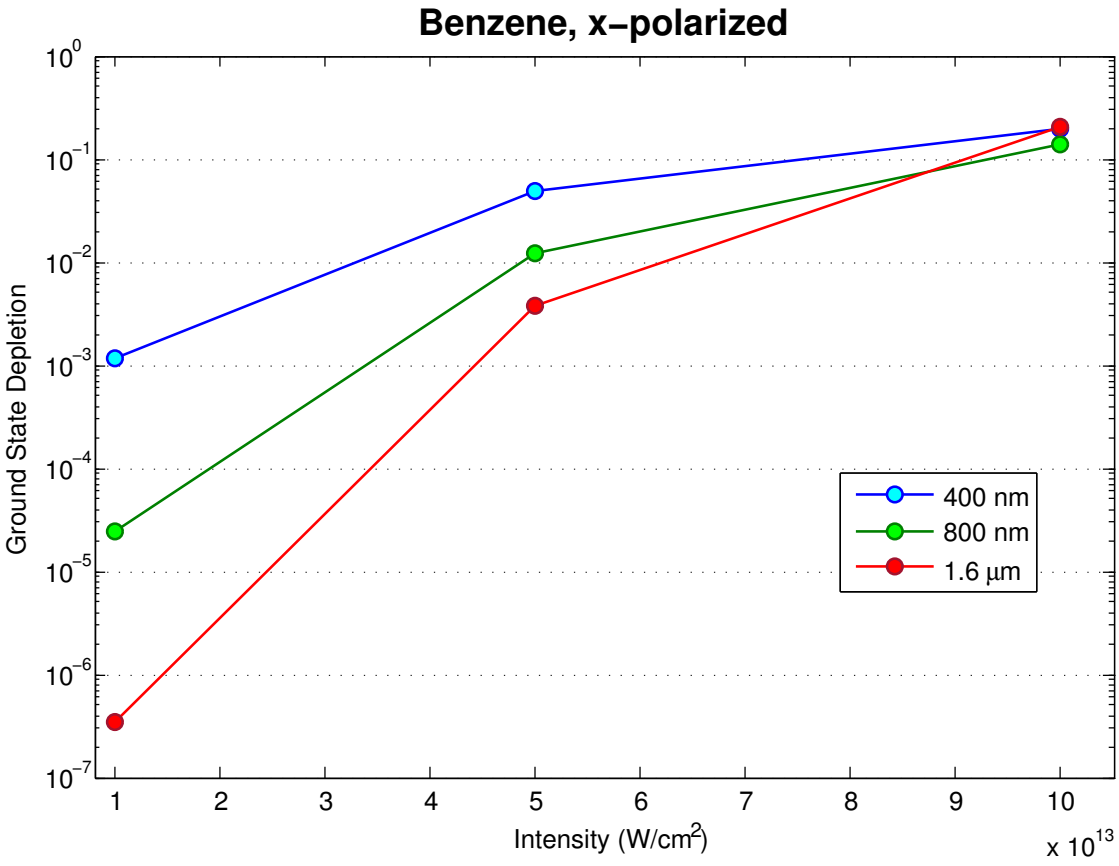

Figure 7.6: Benzene excited by a 4-cycle $\sin^2$ x-polarized laser pulse of 400 nm, 800 nm and 1.6 μm in wavelengths. Plot shows post pulse ground state depletion vs. the intensity. Depletion is generally smaller than those for a z-polarized pulse.

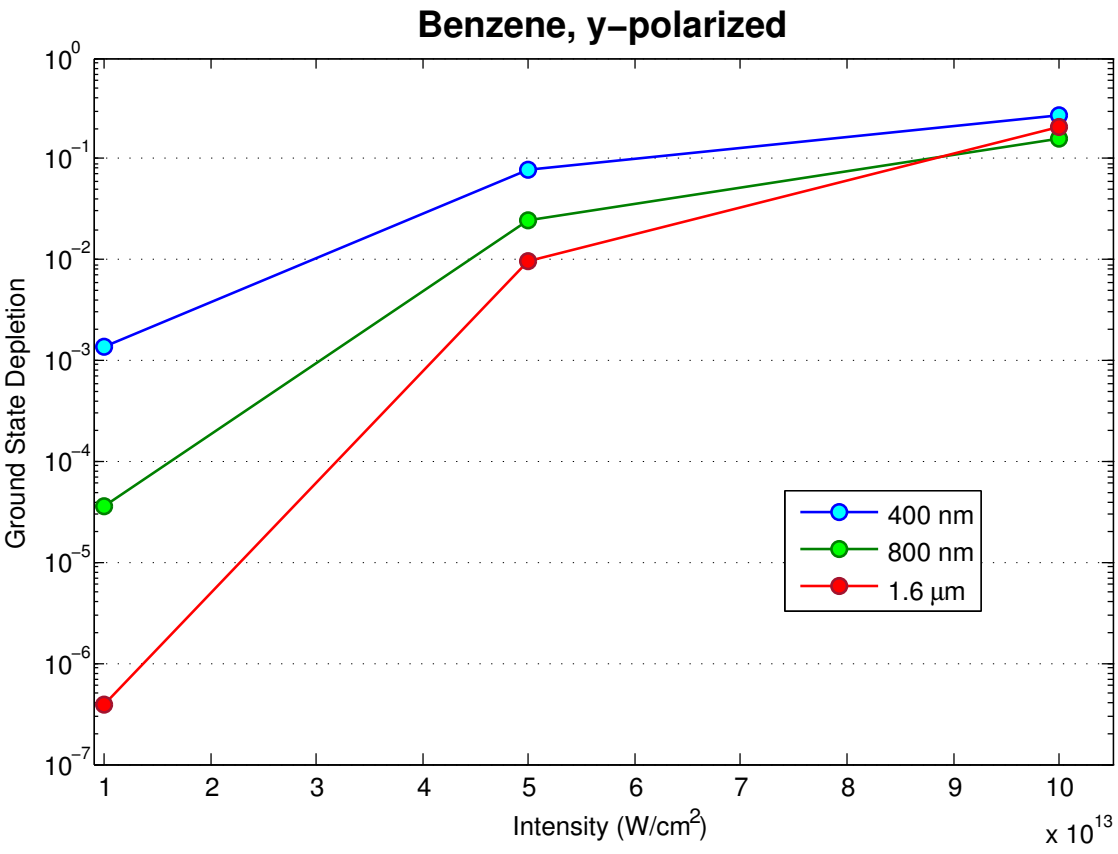

Figure 7.7: Benzene excited by a 4-cycle $\sin^2$ y-polarized laser pulse of 400 nm, 800 nm and 1.6 μm in wavelengths. Plot shows post pulse ground state depletion vs. the intensity. Depletion is generally smaller than those for a z-polarized pulse.

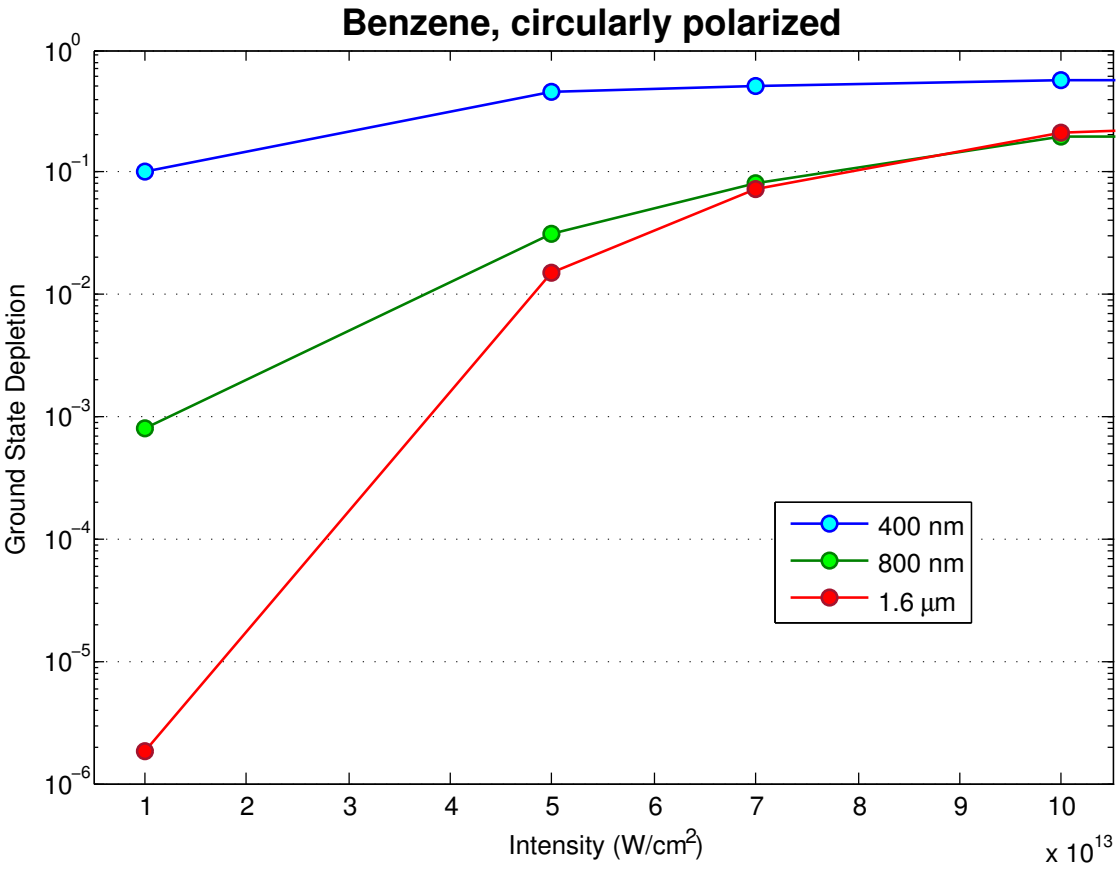

Figure 7.8: Benzene excited by a 4-cycle $\sin^2$ circularly-polarized laser pulse of 400 nm, 800 nm and 1.6 μm in wavelengths. Plot shows post pulse ground state depletion vs. the intensity. The 400 nm data shows strong depletion as compared with linearly polarized and even shows signs of saturation.

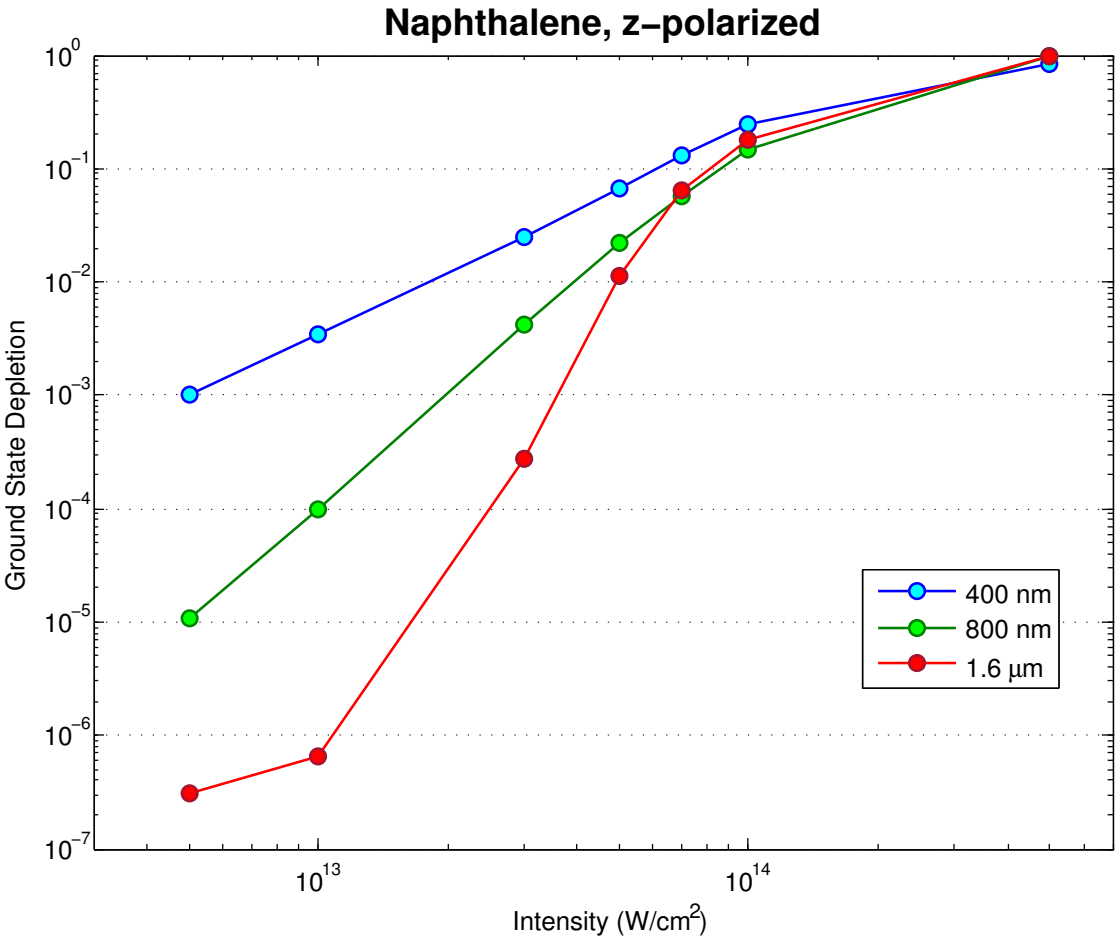

Figure 7.9: Naphthalene excited by a 4-cycle $\sin^2$ z-polarized laser pulse of 400 nm, 800 nm and 1.6 μm in wavelengths. Plot shows post pulse ground state depletion vs. the intensity.

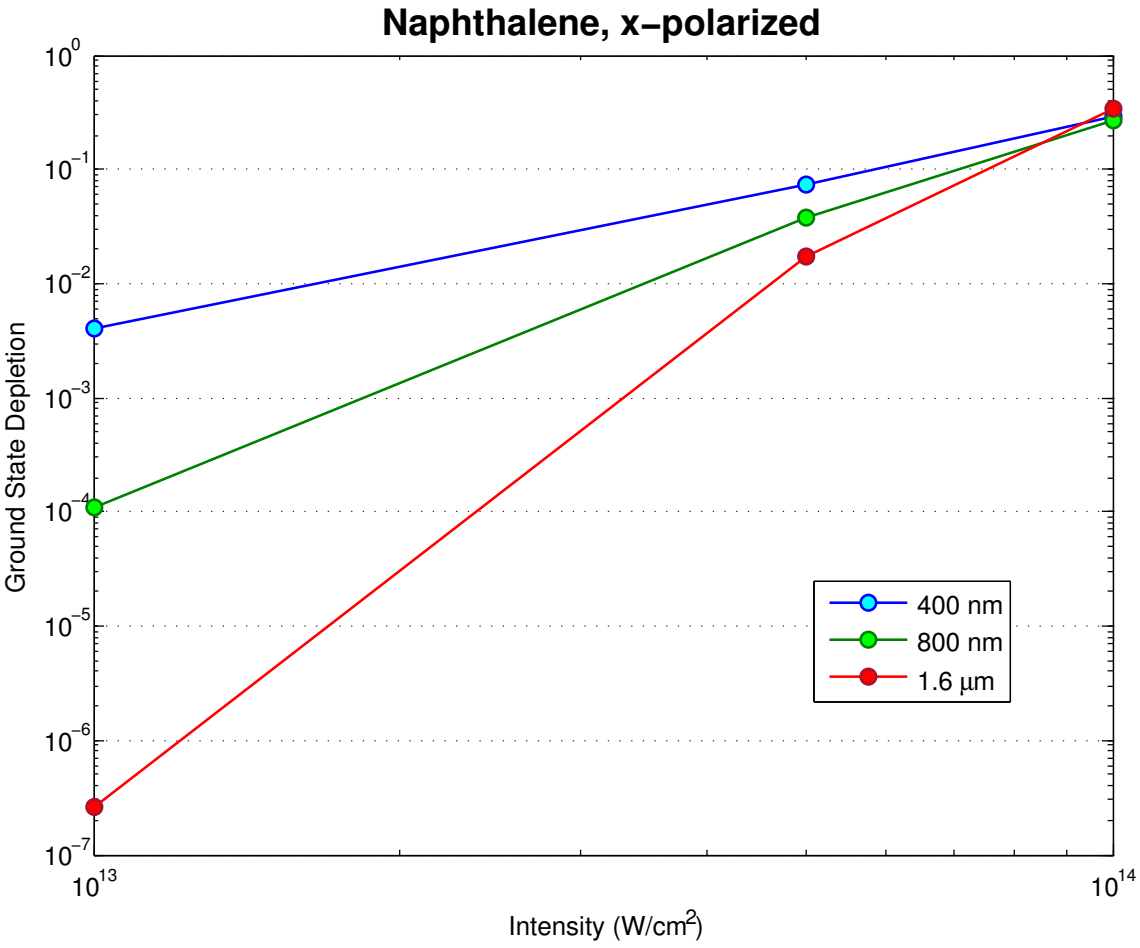

Figure 7.10: Naphthalene excited by a 4-cycle $\sin^2$ x-polarized laser pulse of 400 nm, 800 nm and 1.6 μm in wavelengths. Plot shows post pulse ground state depletion vs. the intensity.

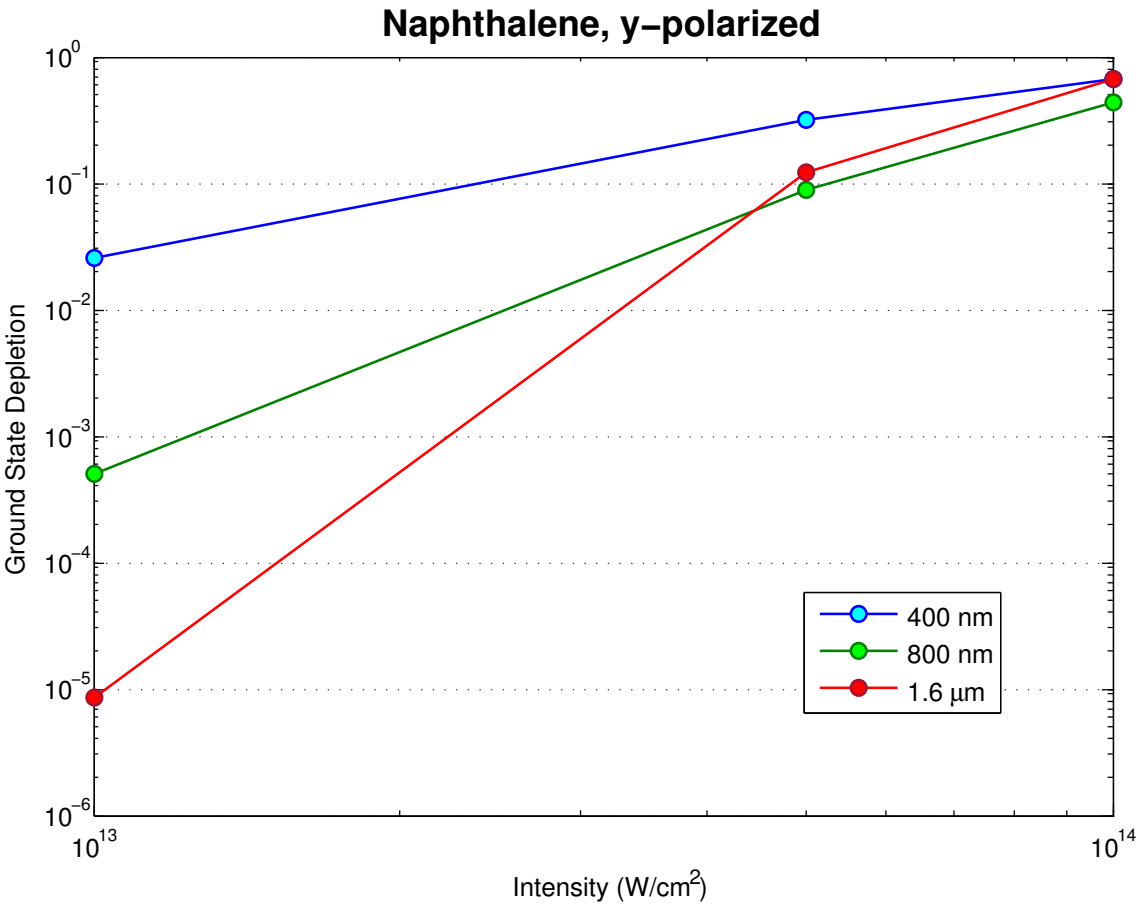

Figure 7.11: Naphthalene excited by a 4-cycle $\sin^2$ y-polarized laser pulse of 400 nm, 800 nm and 1.6 μm in wavelengths. Plot shows post pulse ground state depletion vs. the intensity.

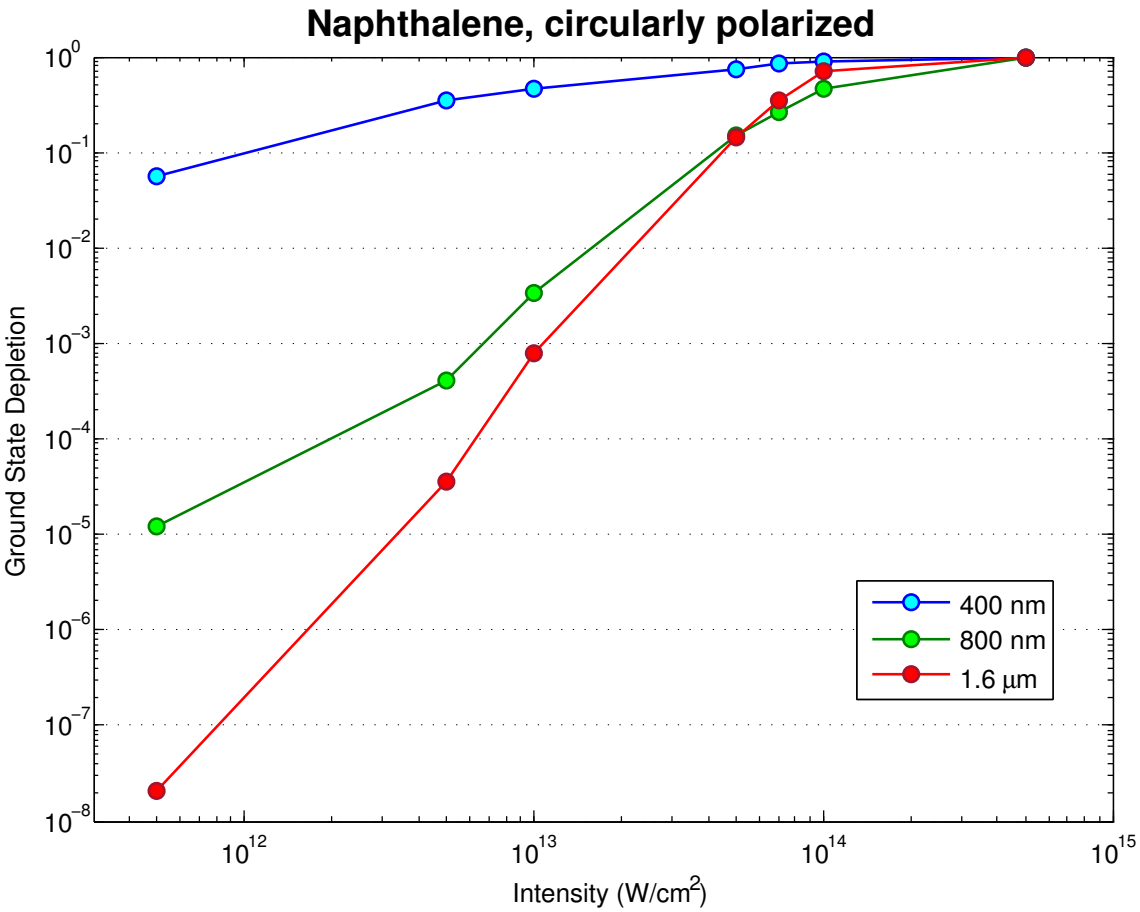

Figure 7.12: Naphthalene excited by a 4-cycle $\sin^2$ circularly-polarized laser pulse of 400 nm, 800 nm and 1.6 μm in wavelengths. Plot shows post pulse ground state depletion vs. the intensity.

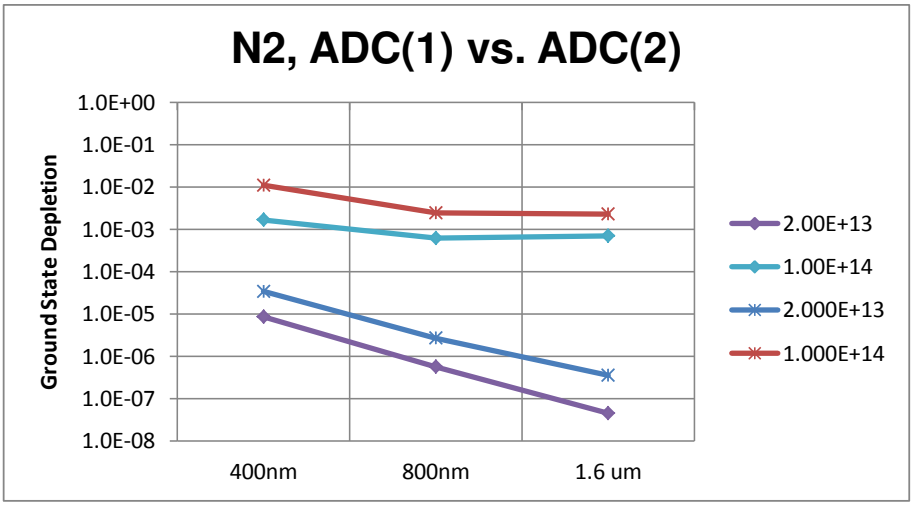

Figure 7.13: Comparison of post pulse ground state depletion of N_2 with ADC(1) (diamond marker), and ADC(2) (cross marker) at two different intensities, 2×10^{13} W/cm^2 and 10^{14} W/cm^2. ADC(2) includes 2p2h states for a more complete description of molecular dynamics. The results show larger depletion for ADC(2) which is an indication that 2p2h states should not be ignored when describing excitation and ionization.

7.8 Conclusion

We have found nonadiabatic behavior as evidenced by post-pulse induced dipole moments and ground state depletion. Using the ADC(1) code and 10% depletion as an arbiter we have found that non-adiabaticity for N_2 kicks in around 3×10^{14} W/cm^2. For benzene and naphthalene, using linear polarizations, the effects kick in earlier namely around $5 - 9 \times 10^{13}$ W/cm^2. As a pattern, non-adiabaticity for 400 nm kicks in for lower intensities than for 800 nm and 1.6 μm. Also, circular polarization at 400 nm has a large effect on benzene and naphthalene, causing non-adiabaticity at much lower intensities. Furthermore, on our limited test set we see that generally the larger the molecule the earlier the onset of non-adiabaticity, although this effect is not very large between benzene and naphthalene for a z-polarized pulse. We also ran ADC(2), which does handle double excitations deemed important for better ionization modelling. Note that it has been shown that ADC(2) outperforms ADC(1) in the calculation of photoionization cross-sections, see Figure 9 and Table II in [65], where

it is shown that ADC(2) is more accurate than ADC(1) in the photon energy range 20-90 eV over an average of eight molecules. However, a full evaluation of the relative performance between these two approaches remains a topic of future research.

For the case of N_2, the overall depletion effect is larger for ADC(2) than for ADC(1), see Figure (7.13). We also completed some ADC(2) runs for benzene, on the more practicable smaller basis sets cc-pVDZ+2s4p3d for C and cc-pVDZ+1s1p1d for H, giving results closer to those of ADC(1). The ADC(2) simulation run requires substantial computational and time resources, especially for the larger molecules, and it should be a worthwhile effort to investigate ADC(2) more fully in the future.

The experiment and simulations by the Max Born Institute (MBI) group [55] used a pump 800 nm pulse at an intensity of 10^{12}W/cm^2, for N_2, CO_2 and C_2H_4. Comparing with our results for N_2 we see that ground state depletion is minuscule in that case and that they operated safely in the adiabatic regime. While the TDDFT calculation used by the MBI group is expected to give consistent results with the ADC approach in the (perturbative) adiabatic regime, there are possible issues for large intensities. There is some concern that the MBI method does not handle double excitations well and further research on high intensities is needed to verify if the ADC(2) method is superior in this respect.

Chapter 8

Summary and Future Work

As the title says, our aim is to make contributions towards the attosecond measurement of dynamics in multi-electron systems. To this end we have made experimental and theoretical/simulation contributions where the latter constitutes the main body of this work. On the experimental side we have built and tested some of the pivotal components of the new Imperial College Beamline. On the theoretical side we have developed our work along three themes that are important for transient absorption measurements:

- Propagation and distortion of probe pulses in absorbing noble gases
- Simulation of atoms and molecules under the effects of pump and probe pulses
- Coherence and polarization effects on transient absorption

We have visited and revisited these themes throughout this thesis. Below we give a summary of the main results and make some suggestions for future research, both experimental and theoretical.

Because attosecond probe pulses are necessarily very broad-band and that, therefore, a large part of their energy spectrum lies above the ionization level of typical atomic and molecular gases, it becomes paramount to understand pulse distortion. We have performed extensive simulations of the propagation of XUV attosecond pulses in helium and argon. To this

end, we developed an effective and stable numerical method that computes the complex index of refraction, via the Kramers-Kronig relations, Möbius transformations and the Fast Fourier Transform, from published absorption data. We then simulated how pulses distort travelling through the absorbing gas. We also used analytically solvable ideal ionization edges in order to improve our simulations. Ionization edges cause strong absorption above the edge and strong phase rotation below the edge. We showed that the pulse distortions obtained include very rich features such as pulse stretching, partial narrowing, partial apparent superluminality, and tail development. It could prove useful to study these features in future experiments.

With the goal of understanding the dynamics of multi-electron systems in mind, we developed a parsimonious mathematical formalism to model the interaction with pump and probe pulses, while avoiding the computational complexity of a full TDSE treatment of ionization. We worked in the density matrix formalism and used the Liouville von Neumann equation, including Lindblad terms, to construct the three Hilbert space source-cation-sink method, modelling the ionization between neutral atoms, cations and multi-cations. Actual simulation was performed by using a Runge-Kutta technique to solve the ordinary differential equation representing the action of the time-dependent Liouvillian on the density matrix. With the mathematical machinery in place for simulation, we needed to obtain the correct physical parameters for simulation of krypton. To this end we used GRASP2K to calculate energy levels and oscillator strengths and compared our results with a group using independent software.

We simulated multi-channel ionization of noble gases and demonstrated how the resulting coherences between the lowest lying cation levels depend on the strength and duration of the NIR pump pulse. We also explained how to understand these coherences in terms of the phase rotation between two extrema of the pump pulse and the LS-splitting of the cation ground state. An interesting avenue for future research is to what extent our method of describing multi-channel ionization from neutral to cation, and the accompanying coherences, agrees

with more elaborate TDSE ionization simulations. We further simulated how a XUV probe pulse can resonantly populate excited cation states and we performed a detailed analysis of the dynamics of level populations, coherences and induced polarizations during and after the probe pulse. The cation-sink part of the source-cation-sink model was used to capture the Auger decay processes from the excited cation states to multi-cations. We also tested pump pulses of varying intensities to establish when nonlinear effects come into play. We explicitly constructed the second and fourth order (in the electric field) effects on the population levels, and the first and third order effects on the induced polarization. We concluded, within our model for krypton, that HHG intensities ($\leq 10^{12}$ W/cm^2) are safely in the linear regime, while nonlinear effects kick in around the free electron laser (FEL) scale ($\sim 10^{17}$ W/cm^2), with the caveat that some processes went unmodeled such as non-Auger ionization and electron recapture effects. Future experimental work could elucidate these nonlinear effects with high intensity probes. Although sub-femtosecond FEL pulses have not been realized yet, we expect them to become available in the future.

We investigated how an XUV pulse propagates through ionized krypton gas and studied the effects of the coherences between the cation levels on the evolution and absorption of the pulse. We derived the induced dipole response and corresponding absorption formulae with special attention to the polarization angle between the probe and pump pulses. The results show absorbances that are periodic in the probe-pump delay time which are strongly polarization angle dependent. The former has been shown experimentally [2] and verifying the latter quantitatively is an interesting direction for future experimental research. Because of the presence of coherence, the naive Beer-Lambert exponential decay law does not apply. We provide an efficient analytical method for computing broken Beer-Lambert absorption and describe the consequences (and correct methods) for the interpretation of experimental absorbance data. The implications for the computation of implied density matrices are material. Testing coherent broken Beer-Lambert law propagation is also an important direction for future experimental research. Note that this a linear effect that is caused by coherence

and the fact that the dipole response to the electric field is not diagonal in frequency space.

Lastly, we studied the dynamics of molecules affected by pump pulses. An important question to answer is for which pump parameters the evolution of the molecule can be considered adiabatic, i.e. the system stays in the ground state while this ground state continuously deforms in time returning to its initial form after the pulse, and when not. This question is of importance to future experiments as well as the future evaluation of competing theoretical (and simulation) approaches to the rather challenging problem of faithfully modelling molecules. We performed numerous simulations for N_2, benzene and naphthalene, for various pump pulse intensities, polarizations and wavelengths, using the QOLS theory group ADC code. We have found nonadiabatic behavior as evidenced by post-pulse induced dipole moments and ground state depletion. Using the ADC(1) code and 10% depletion as an arbiter we have found that non-adiabaticity for N_2 kicks in around 3×10^{14} W/cm^2. For benzene and naphthalene, using linear polarizations, the effects kick in earlier namely around $5 - 9 \times 10^{13}$ W/cm^2. As a pattern, non-adiabaticity for 400 nm kicks in for lower intensities than for 800 nm and 1.6 μm. Also, circular polarization at 400 nm has a large effect on benzene and naphthalene, causing non-adiabaticity at much lower intensities. We also ran ADC(2) simulations, which does handle double excitations deemed important for better ionization modelling, for N_2. The overall depletion effect is larger for ADC(2) than for ADC(1). The ADC(2) simulation run requires substantial computational and time resources, especially for the larger molecules, and it should be a worthwhile effort to investigate ADC(2) more fully in the future.

Bibliography

[1] Zhao, K. *et al.*, "Tailoring a 67 attosecond pulse through advantageous phase-mismatch," *Optics Letters*, v. 37, pp. 3891-3893, (2012).

[2] Goulielmakis, E. *et al.*, "Real-time observation of valence electron motion," *Nature*, v. 466, pp. 739-744, (2010).

[3] Grant, I.S., Phillips, W.R., *Electromagnetism*, pp. 345-358, John Wiley & Sons, Ltd., (1975), ISBN 0471322458.

[4] Lorentz, H.A., *La théorie électromagnétique de Maxwell et son application aux corps mouvants*, Brill, (1892).

[5] Boyd, R. W., *Nonlinear Optics*, pg. 4, pp. 150-185, Second Edition, (2003), ISBN 0-12-121682-9.

[6] P.A. Franken, A. E. Hill, C. W. Peters, and G. Weinreich, "Generation of optical harmonics," *Phys. Rev. Lett.*, v. 7, 118 (1961).

[7] Corkum, P. B., "Plasma perspective on strong-field multiphoton ionization," *Phys. Rev. Lett.*, v. 71, pp. 1994-1997, (1993).

[8] Lewenstein, M., *et al.*, "Theory of high-harmonic generation by low-frequency laser fields," *Phys. Rev. A*, v. 49, p. 2117, (1994).

[9] Agostini, P., *et al.*, "Free-Free Transitions Following Six-Photon Ionization of Xenon Atoms," *Phys. Rev. Lett.*, v. 42, no. 17, pp. 1127-1130, (1979).

[10] Protopapas, M., *et al.*, "Atomic physics with super-high intensity lasers," *Rep. Prog. Phys.*, v. 60, pp. 389-486, (1997).

[11] Ammosov, M., Delone, N., Krainov, V., "Tunnel ionization of complex atoms and of atomic ions in an alternating electromagnetic field", *Sov. Phys. JETP*, 64, 1191-1194 (1986).

[12] Kramida, A., Ralchenko, Yu., Reader, J., and NIST ASD Team (2013). *NIST Atomic Spectra Database (ver. 5.1)*, [Online]. Available: http://physics.nist.gov/asd . (2013). National Institute of Standards and Technology, Gaithersburg, MD.

[13] Keldysh, L.V., "Ionization in the field of a strong electromagnetic wave," *Soviet Physics JETP*, v. 20, No. 5, pp. 1307-1314, (1965).

[14] Hung, T. Y., "Soft X-ray Absorption Spectroscopy," May 2012.

[15] Marr, G.V., West, J.B., "Absolute photoionization cross-section tables for Helium, Neon, Argon and Krypton in the VUV spectral regions," *Atomic data nuclear data tables*, v. 18, pg 497, (1976).

[16] Landau, L.D., and Lifshitz, E.M., *Electrodynamics of Continuous Media*, pp. 256-268, Pergamon Press, (1963).

[17] Lacarini, V., et al., *Kramers-Kronig Relations in Optical Materials Research*, pp. 44-46, Springer, (2005), ISBN-10 3-540-23673-2.

[18] Conway, J. B., *Functions of One Complex Variable*, 2nd Ed., pp. 47-54, Springer-Verlag, (1978), ISBN 0-387-90328-3.

[19] Olver, S., "Computing the Hilbert Transforms and Its Inverse," *Maths. Comp.,* v. 80, pp. 1745-1767, (2011).

[20] Jackson, J.D., *Classical Electrodynamics*, 2nd edition, pp. 217-219, pg. 642, John Wiley & Sons, (1975), ISBN 0-471-43132-X.

[21] Henke, B. L., Berkeley Lab, http://henke.lbl.gov/optical_constants/.

[22] Thorne, A.P., *Spectrophysics*, (2nd ed.), pp. 262-265, Chapman and Hall, (1988), ISBN 0 412 27470 1.

[23] Diener, G., "Superluminal group velocities and information transfer", *Phys. Lett. A*, v.223, pp 327-331, (1996).

[24] Chen, S. *et al.*, "Light-induced states in attosecond transient absorption spectra of laser-dressed helium," *Phys. Rev. A*, v. 86, 063408, (2012).

[25] von Neumann, J., *Mathematical Foundations of Quantum Mechanics, Series: Investigations in Physics, No. 2*, Princeton University Press (1955), ISBN 0691028931.

[26] Lindblad, G., "On the Generators of Quantum Dynamical Semigroups," *Commun. Math. Phys.* v. 48, pp. 119-130, (1976).

[27] Blum, Karl, *Density Matrix Theory and Applications*, Second Edition, pp. 39-89, Academic Press (1996), ISBN 030645341-X.

[28] Mukamel, Shaul, *Principles of Nonlinear Optical Spectroscopy*, pp. 45-75, Oxford University Press (1995), ISBN 0195132912.

[29] Dirac, P.A.M., *The Principles of Quantum Mechanics* (4th ed.), pp. 108-111, Oxford University Press, (1958).

[30] Breuer, H.P., Petruccione, F., *The Theory of Open Quantum Systems*, pp. 130-160, Oxford University Press, (2002), ISBN 0 19 852063 8.

[31] Adler, S.L., "Derivation of the Lindblad Generator Structure by use of Ito Stochastic Calculus," *Phys. Lett. A.*, 265 (2000), pp 58-61.

[32] Kraus, K., *Ann. Phys.* (N.Y.) v. 64, 311 (1971).

[33] Press, W.H. *et al.*, *Numerical Recipes*, pp. 335-380, pp. 550-560, Cambridge University Press, 1987, ISBN 0 521 30811 9.

[34] Shore, B., *The Theory of Coherent Atomic Excitation*, v. 1, pp. 331-363, pp. 691-774, John Wiley & Sons, Inc., (1990), ISBN 0-471-52417-4.

[35] Santra, R. *et al.*, "Theory of attosecond transient photoabsorption spectroscopy of strong-field-generated ions," *Phys. Rev. A*, v. 83, 033405, (2011).

[36] Rohringer N. and Santra R., "Multichannel coherence in strong-field ionization," *Phys. Rev. A*, v. 79, 053402 (2009).

[37] Merzbacher, E., *Quantum Mechanics*, pp. 484-485, John Wiley & Sons, Inc., 2ed (1970).

[38] Sakurai, J., Napolitano, J., *Modern Quantum Mechanics*, 2ed, pp. 371-375, Addison-Wesley, (2011), ISBN 10: 0-8053-8291-7.

[39] Weisskopf, V., Wigner, E., "Berechnung der natürlichen Linienbreite auf Grund der Diracschen Lichttheorie", *Zeitschrift für. Physik*, 63, pp. 54-73 (1930).

[40] Jonsson P., Gaigalas G., Bieron J., Froese Fischer C., Grant I.P., "New version: GRASP2K relativistic atomic structure package," *Computer Physics Communications*, v. 184, pp. 2197-2203 (2013).

[41] Parpia F.A., Froese Fischer C., and Grant I.P., "GRASP92: A package for large-scale relativistic atomic structure calculations," *Computer Physics Communications*, v. 94, pp. 249-271 (1996).

[42] Hagelstein, P.L., *private communications.*

[43] Zeng J.L., Liu P.F., Xiang W.J. and Yuan J.M., "Complete Auger decay pathways of Kr $3d^{-1}$ hole levels including direct double processes," *J. Phys. B: At. Mol. Opt. Phys.*, v. 46 (2013) 215002.

[44] Jurvansuu M. *et al.*, "Inherent lifetime widths of Ar $2p^{-1}$, Kr $3d^{-1}$, Xe $3d^{-1}$, and Xe $4d^{-1}$ states," *Phys. Rev. A*, v. 64, 012502 (2001).

[45] Yudin, G., Ivanov, M., "Nonadiabatic tunnel ionization: Looking inside a laser cycle," *Phys. Rev. A*, v. 64, 013409 (2001).

[46] Butcher, P., Cotter, D., *The Elements of Nonlinear Optics*, pp. 211-220, Cambridge University Press, (1990), ISBN 0-521-34183-3.

[47] Brabec, T., Krausz, F., "Intense few-cycle laser fields: Frontiers of nonlinear optics," *Reviews of Modern Physics*, v. 72, No. 2, Apr 2000.

[48] Bloembergen, N., *Nonlinear Optics*, pp. 20-30, W.A. Benjamin, Inc. (1965), ISBN 0-8053-0938-1.

[49] Delone, N., Krainov, V., *Fundamentals of Nonlinear Optics of Atomic Gases*, pp. 7-46, John Wiley & Sons, Inc. (1988).

[50] Edmonds, A.R., *Angular Momentum in Quantum Mechanics*, pp. 45-50, pp. 75-77, pp. 92-97, Princeton University Press, 2ed (1960).

[51] Skoog, A., West, M., Holler, F., Crouch, S., *Fundamentals of Analytical Chemistry*, 8ed, pp. 729-734, Brooks/Cole (2004), ISBN 10: 0-03-035523-0.

[52] Allen, L., Eberly, J., *Optical Resonance and Two-Level Atoms*, pp. 78-109, Dover (1987), ISBN 0-486-65533-4.

[53] Marangos, J. P., "Topical review Electromagnetically induced transparency", *Journal of Modern Optics*, v. 45, no. 3, pp. 471-503, (1998).

[54] Averbukh, V.,*et al. private communications.*

[55] Ch. Neidel, *et al.*, "Probing Time-Dependent Molecular Dipoles on the Attosecond Time Scale," *Phys Rev Lett*, v. 111, 033001 (2013).

[56] Born, M., Fock, V., "Beweis der Adiabatensatzes," *Zeitschrift für Physik*, A 51(3-4), 165-180.

[57] Schiff, Leonard I., *Quantum Mechanics*, McGraw-Hill, 3ed, pp. 289-292, (1968), ISBN: 0070856435.

[58] Messiah, A., *Quantum Mechanics*, v. II, pp. 747-755, pp. 1053-1078, North-Holland Publishing Company (1965).

[59] Abramowitz, M, Stegun, I., *Handbook of Mathematical Functions*, pg. 298, Dover, 9th printing, (1970), ISBN 0-486-61272-4.

[60] Schirmer, J., "Closed-form intermediate representations of many-body propagators and resolvent matrices," *Phys. Rev. A*, 43, 9, pp. 4647-4659, (1991).

[61] Schirmer, J., "Beyond the random-phase approximation; A new approximation scheme for the polarization propagator," *Phys. Rev. A*, 26, 5, pp. 2395-2416, (1981).

[62] Lanczos, C., "An iteration method for the solution of the eigenvalue problem of linear differential and integral operators", *Journal of Research of the National Bureau of Standards*, 45, pp. 255282, (1950).

[63] Saad, Y., *Iterative methods for sparse linear systems*, pp. 172-179, pp. 210-213, SIAM (2003).

[64] Guan, X., et al., "ALTDSE: An ArnoldiLanczos program to solve the time-dependent Schrdinger equation," *Comp. Phys. Comm.*, v.180, pp.2401-2409, (2009).

[65] Ruberti, M., Yun, R., Gokhberg, K., Kopelke, S., Cederbaum, L.S., Tarantelli, F., and Averbukh, V., "Total molecular photoionization cross-sections by algebraic diagrammatic construction-Stieltjes-Lanczos method: Benchmark calculations," *J. Chem. Phys.*, 139, 144107 (2013).

[66] Ruberti, M., Yun, R., Gokhberg, K., Kopelke, S., Cederbaum, L.S., Tarantelli, F., and Averbukh, V., "Total photoionization cross-sections of excited electronic states by the algebraic diagrammatic construction-Stieltjes-Lanczos method," *J. Chem. Phys.*, 140, 184107(2014).

[67] Feller, D., "The Role of Databases in Support of Computational Chemistry Calculations", *J. Comp. Chem.*, 17(13), 1571-1586 (1996).

[68] Schuchardt, K.L., Didier, B.T., Elsethagen, T., Sun, L., Gurumoorthi, V., Chase, J., Li, J., and Windus, T.L. "Basis Set Exchange: A Community Database for Computational Sciences," *J. Chem. Inf. Model.*, 47(3), 1045-1052, (2007) doi:10.1021/ci600510j.

[69] Kaufmann, K., Baumeister, W., and Jungen, M., "Universal Gaussian basis sets for an optimum representation of Rydberg and continuum wavefunctions," *J. Phys. B*, v.22, pp. 2223, (1989).

[70] Aquilante, F., *et al.*, "MOLCAS 7: the next generation," *J. Comput. Chem.*, v. 31, p. 224 (2010).

[71] Szabo, A., Ostlund, N., *Modern Quantum Chemistry*, pp. 108-229, Dover (1989), ISBN 0-486-69186-1.

[72] Hartree, D.R., "The Wave Mechanics of an Atom with a Non-Coulomb Central Field. Part I. Theory and Methods," *Mathematical Proceedings of the Cambridge Philosophical Society*, v. 24, Issue 01, pp.89-110, January 1928.

[73] Jonsson P., He X., Froese Fischer C., Grant I.P., "The grasp2K relativistic atomic structure package," *Computer Physics Communications*, v. 177, pp. 597-622 (2007).

[74] Grant I.P., *private communications.*

[75] Jonsson P. , *et al.*, *A Practical Guide to GRASP2K*, 2012.

[76] Zare, R.N., *Angular Momentum*, pp. 143-148, pp. 180-186, John Wiley & Sons, Inc. (1988), ISBN 0-471-85892-7.

[77] Cowan, R.D., *The Theory of Atomic Structure and Spectra*, pp. 307-310, pp. 406-410, pp. 694-701, University of California Press (1981), ISBN 0-520-03821-5.

[78] Shore, B.W., Menzel, D.H., "Generalized Tables for the Calculations of Dipole Transition Probabilities", *Astrophysical Journal Supplement*, v. 12, 187 (1965).

[79] Perelemov, A.M., Popov, V.S., Terent'ev, M., "Ionization of atoms in an alternating electric field," *Soviet Phys. JETP* 23, 924 (1966).

[80] Bisgaard, C., Madsen, L., "Tunneling ionization of atoms", *Am. J. Phys.*, 72 (2), Feb 2004.

Appendices

Appendix A

Ultrafast HHG Technology

A.1 Author's Experimental Contribution

While most of the work in this thesis is theoretical/computational, the author also contributed to the initial construction phase of the new Imperial College beamline. A description of the components of the new beamline built, assembled and tested by the author is given. My tasks, many conducted from scratch, included setting up the experiment, designing the interaction chamber, procuring the new chamber, along with preparing a new turbo pump and scroll pump, procuring and assembling components such as the XYZ-manipulator, preparing piezo valves for a gas jet, and assembling components for gas delivery into the interaction chamber. The author also designed a custom metal filter holder for use in a vacuum chamber. This was built by the author and deployed in the beamline to spectrally filter the beam. The experimental setup requires that the filter assembly can be moved in and out of the beam under vacuum conditions. To accommodate this, the author also built a custom vacuum compatible actuator translation stage which can be operated from outside the vacuum chamber. The main components of the experiments which include the interaction chamber and XYZ-manipulator were procured and negotiated by the author. The design details of the interaction chamber were first conceived by the author and approved by her supervisor.

A.2 Interaction Chamber Design

The interaction chamber consists of a custom built Kurt J. Lesker six way cross with viewports designed with adaptibility and adjustibility to existing and future experiments in mind, see Figure (A.1). The 10-inch port specifically is ordered for attaching to the turbopump: an Agilent Navigator Turbo V1001 backed by a scroll pump. The length from the middle of the chamber to the outer rim of the flange is 139.7 mm (i.e. the longest length of the chamber is twice that, or 279.4 mm). The 6 inch port is designed to fit the XYZ-manipulator with miniports for attaching water cooling tubes, gas tube to allow for a piezo kHz gas jet assembly, as well as the HV connectors. The size of the chamber/six way cross is mainly determined by the size of the three main ports of eight inches in size individually. A small port of $4\frac{1}{2}$ inch is designed for an ion pressure gauge.

Atomic gases, He, Ne, Ar and molecular gases, N_2, CO_2 were injected into the interaction chamber by a custom made nozzle with either 200 μm or 100 μm in diameter. The position of the gas jet is controlled by a XYZ-manipulator which provides x,y travel of 0.5 inch and z travel of 6.0 inch. The interaction chamber is also fitted with an evacuation PTFE pipe, attached to a scroll pump. With the 10-inch turbo pump attached directly, no adapter in between, to this 8-inch body six way cross chamber, it is the author's opinion that this setup allows for refreshing of the sample gases with minimal time scales[14].

Typical values of the interaction chamber pressure with 2 bars N_2 gas backing pressure and gas jet of 100 μm nozzle are 3.77×10^{-3} mbar $\pm$ 1 %.

A.3 Experimental Setup

The HHG is driven by a Ti:Sapphire laser, with central wavelength of 790 nm, 35 fs. This laser system can easily produce 5 mJ of energy per pulse. We used 1 mJ to produce HHG from Ar. The focal spot is about 150 μm, with 190 μm easily achievable.

In order to spatially overlap the HHG and NIR beams, a pair of fused silica plates were used, see Figure (A.2). The fused silica plates were manufactured by Optique de Precision J.

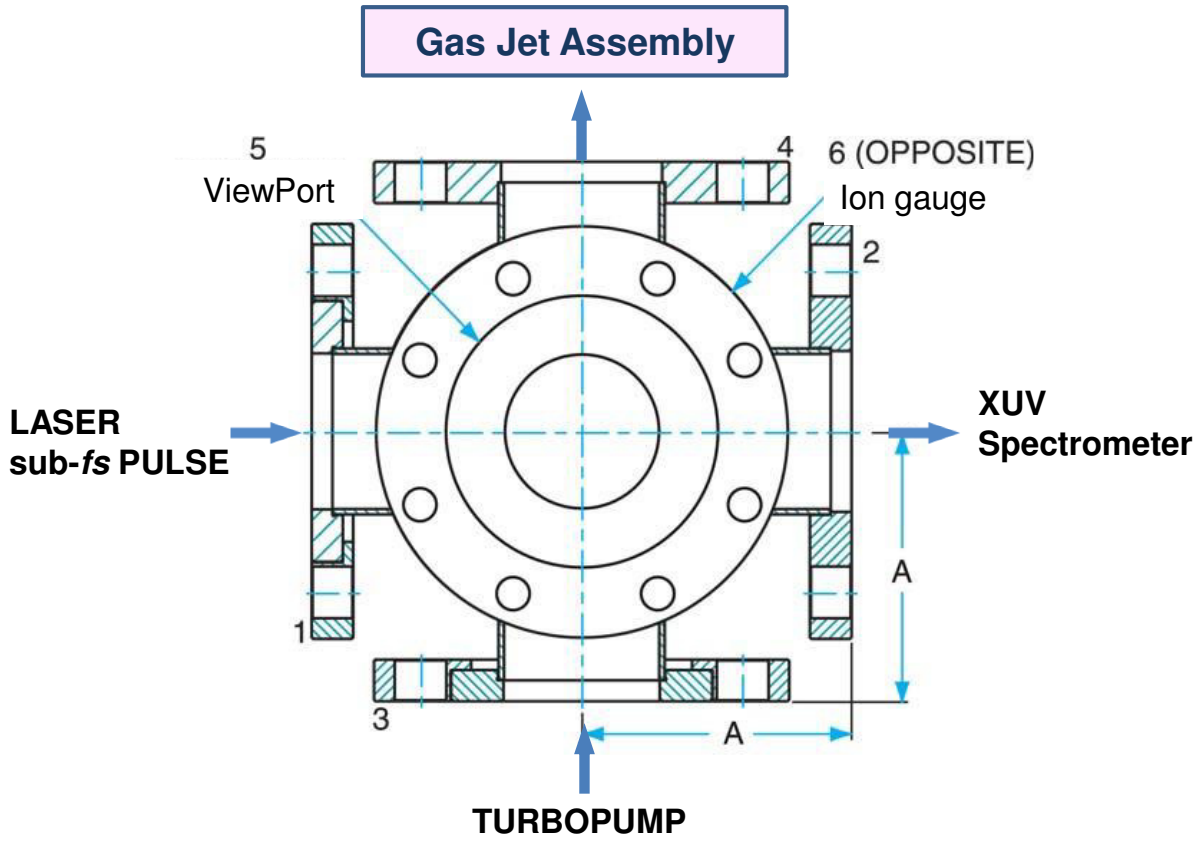

Figure A.1: Design Sketch of the Interaction Chamber. The size of A is 139.7 mm.

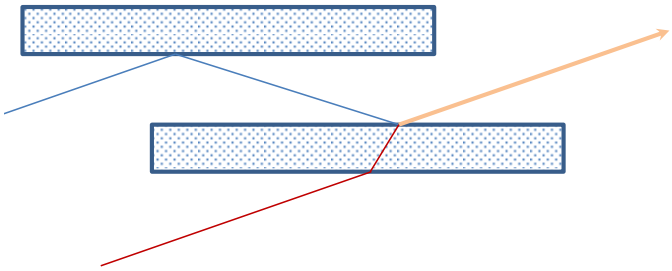

Figure A.2: Fused Silica Recombination Plates: Blue denotes soft x-rays and Maroon denotes NIR beams

Fichou. The specifications are: each of 115 × 20 mm thickness 20 mm (usable area 90× 10 mm), both sides with flatness $\lambda/10$ to $\lambda/20$, roughness < 0.3 nm rms, parallelism 30". The coating on one side is antireflective for 800 nm, incidence angle of 80°, p-polarization, with reflectivity $< 1\%$ (Reflectivity about 95% for s-polarization). The last layer is made of SiO_2 with thickness of about 30 nm. The second side has the characteristics that for s-polarization reflectivity $< 1\%$ (reflectivity about 50% for p-polarization). The last layer is also made of SiO_2 with thickness of about 200 nm.

The HHG beam is focussed by the toroidal mirror with a focal length of 50 cm into the interaction chamber. The toroidal mirror is mounted on a motorized stage with six degrees of freedom: x, y, z, yaw, tip and rotation. The angle of incidence used is 5°.

The detection of the transmission of the XUV or soft x-rays is performed by a soft x-ray spectrometer built by Andor Technology in which a gold coated 1200 g/mm varied-line spaced concave grating disperse the radiation onto a CCD array. The model BN-434 is provided with a CCD array of 1024×1024 pixels, each of 13 μm × 13 μm in size. This resolution has provided us, for 800 nm generated harmonics, energy spacing of the harmonics of $\Delta E \approx 3.10$ eV (due to the selection rule), a sequence of five harmonics to measure absorption from. The

L_{abs}	Densities (m^{-3})
1 cm	1.98×10^{22}
1 mm	1.98×10^{23}
5 cm	3.96×10^{21}

Table A.1: For Argon gas, the absorption length L_{abs} and densities that corresponds to 50% of absorption

CCD arrays are positioned along an arc mimicking the Rowland circle, with settings with a range from 0° to 40°. This provides different ranges of spectral energy to observe from. This CCD detector was initially positioned at 20°.

A.4 Results

In our ultrafast photoabsorption spectroscopy experiment, measurements were conducted for inert gases, Ar, Ne and He and for molecules, N_2 and CO_2. Here we focus on the results for Ar.

The photoabsorption cross sections of inert gases such as Ar can be as high as a few tens of megabarns in the XUV region. The M edge of Ar is near 15.76 eV. The aim of the experiment is to detect an absorption of 50%. This translates to, under thermodynamic equilibrium conditions, absorption lengths of 1 cm at a density on the order of 10^{22} m^{-3}[14] (See Table A.1).

In this ultrafast soft x-ray photoabsorption experiment, Ar gas was delivered into the chamber from a BOC cylinder with backing pressure of 2.6 bar. The nozzle deployed to inject gas is of 200 μm in diameter. This is attached to the flange of XYZ-manipulator with five miniports. HHG probe pulses were produced in a vacuum chamber upstream in which Ar gas is the HHG medium. The pressure maintained in the interaction chamber after 2.6 bar of Ar has been introduced is $\approx 1.5 \times 10^{-2}$ mbar.

The results of ultrafast photoabsorption spectroscopy are presented here. In Figure (A.3), we show the readout by the CCD array detectors. The detection of the CCD array across

the X-axis corresponds to the wavelengths of the soft x-rays. The exposure time of the CCD camera is 25 ms, which for a 1 kHz repetition rate driving beam corresponds to 25 shots. The CCD readout signals along the Y-axis has been combined, or 'binned' by a factor of 8. This improves the readout speed while the spatial resolution in the Y-axis is reduced. The colors in the figures corresponds to intensities, where red is most intense. Please note colors are not to scale.

Figure (A.4) shows the absorbance of the first four peaks shown in Figure (A.3), constructed from the HHG intensity data for the no-gas case and the gas case. The fifth peak, which is at the far end of the detector range and showing near-zero absorbance, has been omitted. We compare our experimental absorbances with the photoionization cross-sections given by Marr and West [15]. We have scaled these cross-sections in the figure to calibrate to our experimental results. Note that the proportionality factor between the absorbance and the cross-sections is the density-distance, i.e. the argon density integrated along the length of the optical path. Note that argon ionizes at 15.76 eV, which is the location of the M-edge. After a jump at that energy the cross-section grows to its maximum at 19 eV and then drops off. Our measurements are in the region of this drop-off and that is why we see a clear reduction in the absorbance with increasing harmonic energy.

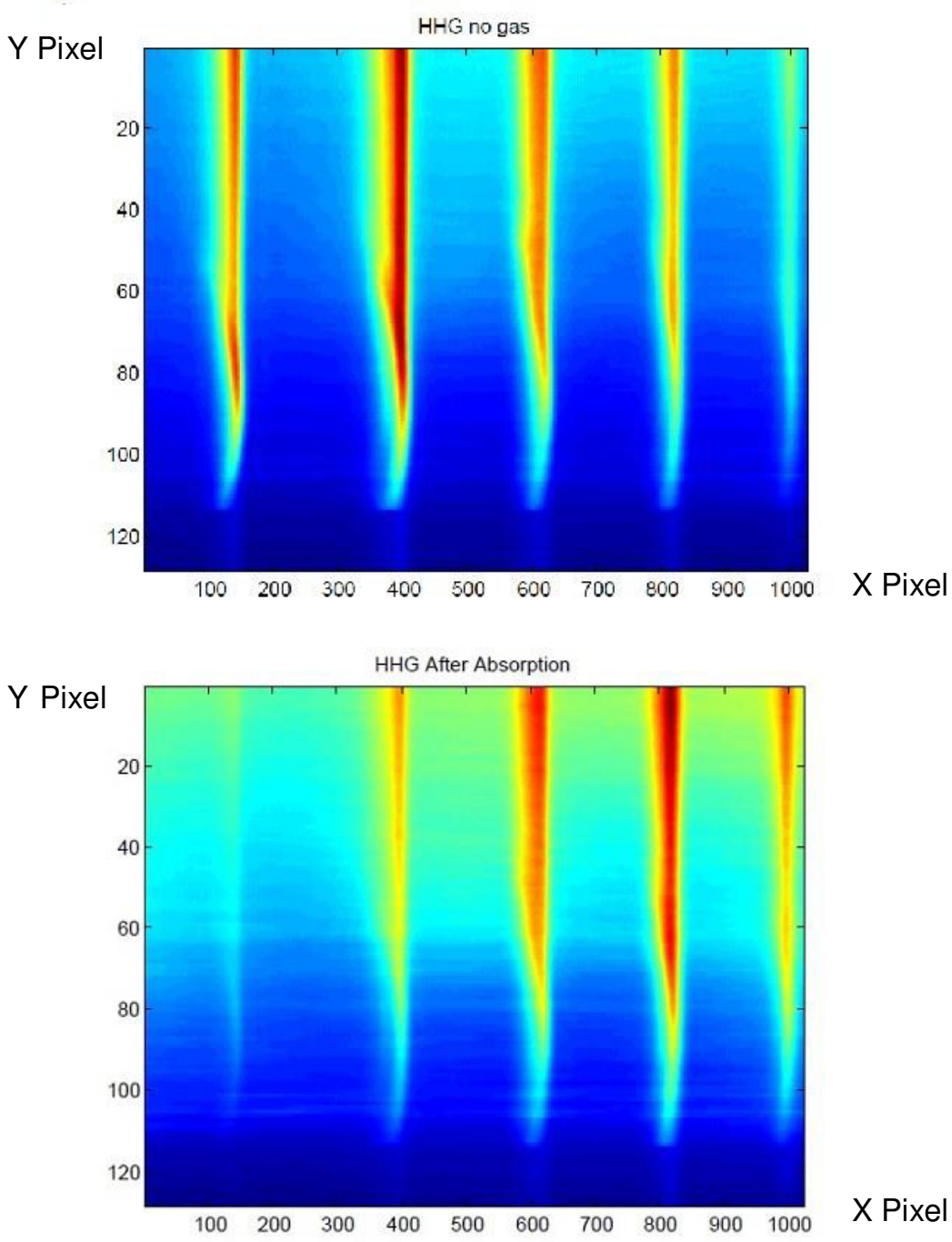

Figure A.3: Raw images from Andor Soft x-ray spectrometer. Top: HHG Spectra with no gas in the Interaction Chamber. Bottom: HHG Spectra with 2.6 bar backing pressure of Ar in the Interaction Chamber. The X axis denotes the pixel number and Y axis denotes a binned pixel number of the CCD detector

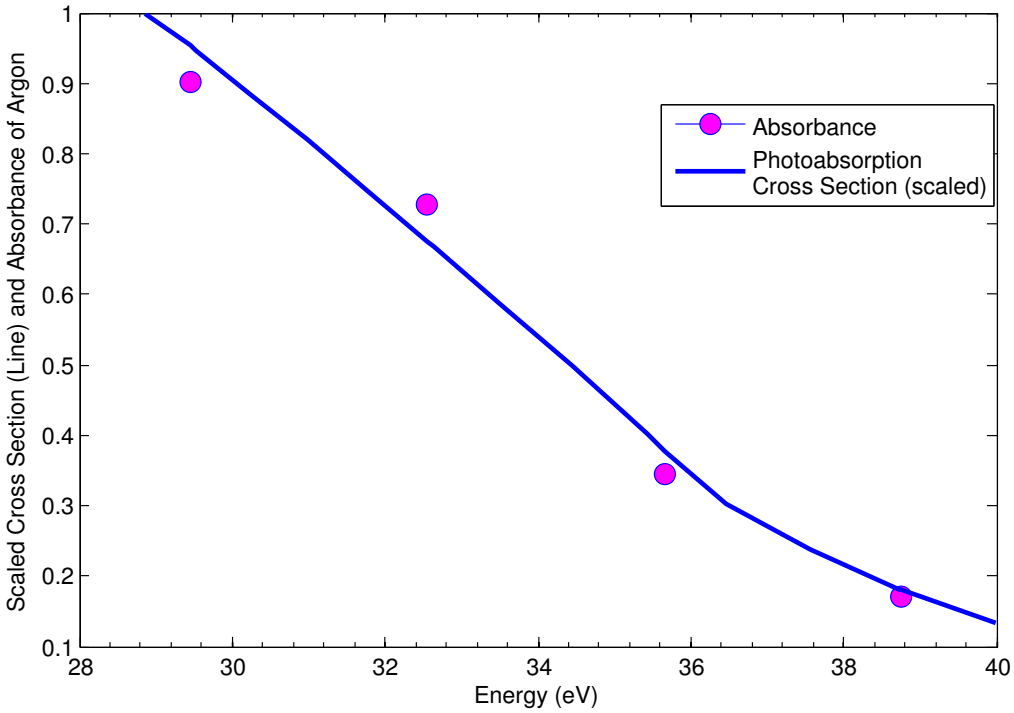

Figure A.4: HHG absorbance in Ar (points), compared to scaled photo-absorption cross-sections from Marr and West [15]. The factor scaling the cross-sections is the density of the Ar gas integrated over the optical path.

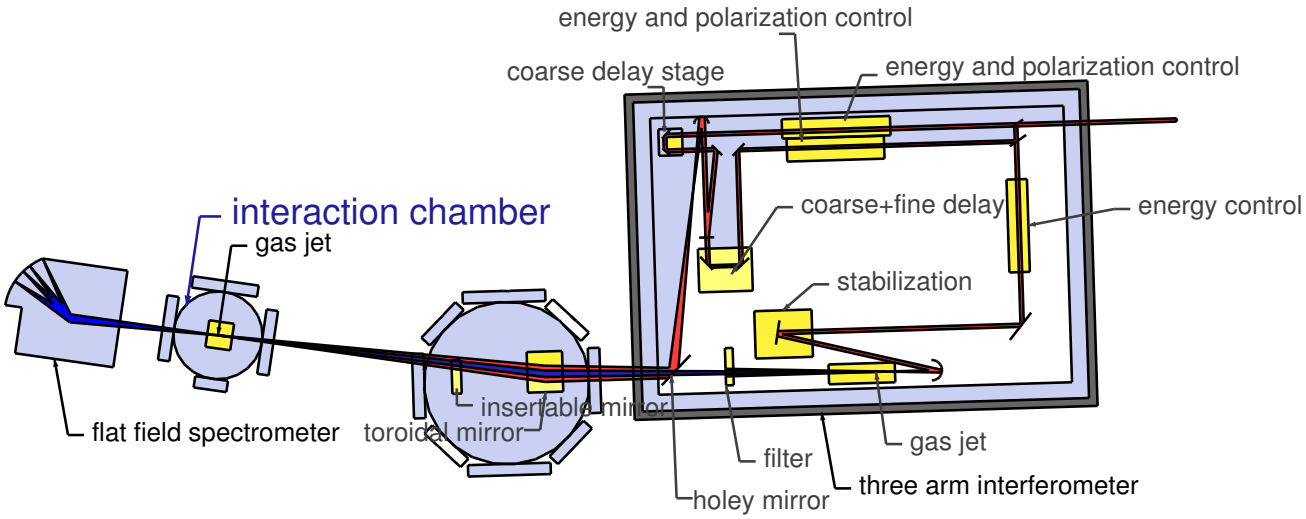

Figure A.5: The New Imperial College Beamline

A.5 New Beamline

This experiment serves as one of the first tests of ultrafast absorption spectroscopy for atoms and molecules for the new beamline set-up, see Figure (A.5). My contributions are mainly the new interaction chamber and the vacuum-grade metal filter holder. The interaction chamber, as designed and implemented, has achieved the amount of absorption which we aimed for, $\approx$ 50 %. The custom built vacuum compatible metal filter holder allows for a range of thin-film metal filters, Al, Zr, or In, to spectrally filter the HHG beam. These features allow for future attosecond transient absorption experiments to take place.

Appendix B

Atomic Units

Hartree [72] atomic units are useful to reign in numerical values, shorten equations and improve understandability on the atomic scale. They are used throughout this thesis

mass	$9.10938291 \times 10^{-31}$	[kg]	electron mass
charge	$1.602176565 \times 10^{-19}$	[C]	elementary charge
action	$1.054571726 \times 10^{-34}$	[Js]	reduced Planck's constant $\hbar$
length	$5.291772192 \times 10^{-11}$	[m]	Bohr radius
time	$2.418884326505 \times 10^{-17}$	[s]	
energy	$4.35974417 \times 10^{-18}$	[J]	$= 27.2113833$ eV
velocity	$2.1876912633 \times 10^{6}$	[m/s]	$= \alpha c$
electric field	$5.14220652 \times 10^{11}$	[V/m]	
electric dipole	$8.47835326 \times 10^{-30}$	[Cm]	electric dipole moment
power	0.1802378114	[W=J/s]	
intensity	$6.436409323 \times 10^{19}$	[W/m^2]	$I = E^2/(8\pi\alpha)$ for laser in a.u.
line strength	$7.188247626 \times 10^{-59}$	[C^2 m^2]	

Appendix C

Numerical Solution of the Liouvillian ODE

We need to solve a time dependent ordinary differential equation of the matrix type. A good algorithm for solving such a problem is 4th order Runge-Kutta [33]. This algorithm is often used but rarely explained even in textbooks, so we present a derivation below.
We would like to solve a problem of the type

$$\dot{f}(t) = L(t)f(t) \tag{C.1}$$

where L is a large time dependent matrix and f is a vector. Starting at time 0 we can give a formal solution in terms of time-ordered integrals

$$f(t) = f(0) + \sum_{n=1} \int_0^t dt_n \int_0^{t_n} dt_{n-1} \cdots \int_0^{t_2} dt_1 L(t_n)L(t_{n-1}) \cdots L(t_1)f(0) \tag{C.2}$$

Expanding $L(t)$s around 0 and doing the integrals we find, using the notation $L_t = L(t)$ and $L = L(0)$,

$$\begin{aligned}
\int_0^t dt_1 L_{t_1} &= tL + \frac{t^2}{2}\dot{L} + \frac{t^3}{6}\ddot{L} + \frac{t^4}{24}\dddot{L} + \mathcal{O}(t^5) \\
\int_0^t\int_0^{t_2} dt_2 dt_1 L_{t_2} L_{t_1} &= \frac{t^2}{2}L^2 + \frac{t^3}{6}(2\dot{L}L + L\dot{L}) + \frac{t^3}{24}(3\ddot{L}L + 3\dot{L}^2 + L\ddot{L}) + \mathcal{O}(t^5) \\
\int_0^t\int_0^{t_3}\int_0^{t_2} dt_3 dt_2 dt_1 L_{t_3} L_{t_2} L_{t_1} &= \frac{t^3}{6}L^3 + \frac{t^4}{24}(3\dot{L}L^2 + 2L\dot{L}L + L^2\dot{L}) + \mathcal{O}(t^5) \\
\int_0^t\int_0^{t_4}\int_0^{t_3}\int_0^{t_2} dt_4 dt_3 dt_2 dt_1 L_{t_4} L_{t_3} L_{t_2} L_{t_1} &= \frac{t^4}{24}L^4 + \mathcal{O}(t^5)
\end{aligned} \tag{C.3}$$

Generally we do not have the time derivatives of L available. Furthermore it is often only computationally feasible to get L at a few points on the interval $[0, t]$. We choose three time points and rewrite the integrals above in terms of L_0, $L_{t/2}$ and L_t only.

$$\begin{aligned}
\int_0^t dt_1 L_{t_1} &= \frac{t}{6}(L_0 + 4L_{t/2} + L_t) + \mathcal{O}(t^5) \\
\int_0^t\int_0^{t_2} dt_2 dt_1 L_{t_2} L_{t_1} &= \frac{t^2}{6}(L_{t/2}L_0 + L_{t/2}^2 + L_t L_{t/2}) + \mathcal{O}(t^5) \\
\int_0^t\int_0^{t_3}\int_0^{t_2} dt_3 dt_2 dt_1 L_{t_3} L_{t_2} L_{t_1} &= \frac{t^3}{12}(L_{t/2}^2 L_0 + L_t L_{t/2}^2) + \mathcal{O}(t^5) \\
\int_0^t\int_0^{t_4}\int_0^{t_3}\int_0^{t_2} dt_4 dt_3 dt_2 dt_1 L_{t_4} L_{t_3} L_{t_2} L_{t_1} &= \frac{t^4}{24}L_t L_{t/2}^2 L_0 + \mathcal{O}(t^5)
\end{aligned} \tag{C.4}$$

The decomposition in the first line is unique and is known as Simpson's rule. The decomposition in the second line is also unique. Note the time ordering of the operators. The decompositions in the third and fourth line are correct but not unique. Their structure is gleaned from what follows now.

The results obtained can be decomposed into a four stage structure as follows

$$\begin{aligned}
k_0 &= L_0 f_0 \\
k_1 &= L_{t/2}(f_0 + \frac{t}{2}k_0) \\
k_2 &= L_{t/2}(f_0 + \frac{t}{2}k_1) \\
k_3 &= L_t(f_0 + tk_2)
\end{aligned} \tag{C.5}$$

leading to

$$f_t = f_0 + \frac{t}{6}(k_0 + 2k_1 + 2k_2 + k_3) + \mathcal{O}(t^5) \tag{C.6}$$

This is the famous Runge-Kutta method applied to a linear ODE. We use this 4th order Runge-Kutta method to simulate the time development of the density matrix via $\dot{\rho} = \mathcal{L}\rho$ in the N^2 by N^2 space.

More sophisticated versions of the Runge Kutta algorithm do exist which can dynamically adjust step size in order to keep error under control. However, these are not needed here. The simulations we ran behaved perfectly well under constant time-step and the size of the time step was determined much more by the fast features of the probe pulse than anything else. A typical time step used was 0.1 a.u. = 2.42 as. The convergence of the numerical results was checked in two ways. First, total conservation of probability was checked, which would start to suffer if time quantization is too rough, and we kept this error under 1 part in 10^{14}. Second, a second simulation was run with half the time step to check the stability of computed values.

Appendix D

GRASP2K

In this thesis, we have utilized the GRASP package developed by I.P. Grant and his team. The most frequently used versions are GRASP92 and GRASP2K [40][41][73]. We have been using the modern version, GRASP2K. The challenge to get this package to work is twofold: first, compilation on the computing platform of choice, second, arranging for proper input parameters as the software is very rich in features.

GRASP2K is about 15MB in size as shipped. The package is designed to run on Ubuntu, Suse and Debian Linux 64-bit and with at least 500MB of RAM. We have ported the code to run under Windows 7 with 6GB of RAM. Makefiles were rewritten to adapt to Windows 7. Paths were modified for the local directories on the disk. The Fortran compiler used is GNU Fortran, Release 4.8.1 for Windows. When compiling the code, the following flags were set: -fcray-pointer -O0 -fno-automatic -static-libgfortran in order to build the libraries and executables successfully. Special thanks go to Prof. Ian Grant for pointing out the difficulties of compiling *jjgen* program with many nested loops [74].

The suite of libraries, such as libblas.a liblapackd.a libdvdson.a, are compiled and linked into the suite of executables. Script files such as rsave have been modified for the local directory structure. Grant's papers [40][41][73][75] provide details of relativistic calculations for Mg I, Li I, B II, Si VIII and Mo XXXVIII. Here we will provide the details of GRASP calculations for Kr II, which are comparable to the results provided by Max-Planck-Institute

für Quantenoptik in Garching (MPQ)[2] and MIT[42].
We include the ground levels of Kr II, the inner-shell holes in 4s and 3d, specifically $4s^{-1}_{1/2}$, $3d^{-1}_{5/2}$ and $3d^{-1}_{3/2}$. The order which the programs is run in is as follows (for the general case see the manual and papers [40][41][73][74][75], here we provide specific details for KrII):

1. **iso** : generates the neutrally charged nuclear data. The ionic state is determined by the number of electrons filled in the orbitals in *jjgen*. For Kr, the atomic number is 36, mass number 84, and the atomic weight is 83.80 a.u. The nuclear spin, nuclear dipole moment and nuclear quadrupole moment are all set to 1, the default value. The output file is isodata and constitutes an input data file for some of the programs below.

2. **jjgen** : the configuration states list (CSL) file is created based on the reference configurations included and treatments of the inner shell and valence electrons. For singly charged Kr, the $4p^{-1}_{3/2}$ and $4p^{-1}_{1/2}$ ground levels are odd and the $4s^{-1}_{1/2}$, $3d^{-1}_{5/2}$ and $3d^{-1}_{3/2}$ are even. The core is chosen to be closed with 18 electrons. The remaining 17 electrons are chosen to be active. Both odd and even states are included in one generation run of jjgen. The number of excitation is chosen to be one.

3. **jsplit** : the program orders the CSL into blocks by J and parity and allows the user to discard any duplicates. In our case, duplicates are not discarded.

4. **mcp** : mcp computes the integrations of angular momentum.

5. **erwf** : the program estimates the relativistic wavefunctions. The program allows one to choose between a Thomas-Fermi potential or screened hydrogenic functions to generate initial estimates for the radial orbitals. Results from previous runs can be used. This program produces an output file, rwfn.inp, which is an input for the next program, rscf.

6. **rscf** : This program determines the expansion coefficients by applying self consistent field (SCF) procedure. For Kr II, the orbitals varied are 3s, 3p, 3d, 4s and 4p. 4f orbitals are not varied as the energies associated are much further away and do not lend to convergence of a solution. The files generated are rmix.out, rwfn.out, rscf.sum.

7. **rsave** : This script file moves the output files from rscf program to a named file with extensions .w, .c, .sum, and .m to be used as input files for rci, jj2lsj, biotra, and bioscl programs.

8. **rci** : This program calculates the configuration interaction (CI) eigenvalues and eigenvectors with corrections for Breit interaction, transverse photon, vacuum polarization. Self energy estimates are done for levels up to n=3. This produces corresponding .cm and .csum files.

9. **bioscl** : After preparing .cbm .bw and .bm files from the corresponding .cm .w and .m files, we can run bioscl to obtain the oscillator strengths, Einstein's A coefficients, line strengths between the energy levels. The oscillator strengths are adjusted for statistical weights. Einstein's coefficients are in s^{-1}. The results are given in both velocity and lengths gauges. For the transitions, , the A coefficients are $9.33306\times10^{9}s^{-1}$ and $9.62556\times10^{9}s^{-1}$ within 3%. The result used by MPQ appears to be 6.91869e-02, the Coulombic (velocity) gauge of line strength.

Appendix E

Wigner Eckart

Some good references regarding the geometrical factors for the matrix elements of operators are Edmonds [50], Messiah [58], Zare [76] and Cowan [77].
The algorithm we used to compute Wigner "3j" symbols and the relationship with Clebsch-Gordan coefficients are explained in Messiah, Volume II, appendix C [58].

$$\begin{pmatrix} j_1 & j_2 & J \\ m_1 & m_2 & -M \end{pmatrix} = \frac{(-)^{j_1-j_2+M}}{\sqrt{2J+1}} \langle j_1 j_2 m_1 m_2 | JM \rangle \tag{E.1}$$

The Wigner-Eckart theorem is stated as follows [50][76][77]

$$\boxed{\langle n_1 j_1 m_1 | T^k_q(A) | n_2 j_2 m_2 \rangle = (-)^{j_1-m_1} \begin{pmatrix} j_1 & k & j_2 \\ -m_1 & q & m_2 \end{pmatrix} \langle n_1 j_1 || T^k(A) || n_2 j_2 \rangle} \tag{E.2}$$

Some sum rules

$$\sum_{m_1 m_2} \begin{pmatrix} j_1 & 1 & j_2 \\ -m_1 & q & m_2 \end{pmatrix}^2 = \frac{1}{3} \tag{E.3}$$

independent of q. Summing over the three values of q gives one.

The Wigner $3j$ symbol has many symmetries one of which is the appearance of a phase factor when all m flip sign [50]

$$\begin{pmatrix} j_1 & j_2 & j_3 \\ -m_1 & -m_2 & -m_3 \end{pmatrix} = (-)^{j_1+j_2+j_3} \begin{pmatrix} j_1 & j_2 & j_3 \\ m_1 & m_2 & m_3 \end{pmatrix} \tag{E.4}$$

Note also that the very same phase factor appears under any odd permutation of the columns. Using these properties we derive, dropping some parameters for simplicity of notation,

$$\begin{aligned} \langle j_1\, {-m}|T^1_q|j_2\, {-m}\rangle &= (-)^{j_1+m} \begin{pmatrix} j_1 & 1 & j_2 \\ m & q & -m \end{pmatrix} \langle j_1||T^1||j_2\rangle \\ &= (-)^{2j_1+1+j_2+m} \begin{pmatrix} j_1 & 1 & j_2 \\ -m & -q & m \end{pmatrix} \langle j_1||T^1||j_2\rangle \\ &= (-)^{j_2-j_1+1} \langle j_1\, m|T^1_{-q}|j_2\, m\rangle \end{aligned} \tag{E.5}$$

This expression is useful for comparing matrix elements of opposite m for a dipole interaction caused by a polarized probe beam. Also useful is, combining odd column permutation with flipping the m values including q,

$$\begin{aligned} (-)^{j_f-m_f} \begin{pmatrix} j_f & k & j_i \\ -m_f & q & m_i \end{pmatrix} &= (-)^{j_f-m_f} \begin{pmatrix} j_i & k & j_f \\ -m_i & -q & m_f \end{pmatrix} \\ &= (-)^{j_f-j_i-q}(-)^{j_i-m_i} \begin{pmatrix} j_i & k & j_f \\ -m_i & -q & m_f \end{pmatrix} \end{aligned} \tag{E.6}$$

displaying the phase factor $(-)^{j_f-j_i-q}$ the Wigner-Eckart factor acquires when exchanging final and initial states, including a flip of q.

Because the dipole tensor is spatially antisymmetric we have

$$T^{1\dagger}_q = (-)^{-q}\, T^1_{-q} \tag{E.7}$$

this can be used to derive [76]

$$\langle \alpha' j' || T^1 || \alpha j \rangle^* = (-)^{j-j'} \langle \alpha j || T^1 || \alpha' j' \rangle \tag{E.8}$$

The tables below give the Wigner-Eckart coefficients

$$(-)^{j_1 - m_1} \begin{pmatrix} j_1 & k & j_2 \\ -m_1 & q & m_2 \end{pmatrix} \tag{E.9}$$

for $k = 1$, $q \in \{-1, 0, 1\}$ and j values useful in this thesis. We computed these tables from algorithms given by Messiah [58]. Note that $m_f = q + m_i$ for a non-zero entry. Therefore, the coefficients for T^1_0 are given on the diagonal of the table, the coefficients for T^1_{-1} are given on the up-shifted diagonal, while the coefficients for T^1_1 are given on the down-shifted diagonal. The asterisk notation means that the final initial exchange phase factor $(-)^{j_f - j_i - q}$ is negative, see equation E.6, and can be used to find the Wigner-Eckart factors for $j_f < j_i$.

$\langle T^1_q \rangle$	$-1/2$	$1/2$
$-3/2$	$1/2$	
$-1/2$	$\sqrt{1/6}^*$	$\sqrt{1/12}$
$1/2$	$\sqrt{1/12}$	$\sqrt{1/6}^*$
$3/2$		$1/2$

Table E.1: Wigner-Eckart coefficients for $j_f = 3/2$, $j_i = 1/2$.

$\langle T^1_q \rangle$	$-3/2$	$-1/2$	$1/2$	$3/2$
$-3/2$	$-\sqrt{3/20}$	$\sqrt{1/10}^*$		
$-1/2$	$-\sqrt{1/10}^*$	$-\sqrt{1/60}$	$\sqrt{2/15}^*$	
$1/2$		$-\sqrt{2/15}^*$	$\sqrt{1/60}$	$\sqrt{1/10}^*$
$3/2$			$-\sqrt{1/10}^*$	$\sqrt{3/20}$

Table E.2: Wigner-Eckart coefficients for $j_f = 3/2$, $j_i = 3/2$.

$\langle T^1_q \rangle$	$-3/2$	$-1/2$	$1/2$	$3/2$
$-5/2$	$\sqrt{1/6}$			
$-3/2$	$\sqrt{1/15}^*$	$\sqrt{1/10}$		
$-1/2$	$\sqrt{1/60}$	$\sqrt{1/10}^*$	$\sqrt{1/20}$	
$1/2$		$\sqrt{1/20}$	$\sqrt{1/10}^*$	$\sqrt{1/60}$
$3/2$			$\sqrt{1/10}$	$\sqrt{1/15}^*$
$5/2$				$\sqrt{1/6}$

Table E.3: Wigner-Eckart coefficients for $j_f = 5/2$, $j_i = 3/2$.

Appendix F

Line Factors

Using the algorithms described in Messiah [58] we have written code for the calculation of Clebsch-Gordan coefficients, Wigner-3j symbols, Wigner-6j symbols and Racah W coefficients. We have computed the line factors for pure LS coupling the doublet $S = 1/2$. The results are consistent with Shore [78]. Note that there is a convention difference with the line factors given by Cowan, appendix I [77]. This difference is explained by a convention difference between the set $\{L, J\}$ and $\{L', J'\}$ which under exchange can flip the sign. The sign factor under flipping is $(-)^{L-L'+J'-J}$. The table is computed from the following expression for the line factors in pure LS coupling [78]

$$\langle \alpha SLJ||R^1||\alpha' S'L'J'\rangle = \sqrt{2J+1}\ \sqrt{2J'+1}\ W(SJL'1;LJ')\ \langle \alpha L||R^1||\alpha' L'\rangle\ \delta_{SS'} \tag{F.1}$$

where the Racah W coefficient is expressed in the Wigner-"6j" symbol as

$$W(SJL'1;LJ') = (-)^{S+J+L'+1} \begin{Bmatrix} S & J & L \\ 1 & L' & J' \end{Bmatrix} \tag{F.2}$$

L	L'	J	J'	Factor	Flip
S	S	1/2	1/2	0	+
S	P	1/2	1/2	$-\sqrt{2}/3$	−
		1/2	3/2	$2\sqrt{3}/3$	+
P	P	1/2	1/2	$2/3$	+
		1/2	3/2	$\sqrt{2}/3$	−
		3/2	1/2	$-\sqrt{2}/3$	−
		3/2	3/2	$\sqrt{10}/3$	+
P	D	1/2	3/2	$\sqrt{2/3}$	+
		3/2	3/2	$-\sqrt{2/15}$	−
		3/2	5/2	$\sqrt{6/5}$	+
D	D	3/2	3/2	$3\sqrt{2}/5$	+
		3/2	5/2	$\sqrt{2}/5$	−
		5/2	3/2	$-\sqrt{2}/5$	−
		5/2	5/2	$2\sqrt{7}/5$	+

Table F.1: Doublet (S=1/2) Line Factors for LS coupling

We derive a symmetry property of the Racah W coefficient. The relationship with the Wigner "6j" symbol is given as

$$W(abcd;ef) = (-)^{a+b+c+d} \left\{ \begin{array}{ccc} a & b & e \\ d & c & f \end{array} \right\} \tag{F.3}$$

See Edmonds [50], page 97, or Zare [76], page 145.

The Wigner "6j" symbol has various symmetries the most important of which are that it is invariant under any permutation of its columns and that it is invariant under the exchange of upper and lower arguments in any two columns [50].

From these symmetries we derive for the Racah W coefficient that

$$W(SJL'1;LJ') = (-)^{S+J+L'+1} \left\{ \begin{array}{ccc} S & J & L \\ 1 & L' & J' \end{array} \right\} = (-)^{S+J+L'+1} \left\{ \begin{array}{ccc} S & L & J \\ 1 & J' & L' \end{array} \right\}$$
$$= (-)^{S+J+L'+1} \left\{ \begin{array}{ccc} S & J' & L' \\ 1 & L & J \end{array} \right\} = (-)^{J-J'+L'-L} W(SJ'L1;L'J) \qquad \text{(F.4)}$$

Appendix G

Molcas, ADC and ALTDSE

The simulation results in Chapter 7 are generated by deploying Molcas [70], ADC [65] and ALTDSE [64][54] programs. First, the basis sets are built from EMSL (Environmental Molecular Sciences Laboratory) Basis Exchange [67] augmented with Kaufmann-Baumeister-Jungen (KBJ) continuum-like diffuse Gaussian functions [69]. The diffuse functions are Gaussian functions with small zetas ζ to better describe the tail portion of the atomic orbitals. For benzene cc-pVTZ (correlation-consistent polarized Valence-only-basis sets with D-double zeta, T-triple zeta, Q-quadruple zeta, 5-quintuple zeta) are deployed. According to the Molcas online documentation Section 6.38.0.3 "Structure of the all electron basis set library", the format of the basis functions are as follows: charge of the atom and the highest angular momentum, then for each of the angular momenta, the number of the ζ exponents and contracted Gaussian-type orbitals (CGTOs), followed by the columns of exponents and for each CGTO, the contracted coefficients.

For running Molcas, the GATEWAY program is first called which produces the character table for benzene:

Character Table for D2h

	E	s(yz)	s(xz)	C2(z)	s(xy)	C2(y)	C2(x)	i	
ag	1	1	1	1	1	1	1	1	
b3u	1	-1	1	-1	1	-1	1	-1	x
b2u	1	1	-1	-1	1	1	-1	-1	y
b1g	1	-1	-1	1	1	-1	-1	1	xy, Rz
b1u	1	1	1	1	-1	-1	-1	-1	z
b2g	1	-1	1	-1	-1	1	-1	1	xz, Ry
b3g	1	1	-1	-1	-1	-1	1	1	yz, Rx
au	1	-1	-1	1	-1	1	1	-1	I

We use the subgroup D2h instead of D6h for benzene because non-abelian point groups were not supported by the ADC software used. We map the first column to integers, b3u→2, b2u→3, b1u→5, and use these as inputs in our next program ADC. In Molcas, the Self Consistent Field (SCF) program is called after the SEWARD program. The MOTRA program within Molcas is called to transform the electron repulsion integrals produced by SEWARD from the atomic orbitals (AO) to the molecular orbital (MO) basis. These outputs are contained in TRAONE and TRAINT.

Two runs are required with the ADC program, first run: with keyword `info` = 1, `hcentre` = 1, and the following pertinent parameters, `method` = 1 (for ADC1), `POLARIZATION = 'LIN'` (linear), `DIPOLESYM`=2,3,5 (as seen in the character table), `nirrep2`=3 (for y as seen in the character table). This will produce an output file in which we can extract the occupied orbital numbers. In the second run, the `hcentre` parameter is updated with these occupied orbital numbers and `info` =0. The Hamiltonian and dipole files are generated subsequently.

The input parameters for the ALTDSE programs are as follows: `peakfield` is the peak intensity in W/cm^2, `phoene` is the photon energy in a.u., `timeduration` is the time duration

of the pulse in seconds, `pulse_type` is 1 for a $\sin^2$ pulse, `DIRECTION` specifies the polarization, `ARNOLDI nkrylov` is 25, the dimension of the Krylov space, and `timestep` and `timestepfree` are in units of the laser cycle. A description of the parameters can be found in [64].

A set of output files are generated: fort.133, fort.140, fort.141, fort.142, fort.143, fort.144. Fort.133 contains the survival probability, fort.140 contains the electric field, fort.(141,142,143) contain the dipole response in the (x,y,z) directions respectively, and fort.144 contains the excitation probability.